Optically addressable spins in silicon carbide and related 2D materials :

the role of symmetry and spin-orbit coupling

Carmem M. Gilardoni

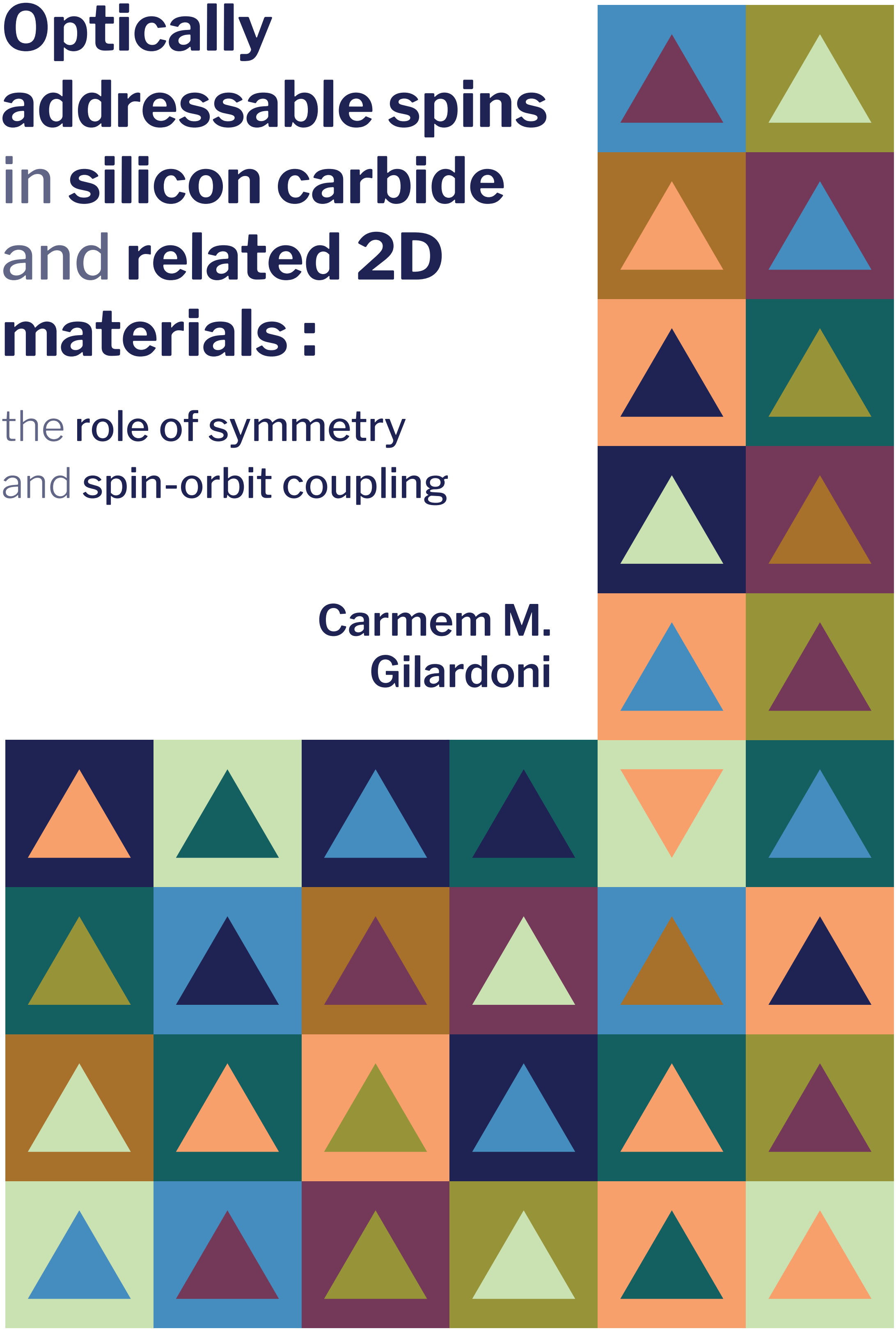

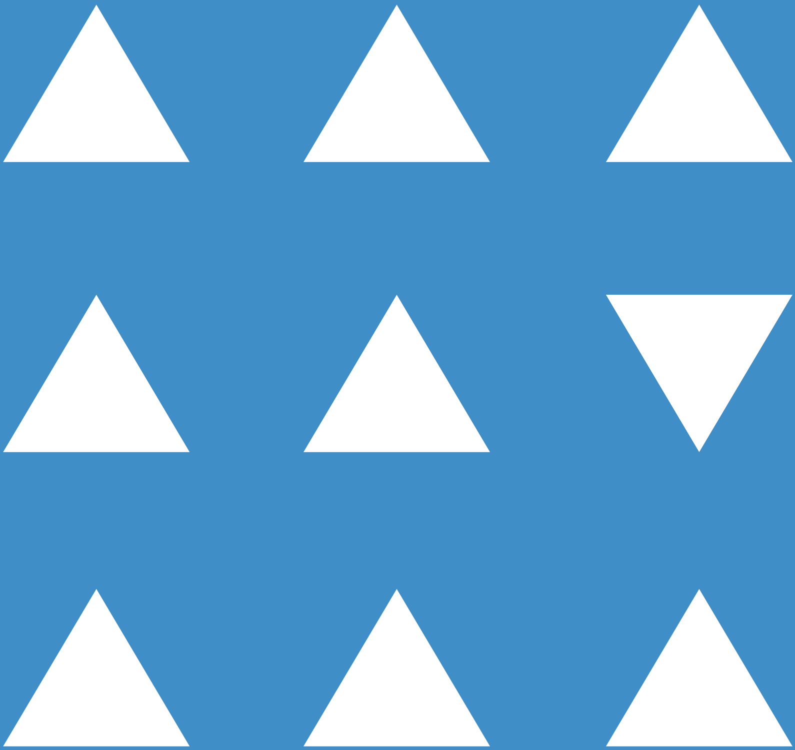

Book cover: Similar to crystals, the pattern is formed by triangular shapes composing colored modules which form a firm structure, through consistency and familiarity, although still subject to defects. Cover design by Átila Perassa Coêlho.

rijksuniversiteit
groningen

Physics of
Nanodevices

Zernike Institute PhD thesis series 2021-32
ISSN: 1570-1530

The work described in this thesis was performed in the research group Physics of Nanodevices of the Zernike Institute for Advanced Materials at the University of Groningen, the Netherlands. The project was funded via the PhD Scholarship Programme of the University of Groningen.

Printed by: GVO drukkers & vormgevers B.V.

rijksuniversiteit
groningen

Optically addressable spins in silicon carbide and related 2D materials

The effect of symmetry and spin-orbit coupling

Proefschrift

ter verkrijging van de graad van doctor aan de
Rijksuniversiteit Groningen
op gezag van de
Rector Magnificus Prof. C. Wijmenga
en volgens besluit van het College voor Promoties.

De openbare verdediging zal plaatsvinden op

vrijdag 3 december 2021 om 14:30 uur

door

Carmem Maia Gilardoni

geboren op 18 februari 1993
te Brasília, Brazilië

Promotor
Prof. dr. ir. C. H. van der Wal

Copromotor
Dr. R. W. A. Havenith

Beoordelingscommissie
Prof. dr. S. S. Faraji
Prof. dr. ir. F. A. Zwanenburg
Prof. dr. M. Atatüre

Contents

Summary

Quantum information technology allows us to process information differently than classical information processing and could enable fundamentally secure communication. The basic building block for the implementation of quantum applications is a qubit, a processing unit whose state is determined by the laws of quantum mechanics. Long-distance remote operation of qubits can be achieved using photons, such that one of the big challenges in the field is to find materials that will efficiently hold onto their quantum information and transfer it into light particles on demand. Some of the major contenders in the field are color centers present in crystalline materials like diamond or silicon. These color centers behave like artificial molecules trapped in the crystals: they vibrate and interact with light as a molecule would, but the shape of these molecule-like systems is determined by the crystal around them. The spin of electrons or nuclei in these color centers can be used to store quantum information efficiently. A photon emitted by such a color center can provide information about the quantum mechanical state of the color center electron spins, offering a pathway for light-matter entanglement protocols necessary for quantum communication.

Of particular relevance are material platforms and color centers that are compatible with existing technological infrastructure. Silicon carbide is a semiconductor that is widely used for high-power, high-temperature electronic applications, and has well-established growth and processing techniques that grant it great versatility with respect to doping and device engineering. Additionally, it hosts a wide range of color centers that are optically active at (or close to) telecom-compatible wavelengths. The variety of color centers present in SiC materials, both extrinsic and intrinsic, provide a huge scope for the exploration of different defect centers. Investigation of the optical and spin-related properties of these color centers is often done on a defect-by-defect basis, and a generalized insight into how different microscopic features (like symmetry, coupling between electronic spins and other degrees of freedom, *etc.*) systematically influence experimental parameters relevant for quantum-optical operation is still lacking. Such insight could lead to a situation where defects can be designed on demand with particular applications in mind. In chapters 3-6 of this thesis, we explore ensembles of transition metal impurity defects in SiC with respect to their optical and spin-related properties, and gradually relate their experimental features to an analysis of their spatial and electronic configuration. Additionally, we generalize our observations for different localized and

delocalized electronic states (chapter 7) with similar symmetries in SiC and related materials.

For quantum-optical operation, some parameters are particularly important. Firstly, understanding how a defect's energy eigenstates depend on its environment may lead to defects especially suited for specific sensing applications, or to the engineering of devices and operation geometries with optimal spin-coherence properties. In chapter 3, we show that the electronic spins of Mo defects in SiC are insensitive (up to our measurement accuracy) to magnetic fields perpendicular to the SiC crystal c-axis. This axial anisotropy arises when the electronic eigenstates associated with the defect have a non-zero orbital angular momentum projection along this axis and spin and orbital degrees of freedom are strongly coupled via spin-orbit coupling. In this chapter, we use this insight to determine the microscopic geometry and charge state of this defect center. Defects with anisotropies of this type, where the electronic spin is only sensitive to magnetic fields in one particular direction, form ensembles with defects whose effective spins are all quantized in a highly homogeneous direction.

Secondly, a defect center must have ground-state spins that are relatively well isolated from the lattice. The timescales at which the localized spins exchange energy with the lattice (that is, the *spin-relaxation time*) and at which their quantum state evolution is disturbed by dynamic changes of their environment (that is, the *decoherence time*) must be long for reliable quantum-state storage and long-distance entanglement protocols. In chapters 4 and 6, we experimentally investigate how the spin-relaxation times of the transition metal defects studied here depend on their environment and the presence of thermally accessible excited states. In general, the coupling between spin and orbital degrees of freedom via spin-orbit coupling is thought to be detrimental to the stability of color-center spins. We show however in chapter 4 that in the particular case of a defect containing a single electron in double degenerate orbital states, spin-orbit coupling gives rise to isolated effective-spin-1/2 doublets that are partially symmetry-protected from direct spin relaxation and environment-induced spin precession. In this particular configuration, spin-orbit coupling in fact stabilizes the electronic spin in the defect center, leading to surprisingly long spin-relaxation times for Mo defects in SiC, above seconds below 3 K. In chapters 5 and 6, we show that this picture changes in the case of V defects in SiC due to the presence of a central nuclear spin-7/2 with 99% natural abundance. Although the electronic part of the eigenstates of Mo and V defects are very similar, the additional presence of the nuclear spin for V defects opens up pathways for magnetic and electric-dipole spin transitions that are forbidden for defects with nuclear spin zero. These additional transitions lead to a situation where the spin-relaxation rate of V defects is strongly dependent on the hyperfine-induced mixing of electronic spin sublevels. Nonetheless, they also enable microwave control with both electric and magnetic fields, with a favorable ratio for the trade-off between control and isolation of the quantum defects. In chapter 7, we show that the same physics responsible for stabilizing the localized electronic eigenstates of Mo defects in SiC leads to differences between electrons and holes in two-dimensional transition metal dichalcogenides with respect to their spin-scattering properties.

Lastly, optical operation of these localized spins relies on the optical initialization, control, and read-out of the spin state. To achieve this, the defects must emit photons preferably into the zero-phonon line (ZPL). The inhomogeneous broadening observed in the ZPL due to interactions between the defects and the crystalline environment must be small (such that two defects can emit photons that are indistinguishable from each other), and we must be able to initialize the ground-state spin via resonant driving of the optical transitions. Throughout this thesis, we demonstrate some of these requirements for ensembles of Mo and V defects in SiC. In chapters 3 and 4, we demonstrate that we can initialize Mo spins in SiC and detect them optically at cryogenic temperatures. Additionally, we show that we can drive the ensemble of Mo defects into a coherent superposition of ground-state sublevels all-optically via two-laser optical driving (coherent population trapping). In chapter 6, we show that the large number of hyperfine-coupled states, combined with the relatively fast spin-relaxation time limits the degree to which an ensemble of V defects can be optically initialized (when compared to ensembles of Mo defects), and achieving this remains a challenge for the implementation of these defect centers for quantum-communication applications. In this chapter, we also show that the inhomogeneous broadening of the optical transition lines depends strongly on the symmetry of the particular eigenstates involved in the transition, even in defect centers that lack inversion symmetry. In this way, the same defect center can have different optical transitions with varying robustness with respect to environmental broadening. This insight should be taken into account when determining optimal operation geometries.

With these results, we show that color centers in solids offer much more engineering choices and spread of performance (with respect to the relevant parameters for quantum-optical operation) than typically expected, even after 20 years of work on related systems. Relating the microscopic structure of these defect centers to the various observed figures of merit for quantum technological applications allows us to understand seemingly unintuitive results, and to predict how related systems will behave. In the fast-growing quantum technological environment, these approaches may open up pathways for the engineering of novel defect centers with particular applications in mind.

Samenvatting

Kwantum-informatietechnologie stelt ons in staat om informatie op een andere manier te verwerken dan op de klassieke wijze en om informatie te versturen op een fundamenteel veilige manier. Het aansturen van qubits op lange afstand kan met fotonen, waardoor één van de grote uitdagingen in dit veld het vinden van materialen is die efficiënt kwantuminformatie kunnen opslaan, maar die tegelijkertijd op afroep deze informatie kunnen afgeven in de vorm van licht. Goede kandidaten hiervoor zijn onder andere atomaire onzuiverheden in kristallijne materialen zoals diamant en silicium. De kleurencentra gedragen zich als kunstmatige moleculen die gevangen zitten in het kristal: ze trillen en reageren op licht op dezelfde manier als een molecuul, maar de vorm van deze molecuulachtige systemen wordt bepaald door het kristal rondom de centra. De elektron- of kernspin in de kleurencentra kan worden gebruikt om kwantuminformatie efficiënt op te slaan. Een foton dat wordt uitgezonden door zo'n centrum bevat informatie over de kwantummechanische toestand van de spin van het kleurencentrum, en biedt daarmee de mogelijkheid om licht en materie te verstrengelen zoals dat nodig is voor kwantumcommunicatie.

Met name de materialen en kleurencentra die inpasbaar zijn in de bestaande telecominfrastructuur zijn interessant. Siliciumcarbide is een halfgeleider die veel wordt gebruikt in toepassingen met hoog vermogen en hoge temperaturen. De processen om SiC te fabriceren en te bewerken zijn goed ontwikkeld, waardoor er veel mogelijk is met betrekking tot dotering en het ontwerpen van *devices*. Bovendien kan het een grote verscheidenheid aan kleurencentra huisvesten die optisch actief zijn bij golflengtes vlak bij of in de telecomband. De verscheidenheid aan kleurencentra, zowel intrinsieke als extrinsieke, die voorkomen in SiC biedt een grote hoeveelheid mogelijkheden om deze defecten nader te bestuderen. Onderzoek naar de optische- en spin-gerelateerde eigenschappen van deze kleurencentra gebeurt vaak per defect, waardoor overkoepelende inzichten over hoe de verschillende microscopische eigenschappen (zoals symmetrie, de koppeling tussen elektronspin en andere vrijheidsgraden, enz.) de experimentele parameters, die relevant zijn voor kwantum-optisch aansturing systematisch beïnvloeden, ontbreken. Zulke inzichten zouden de mogelijkheid kunnen bieden om op basis van de beoogde toepassing de meest geschikte defecten uit te kiezen. In hoofdstukken 3-6 van dit proefschrift bestuderen we de optische- en spin-gerelateerde eigenschappen van ensembles van defecten van overgangsmetalen, waarna we geleidelijk de experimentele kenmerken kunnen koppelen aan groepentheoretisch begrip van de elektronische structuur. Bovendien veralgemenen we onze waarnemingen voor verschillende gelokaliseerde en gedelokaliseerde elektronische toestanden met gelijke symmetrie in zowel SiC als in soortgelijke materialen.

Voor kwantum-optische aansturing zijn een aantal zaken in het bijzonder belangrijk. Ten eerste kan het begrip van hoe de energetische eigentoestanden van een defect afhankelijk zijn van zijn omgeving, ons naar defecten leiden die zeer geschikt zijn voor bepaalde toepassingen als sensor, maar ons ook *devices* of systemen laten ontwerpen voor optimale coherente eigenschappen van de spin. In hoofdstuk 3 tonen we aan dat de elektronenspin van Mo defecten in SiC niet gevoelig zijn (binnen onze meetnauwkeurigheid) voor magneetvelden die loodrecht staan op de c-as van het SiC kristal. Deze axiale anisotropie kan ontstaan wanneer de projectie van het orbitale impulsmoment van de elektronische eigentoestanden van het defect langs deze as niet-nul is en zowel de spin als andere vrijheidsgraden sterk gekoppeld zijn door spin-baankoppeling. In dit hoofdstuk gebruiken we dit inzicht om de microscopische geometrie en de ladingstoestand van dit defect te bepalen. Defecten met soortgelijke anisotropie, waar de elektronspin alleen gevoelig is voor magneetvelden in een zekere richting, vormen ensembles van defecten waarin de effectieve spins allen gekwantiseerd zijn in een zeer homogene richting.

Ten tweede moet een defect de eigenschap hebben dat de spin in de grondtoestand relatief goed is afgeschermd van het kristalrooster, zodat deze stabiel is en meerdere keren kan worden gebruikt voordat de kwantuminformatie verloren raakt. De tijdschaal waarmee gelokaliseerde spins energie uitwisselen (de spin-vervaltijd) en waarmee de voortgang van de kwantumtoestand wordt verstoord door dynamische veranderingen in hun omgeving (de decoherentietijd) moet lang zijn, zodat betrouwbare opslag van kwantumtoestanden mogelijk is en langeafstands-verstrengelingsprotocollen toegepast kunnen worden. In hoofdstuk 4 en 6 bepalen we experimenteel hoe de spin-vervaltijd van de overgangsmetaaldefecten die hier onderzocht worden afhankelijk zijn van hun omgeving en van de aanwezigheid van thermisch toegankelijke aangeslagen toestanden. Over het algemeen wordt aangenomen dat de koppeling tussen spin en orbitale vrijheidsgraden afbreuk doet aan de stabiliteit van spins in kleurencentra. In hoofdstuk 4 laten we echter zien dat in het specifieke geval waarin een defect een enkel elektron in een tweevoudig ontaarde orbitale toestand bevat, de spin-baan koppeling effectieve spin-1/2 doubletten veroorzaakt die gedeeltelijk door symmetrie worden afgeschermd van direct spin-verval en door de omgeving veroorzaakte spinprecessie. In deze specifieke configuratie stabiliseert de spin-baankoppeling juist de elektronische spin in het defect, waardoor verassend lange spin-vervaltijden mogelijk zijn in Mo defecten: meer dan enkele seconden onder de 3 K. In hoofdstuk 5 en 6 laten we zien dat dit beeld veranderd in het geval van V defecten in SiC door de aanwezigheid van een centrale kernspin-7/2, dat van nature met een aandeel van 99% voorkom. Alhoewel het elektronische deel van de eigentoestand van Mo en V defecten heel erg op elkaar lijkt, zorgt de aanwezigheid van kernspin in V defecten ervoor dat magnetische- en elektrische-dipoolspinovergangen die verboden zijn in defecten zonder kernspin, nu wel zijn toegestaan. Deze extra overgangen leiden tot een situatie waarin de spin-halfwaardetijd sterk afhankelijk is van de menging tussen de subniveau's van de elektronspin die wordt veroorzaakt de hyperfijnstructuur. Tegelijkertijd zorgt dit er ook voor dat aansturing met microgolven mogelijk is met zowel elektrische- als magneetvelden, met een gunstige verhouding tussen de aanstuurbaarheid en afscherming van het kwantumdefect. In hoofdstuk 7 tonen we aan dat dezelfde natuurkunde die zorgt voor stabilisatie van de gelokaliseerde elektronische eigentoestanden van Mo defecten in SiC, ook de verschillen in spinverstrooiingseigenschappen tussen elektronen en gaten veroorzaakt in tweedimensionale overgangsmetaaldichalcogeniden.

Ten slotte hangt de optische aansturing af van de optische initialisatie, aansturing en uitlezing van de spintoestand. Om zulke aansturing mogelijk te maken moeten de defecten fotonen uitzenden, bij voorkeur in de *zero-phonon line* (ZPL). De inhomogene verbreding van de ZPL, die wordt veroorzaakt door de wisselwerking tussen de defecten en de kristallijne omgeving, moet klein zijn, zodat als twee defecten elk een foton uitzenden deze niet van elkaar te onderscheiden zijn. Daarnaast moet het mogelijk zijn om de spin van de grondtoestand te initialiseren door de optische overgang resonant aan te slaan. Het werk in dit proefschrift laat zien dat we kunnen voldoen aan enkele van deze eisen met ensembles van Mo en V defecten in SiC. In hoofdstuk 3 en 4 laten we zien dat we Mo spins in SiC kunnen initialiseren en ze optisch kunnen detecteren op cryogene temperaturen. Bovendien tonen we aan dat we een ensemble van Mo defecten in een coherente superpositie van grondtoestandsubniveau's kunnen brengen met een volledig optische methode, namelijk twee-laseraandrijving (*coherent population trapping*). In hoofdstuk 6 laten we zien dat het grote aantal hyperfijn-gekoppelde toestanden, gecombineerd met de relatief snelle spin-vervaltijd, de mate waarin een ensemble van V defecten optisch kan worden geïnitialiseerd beperkt is in vergelijking met Mo defecten. Het blijft vooralsnog een uitdaging om dit te verbeteren voordat deze defecten kunnen worden toegepast in de kwantumcommunicatie. Daarnaast laten we in dit hoofdstuk zien dat de inhomogene verbreding van de optische overgangslijnen sterk afhankelijk is van de symmetrie van de specifieke eigentoestanden die betrokken zijn bij de overgang, zelfs in defecten zonder inversiesymmetrie. Op deze manier kan één en het zelfde defect verschillende optische overgangen hebben met elk een andere robuustheid ten opzichte van verbreding door omgevingsinvloeden. Dit inzicht moet mee worden genomen bij het bepalen van een optimale geometrie voor de aansturing.

Met deze resultaten tonen we aan dat kleurencentra in vaste stoffen veel meer ontwerpkeuzes bieden en een veel groter prestatiebereik hebben (wat betreft de relevante parameters voor kwantumoptische aansturing) dan waar normaal vanuit wordt gegaan, zelfs na meer dan 20 jaar onderzoek naar soortgelijke systemen. Door de microscopische structuur van deze defecten te verbinden aan de verscheidene factoren die belangrijk zijn voor toepassingen in de kwantumtechnologie kunnen we in eerste instantie onlogische resultaten beter begrijpen en voorspellen hoe soortgelijke systemen zich gedragen. In het snel groeiende veld van de kwantumtechnologie kan deze benadering de weg vrijmaken om nieuwe defectcentra te ontwerpen met specifieke toepassingen in het achterhoofd.

Resumo

A tecnologia da informação quântica nos permite processar informação de maneira diferente à tecnologia da informação clássica e poderá, por isso, proporcionar vias de comunicação fundamentalmente seguras. Os blocos básicos para a implementação da comunicação quântica são chamados *qubits*, uma unidade de processamento cujo estado é determinado pelas leis da Mecânica Quântica. As operações em longa distância desses *qubits* podem ser mediadas por fótons. Desse modo, um dos grandes desafios da área está na busca de materiais que podem guardar a informação quântica de seus estados eficientemente, e transferí-la às partículas de luz (fótons) quando necessário. Alguns dos melhores candidatos são os assim chamados *color centers*, presentes em cristais como diamante ou silício. Esses *color centers* funcionam como moléculas artificiais presas nesses cristais: eles vibram e interagem com luz como uma molécula, mas a sua forma é determinada pelo cristal à sua volta. O *spin* dos elétrons e núcleos nesses *color centers* pode ser usado para guardar a informação quântica eficientemente. Os fótons emitidos por esses *color centers* podem now informar sobre o estado quântico dos spins eletrônicos contidos neles. Isso possibilita protocolos de emaranhamento entre matéria e luz que são necessários para a implementação da comunicação quântica.

Nesse contexto, materiais e *color centers* compatíveis com a infraestrutura industrial já existente se tornam particularmente relevantes. Carbeto de silício é um semicondutor amplamente utilizado na indústria em circuitos eletrônicos de alta potência. As já estabelecidas técnicas de crescimento e processamento de SiC tornam esse material muito versátil do ponto de vista da engenharia micro-eletrônica. Além disso, esse semicondutor pode hospedar vários defeitos em sua estrutura cristalina, dando origem a vários *color centers* com atividade ótica em regiões do espectro compatíveis com a, ou próximas da, infraestrutura de telecomunicações. A investigação das propriedades óticas e de spin destes *color centers* é típicamente feita individualmente, defeito a defeito. Assim, esta área do conhecimento ainda carece de uma generalização sobre como a estrutura microscópica dos defeitos cristalinos (tal como simetria, acoplamento entre o spin e outros graus de liberdade, *etc.*) influencia os parâmetros experimentais de relevância para aplicações em tecnologias quânticas. Tal generalização poderia levar a uma situação em que novos defeitos são projetados de antemão para aplicações específicas. Nos capítulos 3-6 desta tese, nós exploramos as propriedades óticas e de *spin* de *ensembles* de defeitos contendo metais de transição em SiC. Gradualmente, nós relacionamos suas características experimentais a uma análise de sua configuração espacial e seus estados eletrônicos. Além disso, nós generalizamos nossas observações para diferentes estados localizados e delocalizados com simetrias semelhantes em outros materiais (capítulo 7).

Para operação quântica, alguns parâmetros são particularmente importantes. Primeiramente, a compreensão sobre como os estados eletrônicos de um defeito dependem da sua vizinhança pode levar a defeitos especialmente projetados para certas aplicações em metrologia, ou à engenharia de dispositivos ou geometrias operacionais com alta coerência quântica. No capítulo 3, nós mostramos que defeitos formados por impurezas de Mo no SiC contêm spins que não são sensíveis a campos magnéticos ortogonais ao eixo-c do SiC (até a nossa precisão instrumental). Essa anisotropia axial acontece quando os estados eletrônicos associados com esse defeito possuem um momento angular orbital finito na direção do eixo-c, e os graus de liberdade de *spin* e espaciais estão fortemente acoplados devido ao acoplamento spin-órbita. Neste capítulo, nós utilizamos essa informação para determinar a estrutura microscópica e a carga eletrônica destes defeitos. *Color centers* com anisotropias deste tipo formam *ensembles* com defeitos que têm seus spins alinhados em uma direção homogênea.

Em segundo lugar, um defeito deve ter seus spins relativamente isolados do resto da rede cristalina. Dois tempos característicos são de importância: o tempo em que um defeito com estados eletrônicos localizados troca energia com a rede cristalina (isto é, seu *tempo de relaxação*), e o tempo no qual a evolução quântica destes estados é influenciada por mudanças dinâmicas do seu ambiente (o *tempo de coerência*). Ambos devem ser suficientemente longos para que a informação quântica seja guardada eficientemente e para a execução de protocolos de emaranhamento a distância. Nos capítulos 4 e 6, nós investigamos experimentalmente como o tempo de relaxação dos defeitos estudados nesta tese dependem da presença de estados excitados acessíveis. Em geral, o acoplamento entre graus de liberade de spin e orbitais é prejudicial à estabilidade de spins eletrônicos. Entretanto, nós mostramos no capítulo 4 que no caso particular de defeitos que contém um único elétron em estados orbitais duplamente degenerados, o acoplamento spin-órbita dá origem a estados eletrônicos caracterizados por dubletos de spin-efetivo-1/2. Nesses dubletos, transições de spin diretas e precessão do spin eletrônico são proibidas devido às suas simetrias. Nessa configuração, o acoplamento spin-órbita estabiliza o spin eletrônico e é parcialmente responsável pelo tempo de relaxação surpreendentemente longo de defeitos contendo Mo, acima de 1 segundo em temperaturas abaixo de 3 K. Nos capítulos 5 e 6, nós mostramos que esse cenário muda no caso de defeitos contendo V em SiC devido à presença de um núcleo com spin-7/2 com 99% de abundância. As estruturas eletrônicas de defeitos contendo Mo e V são análo-

gas. Entretanto, a presença do spin nuclear no caso de defeitos contendo V permite o controle de transições eletrônicas com campos de microondas elétricos e magnéticos, proibidos na ausência do spin nuclear. Essas transições eletrônicas adicionais fazem com que o tempo de relaxação de defeitos contendo V dependa fortemente do acoplamento hiperfino entre o spin do elétron e do núcleo central. No capítulo 7, nós mostramos que os mesmos processos responsáveis por estabilizar o spin dos estados eletrônicos de defeitos contendo Mo em SiC podem ser usados para explicar a diferença entre elétrons e buracos em calcogenetos de metais de transição quanto aos seus processos de relaxação.

Finalmente, o controle dos estados de spin por meio de campos óticos depende da possibilidade de inicializar, controlar e ler o estado eletrônico óticamente. Para alcançar estes objetivos, os defeitos devem emitir fótons preferencialmente na linha de zero fônons (ZPL, acrônimo do termo em inglês *Zero Phonon Line*). A ZPL observa um alargamento inomogêneo de sua largura de linha devido à interação entre os defeitos e seu ambiente. Esse alargamento deve ser pequeno, tal que os fótons emitidos por dois defeitos diferentes sejam indistinguíveis. Além disso, nós devemos ser capazes de inicializar o spin do estado fundamental via transições óticas. Ao decorrer desta tese, nós demonstramos alguns destes requerimentos para defeitos contendo Mo e V em SiC. Nos capítulos 3 e 4, nós mostramos que o spin de defeitos contendo Mo podem ser inicializados e detectados óticamente quando a amostra está em temperaturas criogênicas. Adicionalmente, nós mostramos que *ensembles* de defeitos contendo Mo podem ser preparadas em uma superposição coerente de spins na presença de dois lasers (*coherent population trapping*). No capítulo 6, nós mostramos que a combinação entre o grande número de estados hiperfinos e o tempo de relaxação reduzido de defeitos contendo V limita a eficiência da inicialização de spin para estes defeitos (quando comparado a defeitos contendo Mo). A otimização deste processo de inicialização ainda é um dos grandes obtáculos para a implementação destes defeitos em tecnologias quânticas. Neste capítulo, nós ainda mostramos que a largura de linha inomogênea das transições óticas depende fortemente do caráter de simetria dos estados eletrônicos envolvidos, mesmo em defeitos que não têm simetria de inversão. Assim, um mesmo defeito pode ter transições óticas que respondem diferentemente a perturbações de seu ambiente. Isso deve ser levado em consideração ao determinar as geometrias operacionais que otimizam a performance desses defeitos.

Com estes resultados, nós mostramos que defeitos em semicondutores oferecem mais oportunidades de engenharia e variabilidade de performance com respeito aos parâmetros relevantes para operação quântica do que típicamente esperado, mesmo depois de mais de 20 anos de pesquisa nestes sistemas. Relacionar a estrutura microscópica destes defeitos às figuras de mérito para aplicações em

tecnologias quânticas nos permite compreender resultados aparentemente surpreendentes, e fazer previsões sobre o comportamento de sistemas relacionados. Em um ambiente de tecnologias quânticas que está crescendo rapidamente, essas iniciativas podem levar à engenharia de novos defeitos com aplicações específicas.

chapter 1

Quantum technologies and their material platforms: the potential of SiC

Quantum technologies (quantum computing, sensing, and communication) have had a prominent place in news outlets in the past years. These technologies gain advantage from or are made possible by the quantum-mechanical (*i.e.* non-classical) states of its physical components. From proof-of-principle experiments demonstrating some of the most widely debated physical concepts of the last century [1–3], to engineering feats delivering ever bigger quantum processors [4–9], the past decade has seen rapid and important steps towards functional quantum technologies.

The sight of commercial parties taking an increasingly important role in the development of these technologies might lead to the belief that the time for fundamental exploration of platforms for their implementation is past. This view is short-sighted and overlooks the complexity of the quantum-technological milieu. On the one hand, characterization of novel and existing quantum systems for quantum-technology applications is still unraveling exciting and surprising quantum mechanical behavior [1, 10–18]. On the other hand, the discussion of which material platform to use when developing quantum technologies is not a simple one, and several arguments must be considered [19–21]. It is likely that different platforms will fulfill specific needs for different applications, and that several of these systems will coexist in a larger quantum-technological context.

This thesis is focused on the characterization of several quantum systems in a semiconductor platform (SiC) for quantum-communication applications. To motivate this effort, in this chapter we discuss some of the potential outcomes of the various quantum technologies and the material platforms currently being considered for their implementation, along with their benefits and limitations. Finally, we show how SiC and its color centers overcome some of the limitations of other systems and are thus interesting platforms to explore.

1.1. The promises of quantum technologies

As was the case in the early development of classical computational technologies, it is hard to fully envision the future capabilities of quantum-based technologies and their related algorithms. Nevertheless, in some areas, we can already identify future and present applications that promise to revolutionize various fields.

Quantum computing relies on the quantum-mechanical properties of qubits to enhance computational speeds and access problems that are currently intractable to classical computers [22, 23]. Whereas a classical bit can only be in 2 states (0 or 1 from here on), a quantum bit (qubit) may be in any superposition of these states (see Fig. 1.1(a)). Thus, in order to describe the configuration of a single qubit, we need to know how this particular superposition looks like and evolves, which is translated into the *phase* and *probability amplitudes* associated with this superposition. Furthermore, a collection of interacting qubits can be *entangled* in such a way that their states are quantum-mechanically intertwined. When this happens, the state of each qubit cannot be described independently, and the description of the full quantum-mechanical state depends on the collective evolution of the entire set of qubits. It is in these quantum mechanical properties – *superposition* and *entanglement* – that lies the great advantage of quantum systems over their classical counterparts when considering some specific computational tasks. Algorithms mapping search and optimization protocols into the evolution of the phase of a collective quantum state, for example, undeniably show that large-scale quantum computers could represent a huge leap for fields related to optimization and logistics [7, 24, 25]. Finally, processes that are fundamentally quantum in their nature – such as material formation and molecular interactions – can be more effectively simulated in quantum, rather than classical processing units [4, 26–29]. Thus, fields like pharmacy and materials design will benefit from operational quantum computers, with possible consequences for the development of new drugs, or energy-transition friendly materials, for example.

The phase information of a (collective) quantum state is very fragile and thus constitutes both the hidden weapon of quantum systems and their Achilles' heal. This phase is extremely sensitive to environmental perturbations, and its information is effectively lost as the quantum system interacts with its environment. Quantum sensing relies on this enhanced sensitivity of quantum systems to their environment to provide detailed information on local properties such as electromagnetic fields, temperature, and pressure with nanoscale resolution [30–36]. These techniques are already currently used to investigate material properties and biological processes, for example [33, 37].

Finally, quantum communication technologies aim at establishing long-distance distribution of entangled states through so-called flying qubits. This type of network would enable the distribution of cryptographic keys fundamentally secured by the laws of quantum mechanics [38–40]. The entangled states associated with these quantum passwords cannot be intercepted without being disturbed. Therefore, any attempt to eavesdrop on the password would be known to the party sharing the key. These quantum key distribution protocols would represent a large advancement in the field of cryptography and are especially important in light of the fact that a functional quantum computer will enable fast factorization of large prime numbers, rendering some of the most important classical cryptography protocols obsolete [24].

The natural choice for these flying qubits for the implementation of quantum networks is optical pulses since we know that photons can hold onto their coherent properties while traveling over long distances through optical fibers. Especially photons at the near-infrared regions of the spectrum, at the so-called telecom bands, can be transmitted through the existing telecommunication infrastructure with low losses. Nonetheless, the distances covered by photons in optical fibers before they are absorbed are limited to a few hundreds of kilometers, even in the highest quality, lowest-loss optical fibers [41]. Expanding the scope of quantum networks relies, then, on material-based quantum memories that are long-lived and can be effectively entangled with these flying qubits, such that the quantum information can be temporarily stored in a stationary qubit and retrieved on demand [42]. There is still no consensus on which material platform is ideally suited for this application. The development of these quantum networks relies on identifying material platforms with long-lived embedded quantum systems with efficient optical interfaces. This hybrid implementation of stationary and flying qubits would also largely aid in the effort to scale-up quantum computing architectures since it would enable us to harness the total power of several small-scale quantum computers through distributed quantum computing [43].

1.2. Material qubits for communication applications

A qubit is a two-level quantum system that is, in the ideal case, isolated from its environment but still efficiently addressable. In other words, it takes a long time for the qubit to lose its phase information to its environment, but we can effectively modify its quantum state via well-controlled quantum *gate* operations. The timescale at which the qubit loses its phase information to the environment without the possibility of recovery is called its *coherence time* T_2. The coherence time is fundamentally limited by the timescale T_1 (the *relaxation time*) at which the qubit exchanges energy with its environment, but T_2 may be much shorter than T_1 (see Fig. 1.1(b)). In order to be functional as a qubit, a two-level system must have T_2 that is orders of magnitude longer than its operation time, such that many operations are possible before the quantum information is lost. Thus, some of the most important figures of merit for all areas of quantum applications are the relaxation, coherence, and operation times.

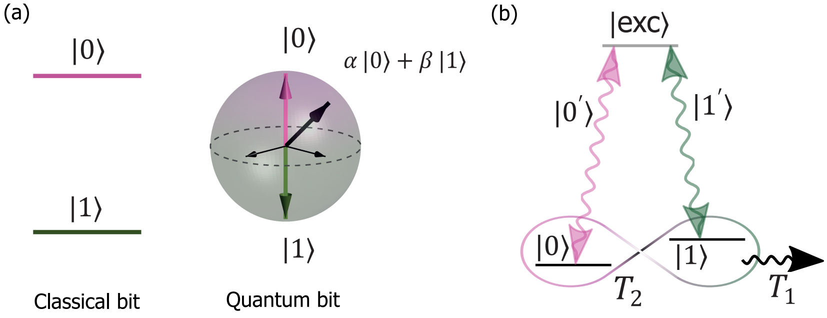

Figure 1.1: **A quantum bit and its optical interface** (a) Whereas a classical bit can be in one of two states ($|0\rangle$ or $|1\rangle$), a quantum bit can be in any superposition of the two basis states. The space spanned by the possible superposition states can be represented as points on the Bloch sphere. (b) Besides the two qubit states $|0\rangle$ and $|1\rangle$, the quantum system may have additional excited states, and the qubit may interact with these states via optical fields. If this interaction depends on the qubit state, an optical interface arises for entanglement between the state of the photonic field ($|0'\rangle$ or $|1'\rangle$) and the state of the stationary qubit ($|0\rangle$ or $|1\rangle$). The quantum superposition of a qubit is lost in a timescale T_2, which is fundamentally limited by the timescale T_1, at which the qubit exchanges energy with its environment.

A material-based qubit may also have other available (excited) quantum states. These states may be detrimental for quantum operation, leading to additional dephasing and relaxation of the stationary qubit. However, the presence of excited states may also lead to an interface for entanglement or quantum-state transfer between photonic states and the stationary qubit, if direct mapping between them is available [11, 38, 39] (see Fig. 1.1(b)). Thus, isolated quantum systems with addressable optically-excited states are very interesting platforms for quantum sensing and quantum communication applications. When considering such systems, additional figures of merit play an important role. For quantum communication applications, for example, creating entanglement between remote stationary nodes at an appreciable rate (such that entanglement can be obtained much faster than the qubit loses its quantum information, and fast enough to reduce experimental noise accumulation) is an important goal [20, 44, 45]. Thus, the rate at which one can operate on stationary qubits and associated photons, and how far these photons can then travel before losing their quantum information are the key parameters, and fundamentally limit the operation times of a quantum network.

1.2.1. Current contenders

When considering platforms for the implementation of quantum communication protocols, one must search for quantum systems whose phase information is robust (that is, T_1 and T_2 are long), but that also interact with light in such a way that the stationary qubit state can be mapped onto properties of photonic states (and vice-versa). At present, the most widely studied platforms are trapped ions, semiconductor quantum dots, and solid-state color centers. All of these systems rely on storing the quantum information in the *spin* (a relativistic and quantum mechanical angular momentum) of charged particles (electrons, holes, or nuclei). The considerations of this section are summarized in Fig. 1.2.

In ion trap qubits, the quantum information is stored in the electronic or nuclear-spin eigenstates of ions, trapped in vacuum due to strong electromagnetic fields [46–48]. Since the ions are isolated in vacuum, interacting only with the electromagnetic fields used for trapping and qubit control, these qubits may live for virtually infinite times [49]. Their coherence properties are often limited by noise of the trapping and control electric fields [50, 51]. However, scaling up these systems and integrating them with other semiconductor device platforms remains a challenge [19].

Alternatively, semiconductor quantum dots can host isolated and localized electrons or holes. These charge-carrier spins may be long-lived and can thus be used to store quantum information in these systems [52–54]. The trapping potential responsible for these quantum dots may arise from lithographically designed electrostatic gates [54], via bottom-up self-assembly of islands during growth of semiconductor materials (zero-dimensional analogs of the two-dimensional electron gas) [52], or via localization of excitons around lattice impurities [55–57]. Quantum dots formed in III-V or II-VI semiconductors via self-assembly methods create trapping potentials for both electrons and holes and thus give rise to localized spins that are optically addressable [52, 55, 58–60]. These systems may be telecom-compatible [61], but scaling them up is hindered by the large variability of quantum-dot properties [62, 63]. Furthermore, III-V semiconductors are composed of elements that do not have nuclear-spin zero isotopes, and the nuclear-spin bath is an important source of decoherence for the localized electronic spins [19, 20, 64].

Finally, solid-state color centers arise when defects in the lattice of an insulator or semiconductor lead to localized electronic states strongly confined around the defect site [21, 45, 65]. The coupled electronic and spin properties of these defect centers can be used to store quantum information. When these defects have an additional accessible excited state within the bandgap of the host material, the defect can efficiently interact with light resonant with the transition between ground and excited states, and this interaction may be spin-dependent [66–69]. The spin and optical properties of these color centers depend on a wide variety of parameters, for example the geometry and symmetry of the defect site, their charge state, and whether or not impurity atoms are present in the defect complex [20, 21, 65, 70, 71].

The investigation of color centers in solids has enabled some ground-breaking

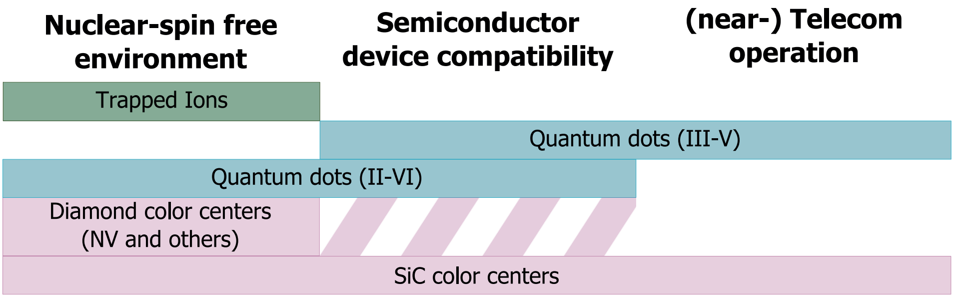

Figure 1.2: **Material platforms for application in quantum communication and their limitations.** A list of the current material platforms being developed for quantum communication applications, classified with respect to some key requirements for technological compatibility. Decoherence of the functional spin qubit due to interaction between the stationary qubits and neighboring nuclear spins can be mitigated by having a nuclear-spin-free environment. In trapped ions, this is intrinsically achieved by the vacuum environment. Insulator or semiconductor spin quantum states require isotopic purification of the host material, and this is not always possible. Device engineering may lead to devices where the quantum system has enhanced optical and spin properties, like strong optical transitions in photonic cavities, or enhanced spin lifetimes if the electrostatic environment is controlled via gating. Quantum systems that interact with light at the telecom range will profit from optimal operation at wavelengths compatible with the existing telecommunication infrastructure

demonstration of the basic requirements for functional quantum networks, such as long-distance entanglement of remote qubits [1, 72]. For the largest part, these results were realized on nitrogen-vacancy (NV) complexes in diamond. This lattice defect, comprising a negatively charged nitrogen impurity next to a carbon vacancy in the diamond lattice, has a spin-1 with long coherence and long relaxation times up to room temperature, and can be optically initialized, manipulated, and read out [67, 73–77]. Although NV centers in diamond have been extremely useful for demonstrating the feasibility of important steps towards quantum networks, this platform still shows some significant shortcomings that motivate the further search for solid-state defects with long-lived spins, bright optical interfaces, and suitable host properties. Firstly, NV centers interact with light in the visible range, far from the preferred wavelengths for low-loss communication through telecom fibers. Although there are protocols for up and downconverting photons generated by these NV centers while preserving the photon coherence [78], these protocols are technically demanding and incur extra losses that limit the maximum entanglement rates achievable. This also represents a challenge for remote bio-sensing applications due to strong absorption of visible photons by salty water (whereas near-infrared photons penetrate better into biological media). Secondly, the NV center suffers from strong coupling to phonon modes in the material, which leads to predominant emission of photons into a broad phonon band that hinders the entanglement between the defect spin and the photonic states [65]. This brings us to the third, and perhaps most important, shortcoming of NV centers and diamond as a material platform: a clear path towards the improvement of the optical and spin coherence properties of color centers is embedding them in engineered devices. Photonic cavities, for example, can enhance the coherence properties of the emitted photons [79], whereas phononic cavities may be engineered to reduce the population of phonons responsible for limiting the spin-relaxation times [20]. Additionally, electrostatic devices may be used to locally stabilize the semiconductor electrostatic environment [80, 81], suppressing detrimental processes like charging of defect centers, and device engineering could lead to on-chip integration of defect centers with electrical control and detection [82, 83]. However, diamond's hardness and the difficulty involved in doping it mean that processing diamond into these types of devices is challenging.

For these reasons, a wide array of defects beyond the NV center in diamond have been explored in the past years. For example, group-IV impurities in diamond form optically active spin-3/2 defects [84–87]. These defects' symmetries lead to outstanding optical properties, including very narrow optical emission lines (meaning that there is very large coherence between the interacting spin and photonic states). Furthermore, the systematic study of several different group-IV defects shows that the defect properties are tunable by changing the type of impurity ion [84, 85]. Although diamond itself hosts a whole zoo of optically active lattice defects, in order to overcome its limitations as a host material, we must look for alternative semiconductor platforms that host similar optically active defects. An intuitive choice is silicon carbide, a wide-bandgap semiconductor that has been extensively used in the semiconductor industry as an alternative to silicon for high-power, high-temperature device applications [88].

1.3. SiC and its color centers

Silicon carbide is formed by stacked and alternating carbon and silicon layers and can be almost seen as a combination of diamond and silicon. It is extremely robust and has a wide band-gap which makes it transparent for most wavelengths in the visible and near-infrared ranges of the spectrum (like diamond), yet it can be grown with extremely high quality and controllable doping, and its processing technologies have gone through decades of improvement for applications in the semiconductor industry (like silicon). A set of high-quality commercial SiC wafers is shown in Fig. 1.3(a).

Silicon carbide can host a wide array of defect centers [70, 89–95]. These may be intrinsic, like vacancy and divacancy complexes, or extrinsic due to impurities added during or implanted after growth. Furthermore, the material can be grown

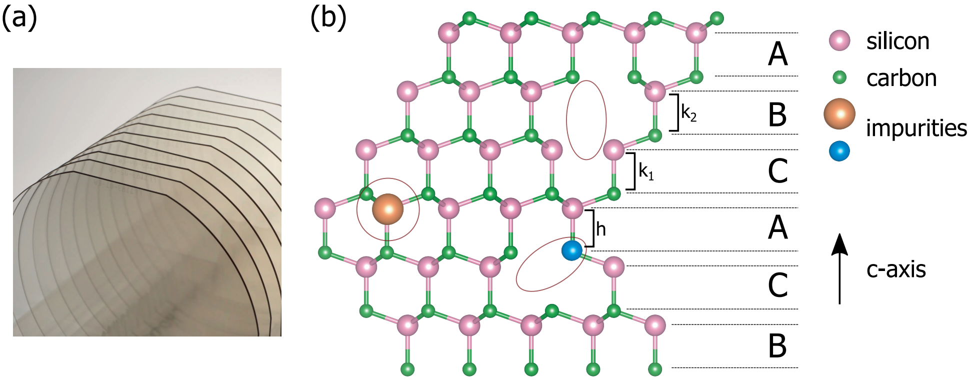

Figure 1.3: **Silicon carbide and its defects** (a) A series of industrial SiC wafers (photo courtesy of II-VI Inc.). (b) The crystal is composed of alternating Si and C layers. Stacking these layers in different orders leads to different SiC polytypes. Depicted here is 6H-SiC, with stacking order ABCACB. Lattice sites in different layers differ in local symmetries (here denoted by h, k_1 and k_2, see main text for details). Silicon carbide can host a myriad of different lattice defects. Various examples are depicted here, circled. From top to bottom, these are a divacancy, a substitutional defect, and an impurity neighboring a vacancy.

in different polytypes – that is, different crystal forms that vary in how the carbon and silicon layers are stacked. These various polytypes have lattice sites with different local symmetries. In Fig. 1.3(b) we show the crystal structure of 6H-SiC, characterized by stacking of the type ABCACB. In this particular polytype, C and Si atoms can occupy lattice sites with *quasi*-cubic (k_1 and k_2 sites) or *quasi*-hexagonal (h) symmetries. Since the defect symmetry plays a significant role in determining its optical and spin-related properties, this feature can be used to engineer defects with desirable interactions with electromagnetic fields [96]. Combined with the outstanding list of impurities that are stable in the SiC lattice, this provides a huge parameter space to explore when searching for defects with suitable optical and spin properties.

Many of the defects centers present in SiC are optically active in the near-infrared range [70, 97], and thus highly interesting for quantum-communication applications through the existing telecom infrastructure. Some of them have been explored to date. Divacancies, for example (complexes with neighboring carbon and silicon vacancies) are highly analogous to NV centers, with a spin-1 ground state that can be optically initialized and has long coherence times [64, 98–101]. Their optical transitions (between 1000 and 1200 nm) are still not fully compatible with current telecommunication infrastructure (in the intervals 1260 - 1360 nm or 1530 - 1565 nm), but proof-of-principle device integration of these defects demonstrates the potential of SiC as a host material [79, 81, 82]. Other defects, including some that interact with light at the telecom bands, have not been thoroughly investigated and still need to be fully characterized with respect to their ground and excited-state spin properties. In particular, understanding how the various energy scales responsible for a defect's electronic structure influence their spin and its interaction with the environment may lead to informed engineering of novel defects that fulfill specific needs for quantum communication applications. This is the focus of this thesis. We look at transition metal defect centers in SiC with optical techniques in order to understand how their microscopic environment leads to their spin and optical properties, and whether these fulfill the requirements for quantum communication applications.

1.4. This thesis

In this thesis, we investigate transition-metal defects in SiC with experimental and theoretical means. We apply optical characterization techniques to determine their microscopic configuration, whether the spins associated with these defect centers can be optically initialized, what is the timescale and what physical processes dominate the spin relaxation and inhomogeneous coherence times of these defects. In the process of doing this, we unravel defect centers with spins that are surprisingly robust, and whose electronic structure gives rise to behavior that is much richer than originally anticipated. We show that, in particular geometries, the coupling between the electronic spin states and its orbital states via spin-orbit coupling can in fact stabilize these spins, which can have spin-relaxation times up to seconds at low (few kelvin) temperatures. Furthermore, we theoretically investigate the possibility of manipulating these defect centers via microwave electromagnetic fields. The thesis is organized as follows:

- **Chapter 2** presents background information on theoretical and experimental concepts and techniques applied in the subsequent chapters. This includes a short and didactical recap of group theory concepts and how they lead to selection rules for transitions between different eigenstates. These concepts underline most of the theoretical arguments presented in this thesis. Furthermore, we describe in this chapter the experimental setup and geometries used to obtain the experimental results presented in this thesis.

- **Chapter 3** presents group-theoretical arguments that led to the identification of the microscopic configuration of a substitutional defect containing a Mo impurity in SiC, motivated by experimental results within our team. We show that a model based on group theory encompasses the unusual anisotropic magneto-optical spectra associated with these defect centers, and this enables us to determine their lattice site and charge configuration.

- **Chapter 4** presents time-resolved measurements that unravel surprisingly long spin-relaxation times of the Mo defect in SiC. Based on the temperature dependence of the spin-relaxation rate and an analysis of the electronic structure of these defects, we identify the physical mechanisms leading to spin relaxation in these defects. We show how the symmetry of the defect, combined with spin-orbit coupling, leads to specific symmetry-protected selection rules that are responsible for the long spin lifetimes of these defect centers. Unfortunately, these selection rules may hinder microwave control of the defect spins.

- **Chapter 5** presents our theoretical results showing that the presence of a hyperfine-coupled nuclear spin may be fundamental to enable the control of the electronic spin of Mo and V defects in SiC via microwave fields in unconventional geometries. These results indicate that the symmetry-related limitations for microwave control (mentioned in chapter 4) may be overcome in the presence of a nuclear spin. We show that the interaction with the nuclear spin opens up transitions that are originally forbidden, leading to allowed spin resonances due to electric and magnetic microwave fields, with important technological consequences for the device integration of these defect centers.

- **Chapter 6** presents experimental spectroscopic results on ensembles of V defects in SiC. We use emission and novel absorption approaches to demonstrate high-contrast magneto-spectroscopy of the hyperfine-coupled spin sublevels. Based on time-resolved experiments, we determine the spin-relaxation time of these defects. The magnetic-field dependence of the spin-relaxation rate provides evidence for hyperfine-mediated spin-relaxation mechanisms.

- **Chapter 7** presents a group-theoretical derivation of scattering mechanisms of charge carriers in two-dimensional transition metal dichalcogenides. These results help explain a series of transport experiments in TMDs and are derived from those presented in chapter 3 for defects in SiC. This shows that the theoretical techniques explored in this thesis are very general and can provide transferable insight into a wide class of physical platforms and phenomena.

References

[1] B. Hensen et al., “Loophole-free bell inequality violation using electron spins separated by 1.3 kilometres”, Nature **526**, 682 (2015).

[2] G. Pagano et al., “Quantum approximate optimization of the long-range ising model with a trapped-ion quantum simulator”, Proc. Natl. Acad. Sci. U S A **117**, 25396 (2020).

[3] X. X. Zhang et al., “Magnetic brightening and control of dark excitons in monolayer WSe_2”, Nat. Nanotechnol. **12**, 883 (2017).

[4] A. I. Q. Google and Collaborators, “Hartree-fock on a superconducting qubit quantum computer”, Science **369**, 1084 (2020).

[5] A. Kandala, K. Temme, A. D. Corcoles, A. Mezzacapo, J. M. Chow, and J. M. Gambetta, “Error mitigation extends the computational reach of a noisy quantum processor”, Nature **567**, 491 (2019).

[6] P. Jurcevic et al., “Demonstration of quantum volume 64 on a superconducting quantum computing system”, ArXiv **2008.08571v2** (2020).

[7] F. Arute et al., “Quantum supremacy using a programmable superconducting processor”, Nature **574**, 505 (2019).

[8] K. Wright et al., “Benchmarking an 11-qubit quantum computer”, Nat. Commun. **10**, 5464 (2019).

[9] N. Friis et al., “Observation of entangled states of a fully controlled 20-qubit system”, Phys. Rev. X **8**, 021012 (2018).

[10] V. A. Norman, S. Majety, Z. Wang, W. H. Casey, N. Curro, and M. Radulaski, “Novel color center platforms enabling fundamental scientific discovery”, InfoMat, 1 (2020).

[11] E. Togan et al., “Quantum entanglement between an optical photon and a solid-state spin qubit”, Nature **466**, 730 (2010).

[12] W. Pfaff et al., “Unconditional quantum teleportation between distant solid-state quantum bits”, Science **345**, 532 (2014).

[13] P. W. Anderson, B. I. Halperin, and C. M. Varma, “Anomalous low-temperature thermal properties of glasses and spin glasses”, The Philos. Mag. **25**, 1 (1972).

[14] T. B. Boykin, G. Klimeck, M. A. Eriksson, M. Friesen, S. N. Coppersmith, P. von Allmen, F. Oyafuso, and S. Lee, “Valley splitting in strained silicon quantum wells”, Appl. Phys. Lett. **84**, 115 (2004).

[15] D. L. Creedon, Y. Reshitnyk, W. Farr, J. M. Martinis, T. L. Duty, and M. E. Tobar, “High q-factor sapphire whispering gallery mode microwave resonator at single photon energies and millikelvin temperatures”, Appl. Phys. Lett. **98**, 222903 (2011).

[16] M. Harlander, M. Brownnutt, W. Hänsel, and R. Blatt, “Trapped-ion probing of light-induced charging effects on dielectrics”, New J. of Phys. **12**, 093035 (2010).

[17] T. Tanttu et al., “Controlling spin-orbit interactions in silicon quantum dots using magnetic field direction”, Phys. Rev. X **9**, 021028 (2019).

[18] G. Wang, A. Chernikov, M. M. Glazov, T. F. Heinz, X. Marie, T. Amand, and B. Urbaszek, “Colloquium: excitons in atomically thin transition metal dichalcogenides”, Rev. of Mod. Phys. **90** (2018).

[19] N. P. de Leon et al., “Materials challenges and opportunities for quantum computing hardware”, Science **372**, eabb2823 (2021).

[20] G. Wolfowicz, F. J. Heremans, C. P. Anderson, S. Kanai, H. Seo, A. Gali, G. Galli, and D. D. Awschalom, “Qubit guidelines for solid-state spin defects”, Nat. Rev. Mater. (2021).

[21] L. C. Bassett, A. Alkauskas, A. L. Exarhos, and K.-M. C. Fu, “Quantum defects by design”, Nanophotonics **8**, 1867 (2019).

[22] M. A. Nielsen and I. L. Chuang, *Quantum computation and quantum information: 10th anniversary edition* (Cambridge University Press, 2010).

[23] R. P. Feynman, “Simulating physics with computers”, Int. J. of Theor. Phys. **21**, 467 (1982).

[24] P. W. Shor, “Polynomial-time algorithms for prime factorization and discrete logarithms on a quantum computer”, SIAM Review **41**, 303 (1999).

[25] A. Montanaro, “Quantum algorithms: an overview”, npj Quantum Information **2**, 15023 (2016).

[26] C. Kokail et al., “Self-verifying variational quantum simulation of lattice models”, Nature **569**, 355 (2019).

[27] S. McArdle, S. Endo, A. Aspuru-Guzik, S. C. Benjamin, and X. Yuan, “Quantum computational chemistry”, Rev. of Mod. Phys. **92**, 015003 (2020).

[28] Y. Nam et al., “Ground-state energy estimation of the water molecule on a trapped-ion quantum computer”, npj Quantum Information **6**, 33 (2020).

[29] M. Reiher, N. Wiebe, K. M. Svore, D. Wecker, and M. Troyer, “Elucidating reaction mechanisms on quantum computers”, Proc. Natl. Acad. Sci. U S A **114**, 7555 (2017).

[30] M. H. Abobeih, J. Randall, C. E. Bradley, H. P. Bartling, M. A. Bakker, M. J. Degen, M. Markham, D. J. Twitchen, and T. H. Taminiau, “Atomic-scale imaging of a 27-nuclear-spin cluster using a quantum sensor”, Nature **576**, 411 (2019).

[31] J. F. Barry, J. M. Schloss, E. Bauch, M. J. Turner, C. A. Hart, L. M. Pham, and R. L. Walsworth, “Sensitivity optimization for NV-diamond magnetometry”, Rev. of Mod. Phys. **92**, 015004 (2020).

[32] J. Bylander et al., “Noise spectroscopy through dynamical decoupling with a superconducting flux qubit”, Nat. Phys. **7**, 565 (2011).

[33] F. Casola, T. van der Sar, and A. Yacoby, “Probing condensed matter physics with magnetometry based on nitrogen-vacancy centres in diamond”, Nat. Rev. Mater. **3**, 17088 (2018).

[34] J. C. Jaskula, B. J. Shields, E. Bauch, M. D. Lukin, A. S. Trifonov, and R. L. Walsworth, “Improved quantum sensing with a single solid-state spin via spin-to-charge conversion”, Phys. Rev. Appl. **11**, 064003 (2019).

[35] Y. Romach et al., “Spectroscopy of surface-induced noise using shallow spins in diamond”, Phys. Rev. Lett. **114**, 017601 (2015).

[36] H. Kraus, V. A. Soltamov, F. Fuchs, D. Simin, A. Sperlich, P. G. Baranov, G. V. Astakhov, and V. Dyakonov, “Magnetic field and temperature sensing with atomic-scale spin defects in silicon carbide”, Sci. Rep. **4**, 5303 (2014).

[37] T. Zhang et al., “Toward quantitative bio-sensing with nitrogen–vacancy center in diamond”, ACS Sensors **6**, 2077 (2021).

[38] L.-M. Duan, M. D. Lukin, J. I. Cirac, and P. Zoller, “Long-distance quantum communication with atomic ensembles and linear optics”, Nature **414**, 413 (2001).

[39] H. J. Kimble, “The quantum internet”, Nature **453**, 1023 (2008).

[40] T. E. Northup and R. Blatt, “Quantum information transfer using photons”, Nat. Photonics **8**, 356 (2014).

[41] Y. Colombe, D. H. Slichter, A. C. Wilson, D. Leibfried, and D. J. Wineland, “Single-mode optical fiber for high-power, low-loss uv transmission”, Optics express **22**, 19783 (2014).

[42] D. Awschalom et al., “Development of quantum interconnects (quics) for next-generation information technologies”, PRX Quantum **2**, 017002 (2021).

[43] K. Nemoto et al., “Photonic architecture for scalable quantum information processing in diamond”, Phys. Rev. X **4**, 031022 (2014).

[44] G. Zhang, Y. Cheng, J.-P. Chou, and A. Gali, “Material platforms for defect qubits and single-photon emitters”, Appl. Phys. Rev. 7, 031308 (2020).

[45] S. Castelletto and A. Boretti, “Silicon carbide color centers for quantum applications”, Journal of Physics: Photonics **2**, 022001 (2020).

[46] C. D. Bruzewicz, J. Chiaverini, R. McConnell, and J. M. Sage, “Trapped-ion quantum computing: progress and challenges”, Appl. Phys. Rev. **6**, 021314 (2019).

[47] M. Saffman, T. G. Walker, and K. Mølmer, “Quantum information with Rydberg atoms”, Rev. of Mod. Phys. **82**, 2313 (2010).

[48] C. J. Ballance, T. P. Harty, N. M. Linke, M. A. Sepiol, and D. M. Lucas, “High-fidelity quantum logic gates using trapped-ion hyperfine qubits”, Phys. Rev. Lett. **117**, 060504 (2016).

[49] P. Wang et al., “Single ion qubit with estimated coherence time exceeding one hour”, Nat. Commun. **12**, 233 (2021).

[50] H. Levine et al., “High-fidelity control and entanglement of rydberg-atom qubits”, Phys. Rev. Lett. **121**, 123603 (2018).

[51] J. E. Christensen, D. Hucul, W. C. Campbell, and E. R. Hudson, “High-fidelity manipulation of a qubit enabled by a manufactured nucleus”, npj Quantum Information **6**, 35 (2020).

[52] Y. Kondo, M. Ono, S. Matsuzaka, K. Morita, H. Sanada, Y. Ohno, and H. Ohno, “Multipulse operation and optical detection of nuclear spin coherence in a gaas/algaas quantum well”, Phys. Rev. Lett. **101**, 207601 (2008).

[53] K. D. Petersson, J. R. Petta, H. Lu, and A. C. Gossard, “Quantum coherence in a one-electron semiconductor charge qubit”, Phys. Rev. Lett. **105**, 246804 (2010).

[54] J. R. Petta, A. C. Johnson, J. M. Taylor, E. A. Laird, A. Yacoby, M. D. Lukin, C. M. Marcus, M. P. Hanson, and A. C. Gossard, “Coherent manipulation of coupled electron spins in semiconductor quantum dots”, Science **309**, 2180 (2005).

[55] T. A. Kennedy, J. Whitaker, A. Shabaev, A. S. Bracker, and D. Gammon, “Detection of magnetic resonance of donor-bound electrons in GaAs by Kerr rotation”, Phys. Rev. B **74**, 161201(R) (2006).

[56] A. R. Onur, J. P. de Jong, D. O’Shea, D. Reuter, A. D. Wieck, and C. H. van der Wal, “Stabilizing nuclear spins around semiconductor electrons via the interplay of optical coherent population trapping and dynamic nuclear polarization”, Phys. Rev. B **93**, 161204 (2016).

[57] M. Sladkov, A. U. Chaubal, M. P. Bakker, A. R. Onur, D. Reuter, A. D. Wieck, and C. H. van der Wal, “Electromagnetically induced transparency with an ensemble of donor-bound electron spins in a semiconductor”, Phys. Rev. B **82**, 121308 (2010).

[58] D. Press et al., “Ultrafast optical spin echo in a single quantum dot”, Nat. Photonics **4**, 367 (2010).

[59] D. Press, T. D. Ladd, B. Zhang, and Y. Yamamoto, “Complete quantum control of a single quantum dot spin using ultrafast optical pulses”, Nature **456**, 218 (2008).

[60] A. Greilich, A. Shabaev, D. R. Yakovlev, A. L. Efros, I. A. Yugova, D. Reuter, A. D. Wieck, and M. Bayer, “Nuclei-induced frequency focusing of electron spin coherence”, Science **317**, 1896 (2007).

[61] P. Holewa, M. Burakowski, A. Musial, N. Srocka, D. Quandt, A. Strittmatter, S. Rodt, S. Reitzenstein, and G. Sek, “Thermal stability of emission from single ingaas/gaas quantum dots at the telecom o-band”, Sci. Rep. **10**, 21816 (2020).

[62] H. Ollivier et al., “Reproducibility of high-performance quantum dot single-photon sources”, ACS Photonics **7**, 1050 (2020).

[63] L. Zhai, M. C. Lobl, G. N. Nguyen, J. Ritzmann, A. Javadi, C. Spinnler, A. D. Wieck, A. Ludwig, and R. J. Warburton, “Low-noise GaAs quantum dots for quantum photonics”, Nat. Commun. **11**, 4745 (2020).

[64] H. Seo, A. L. Falk, P. V. Klimov, K. C. Miao, G. Galli, and D. D. Awschalom, “Quantum decoherence dynamics of divacancy spins in silicon carbide”, Nat. Commun. **7**, 12935 (2016).

[65] F. Jelezko and J. Wrachtrup, “Single defect centres in diamond: a review”, Phys. Stat. Sol. (a) **203**, 3207 (2006).

[66] M. W. Doherty, N. B. Manson, P. Delaney, F. Jelezko, J. Wrachtrup, and L. C. L. Hollenberg, “The nitrogen-vacancy colour centre in diamond”, Phys. Rep. **528**, 1 (2013).

[67] J. R. Maze, A. Gali, E. Togan, Y. Chu, A. Trifonov, E. Kaxiras, and M. D. Lukin, “Properties of nitrogen-vacancy centers in diamond: the group theoretic approach”, New J. of Phys. **13**, 025025 (2011).

[68] D. M. Lukin et al., “4H-silicon-carbide-on-insulator for integrated quantum and nonlinear photonics”, Nat. Photon. **14**, 330 (2019).

[69] D. D. Awschalom, R. Hanson, J. Wrachtrup, and B. B. Zhou, “Quantum technologies with optically interfaced solid-state spins”, Nat. Photonics **12**, 516 (2018).

[70] J. Baur, M. Kunzer, and J. Schneider, “Transition metals in SiC polytypes, as studied by magnetic resonance techniques”, Phys. Stat. Sol. A **162**, 153 (1997).

[71] N. T. Son et al., “Developing silicon carbide for quantum spintronics”, Appl. Phys. Lett. **116**, 190501 (2020).

[72] M. Pompili et al., “Realization of a multinode quantum network of remote solid-state qubits”, Science **372**, 259 (2021).

[73] L. Childress and R. Hanson, “Diamond NV centers for quantum computing and quantum networks”, MRS Bull **38**, 134 (2013).

[74] M. W. Doherty, N. B. Manson, P. Delaney, and L. C. L. Hollenberg, “The negatively charged nitrogen-vacancy centre in diamond: the electronic solution”, New J. of Phys. **13**, 025019 (2011).

[75] L. Childress, M. V. Gurudev Dutt, J. M. Taylor, A. S. Zibrov, F. Jelezko, J. Wrachtrup, P. R. Hemmer, and M. D. Lukin, “Coherent dynamics of coupled electron and nuclear spin qubits in diamond”, Science **314**, 281 (2006).

[76] G. Balasubramanian et al., “Nanoscale imaging magnetometry with diamond spins under ambient conditions”, Nature **455**, 648 (2008).

[77] X. Rong et al., “Experimental fault-tolerant universal quantum gates with solid-state spins under ambient conditions”, Nat. Commun. **6**, 8748 (2015).

[78] A. Dréau, A. Tcheborateva, A. El Mahdaoui, C. Bonato, and R. Hanson, “Quantum frequency conversion of single photons from a nitrogen-vacancy center in diamond to telecommunication wavelengths”, Phys. Rev. Appl. **9**, 064031 (2018).

[79] A. L. Crook et al., “Purcell enhancement of a single silicon carbide color center with coherent spin control”, Nano Lett. **20**, 3427 (2020).

[80] M. E. Bathen and L. Vines, “Manipulating single-photon emission from point defects in diamond and silicon carbide”, Adv. Quantum Technol., 2100003 (2021).

[81] C. P. Anderson et al., “Electrical and optical control of single spins integrated in scalable semiconductor devices”, Science **366**, 1225 (2019).

[82] P. V. Klimov, A. L. Falk, B. B. Buckley, and D. D. Awschalom, “Electrically driven spin resonance in silicon carbide color centers”, Phys. Rev. Lett. **112**, 087601 (2014).

[83] A. L. Falk, P. V. Klimov, B. B. Buckley, V. Ivády, I. A. Abrikosov, G. Calusine, W. F. Koehl, A. Gali, and D. D. Awschalom, “Electrically and mechanically tunable electron spins in silicon carbide color centers”, Phys. Rev. Lett. **112**, 187601 (2014).

[84] G. Thiering and A. Gali, “*Ab Initio* magneto-optical spectrum of group-IV vacancy color centers in diamond”, Phys. Rev. X **8**, 021063 (2018).

[85] A. Sipahigil, K. D. Jahnke, L. J. Rogers, T. Teraji, J. Isoya, A. S. Zibrov, F. Jelezko, and M. D. Lukin, “Indistinguishable photons from separated silicon-vacancy centers in diamond”, Phys. Rev. Lett. **113**, 113602 (2014).

[86] C. Bradac, W. Gao, J. Forneris, M. E. Trusheim, and I. Aharonovich, “Quantum nanophotonics with group IV defects in diamond”, Nat. Commun. **10**, 5625 (2019).

[87] C. Hepp et al., “Electronic structure of the silicon vacancy color center in diamond”, Phys. Rev. Lett. **112**, 036405 (2014).

[88] P. Friedrichs, T. Kimoto, L. Ley, and G. Pensl, *Silicon carbide*, Vol. 1 (Wiley, Weinheim, 2010).

[89] S. Castelletto, B. C. Johnson, V. Ivády, N. Stavrias, T. Umeda, A. Gali, and T. Ohshima, “A silicon carbide room-temperature single-photon source”, Nat. Mater. **13**, 151 (2014).

[90] K. F. Dombrowski, U. Kaufmann, M. Kunzer, K. Maier, J. Schneider, V. B. Shields, and M. G. Spencer, “Deep donor state of vanadium in cubic silicon carbide (3C□SiC)”, Appl. Phys. Lett. **65**, 1811 (1994).

[91] F. Fuchs, B. Stender, M. Trupke, D. Simin, J. Pflaum, V. Dyakonov, and G. V. Astakhov, “Engineering near-infrared single-photon emitters with optically active spins in ultrapure silicon carbide”, Nat. Commun. **6**, 7578 (2015).

[92] W. F. Koehl, B. Diler, S. J. Whiteley, A. Bourassa, N. T. Son, E. Janzén, and D. D. Awschalom, “Resonant optical spectroscopy and coherent control of Cr^{4+} spin ensembles in SiC and GaN”, Phys. Rev. B **95**, 035207 (2017).

[93] M. Widmann et al., “Coherent control of single spins in silicon carbide at room temperature”, Nat. Mater. **14**, 164 (2015).

[94] S. A. Zargaleh, S. Hameau, B. Eble, F. Margaillan, H. J. von Bardeleben, J. L. Cantin, and W. Gao, “Nitrogen vacancy center in cubic silicon carbide: a promising qubit in the 1.5μm spectral range for photonic quantum networks”, Phys. Rev. B **98**, 165203 (2018).

[95] T. Bosma et al., “Identification and tunable optical coherent control of transition-metal spins in silicon carbide”, npj Quantum Information **4**, 48 (2018).

[96] A. L. Falk, B. B. Buckley, G. Calusine, W. F. Koehl, V. V. Dobrovitski, A. Politi, C. A. Zorman, P. X.-L. Feng, and D. D. Awschalom, “Polytype control of spin qubits in silicon carbide”, Nat. Commun. **4**, 1819 (2013).

[97] B. Magnusson and E. Janzén, “Optical characterization of deep level defects in SiC”, Mater. Sci. For. **483**, 341 (2005).

[98] D. J. Christle, A. L. Falk, P. Andrich, P. V. Klimov, J. U. Hassan, N. T. Son, E. Janzén, T. Ohshima, and D. D. Awschalom, “Isolated electron spins in silicon carbide with millisecond coherence times”, Nat. Mater. **14**, 160 (2015).

[99] D. J. Christle et al., “Isolated spin qubits in SiC with a high-fidelity infrared spin-to-photon interface”, Phys. Rev. X **7**, 021046 (2017).

[100] P. V. Klimov, A. L. Falk, D. J. Christle, V. V. Dobrovitski, and D. D. Awschalom, “Quantum entanglement at ambient conditions in a macroscopic solid-state spin ensemble”, Sci. Adv. **1**, e1501015 (2015).

[101] W. F. Koehl, B. B. Buckley, F. J. Heremans, G. Calusine, and D. D. Awschalom, “Room temperature coherent control of defect spin qubits in silicon carbide”, Nature **479**, 84 (2011).

chapter 2

Physical concepts and experimental techniques

Localized defects in crystals can to some degree be seen as molecules embedded in a solid-state matrix. As such, many of the well-established techniques used to characterize the behavior of molecules can be extended and applied towards understanding solid-state defects. Experimentally, optical (e.g. photoluminescence) and spin-resonance techniques – as well as their hybrids – allow us to characterize many of these defects and identify, in practice, their electronic levels and the associated selection rules for transitions between them. Theoretically, group-theoretical analyses of the defects' symmetries have been of core importance to identify the solid-state defects via comparison with experiments, and to understand their optical, spin, and thermal properties in terms of their microscopic environment. In this chapter, we present the theoretical and experimental toolboxes we use to investigate and understand the spectra of lattice defects in SiC. Namely, we present a recap on group theory and how the symmetries of a defect lead to selection rules that help in determining the defects' microscopic configuration. Furthermore, we introduce different photoluminescence-based experimental techniques, and how they allow us to investigate different energy scales with increasing resolution, as well as the time-resolved dynamics of spin relaxation.

In order to identify suitable spin-active defects for quantum communication applications, the first step is to determine the defects' electronic structure (that is, what are the stable configurations of the quantum system and their energies), and how these defects interact with external influences (electromagnetic fields, applied strain, lattice vibrations, *etc.*) [1]. On the one hand, the relevant energy scales for optical and electronic transitions are determined by the defects' electronic structure. One of our goals in this thesis is thus to understand these different energy scales, and how they influence the relevant spin-related metrics. This may help narrowing down, for instance, temperature ranges where the defect is not disturbed by phonons in the lattice. On the other hand, identifying possible selection rules for interaction with electromagnetic fields allows us to identify optimal operation geometries for qubit control and light-matter entanglement protocols, for example.

Localized defects in a solid-state environment can to some degree be seen as molecules embedded in a solid-state matrix. Some defects disturb the lattice environment only slightly (for instance, shallow dopants in semiconductor materials, like nitrogen or boron in SiC). These defects' electronic eigenstates are strongly mixed with the crystalline delocalized Bloch states. Other defects, however, strongly break the periodicity of the lattice and disturb the crystalline structure enough to be (partially) decoupled from the lattice, giving rise to strongly localized electronic eigenstates whose properties arise from electrons at or neighboring the defect site. These are the defects of interest in this thesis. Many of the well-established theoretical (symmetry analysis and first-principle calculations) and experimental (photoluminescence, spin-resonance, and their hybrids) techniques used to characterize and understand the behavior of molecules can be extended and applied towards understanding these solid-state defects. Combined, these experimental and theoretical approaches provide access, in the best-case scenario, to these defects' microscopic configuration via their experimental signatures.

In this chapter, we present in a pedagogical way the group theory and experimental techniques that we use in order to study the spectra of defects in SiC, and how these theoretical and experimental techniques relate to each other. We provide to the reader a recap of group theory as a way to summarize the set of symmetries of a certain quantum system. We show how these symmetries result in selection rules that restrict the possible interactions between the quantum system of interest and its environment. Finally, we introduce the concept of spin and spin-orbit coupling from a group-theory perspective. We also present different experimental (time-resolved) spectroscopic techniques, and how each of them allows us to access and investigate different energy scales with increasing resolution, as well as the time-resolved dynamics of spin relaxation.

2.1. Symmetry analysis

Symmetry analysis is a powerful and ubiquitous tool in physics and is used to explain physical phenomena across all energy scales, from superconductors at mK temperatures, to high-energy particles. In fact, the conservation laws that govern classical as well as quantum mechanical behavior (conservation of linear and angular momentum, energy, electrical charge), can each be linked to a different symmetry (translation and rotation, time-reversal and global phase invariance, respectively) [2]. The symmetries of a certain physical object consist of the set of operations that, when acting on this physical object, give a result that cannot be distinguished from the original object itself. In the context of molecular and solid-state systems, the most important symmetries relate to spatial symmetries (translations and rotations, mirroring operations, space inversion, *etc.*) or time-reversal symmetries (if a certain system or physical process remains unchanged if the arrow of time is reversed) [3–6]. These are the symmetries that we focus on in this section.

The spatial symmetries of lattice defects and molecules determine the orbital part of their electronic eigenstates, that is, the spatial configuration of electrons around the core nuclei. Additionally, since electrons are spin-$1/2$ particles, the full description of spin-active defects from a symmetry perspective must also take into account the transformation properties of a spin-$1/2$. These half-integer spins are spinors and transform in special ways since, upon a rotation of 360° around any given axis, these spinors go into minus themselves [3].

These special properties of half-integer spins can be included in our symmetry analysis of the experimental properties of spin-active defects through the formalism of double groups [3, 6]. However, they do not change the steps we have to go through to obtain, from the symmetry of a certain defect, the degeneracy of its energy eigenstates, and the corresponding selection rules. For this reason and for illustration purposes, we will for now ignore half-integer spins, and focus on simple spinless spatial point groups. Later on, we will also consider the effect of half-integer spins through the formalism of double groups (Sec. 2.1.3), including how it encompasses the coupling of spin and orbital degrees of freedom, and how some special selection rules arise from the concept of time-reversal symmetry.

2.1.1. Point groups: spatial symmetries

In order to visualize the concepts described in this chapter, we focus on two hypothetical molecules with different degrees of symmetry. We name these molecules, for simplicity, a low symmetry molecule (LS), and a high symmetry molecule (HS) (Fig. 2.1(a) and (b), respectively), and we name the atoms composing them by their colors. The low symmetry molecule is composed of a central pink atom, bound to four different (blue, indigo, green, and yellow) atoms in a tetrahedral geometry. The high symmetry molecule, instead, is composed of a central pink atom bound to three green atoms and a single indigo atom, also in a tetrahedral geometry.

Point group and symmetry operations

The spatial distribution of atoms in these molecules has certain symmetries. Within the context of group theory, the concept of a *point group* allows us to summarize these symmetries systematically. Beyond a formal mathematical definition [6, 7], this point group is nothing more than a summary of the closed set of symmetry operations that are applicable to the molecule or solid of interest. For example, it is clear that there is no operation (besides doing nothing) that will preserve the shape of LS. Thus, the point group that describes the symmetry of LS is C_1 (in Schönflies notation), which contains only the identity operation. In contrast, we can operate on HS in a few different ways and end up with a product that is indistinguishable

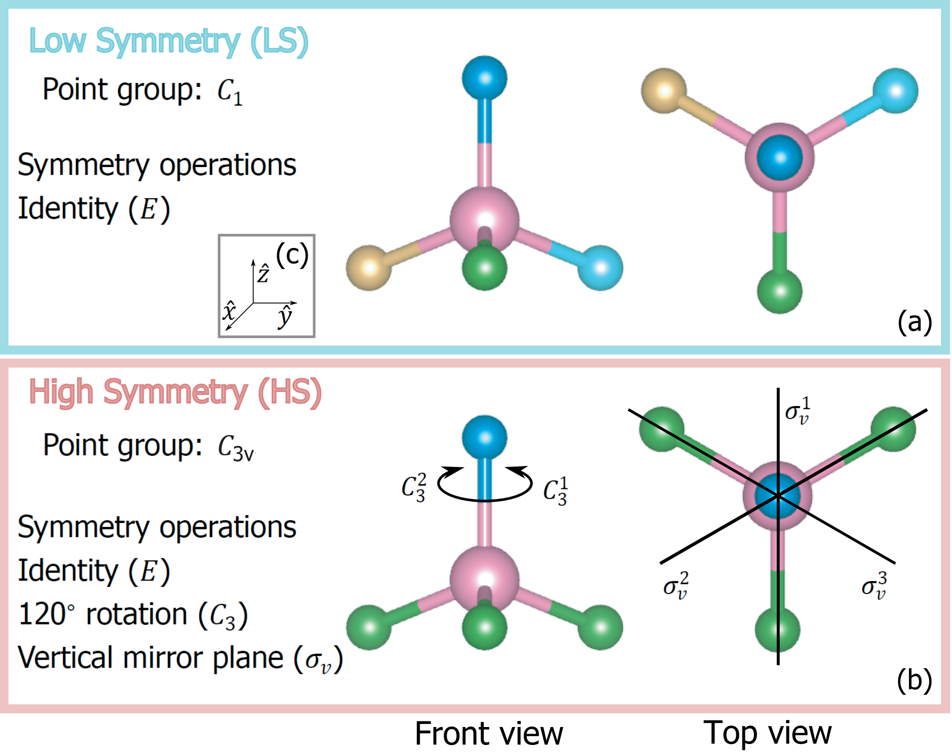

Figure 2.1: **Two hypothetical molecules with different symmetries.** (a) The LS molecule, with four different atoms bound to the central atom, has only one symmetry operation – the identity. The point group describing its symmetries is the C_1. (b) In contrast, the HS molecule has three identical green atoms and a single indigo atom bound to the central pink atom. Rotating (C_3 operation) and mirroring (σ_v operations) this molecule in different ways gives a result that is indistinguishable from the original molecule. Thus, the symmetries of this hypothetical molecule correspond to point group C_{3v}. (c) Coordinate convention for the discussion of matrix representations (see text).

from the original molecule. For instance, we can rotate it 120° in the clockwise or counter-clockwise direction around an axis that connects the pink and the indigo atoms (operations $C_3^{1,2}$, where C_3 indicates a rotation around the three-fold rotational axis, and the superindices indicates that there are two such rotations possible), or we can mirror it across any mirror plane that contains the pink, the indigo and one of the green atoms (operations $\sigma_v^{1,2,3}$, where σ_v indicates a mirroring operation across a plane containing the high-symmetry rotation axis, and the superindices indicate that there are three equivalent mirror planes). Thus, the point group containing all of these symmetry operations, C_{3v}, describes the symmetry of the hypothetical HS molecule.

Irreducible representations

The symmetry operations described above correspond to transformations of the spatial coordinates and, as such, can be represented by matrices [5–7]. For example, we can describe the action of the operations of the point group C_{3v} on a vector $\vec{r} = x\hat{x} + y\hat{y} + z\hat{z}$ (according to the coordinate convention in Fig. 2.1(c)) with the matrices

$$D(E) = R(0^\circ) = \begin{bmatrix} 1 & 0 & 0 \\ 0 & 1 & 0 \\ 0 & 0 & 1 \end{bmatrix}, \tag{2.1}$$

$$D(C_3^{1,2}) = R(\pm 120^\circ) = \begin{bmatrix} \cos(\pm 120^\circ) & \sin(\pm 120^\circ) & 0 \\ -\sin(\pm 120^\circ) & \cos(\pm 120^\circ) & 0 \\ 0 & 0 & 1 \end{bmatrix}, \tag{2.2}$$

$$D(\sigma_v^{1,2,3}) = R(0^\circ, \pm 120^\circ) \begin{bmatrix} 1 & 0 & 0 \\ 0 & -1 & 0 \\ 0 & 0 & 1 \end{bmatrix}, \tag{2.3}$$

where D stands for the matrix representation of a certain operation, and $R(\theta)$ corresponds to a rotation of an angle θ around the symmetry axis. We notice from these matrix representations that, when subject to the symmetry operations of this particular point group, vectors along the $\hat{z}$ axis behave differently from vectors in the xy plane. The component along the $\hat{z}$ axis is unchanged upon any operation of the group C_{3v}. In contrast, the components along the $\hat{x}$ and $\hat{y}$ axes cannot be treated independently: they are fundamentally connected by the operations $C_3^{1,2}$ and $\sigma_v^{1,2,3}$. Mathematically, this property translates into the fact that the matrices presented in Eqs. 2.1-2.3 are block-diagonal. They are all formed by a 2×2 matrix acting on the vector projections in the xy plane, and a 1×1 matrix acting on the vector projection along the $\hat{z}$ axis. These matrices cannot be further reduced: there exists no similarity transformation that will further diagonalize them. For this reason, we call them *irreducible representations* (or *irreps*, for those who are intimate enough with them) of the point group C_{3v} [5–7]. These irreps indicate how different objects (vectors, pseudovectors, operators, *etc.*) transform when subject to the symmetry operation of a certain point group.

Transformation matrices analogous to Eqs. 2.1-2.3 for pseudovectors (that is, vectors like the magnetic field, that gain a negative sign under mirroring operations) can be obtained in a similar way. These show that, whereas pseudovectors in the xy plane transform similarly to vectors in the xy plane, a pseudovector in the $\hat{z}$ direction does not transform as its vectorial counterpart. Instead, this pseudovector gets a negative sign upon a reflection on any of the mirror planes $\sigma_v^{1,2,3}$ (that is, it goes into minus itself). In this way, the point group $C_{3\mathrm{v}}$ has three different irreducible representations: objects that transform like a vector in the $\hat{z}$ direction belong to irrep A_1, objects that transform as a pseudovector in the $\hat{z}$ direction belong to irrep A_2, and objects that transform as vectors in the xy plane belong to irrep E. The irreps A_1 and A_2 are non-degenerate, that is, they act on spaces that are one-dimensional. The irrep E acts on a two-dimensional space, that is, it is doubly degenerate.

In contrast, if we think about the LS molecule and its corresponding point group C_1, the only available symmetry operation is the identity (E), as seen in Fig. 2.1(a). The matrix representation of this operation on a three-dimensional vector space is the identity matrix (Eq. 2.1). This representation is already block-diagonal since it has the same 1×1 matrix repeated across the diagonal entries. Thus, with respect to the symmetry operations of the point group C_1, vectors along the $\hat{x}$, $\hat{y}$ or $\hat{z}$ directions transform similarly. This point group has only one irrep, called A_1.

The properties of each of these irreps with respect to the point-group operations are summarized by their *characters*, or the trace of their matrix representation, and collected into so-called *character tables*. These character tables for the different point groups are extensively tabulated [8], and presented explicitly for the point group $C_{3\mathrm{v}}$ in Tab. 2.1. Using these character tables, we can easily figure out how different functions transform when subject to the point-group operations. For example, if we are interested in figuring out how a function of the product xz transforms under the operations of the point group $C_{3\mathrm{v}}$, all we have to do is multiply the irreps A_1 (describing how z transforms) and E (which describes how x transforms) by multiplying their characters for each point-group operation. This product, $\mathrm{A}_1 \otimes \mathrm{E}$, gives as a result the irrep E. Thus, the product xz transforms in the same way as a vector in the $\hat{x}$ direction. Finally, the characters of a representation also allow us to easily decompose reducible representations – representations that can be further diagonalized into different subspaces that each transform as an irrep of the group of interest – into its constituting irreps. For example, the product of irreps $\mathrm{E} \otimes \mathrm{E}$ is reducible, and can be decomposed into a sum of irreps such that $\mathrm{E} \otimes \mathrm{E} = \mathrm{A}_1 \oplus \mathrm{A}_2 \oplus \mathrm{E}$ (see Tab. A.2). The mathematical formalism necessary to perform this decomposition can be extensively found in group theory books [3–7].

Table 2.1: Character table for the point group $C_{3\mathrm{v}}$.

$C_{3\mathrm{v}}$	E	$C_3^{1,2}$	$\sigma_v^{1,2,3}$
A_1	1	1	1
A_2	1	1	-1
E	2	-1	0

2.1.2. Electronic structure and selection rules

The electronic states of molecules or lattice defects, and their associated energy levels can, in principle, be self-consistently calculated from the Schrödinger equa-

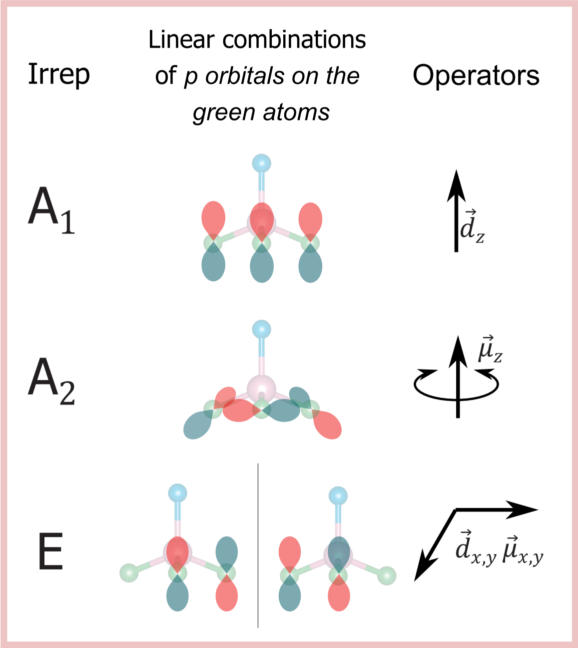

Figure 2.2: **Transformation properties of wavefunctions and operators.** For the hypothetical HS molecule, we can construct several symmetry adapted linear combination (SALC) of green-atom p orbitals. The wavefunctions are represented by blue and red shaded regions, where blue (red) shaded regions correspond to negative (positive) contributions to the wavefunctions. Each SALC transforms as a particular irreducible representation of the point group C_{3v}. Operators can also be classified with respect to how they transform under the symmetry operations of the group. An electric dipole moment in the $\hat{z}$ direction ($\vec{d}_z$) transforms as irrep A_1, whereas a magnetic dipole in the same direction ($\vec{\mu}_z$) transforms as the irrep A_2. Electric and magnetic dipole moments in the xy plane transform according to irrep E.

tion through first-principles quantum-chemical calculations based on Hartree-Fock and density functional theory [4, 9, 10]. These calculations provide valuable information about the microscopic configuration (spatial distribution of core nuclei, number of paired and unpaired electrons, *etc.*) of molecules or defects. They may, however, be computationally demanding (especially if we are also interested in excited state properties [11]). Especially at the stage when the particular geometry and charge state of a defect is not yet known, calculating the electronic structure of all possible configurations to narrow down which ones have the experimentally observed fingerprints may be impossible. In contrast, group theory allows us to quickly analyze a wide array of possible defect configurations based on their symmetries. This analysis informs us about the number and degeneracy of the electronic eigenstates and the selection rules for transitions between them [4]. This insight can be directly compared to experiments to narrow down or determine the possible microscopic configuration of the defect of interest.

Electronic structure

Let us consider, for example, the hypothetical HS molecule. The spatial distribution of electron density in HS must have the same symmetry as the molecule itself. We can understand this intuitively: the electron density is determined by the Coulomb interaction between the electrons and nuclei that constitute the molecule.

If the spatial distribution of the core nuclei does not change when we perform on the molecule the symmetry operations of the group ($C_3^{1,2}$, $\sigma_v^{1,2,3}$), neither should the electron density. Additionally, the electronic eigenstates in this molecule can be written as linear combinations of the atomic orbitals of its valence electrons (s, p, d, *etc.*) in each of the different atoms composing the molecule [4, 5, 9, 12]. Since the electron density in the molecule has the same symmetry as the distribution of core nuclei, these linear combinations of atomic orbitals must be symmetry adapted; in other words, the spatial part of the wavefunctions corresponding to the electronic eigenstates must transform as one of the irreps of the point group $C_{3\mathrm{v}}$.

Figure 2.2 shows a graphical representation of some of these linear combinations. Here, we consider linear combinations of the p orbitals on the green atoms. The p_x, p_y and p_z orbitals have wavefunctions whose amplitude is proportional to the x, y and z components of the electron position, respectively. Thus, at the origin, an orbital p_x (p_y, p_z) transforms as a vector along the $\hat{x}$ ($\hat{y}$, $\hat{z}$) direction (similarly, an orbital d_{xy} transforms as the product of the x and y components). Linear combinations of these orbitals in several atoms may transform differently, however. For example, from the p_z orbitals in the green atoms, we can construct a linear combination that transforms as A_1 (is unchanged upon any operation of the point group), and linear combinations that transform as E (sets of two linearly independent wavefunctions that are fundamentally connected by the operations $C_3^{1,2}$ and σ_v). These sets of linearly independent wavefunctions connected by the symmetry operations of the group are equivalent from a symmetry point of view, and thus must have the same energy. Thus, the degeneracy of an electronic eigenstate corresponds to the dimension of its corresponding irrep. Finally, a linear combination of p_y orbitals on the green atoms transforms as A_2 (the linear combination is unchanged upon rotations around the three-fold axis, but goes into minus itself when mirrored on the planes $\sigma_v^{1,2,3}$).

One of the shortcomings of this group-theoretical approach is that symmetry does not tell us the particular energy ordering of the various possible symmetry adapted molecular orbitals. This means that we cannot, from symmetry considerations alone, determine the energy order of the various wavefunctions depicted in Fig. 2.2. This information must be obtained from an analysis of the valence of the various atoms involved, or – more accurately – from first-principle calculations [10]. In a defect or molecule, the core electrons that participate in bonding have their spin paired into singlets according to Pauli's principle. Thus, the ground-state electronic spin properties in these systems arise (at least in a rough approximation where we disregard exchange interaction with core electrons) from unpaired valence electrons. We can identify the relevant atomic orbitals for the unpaired electron spins from the atomic number of each atom constituting the molecule. Once

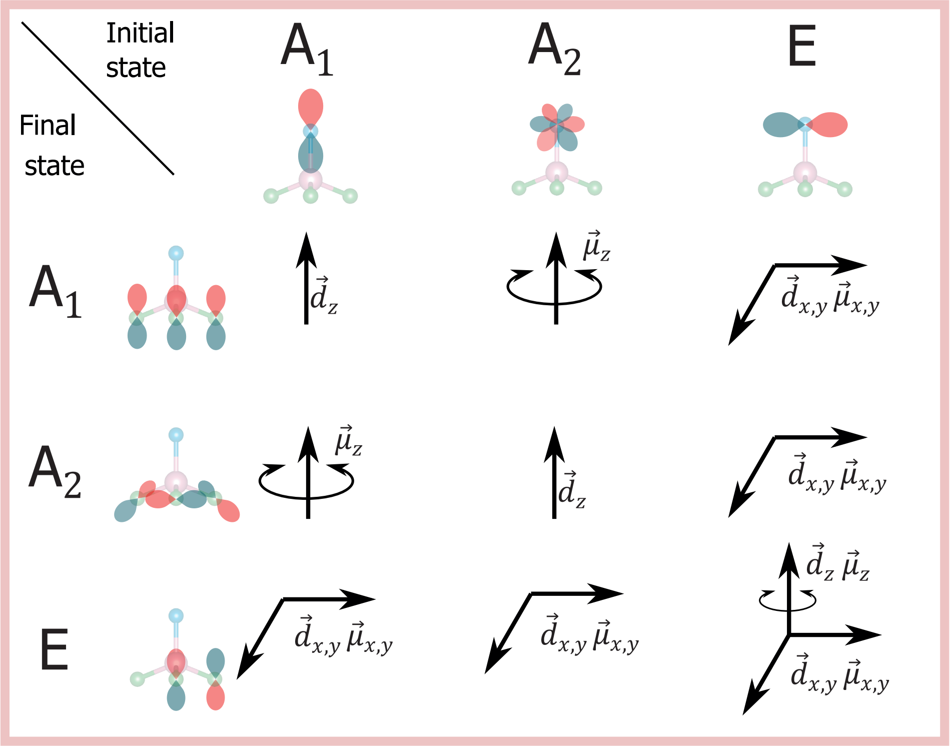

Figure 2.3: **Selection rules for transitions between various electronic eigenstates of the HS molecule**. We show the operators that can drive transitions between eigenstates of different symmetries. The cartoons corresponding to states of each symmetry are intended for illustration purposes and are not the only states with those symmetries. Transitions between two eigenstates transforming as A_1 (or two eigenstates transforming as A_2) can only happen due to an electric dipole moment in the $\hat{z}$ direction. Transitions between a state transforming as A_1 and a state transforming as A_2 requires interaction with an operator that transforms as the magnetic dipole moment in the $\hat{z}$ direction. Electric or magnetic moments in the xy plane can drive transitions between states that transform as A_1 or A_2 and states that transform as E. Finally, electric or magnetic fields in any direction can drive transitions between eigenstates transforming as E.

that is done, we can obtain the symmetry adapted linear combination of these relevant atomic orbitals, and this tells us the degeneracy and symmetry of the relevant electronic eigenstates.

Selection rules

Given the symmetry of the eigenstates, obtained as outlined in the previous section, we can go on to calculate the selection rules for transitions between them. According to Fermi's golden rule, the transition rate $\Gamma_{i\to f}$ (that is, the transition probability per unit of time) between an initial state $|i\rangle$ and a final state $|f\rangle$ is proportional to the matrix element $\langle f|H'|i\rangle$, where H' is the perturbation responsible for driving the transition [4, 13]. Explicitly, these matrix elements can be calculated from the wavefunctions describing the defect eigenstates, such that

$$\langle f|H'|i\rangle = \int_V \psi_f^*(\vec{r},t)H'\psi_i(\vec{r},t)d\vec{r} \tag{2.4}$$

where $\psi_{i,f}(\vec{r},t)$ denotes the wavefunction associated with the initial and final states, respectively, the asterisk corresponds to complex conjugation and the integral is evaluated over the entire space. In general, the integral in Eq. 2.4 will be non-zero. However, the fact that the matrix element is calculated from an integral evaluated over the entire space incurs in some symmetry-based restrictions that lead to identically zero matrix elements in some cases. If the product $\psi_f^*(\vec{r},t)H'\psi_i(\vec{r},t)$ does not contain a part that transforms as the fully symmetric representation A_1, it will be identically zero. Looking at Fig. 2.2, it is evident that functions that transform as A_2 or E are odd functions of at least one spatial coordinate, and as such their integrals over the entire space result in zero. In contrast, functions transforming as A_1 are even functions of all spatial variables, such that their integral over the entire space may be non-zero.

In this way, in order to determine if a certain transition is symmetry allowed, we need to determine how the product $\psi_f^*(\vec{r},t)H'\psi_i(\vec{r},t)$ transforms when we apply the symmetry operations of the relevant point group. As previously stated in Sec. 2.1.1, the symmetry properties of this product can be obtained by multiplying the irreps associated with each one of the terms by each other. Mathematically, $\Gamma_{\langle f|H'|i\rangle} = \Gamma_{\psi_f}^* \otimes \Gamma_{H'} \otimes \Gamma_{\psi_i}$, where Γ denotes the reducible or irreducible representation associated with each term.

The symmetry properties of the perturbation H' ($\Gamma_{H'}$) can be obtained by applying, to the operator on its own, the symmetry operations of the group. In Fig. 2.2, right column, we show explicitly how the electric dipole moment ($\vec{d}$) and magnetic dipole moment ($\vec{\mu}$) operators transform under the operations of the point group $C_{3\text{v}}$. Given the symmetry of these operators and the relevant wavefunctions, we can now easily determine whether $\langle f|H'|i\rangle$ is allowed to be non-zero by symmetry. Figure 2.3 presents a summary of the selection rules for electric and magnetic dipole transitions between electronic eigenstates of a molecule or defect with point-group symmetry $C_{3\text{v}}$. We list, for initial and final eigenstates transforming as each of the irreps of the point group, which electric or magnetic dipole moments can drive transitions between the various levels. For illustration purposes, we also present two examples of wavefunctions transforming as each irrep (one for the initial state, and one for the final state). From this figure it is clear, for example, that we could never drive transitions between an eigenstate transforming as A_1 and an eigenstate transforming as E with an electric field in the $\hat{z}$ direction. This is a result of group theory, but can be intuitively understood by looking at the illustrated wavefunctions presented. In order to go from a state transforming as A_1 into a state transforming as E we need to shift the electron density in the xy plane, and this is not possible with an electric field along the symmetry axis. Similarly, an electric field in the xy plane cannot lead to transitions between two states transforming as A_1, since in this case, we need to shift the electron density along the symmetry axis.

2.1.3. Double groups: spin and spin-orbit coupling

Historically, the concept of an intrinsic angular momentum associated with electrons (their *spin*) arose directly from experimental observations. Explaining the spectra of various atoms in a magnetic field, or the results of the Stern-Gerlach experiment that measured the deflection of accelerated silver atoms in a magnetic field, required the assumption that the electron has an intrinsic angular momentum quantized in half-integer multiples of $\hbar$ [9]. It was not until Dirac combined Schrödinger's equations with relativistic mechanics, however, that a formal and generalized description of the spin arose. Dirac's equations showed that the half-integer spin is an intrinsic property of various particles, much like electric charge, and arises directly from relativistic space-time transformations.

Dirac's equations also showed that the spin is described by a *spinor*, not by a vector. This means that a rotation of an angle of 360° around a general axis takes a spin-1/2 into minus itself [3, 6]. In contrast, a rotation of any vector by an angle of 360° around any axis keeps it unchanged. This fundamental difference means that, when half-integer spins are present, the simple point-group description developed in the previous section is not enough to describe the symmetry properties of an electronic wavefunction. In order to encompass the behavior of half-integer spins, we must extend the relevant point group by including additionally all of the already mentioned symmetry operations followed by a rotation of 360° around the high-symmetry axis. This new, extended group is called a *double group*, and is denoted by an upper bar. For example, the double group $\bar{C}_{3\mathrm{v}}$ is associated with the point group $C_{3\mathrm{v}}$. Besides the operations E, $C_3^{1,2}$ and $\sigma_v^{1,2,3}$, it also contains the operations $\mathcal{R}E$, $\mathcal{R}C_3^{1,2}$ and $\mathcal{R}\sigma_v^{1,2,3}$, where $\mathcal{R}$ denotes a rotation of 360° around the C_3 axis.

These extra symmetry operations give rise to additional irreps which describe directly the symmetry properties of half-integer spins. The spin-up and down spinors associated with a spin-1/2, for example, transform according to the irrep Γ_4 of the double group $\bar{C}_{3\mathrm{v}}$. This irrep is doubly degenerate (that is, it has character 2 for the identity operation), which means that the spins up and down are fundamentally connected by the symmetry operations of the group. Additionally, the operations $\mathcal{R}E$, $\mathcal{R}C_3^{1,2}$ and $\mathcal{R}\sigma_v^{1,2,3}$ have the same characters as the operations E, $C_3^{1,2}$ and $\sigma_v^{1,2,3}$, respectively, with a minus sign.

In the same way as described previously for spinless wavefunctions, we can obtain the symmetry properties of more complex wavefunctions by multiplying the representations associated with each part. For example, two coupled spin-1/2 particles give rise to 4 states that are split into a singlet and a triplet. In an environment that has $C_{3\mathrm{v}}$ symmetry, this translates into the fact that two doublets transforming as Γ_4 can be coupled into 4 states such that $\Gamma_4 \otimes \Gamma_4 = \mathrm{A}_1 \oplus \mathrm{A}_2 \oplus \mathrm{E}$, where the singlet state transforms as A_1, and the triplet states transform as $\mathrm{A}_2 \oplus \mathrm{E}$.

Spin-orbit coupling

An electron's spin interacts with the magnetic fields arising from its orbital motion, as well as the motion of the neighboring charges, via spin-orbit coupling [3, 4, 9]. This interaction couples spin and orbital variables, and means that the full description of the electronic configuration of a molecule or solid-state defect must consider the spin, position, and velocity of all charges involved, and how these properties interact with each other. Calculating these spin-orbit coupled wavefunctions *ab initio* may be hard and is especially complicated for defects and molecules containing heavy elements, where relativistic effects and exchange interaction are especially relevant. The symmetry properties of these wavefunctions, however, are easily accessible through group theory. If we know how both the spinless spatial part of a wavefunction and its spin-related part transform, we can multiply their associated representations by each other to get the symmetry properties of the coupled states [3].

For a single-electron wavefunction, we can illustrate this easily based on the spatial eigenstates presented in Fig 2.2, middle column. An electron (which can have spin up or down, and transforms as the irrep Γ_4) in an orbital that transforms as A_1 gives rise to two degenerate spin-orbit coupled eigenstates that transform as Γ_4, since $\mathrm{A}_1 \otimes \Gamma_4 = \Gamma_4$. In contrast, an electron in a spatial wavefunction transforming as E gives rise to 4 different spin-orbit coupled eigenstates: two degenerate states transforming as the doubly-degenerate irrep Γ_4, and two degenerate states transforming as the irreps $\Gamma_{5,6}$. (Although the irreps $\Gamma_{5,6}$ are non-degenerate, they are connected by time-reversal symmetry and must have the same energy if this symmetry is preserved, see below). Mathematically, this arises from the fact that $\mathrm{E} \otimes \Gamma_4 = \Gamma_4 \oplus \Gamma_{5,6}$. Symmetry thus dictates that, when a spin-1/2 particle occupies a doubly-degenerate orbital eigenstate, an energy splitting may arise that splits the 4 spin-orbit coupled states into two doublets. This energy splitting is a direct result of spin-orbit coupling.

The selection rules for transitions between the spin-orbit coupled states can be obtained by simple multiplication of representations, as presented for spinless wavefunctions in Sec. 2.1.2, but considering the irreducible representations associated with the spin-orbit coupled states instead.

Kramers degeneracy

The spinors associated with the up ($|\uparrow\rangle$) and down ($|\downarrow\rangle$) spin states of a spin-1/2 are connected by time-reversal symmetry [3, 6]. Thus, if $\mathcal{T}$ denotes a time-reversal operation, $\mathcal{T}\,|\uparrow\rangle = |\downarrow\rangle$. This has important consequences for the degeneracy of spin-orbit coupled states arising from half-integer spins and the selection rules for transitions between them.

The first consequence is that half-integer spin states must be at least doubly degenerate in the presence of time-reversal symmetry, an observation mathematically formalized through Kramers Theorem [14]. If the Hamiltonian H is symmetric with respect to time-reversal symmetry (that is, if the commutator $[\mathcal{T}, H] = 0$) and the state $|\psi_1\rangle$ is one of its eigenstates, the state $|\psi_2\rangle = \mathcal{T}\,|\psi_1\rangle$ must also be an eigenstate of H, with the same energy as $|\psi_1\rangle$. For states containing half-integer spins, $|\psi_1\rangle \neq |\psi_2\rangle$. Thus, in the presence of time-reversal symmetry, these states are always part of degenerate doublets consisting of $|\psi_1\rangle$ and $|\psi_2\rangle$.

Another related consequence is that operators that preserve time-reversal symmetry cannot drive transitions between states that are each other's time-reversal conjugate, even when these states are no longer degenerate. This can also be understood based on Kramers Theorem. Let $\mathcal{O}$ be a time-reversal symmetric operator (for example, an electric dipole moment in the $\hat{z}$ direction, then $[\mathcal{T}, \mathcal{O}] = 0$. Thus, the matrix elements of $\mathcal{O}$ must obey the conditions $\langle\psi_1|\mathcal{O}|\psi_1\rangle = \langle\psi_2|\mathcal{O}|\psi_2\rangle$ and $\langle\psi_1|\mathcal{O}|\psi_2\rangle = \langle\psi_2|\mathcal{O}|\psi_1\rangle^*$. Since, in the presence of time-reversal symmetry, $\mathcal{O}$ cannot break the degeneracy between the states $|\psi_1\rangle$ and $|\psi_2\rangle$, then $\langle\psi_1|\mathcal{O}|\psi_2\rangle = \langle\psi_2|\mathcal{O}|\psi_1\rangle^* = 0$.

2.2. Spectroscopic techniques

Experimentally, we can only probe the electronic structure of a molecule or defect center as it interacts with the external world (our experimental equipment). That is, if a defect center is in one of its eigenstates and is not disturbed, it does not exchange energy with our measurement equipment and we can, thus, not measure its energy levels. We can, however, peak into the electronic structure of these defects by disturbing the system in such a way that it transitions between different eigenstates. In this process, it absorbs energy from or emits energy into the outside world. The results of this exchange can be measured, and provide information about the energy difference between the eigenstates involved in the electronic transition and which transitions are allowed.

Here, we focus on the optical characterization of ensembles of defects in SiC. We experimentally investigate how these defect centers interact with (absorb and emit) photons with near-infrared wavelengths in order to determine their electronic structure and whether we can, for example, optically initialize the ensemble spins into a well-defined spin state. In order to do this, we apply different all-optical spectroscopic techniques: photoluminescence (PL), photoluminescence excitation (PLE), two laser spectroscopy, and coherent population trapping (CPT). (In chapter 6, we also use related absorption techniques. These are presented in Sec. 2.3.) Each of these techniques allows us to investigate a different energy range, and to probe the energy of optical transition lines with various resolutions. In fact, these two parameters (resolution and range) are anticorrelated: a measurement with large energy resolution (that allows distinguishing between two small energy differences), usually can only cover a narrow energy range. Thus, these different techniques are highly complementary, and each of them provides unique and valuable information about the full energy structure of spin defects. In what follows, we present a step-by-step introduction of these different experimental techniques and what type of information we can extract from their spectra, based on Fig. 2.4.

2.2.1. Photoluminescence

Of the techniques presented in this chapter, photoluminescence allows us to cover the widest energy range. In these experiments, we excite the sample with photons that have energy much larger than the optical transitions of the defects under study and collect the light emitted by the sample in an energy-resolved manner (see Fig. 2.4(a), right panel). This collected light is passed through a grating, a prism (dispersive spectroscopy) or an interferometer (Fourier-transform spectroscopy) [13, 15], such that its different energy components can be resolved. As a result, we get a spectrum of the intensity of light emitted by the sample versus its energy, as shown in Fig. 2.4(a), left panel. The resolution of these measurements can vary a lot depending on which particular equipment is used to separate the energy components of the detected light. For example, in dispersion spectroscopy, where the light emitted by the sample is diffracted by a grating or prism and then collected in a CCD camera, the parameters of importance to determine the energy resolution are the grating density, the distance between the grating and the CCD sensor, and the pixel density at the sensor [15]. In contrast, in Fourier-transform spectroscopy, the minimum resolution depends on the path difference in an interferometry setup (much like a Michelson interferometer) [16]. Table-top setups of both types usually have maximum energy resolution (in the near-infrared part of the spectrum) on the order of $0.1 - 0.01$ meV.

In order to understand the different features of a PL spectrum, we need to relate the measurement and its associated physical processes to the energy structure of the defects being investigated in more detail. This can be done based on the schematics of Fig. 2.4(a), right panel. In these schematics, each parabola corresponds to an electronic eigenstate of the defect; upwards, straight arrows indicate excitation whereas downwards, wiggly arrows indicate optical emission. Ground and optically-excited states have different energies, as indicated by the vertical displacement of the parabolas corresponding to each of these states. Additionally, the defects' ground and optically-excited states are characterized by a different set of configuration coordinates (the horizontal axis). These configuration coordinates may include but are not limited to the coordinates of the nuclei at or neighboring the defect center and the defect spin and charge state [5, 11, 13], for example. Both ground and optically-excited states can interact with localized vibrations, just like molecules. Thus, ground and optically-excited states are characterized by a zero-phonon state lowest in energy (represented by the lowest horizontal line in each of the parabolas in this schematic) followed by a set of phonon-coupled states higher in energy (represented by the other horizontal lines in the parabolas) [5]. The strength of optical transitions between eigenstates with different degrees of freedom (phonon coupling, spin, *etc.*) can be reduced as compared to optical transitions between pure electronic orbital eigenstates (Franck-Condon principle, [13]). This strength may even become zero when the spin/phonon part of the wavefunctions associated with the initial and final states are orthogonal to each other.

In a photoluminescence experiment, the energy of the photons used to excite the defects is much larger than the energy difference between ground and optically-excited states under study. Thus, as a defect in the ground state absorbs a photon, it ends up in a highly excited band or vibronic state. The defect quickly relaxes non-radiatively as this excess in energy is transferred to the lattice through vibrations or collisions with band electrons or holes, for example. Eventually (if the temperature is low enough), the defect ends up in the zero-phonon optically-excited state, and the only way in which it can further lose its excess energy is through optical transitions. Thus, from the zero-phonon optically-excited state the defect decays back to the ground state through the emission of photons.

When the defect decays directly from the zero-phonon optically-excited state into the zero-phonon ground state, it emits photons into the zero-phonon line (ZPL, see Fig. 2.4(a), left panel). The zero-phonon line is often broadened by inhomogeneity in the sample well beyond the natural linewidth of individual defects, limited by the optically-excited state lifetime. In the case of measurements on ensembles, each different defect sits in a different part of the crystal and thus sees a slightly different electrostatic environment (due to strain, phonons, or charge instability of other neighboring defects). If the energy of both ground and optically-excited states is sensitive to electrostatic fields, the energy difference between them will differ slightly for different defect centers, leading to both temporally and spatially *inhomogeneously broadened* ZPL emission. This inhomogeneous broadening of the optical transitions of the defect centers is an important parameter for quantum

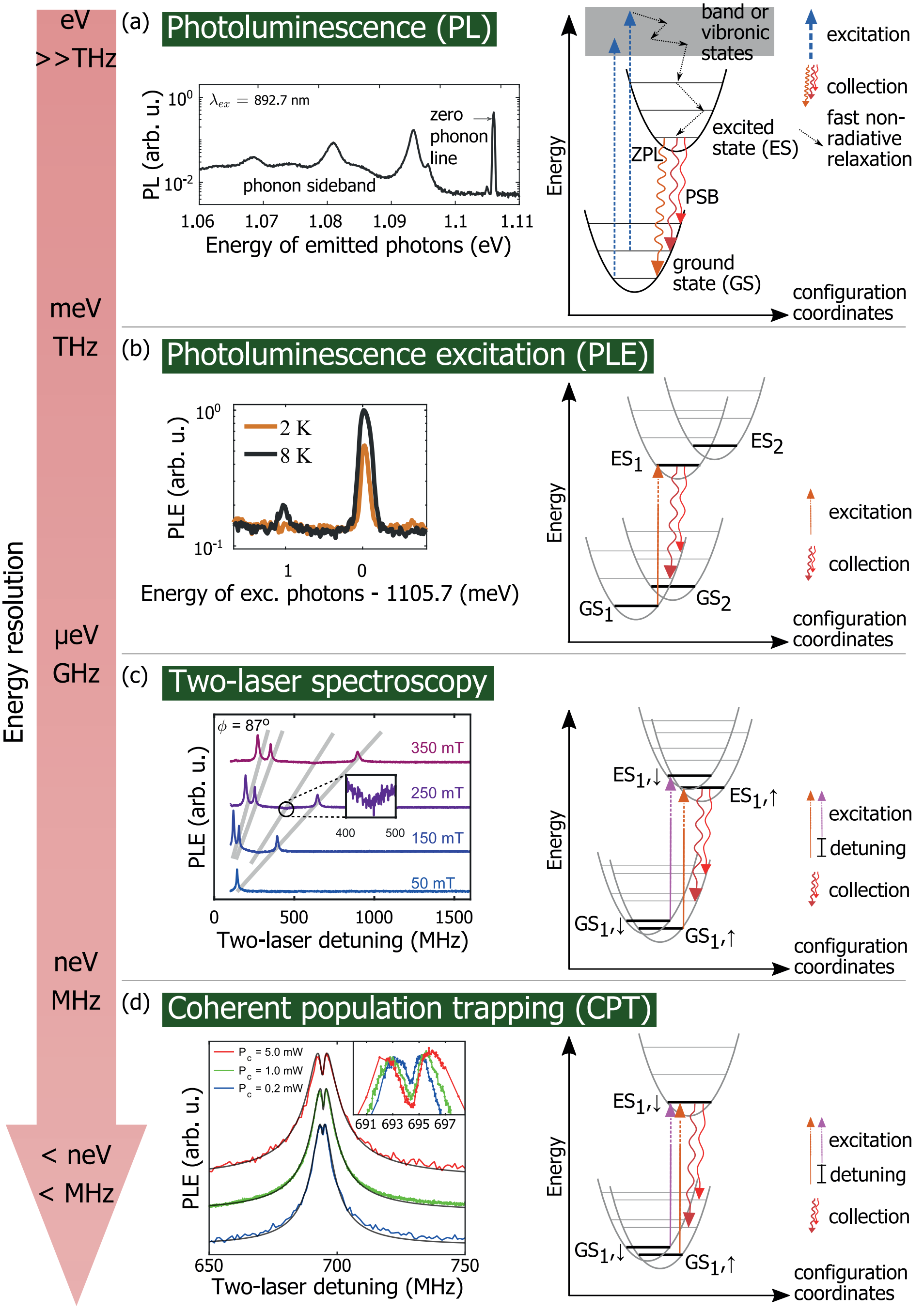

Figure 2.4: **Spectroscopic techniques**. Continued caption in next page

Figure 2.4: The spectra obtained with the different spectroscopic techniques considered (a-d, left panels) provide information about the energy levels of the defect centers (a-d, right panel) with increasing energy resolution. In this way, the different techniques presented here are complimentary: (a) photoluminescence informs us about the energy splitting between ground and optically-excited states, and what are the energies of the vibrational modes that can couple to the electronic ground state; (b) photoluminescence excitation informs us about the inhomogenous broadening of the optical transitions within the ensemble, and whether there are (near) degenerate electronic states accessible to the defects; (c) two-laser spectroscopy allows us to probe energy splittings smaller than the inhomogeneous broadening of single-laser PLE lines, such as the magnetic-field dependent splitting between spin sublevels in ground and optically-excited states, and (d) coherent population trapping informs us about the timescale at which the ensemble spins dephase.

information applications. In order to entangle two defects via optical fields, the photons emitted by the two defects must be indistinguishable. Thus, defect centers that suffer from strong inhomogeneous broadening create additional challenges for establishing long-distance entanglement. For defect centers with little inhomogeneous broadening (in the tens of GHz range), the width of the ZPLs in a PL spectrum may be a convolution of the width of the inhomogeneously broadened optical transitions and the resolution of the spectrometer.

Additionally, the defect can also decay into one of the vibronic states of the ground state. These decay processes result in a broad phonon-sideband emission at energies lower than the ZPL. In the particular spectrum we have chosen to illustrate this technique (Fig. 2.4(a), left panel), there is a gap between the ZPL and the PSB, and we can recognize in the PSB a series of peaks regularly spaced. The gap between the ZPL and the onset of the PSB indicates that the vibrational modes to which the ground state couples are localized: strongly delocalized phonon modes have energies in a continuum, whereas localized vibrational modes have quantized energies. This is corroborated by the regular spacing of the peaks appearing in the PSB: each peak corresponds to a phonon replica of the electronic ground state.

2.2.2. Photoluminescence excitation

Due to symmetry (see Sec. 2.1.2, Fig. 2.2), the ground and optically-excited state manifolds of a certain defect center may be composed of a set of degenerate or nearly degenerate spatial eigenstates ($\mathrm{GS}_{1,2}$ and $\mathrm{ES}_{1,2}$ in Fig. 2.4(b), right panel). If the energy splitting between different states within the ground or optically-excited state manifolds is small enough (smaller than the resolution of the spectrometer or interferometer), transitions between these states will give rise to ZPLs that cannot be distinguished in a PL spectrum. In this case, we need a spectroscopy technique with higher resolution to characterize the ground and optically-excited state manifolds in detail. The technique of choice in this case is photoluminescence excitation [17–20]. In this technique, we excite the defects resonantly with a narrow-line laser

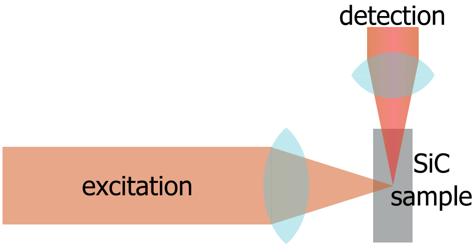

Figure 2.5: **Measurement geometry.** In spectroscopic techniques based on emission, we collect light emitted by the sample in a direction orthogonal to the propagation direction of the excitation optical beam. In measurements where we only detect light emitted into the phonon sideband, an additional long-pass filter is placed between the sample and the detector in order to suppress scattered excitation light.

tuned to the energy of the ZPL in a PL spectrum – that is, the energy of the photons used to excite the defect centers matches the energy splitting between ground and excited states. Using a tunable laser, we can scan the energy of the photons impinging into the sample with high accuracy and in very small steps. In fact, the smallest step size possible is in the sub-MHz range (that is, below a neV). However, in practice we often take steps of a few GHz (or a few μeV), since this allows us to scan a few meV energy range within a few hours. As we scan the energy of the excitation photons (horizontal axis in the PLE spectrum of Fig. 2.4(b)), we measure the integrated number of photons emitted by the sample into the phonon sideband (vertical axis in the PLE spectrum). We do this by collecting the light emitted by the sample into a direction orthogonal to the propagation direction of the excitation light, and feeding it to an avalanche photodiode that can detect single photons (Fig. 2.5). We filter out the scattered excitation light with a long-pass filter (a filter that significantly suppresses light with wavelength shorter than a threshold, but allows light with longer wavelengths to go through). The amount of light emitted into the phonon sideband depends on the population of defects that can be optically excited by the excitation laser. Thus, as the excitation laser is resonant with optical transitions starting from thermally populated states in the ground state manifold, the amount of light emitted into the phonon sideband strongly increases leading to a peak in the PLE spectrum (Fig. 2.4(b), left panel).

Additionally to showing whether or not the ground and optically excited manifolds are composed of (near) degenerate orbital states, a PLE spectrum also provides much clearer insight into the inhomogeneous broadening of the optical transitions. The width of a peak in a PLE spectrum is a direct result of the energy broadening and relative shifts of the optical transition lines for the various defects that compose the ensemble. In the PLE spectrum shown in Fig. 2.4(b), this inhomogeneous broadening is approximately 25 GHz (or 100 μeV).

2.2.3. Two-laser spectroscopy

Spin-related energy splittings (e.g. hyperfine lines or Zeeman splittings between electronic spin sublevels at small magnetic fields) are often much smaller than the inhomogeneous broadening of the optical transition lines of solid-state defects. In this way, these features are not accessible via single-laser spectroscopy techniques like PL or PLE. In order to characterize the spin-related energy structure of these defects at small magnetic fields, we must use yet another technique. In this thesis, we make use of two-laser spectroscopy techniques (Fig. 2.4(c)) [21–23].

As mentioned before, the energy splitting between ground and optically-excited states is sensitive to electrostatic inhomogeneities in the lattice, giving rise to the inhomogeneous broadening of the optical transition. The energy splitting between the spin sublevels in the ground and optically-excited states, however, is mainly determined by the Zeeman coupling between the magnetic moment of the electronic state and the external magnetic field, and the coupling between the electronic spin and neighboring nuclear spins. The Zeeman interaction may be influenced by inhomogeneous electric fields only in second order, through spin-orbit coupling. Thus, throughout an ensemble, the Zeeman splitting observed by different defects suffers much less from inhomogeneous broadening than the splitting between ground and optically-excited states.

Two-laser spectroscopy makes use of this fact. In these experiments, we excite the sample with two different lasers (a control and a probe beam), and collect the light emitted by the defects into the phonon sideband (Fig. 2.4(c), right panel). We use the same geometry as in Fig. 2.5. We can control the detuning between the control and the probe beams (that is, the energy difference between the photon energies in the two optical fields) with high accuracy, down to sub-MHz energy differences. If the spin-sublevels in ground and excited states are non-degenerate, the control beam may lead to spin polarization in the ground state sublevels. This is due to the fact that the optical decay from optically-excited states into ground state sublevels may cause a ground-state spin flip. When this happens, the defect ends up in a *dark* spin state, that is, a spin state which is not resonantly driven into the optically-excited state by the control laser. The probe laser, however, may drive optical transitions from this dark spin sublevel, depending on its detuning with respect to the control beam. As we scan the detuning between the two optical fields (horizontal axis in Fig. 2.4(c), left panel), the amount of light emitted into the phonon sideband (vertical axis in the same figure) is enhanced or suppressed when control and probe beams are simultaneously resonant with two distinct spin-resolved optical transitions, giving rise to peaks or dips in the two-laser PLE spectrum. Measuring the multiplicity of features in a two-laser spectrum and their dependency on the magnetic field provides important information about the multiplicity of the

Figure 2.6: **Measurement geometry and time-resolved signal in a time-resolved PLE experiment.** (a) We excite the sample with pump and probe pulses separated by a delay τ, and (b) collect the photons emitted by the sample into the phonon sideband in a time-resolved manner.

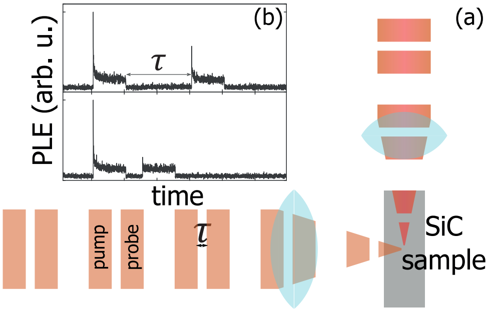

spin sublevels (that is, if the ground and optically excited electronic states have a spin 1/2, 1, *etc.*) and how they couple to external magnetic fields [18, 19, 21].

2.2.4. Optically probing spin dynamics

We can use optical techniques derived from PLE and two-laser spectroscopy to probe the time evolution of the spin. On the one hand, *time-resolved PLE* provides access to the spin-relaxation time (T_1), the time it takes for a spin-polarized ensemble to relax back to its equilibrium configuration. On the other hand, *coherent population trapping* allows us to probe the ensemble inhomogeneous coherence time (or ensemble dephasing time T_2^*). This is the time it takes for an ensemble of defects in a collective coherent state to lose its phase information due to the influence of an inhomogeneously interacting environment. Below, we provide a few more details on each of these techniques.

Time-resolved PLE

In time-resolved PLE experiments, we use a single laser (from which we create pump and probe temporal pulses that have the same photon energy) to excite the ensemble, and we collect the photons emitted by the defects into the phonon sideband in a time-resolved manner (Fig. 2.6).

As explained previously in Sec. 2.2.3, the amount of light emitted by the ensemble into the phonon sideband is proportional to the fraction of the ensemble that can be resonantly driven into the optically-excited state. The pump pulse is long enough to polarize the ensemble into a dark spin sublevel via spin-flipping optical transitions. As the pump pulse is turned off, the ensemble relaxes back to its equilibrium configuration (at cryogenic temperatures of a few K and magnetic fields below a few T, the spin sublevels are approximately equally occupied in equilibrium) in a characteristic spin-relaxation time T_1. A second (probe) pulse excites the ensemble after a delay time τ. As a second probe pulse excites the ensemble, the number of emitted photons depends on the fraction of the ensemble that has relaxed back into a *bright* spin sublevel (that is, the spin sublevel that can be resonantly driven into the optically-excited state). By measuring the ensemble photon emission (just as in PLE experiments) versus the variable delay τ between the pump and probe pulses (Fig. 2.6(b)) we can determine the spin-relaxation time constant T_1 [19, 24].

Coherent population trapping

As mentioned above, coherent population trapping allows us to determine the ensemble dephasing time T_2^*. This technique consists of exciting the ensemble with two lasers (as in two-laser spectroscopy), but focusing on a region of the spectrum where the two lasers resonantly drive transitions from two different ground states ($\mathrm{GS}_1, \downarrow$ and $\mathrm{GS}_1, \uparrow$ in Fig. 2.4(d), right panel) into a common excited state ($\mathrm{ES}_1 \downarrow$ in the same figure). When one of the optical fields is strong enough, the two lasers are on or near resonance with the two possible spin-resolved optical transitions and the difference in photon energy between the two optical fields matches the ground-state energy splitting between the two spin sublevels, the electronic eigenstates are modified by the presence of the additional optical fields. The new eigenstates must be obtained considering the coupled light-matter dynamics [25]. One of the resulting eigenstates is the so-called CPT state, a coherent superposition of ground-state sublevels that is *dark*, that is, it cannot be resonantly excited into the optically-excited state. This coherent superposition depends on the amplitude and relative phase of the optical fields. Thus, as the coupled light-matter system evolves and defects in the optically-excited state dacay into this dark eigenstate, the emission of photons from the ensemble is suppressed, giving rise to a dip in a broader two-laser spectroscopy peak (Fig. 2.4(d), left panel). The depth and width of this dip depends on both the power in the optical fields and the dephasing time of the spin ensemble [25].

2.3. Appendix: Absorption spectroscopy

As defect centers interact with an on-resonance excitation beam, they absorb photons and this changes the power of the excitation laser as it propagates through the sample. According to Beer's Law [13], a beam with intensity I_0 propagating through a sample of length L with concentration of defects that interact resonantly with the optical field N is attenuated such that, after the sample, its intensity is given by

$$I = I_0 e^{-\sigma N L}. \tag{2.5}$$

Here, σ is the absorption cross section in units of area related to a particular defect center and photon energy. In reality, as the beam propagates through the experimental setup it is also attenuated due to processes independent of the defects that we study experimentally, such as reflections off of interfaces. We should take for

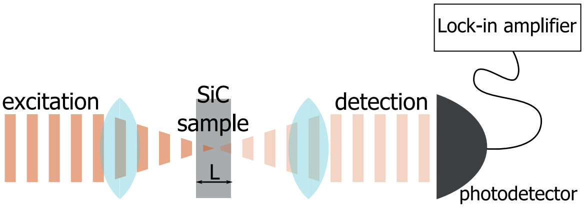

Figure 2.7: **Measurement geometry for absorption spectroscopy.** The transmitted excitation beam is monitored in an analog photodetector. To increase the signal-to-noise ratio in these measurements, the excitation beam can be modulated in time, and the voltage at the photodetector can be fed to a lock-in amplifier.

the intensity I_0 a reference value that accounts for these sample-independent processes. Thus, we can construct measurement techniques analogous to PLE and two-laser spectroscopy where, instead of measuring the light emitted by the sample, we measure how the defects modify the intensity of the beam transmitted through the sample, in a geometry as shown in Fig. 2.7.

For instance, we can measure the inhomogeneous broadening of optical transitions by probing the spectral shape of the absorption lines related to a certain defect by scanning the excitation laser energy. This measurement is analogous to PLE. We can also investigate how the absorption of an on-resonance laser changes when a second detuned beam is also present, in a measurement analogous to two-laser spectroscopy. Finally, we can excite the sample with time-resolved pump and probe pulses, and monitor how the absorption of the probe pulse changes as a function of the delay time between pump and probe. This measurement is analogous to the time-resolved PLE experiments introduced earlier.

One of the advantages of measuring changes in the transmission of a beam propagating through the sample is that, since a laser beam is composed of many photons, its intensity can be directly measured by an analog photodetector. In these measurements, every defect that the laser beam encounters influences the transmitted power of the optical field, such that there is very little geometrical loss of signal in an absorption measurement. In contrast, experiments that rely on measuring the emission from the defects usually require single-photon counters orders of magnitude more expensive than a photodetector. This is due to the fact that emission from the defects is usually non-directional, such that when we collect light emitted by the ensemble into a certain direction we only collect a small fraction of the total emission, and geometrical losses thus play a significant role.

Another related advantage is that absorption measurements – especially time-resolved measurements – can be much faster than their emission counterparts. This is due to the fact that an avalanche photodiode (APD) tuned for single-photon counting measures single photons and returns their time tags in a digital signal. After each photon-counting event, the APD needs some time to reset itself to its equilibrium configuration, such that each photon-counting event is followed by a dark time in which no photons can be measured. Thus, in time-resolved experiments where a significant number of photons needs to be collected for acceptable signal-to-noise ratios considering Poisson statistics, the measurement times are significantly extended. In contrast, an analog photodetector yields, as a signal, a voltage proportional to the number of photons impinging on its sensor. Thus, when compared to measuring on an APD, measurements taken on analog photodetectors can be faster by at least a factor proportional to the number of photons collected times the APD dead time.

The catch involved with measuring absorption signals directly on analog photodetectors is that the influence of the sample on the transmitted laser beam must be significant. That is, there must be a detectable sample-induced difference between I and I_0 in Eq. 2.5. If a significant portion of the excitation beam is absorbed when on-resonance with the optical transitions of the defect of interest, that is, if the product σNL is considerable (≥ 1), we say that the sample is *optically thick*.

In order to improve the signal-to-noise ratio in absorption experiments, we may choose to periodically modulate the excitation laser in time and feed the signal from the analog photodetector into a lock-in amplifier. A lock-in amplifier is a voltage amplifier designed to extract signals with certain frequency components from a noisy background [26]. Given a certain reference periodic signal (the frequency at which we modulate the excitation, which we feed to the lock-in) with frequency f_{ref}, the lock-in amplifier uses a frequency-filtering operation to extract the component of an input voltage signal (the signal that is output by the photodetector, V_{noisy}) oscillating at the frequency f_{ref}. Besides removing static backgrounds, this setup also removes a big part of the noise spectrum in the signal, in particular the low-frequency drift and noise that typically has the highest amplitudes. In this way, we can eliminate the influence of scattered light, modulations of the excitation laser beam at different frequencies than f_{ref}, or electrical noise due to the connections of the photodetector itself. In chapter 6, we present the specific measurement protocols used for measuring time-resolved PLE and two-laser spectra based on absorption and aided by a lock-in amplifier.

References

[1] G. Wolfowicz, F. J. Heremans, C. P. Anderson, S. Kanai, H. Seo, A. Gali, G. Galli, and D. D. Awschalom, “Qubit guidelines for solid-state spin defects”, Nat. Rev. Mater. (2021).

[2] R. P. Feynman, R. B. Leighton, and M. L. Sands, *The Feynman lectures on physics* (Addison-Wesley, 1989).

[3] M. S. Dresselhaus, G. Dresselhaus, and A. Jorio, *Group theory, Application to the physics of condensed matter* (Springer-Verlag Berlin Heidelberg, 2008).

[4] M. Tinkham, *Group theory and quantum mechanics* (Dover Publications, 2003).

[5] D. C. Harris and M. D. Bertolucci, *Symmetry and spectroscopy: an introduction to vibrational and electronic spectroscopy* (Dover Publications, 1989).

[6] P. W. M. Jacobs, *Group theory with applications in chemical physics* (Cambridge University Press, 2005).

[7] H. F. Jones, *Groups, representations and physics*, 2nd edition. (Taylor & Francis, 1998).

[8] G. F. Koster, J. D. Dimmock, R. G. Wheeler, and H. Statz, *Properties of the thirty-two point groups* (M.I.T. Press, 1963).

[9] C. Cohen-Tannoudji, B. Diu, F. Laloe, and S. Reid Hemley, *Quantum mechanics* (John Wiley, 1977).

[10] I. N. Levine, *Quantum chemistry*, 4th edition. (Prentice Hall, 1991).

[11] Y. Jin, M. Govoni, G. Wolfowicz, S. E. Sullivan, F. J. Heremans, D. D. Awschalom, and G. Galli, *Photoluminescence spectra of point defects in semiconductors: validation of first principles calculations*, 2021.

[12] P. W. Atkins and J. De Paula, *Physical chemistry*, 9th edition. (W.H. Freeman and Company, 2010).

[13] M. Fox, *Optical properties of solids*, 2nd edition. (Oxford University Press, 2010).

[14] H. A. Kramers, "Théorie générale de la rotation paramagnétique dans les cristaux", Proceedings of the Royal Netherlands Academy of Arts and Sciences **33**, 959 (1930).

[15] I. Pelant and J. Valenta, *Luminescence spectroscopy of semiconductors*, 1st edition. (Oxford Univ. Pr., 2012).

[16] P. R. Griffiths and J. A. De Haseth, *Fourier transform infrared spectrometry*, Chemical analysis ; v. 83 (Wiley, 1986).

[17] O. V. Zwier, D. O'Shea, A. R. Onur, and C. H. van der Wal, "All–optical coherent population trapping with defect spin ensembles in silicon carbide", Sci. Rep. **5**, 10931 (2015).

[18] T. Bosma et al., "Identification and tunable optical coherent control of transition-metal spins in silicon carbide", npj Quantum Information **4**, 48 (2018).

[19] G. Wolfowicz, C. P. Anderson, B. Diler, O. G. Poluektov, F. J. Heremans, and D. D. Awschalom, "Vanadium spin qubits as telecom quantum emitters in silicon carbide", Sci. Adv. **6**, eaaz1192 (2020).

[20] B. Diler, S. J. Whiteley, C. P. Anderson, G. Wolfowicz, M. E. Wesson, E. S. Bielejec, F. J. Heremans, and D. D. Awschalom, "Coherent control and high-fidelity readout of chromium ions in commercial silicon carbide", npj Quantum Information **6**, 11 (2020).

[21] O. V. Zwier, *Two-laser spectroscopy and coherent manipulation of color-center spin ensembles in silicon carbide*, Zernike Institute PhD thesis series, ISSN 1570-1530 (University of Groningen, 2016).

[22] N. B. Manson and C. Wei, "Transient hole burning in NV centre in diamond", J. Lumin. **58**, 158 (1994).

[23] C. Santori et al., "Coherent population trapping in diamond NV centers at zero magnetic field", Opt. Express **14**, 7986 (2006).

[24] C. M. Gilardoni, T. Bosma, D. van Hien, F. Hendriks, B. Magnusson, A. Ellison, I. G. Ivanov, N. T. Son, and C. H. van der Wal, "Spin-relaxation times exceeding seconds for color centers with strong spin–orbit coupling in SiC", New J. of Phys. **22**, 103051 (2020).

[25] M. Fleischhauer, A. Imamoglu, and J. P. Marangos, “Electromagnetically induced transparency: optics in coherent media”, Rev. Mod. Phys. 77, 633 (2005).

[26] *MODEL SR830 DSP Lock-In Amplifier*, Revision 2.5, Stanford Research Systems (Sunnyvale, California, 2011).

chapter 3

Spectroscopy of a spin-1/2 transition metal defect in SiC

Color centers in wide-bandgap semiconductors are attractive systems for quantum technologies since they can combine long-coherent electronic spin and bright optical properties. Several suitable centers have been identified, most famously the nitrogen-vacancy defect in diamond. However, integration in communication technology is hindered by the fact that their optical transitions lie outside telecom wavelength bands. Several transition-metal impurities in silicon carbide do emit at and near telecom wavelengths, but knowledge about their spin and optical properties is incomplete. We present all-optical identification and coherent control of molybdenum-impurity spins in silicon carbide with transitions at near-infrared wavelengths. Our results identify spin $S = 1/2$ *for both the electronic ground and excited state, with highly anisotropic spin properties that we apply for implementing optical control of ground-state spin coherence. We identify, based on a group-theoretical analysis of the magneto-optical spectra, the microscopic configuration of the defect. Our results show that the defect has optical lifetimes of ~60 ns and inhomogeneous spin dephasing times of ~0.3 μs, establishing relevance for quantum spin-photon interfacing.*

3.1. Introduction

Electronic spins of lattice defects in wide-bandgap semiconductors have come forward as an important platform for quantum technologies [2], in particular for applications that require both manipulation of long-coherent spin and spin-photon interfacing via bright optical transitions. In recent years this field showed strong development, with demonstrations of distribution and storage of non-local entanglement in networks for quantum communication [3–7], and sensing applications [8–12]. The nitrogen-vacancy defect in diamond is the material system that is most widely used [13, 14] and best characterized [15–17] for these applications. However, its zero-phonon-line (ZPL) transition wavelength (637 nm) is not optimal

---

Parts of this chapter have been published in npj Quantum Information **4**, 48 (2018) [1].

for integration with standard telecom technology, which uses near-infrared wavelength bands where losses in optical fibers are minimal. A workaround could be to convert photon energies between the emitter-resonance and telecom values [18–20], but optimizing these processes is very challenging.

This situation has been driving a search for similar lattice defects that do combine favorable spin properties with bright emission directly at telecom wavelength. Both diamond and silicon carbide (SiC) can host many other spin-active color centers that could have suitable properties [21–24] (where SiC is also an attractive material for its established position in the semiconductor device industry [25, 26]). However, for many of these color centers detailed knowledge about the spin and optical properties is lacking. In SiC, the divacancy [27–29] and silicon vacancy [11, 30–32] were recently explored, and these indeed show millisecond homogeneous spin coherence times with bright ZPL transitions closer to the telecom band.

We present here a study of transition-metal impurity defects in SiC, which exist in great variety [33–38]. We focus here (directed by availability of lasers in our lab) on the molybdenum impurity with ZPL transitions at 1076 nm (in 4H-SiC) and 1121 nm (in 6H-SiC). Our results lead to the identification of the microscopic configuration of this defect and show that the Mo defect is highly analogous to the neutral V defect emitting directly in the telecom O-band [34]. Theoretical investigations [39], early electron paramagnetic resonance [34, 40] (EPR), and photoluminescence (PL) studies [41–43] indicate that these transition-metal impurities have promising properties. These studies show that they are deep-level defects that can be in several stable charge states, each with a distinctive value for its electronic spin S and near-infrared optical transitions. Further tuning and engineering possibilities come from the fact that these impurities can be embedded in a variety of SiC polytypes (4H, 6H, *etc.*, see Fig. 3.1(a)). Recent work by Koehl *et al.* [38] studied chromium impurities in 4H-SiC using optically detected magnetic resonance. They identified efficient ZPL (little phonon-sideband) emission at 1042 nm and 1070 nm, and their charge state as neutral with an electronic spin $S = 1$ for the ground state.

Our work is an all-optical study of ensembles of molybdenum impurities in p-type 4H-SiC and 6H-SiC material. The charge and spin configuration of these impurities, and the defect configuration in the SiC lattice that is energetically favored, was until our work not yet identified with certainty. Our results show that these Mo impurities are in the $\text{Mo}^{5+}(4d^1)$ charge state (we follow here conventional notation [34]: the label 5+ indicates that of an original Mo atom 4 electrons participate in bonds with SiC and 1 electron is transferred to the p-type lattice environment). The single remaining electron in the $4d$ shell gives spin $S = 1/2$ for the ground state and optically-excited state that we address. While we will show later that this can be concluded from our measurements, we assume it as a fact from the beginning since this simplifies the explanation of our experimental approach.

In addition to this identification of the impurity properties, we explore whether ground-state spin coherence is compatible with optical control. Using a two-laser magneto-spectroscopy method [29, 44, 45], we identify the spin Hamiltonian of the $S = 1/2$ ground state and optically-excited state, which behave as doublets with highly anisotropic Landé g-factors. This gives insight in how a situation with only spin-conserving transitions can be broken, and we find that we can use a weak magnetic field to enable optical transitions from both ground-state spin levels to a common excited-state level (Λ level scheme). Upon two-laser driving of such Λ schemes, we observe coherent population trapping (CPT, all-optical control of ground-state spin coherence and fundamental to operating ensemble-based quantum memories optically[46, 47]). The observed CPT reflects inhomogeneous spin dephasing times comparable to that of the SiC divacancy [29, 48] (near 1 μs).

In what follows, we first present our methods and results of single-laser spectroscopy performed on ensembles of Mo impurities in both SiC polytypes. Next, we discuss a two-laser method where optical spin pumping is detected. This allows for characterizing the spin sublevels in the ground and excited states, and we demonstrate how this can be extended to controlling spin coherence. Finally, we describe how the experimental magneto-optical properties of these defects allow us to determine its charge state and microscopic configuration.

3.2. Materials and experimental methods

Both the 6H-SiC and 4H-SiC (Fig. 3.1(a)) samples were intentionally doped with Mo. There was no further intentional doping, but near-band-gap photoluminescence revealed that both materials had p-type characteristics. The Mo concentrations in the 4H and 6H samples were estimated [42, 43] to be in the range 10^{15}-10^{17} cm^{-3} and 10^{14}-10^{16} cm^{-3}, respectively. The samples were cooled in a liquid-helium flow cryostat with optical access, which was equipped with a superconducting magnet system. The setup geometry is depicted in Fig. 3.1(b). The angle ϕ between the direction of the magnetic field and the c-axis of the crystal could be varied, while both of these directions were kept orthogonal to the propagation direction of excitation laser beams. In all experiments where we resonantly addressed ZPL transitions the laser fields had linear polarization, and we always kept the direction of the linear polarization parallel to the c-axis. Earlier studies [39, 42, 43] of these materials showed that the ZPL transition dipoles are parallel to the c-axis. For our experiments we confirmed that the PLE response was clearly the strongest with linear polarization parallel to the c-axis, for all directions and magnitudes of the magnetic fields that we applied. All results presented in this work come from photoluminescence (PL) or photoluminescence-excitation (PLE) measurements. The excitation lasers were focused to a ~100 μm spot in the sample. PL emission was measured from the side. A more complete description of experimental aspects is presented in Sec. 3.10.2.

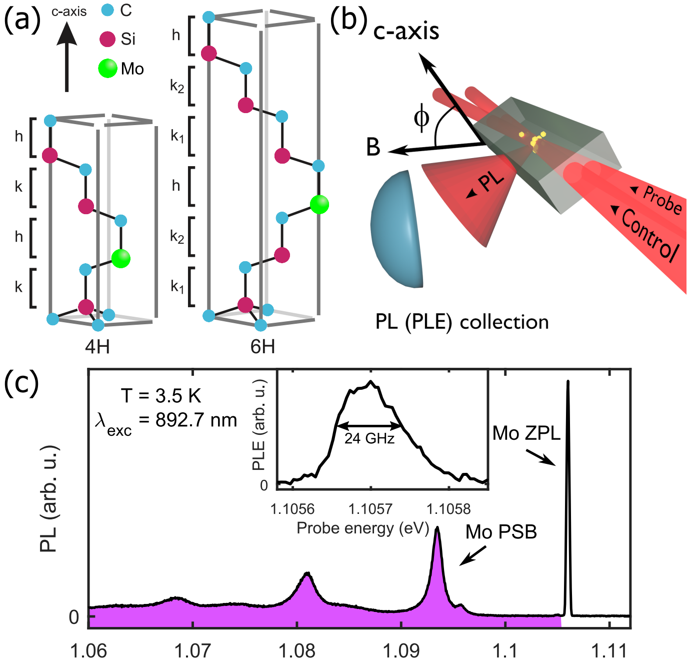

Figure 3.1: **Crystal structures of SiC, setup schematic and optical signatures of Mo in 6H-SiC.** (a), Schematic illustration of the stacking of Si-C bilayers in the crystal structure of the 4H-SiC and 6H-SiC polytypes, which gives lattice sites with *quasi*-cubic and *quasi*-hexagonal local environment labeled by $k_{(1,2)}$ and h, respectively. Our work revisits the question whether Mo impurities are present as substitutional atoms (as depicted) or residing inside Si-C divacancies. The c-axis coincides with the growth direction. (b) Schematic of SiC crystal in the setup. The crystal is placed in a cryostat with optical access. Laser excitation beams (control and probe for two-laser experiments) are incident on a side facet of the SiC crystal and propagate normal to the c-axis. Magnetic fields **B** are applied in a direction orthogonal to the optical axis and at angle ϕ with the c-axis. Photoluminescence (PL) is collected and detected out of another side facet of the SiC crystal. (c) PL from Mo in 6H-SiC at 3.5 K and zero field, resulting from excitation with an 892.7 nm laser, with labels identifying the zero-phonon-line (ZPL, at 1.1057 eV) emission and phonon replicas (shaded and labeled as phonon sideband, PSB). The inset shows the ZPL as measured by photoluminescence excitation (PLE). Here, the excitation laser is scanned across the ZPL peak and emission into the PSB is used for detection.

3.3. Single-laser characterization

For initial characterization of Mo transitions in 6H-SiC and 4H-SiC we used PL and PLE spectroscopy (see Sec. 3.10.2). Figure 3.1(c) shows the PL emission spectrum of the 6H-SiC sample at 3.5 K, measured using an 892.7 nm laser for excitation. The

ZPL transition of the Mo defect visible in this spectrum is studied in detail throughout this work. The shaded region indicates the emission of phonon replicas related to this ZPL [42, 43]. While we could not perform a detailed analysis, the peak area of the ZPL in comparison with that of the phonon replicas indicates that the ZPL carries clearly more than a few percent of the full PL emission. Similar PL data from Mo in the 4H-SiC sample, together with a study of the temperature dependence of the PL, can be found in Sec. 3.10.3, Fig. 3.7.

For a more detailed study of the ZPL of the Mo defects, PLE was used. In PLE measurements, the photon energy of a narrow-linewidth excitation laser is scanned across the ZPL part of the spectrum, while resulting PL emission into the phonon sideband is detected (Fig. 3.1(b)). We used filters to keep light from the excitation laser from reaching the detector, see Sec. 3.10.2. The inset of Fig. 3.1(c) shows the resulting ZPL for Mo in 6H-SiC at 1.1057 eV (1121.3 nm). For 4H-SiC we measured the ZPL at 1.1521 eV (1076.2 nm, see Sec. 3.10.3). Both are in close agreement with literature [42, 43]. Temperature dependence of the PLE from the Mo defects in both 4H-SiC and 6H-SiC can be found in the Sec. 3.10.3, Fig. 3.8.

The width of the ZPL is governed by the inhomogeneous broadening of the electronic transition throughout the ensemble of Mo impurities, which typically happens due to nonuniform strain in the crystal. For Mo in 6H-SiC we observe a broadening of 24 ± 1 GHz FWHM, and 23 ± 1 GHz for 4H-SiC. This inhomogeneous broadening is larger than the anticipated electronic spin splittings [34], and it thus masks signatures of spin levels in optical transitions between the ground and excited state.

3.4. Two-laser characterization

In order to characterize the spin-related fine structure of the Mo defects, a two-laser spectroscopy technique was employed [29, 44, 45]. We introduce this for the four-level system sketched in Fig. 3.2(a). A laser fixed at frequency f_0 is resonant with one possible transition from ground to excited state (for the example in Fig. 3.2(a) $|g_2\rangle$ to $|e_2\rangle$), and causes PL from a sequence of excitation and emission events. However, if the system decays from the state $|e_2\rangle$ to $|g_1\rangle$, the laser field at frequency f_0 is no longer resonantly driving optical excitations (the system goes dark due to optical pumping). In this situation, the PL is limited by the (typically long) lifetime of the $|g_1\rangle$ state. Addressing the system with a second laser field, in frequency detuned from the first by an amount δ, counteracts optical pumping into off-resonant energy levels if the detuning δ equals the splitting Δ_g between the ground-state sublevels. Thus, for specific two-laser detuning values corresponding to the energy spacings between ground-state and excited-state sublevels the PL response of the ensemble is greatly increased. Notably, this technique gives a clear signal for sublevel splittings that are smaller than the inhomogeneous broadening of the optical transition, and

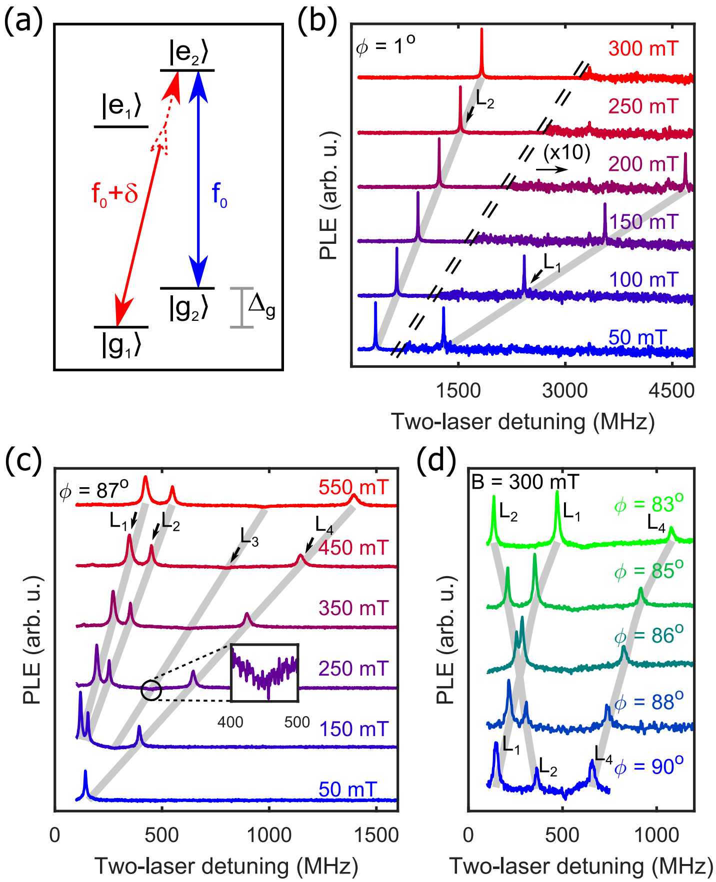

Figure 3.2: **Two-laser spectroscopy results for Mo in 6H-SiC**. (a) Working principle of two-laser spectroscopy: one laser at frequency f_0 is resonant with the $|g_2\rangle$-$|e_2\rangle$ transition, the second laser is detuned from the first laser by δ. If δ is such that the second laser becomes resonant with another transition (here sketched for $|g_1\rangle$-$|e_2\rangle$) the photoluminescence will increase since optical spin-pumping by the first laser is counteracted by the second and vice versa. (b-d) Photoluminescence excitation (PLE) signals as a function of two-laser detuning at 4 K. (b) Magnetic field dependence with field near-parallel to the c-axis ($\phi = 1°$). For clarity, data in the plot have been magnified by a factor 10 right from the dashed line. Two peaks are visible, labeled L_1 and L_2 (the small peak at 3300 MHz is an artefact from the Fabry-Pérot interferometer in the setup). (c) Magnetic field dependence with the field nearly perpendicular to the c-axis ($\phi = 87°$). Three peaks and a dip (enlarged in the inset) are visible. These four features are labeled L_1 through L_4. The peak positions as a function of field in (b,c) coincide with straight lines through the origin (within 0.2% error). (d) Angle dependence of the PLE signal at 300 mT. Peaks L_1 and L_4 move to the left with increasing angle, whereas L_2 moves to the right. The data in (b-d) are offset vertically for clarity.

the two-laser spectral features reflect the homogeneous linewidth of optical transitions [29, 48].

In our measurements a 200 μW continuous-wave control and probe laser were

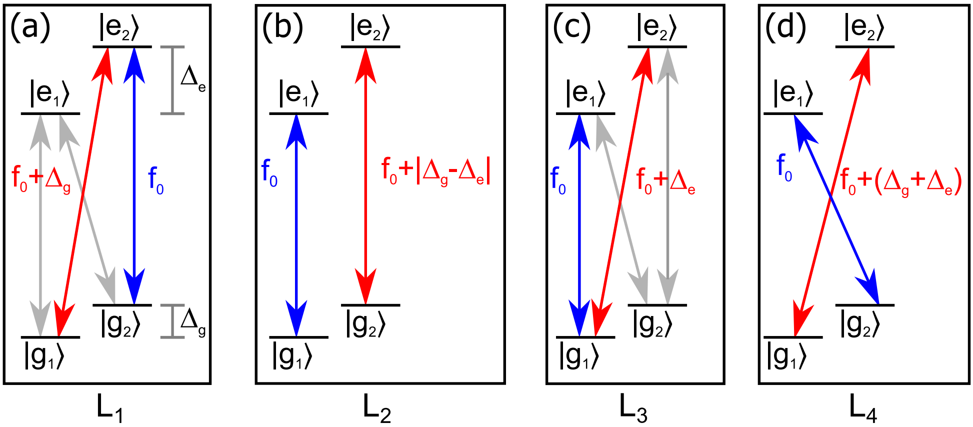

Figure 3.3: **Two-laser pumping schemes with optical transitions between $S = 1/2$ ground and excited states**. (a) Λ scheme, responsible for L_1 emission feature: Two lasers are resonant with transitions from both ground states $|g_1\rangle$ (red arrow) and $|g_2\rangle$ (blue arrow) to a common excited state $|e_2\rangle$. This is achieved when the detuning equals the ground-state splitting Δ_g. The gray arrows indicate a secondary Λ scheme via $|e_1\rangle$ that is simultaneously driven in an ensemble when it has inhomogeneous values for its optical transition energies. (b) Π scheme, responsible for L_2 emission feature: Two lasers are resonant with both vertical transitions. This is achieved when the detuning equals the difference between the ground-state and excited-state splittings, $|\Delta_g - \Delta_e|$. (c) V scheme, responsible for L_3 emission feature: Two lasers are resonant with transitions from a common ground state $|g_1\rangle$ to both excited states $|e_1\rangle$ (blue arrow) and $|e_2\rangle$ (red arrow). This is achieved when the laser detuning equals the excited state splitting Δ_e. The gray arrows indicate a secondary V scheme that is simultaneously driven when the optical transition energies are inhomogeneously broadened. (d) X scheme, responsible for the L_4 emission feature: Two lasers are resonant with the diagonal transitions in the scheme. This is achieved when the detuning is equal to the sum of the ground-state and the excited-state splittings, $(\Delta_g + \Delta_e)$.

made to overlap in the sample. For investigating Mo in 6H-SiC the control beam was tuned to the ZPL at 1121.32 nm ($f_{\mathrm{control}} = f_0 = 267.3567$ THz), the probe beam was detuned from f_0 by a variable detuning δ (*i.e.* $f_{\mathrm{probe}} = f_0 + \delta$). In addition, a 100 μW pulsed 770 nm re-pump laser was focused onto the defects to counteract bleaching of the Mo impurities due to charge-state switching [29, 49, 50] (which we observed to only occur partially without re-pump laser). All three lasers were parallel to within 3° inside the sample. A magnetic field was applied to ensure that the spin sublevels were at non-degenerate energies. Finally, we observed that the spectral signatures due to spin show strong broadening above a temperature of ∼ 10 K, and we thus performed measurements at 4 K (unless stated otherwise).

Figure 3.2(b) shows the dependence of the PLE on the two-laser detuning for the 6H-SiC sample (4H-SiC data in Sec. 3.10.5, Fig. 3.12), for a range of magnitudes of the magnetic field (here aligned close to parallel with the c-axis, $\phi = 1°$). Two emission peaks can be distinguished, labeled line L_1 and L_2. The emission (peak height) of L_2 is much stronger than that of L_1. Figure 3.2(c) shows the results of a similar measurement with the magnetic field nearly orthogonal to the crystal c-axis

($\phi = 87°$), where four spin-related emission signatures are visible, labeled as lines L_1 through L_4 (a very small peak feature left from L_1, at half its detuning, is an artifact that occurs due to a leakage effect in the spectral filtering that is used for beam preparation, see Sec. 3.10.2). The two-laser detuning frequencies corresponding to all four lines emerge from the origin ($B = 0$, $\delta = 0$) and evolve linearly with magnetic field (we checked this up to 1.2 T). The slopes of all four lines (in Hertz per Tesla) are smaller in Fig. 3.2(c) than in Fig 3.2(b). In contrast to lines L_1, L_2 and L_4, which are peaks in the PLE spectrum, L_3 shows a dip.

In order to identify the lines at various angles ϕ between the magnetic field and the c-axis, we follow how each line evolves with increasing angle. Figure 3.2(d) shows that as ϕ increases, L_1, L_3, and L_4 move to the left, whereas L_2 moves to the right. Near 86°, L_2 and L_1 cross. At this angle, the left-to-right order of the emission lines is swapped, justifying the assignment of L_1, L_2, L_3 and L_4 as in Fig. 3.2(b,c). Section 3.10.4 presents further results from two-laser magneto-spectroscopy at intermediate angles ϕ.

We note that part of the naturally abundant Mo isotopes ($\approx$ 25.5%) have nonzero nuclear spin, which gives rise to a subensemble of defects that have their electronic spin coupled to a central nuclear spin via hyperfine coupling. In our results, we see no evidence of hyperfine-coupled energy levels. Progressing insight from the next chapters in this thesis (particularly chapter 5 and 6) show that the presence of the nuclear spin leads to a reduced spin-relaxation time. This relatively short spin-relaxation time decreases the contrast in two-laser experiments. Thus, this could explain why we see no evidence of a hyperfine-coupled sub ensemble in the experiments presented in this chapter.

3.5. Analysis

We show below that the results in Fig. 3.2 indicate that the Mo impurities have electronic spin $S = 1/2$ for the ground and excited state. This contradicts predictions and interpretations of initial results [34, 39, 42, 43]. Theoretically, it was predicted that the defect associated with the ZPL under study here is a Mo impurity in the asymmetric split-vacancy configuration (Mo impurity asymmetrically located inside a Si-C divacancy), where it would have a spin $S = 1$ ground state with zero-field splittings of about 3 to 6 GHz [34, 39, 42, 43]. However, this would lead to the observation of additional emission lines in our measurements. Particularly, in the presence of a zero-field splitting, we would expect to observe two-laser spectroscopy lines emerging from a nonzero detuning [29]. We have measured near zero fields and up to 1.2 T, as well as from 100 MHz to 21 GHz detuning (Sec. 3.10.4), but found no other peaks besides the four present in Fig. 3.2(c). A larger splitting would have been visible as a splitting of the ZPL in measurements as presented in the inset of

Fig. 3.1(c), which was not observed in scans up to 1000 GHz. Additionally, a zero-field splitting and corresponding avoided crossings at certain magnetic fields would result in curved behavior for the positions of lines in magneto-spectroscopy. Thus, our observations rule out that there is a zero-field splitting for the ground-state and excited-state spin sublevels. In this case the effective-spin Hamiltonian [51] can only take the form of a Zeeman term

$$H_{g(e)} = \mu_B g_{g(e)} \mathbf{B} \cdot \tilde{\mathbf{S}} \tag{3.1}$$

where $g_{g(e)}$ is the g-factor for the electronic ground (excited) state (both assumed positive), μ_B the Bohr magneton, **B** the magnetic field vector of an externally applied field, and $\tilde{\mathbf{S}}$ the effective spin vector. The observation of four emission lines can be explained, in the simplest manner, by a system with spin $S = 1/2$ (doublet) in both the ground and excited state.

For such a system, Fig. 3.3 presents the two-laser optical pumping schemes that correspond to the observed emission lines L_1 through L_4. Addressing the system with the V-scheme excitation pathways from Fig. 3.3(c) leads to increased pumping into a dark ground-state sublevel, since two excited states contribute to decay into the off-resonant ground-state energy level while optical excitation out of the other ground-state level is enhanced. This results in reduced emission observed as the PLE dip feature of L_3 in Fig. 3.2(c) (for details see Sec. 3.10.7).

We find that the g-factor values g_g and g_e strongly depend on ϕ, that is, they are uniaxially anisotropic. While this is in accordance with earlier observations for transition metal defects in SiC [34], we did not find a comprehensive report on the underlying physical picture. In Sec. 3.10.1 we present a group-theoretical analysis that explains the anisotropy $g_g \approx 1.7$ for $\phi = 0°$ and $g_g = 0$ for $\phi = 90°$, and similar behavior for g_e (which we also use to identify the orbital character of the ground and excited state). In this scenario the effective Landé g-factor [51] is given by

$$g(\phi) = \sqrt{\left(g_{\parallel} \cos\phi\right)^2 + \left(g_{\perp} \sin\phi\right)^2} \tag{3.2}$$

where $g_{\parallel}$ represents the component of g along the c-axis of the silicon carbide structure and $g_{\perp}$ the component in the basal plane. Figure 3.4 shows the ground and excited state effective g-factors extracted from our two-laser magnetospectroscopy experiments for 6H-SiC and 4H-SiC (additional experimental data can be found in Sec. 3.10.5). The solid lines represent fits to the equation (3.2) for the effective g-factor. The resulting $g_{\parallel}$ and $g_{\perp}$ parameters are given in table 3.1.

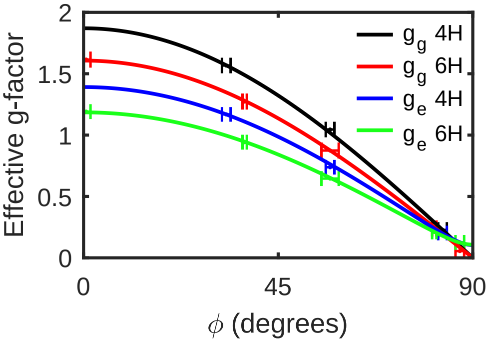

Figure 3.4: **Effective g-factors for the spin of Mo impurities in SiC.** Angular dependence of the g-factor for the $S = 1/2$ ground (g_g) and excited states (g_e) of the Mo impurity in 4H-SiC and 6H-SiC. The solid lines indicate fits of equation (3.2) to the data points extracted from two-laser magneto-spectroscopy measurements as in Fig. 3.2(b,c).

Table 3.1: **Components of the g-factors for the spin of Mo impurities in SiC**

	$g_\parallel$	$g_\perp$
4H-SiC		
ground state	1.87 ± 0.2	0.04 ± 0.04
excited state	1.39 ± 0.2	0.10 ± 0.02
6H-SiC		
ground state	1.61 ± 0.02	0.000 ± 0.004
excited state	1.20 ± 0.02	0.11 ± 0.02

The reason why diagonal transitions (in Fig. 3.3 panels a,c), and thus the Λ and V schemes are allowed, lies in the different behavior of g_e and g_g. When the magnetic field direction coincides with the internal quantization axis of the defect, the spin states in both the ground and excited state are given by the basis of the S_z operator, where the z-axis is defined along the c-axis. This means that the spin-state overlap for vertical transitions, *e.g.* from $|g_1\rangle$ to $|e_1\rangle$, is unity. In such cases, diagonal transitions are forbidden as the overlap between *e.g.* $|g_1\rangle$ and $|e_2\rangle$ is zero. Tilting the magnetic field away from the internal quantization axis introduces mixing of the spin states. The amount of mixing depends on $g_\perp$, such that it differs for the ground and excited states. This results in a tunable non-zero overlap for all transitions, allowing all four schemes to be observed (as in Fig. 3.2(b) where $\phi = 87°$). This reasoning also explains the suppression of all emission lines except L_2 in Fig. 3.2(b), where the magnetic field is nearly along the c-axis. A detailed analysis of the relative peak heights in Fig. 3.2(b,c) compared to wave function overlap can be found in Sec. 3.10.6.

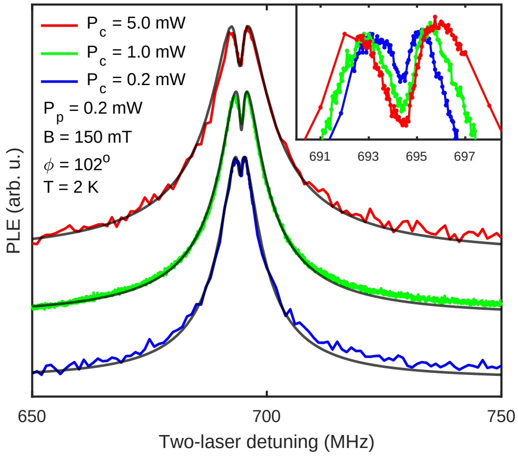

Figure 3.5: **Signatures of coherent population trapping of Mo spin states in 6H-SiC**. Two-laser spectroscopy of the L_1 peak in the PLE signals reveals a dipped structure in the peak at several combinations of probe-beam and control-beam power. This results from coherent population trapping (CPT) upon Λ-scheme driving. Temperature, magnetic field orientation and magnitude, and laser powers, were as labeled. The data are offset vertically for clarity. Solid lines are fits of a theoretical model of CPT (see main text). The inset shows the normalized CPT feature depths.

3.6. Coherent Population Trapping

The Λ driving scheme depicted in Fig. 3.3(a), where both ground states are coupled to a common excited state, is of particular interest. In such cases it is possible to achieve all-optical coherent population trapping (CPT) [46], which is of great significance in quantum-optical operations that use ground-state spin coherence. This phenomenon occurs when two lasers address a Λ system at exact two-photon resonance, *i.e.* when the two-laser detuning matches the ground-state splitting. The ground-state spin system is then driven towards a superposition state that approaches $|\Psi_{CPT}\rangle \propto \Omega_2\,|g_1\rangle - \Omega_1\,|g_2\rangle$ for ideal spin coherence. Here Ω_n is the Rabi frequency for the driven transition from the $|g_n\rangle$ state to the common excited state. Since the system is now coherently trapped in the ground state, the photoluminescence decreases.

In order to study the occurrence of CPT, we focus on the two-laser PLE features that result from a Λ scheme. A probe field with variable two-laser detuning relative to a fixed control laser was scanned across this line in frequency steps of 50 kHz, at 200 μW. The control laser power was varied between 200 μW and 5 mW. This indeed yields signatures of CPT, as presented in Fig. 3.5. A clear power dependence is visible: when the control beam power is increased, the depth of the CPT dip increases (and can fully develop at higher laser powers or by concentrating laser fields in SiC waveguides [48]). This observation of CPT confirms our earlier interpretation of lines L_1-L_4, in that it confirms that L_1 results from a Λ scheme. It also strengthens the conclusion that this system is $S = 1/2$, since otherwise optical spin-pumping into the additional (dark) energy levels of the ground state would be detrimental for the observation of CPT.

Using a standard model for CPT [46], adapted to account for strong inhomogeneous broadening of the optical transitions [48] (see also Sec. 3.10.8) we extract an inhomogeneous spin dephasing time T_2^* of 0.32 ± 0.08 μs and an optical lifetime of the excited state of 56 ± 8 ns. The optical lifetime is about a factor two longer than that of the nitrogen-vacancy defect in diamond [13], indicating that the Mo defects can be applied as bright emitters (although we were not able to measure their quantum efficiency). The value of T_2^* is relatively short but sufficient for applications based on CPT [46]. Moreover, the EPR studies by Baur *et al.* [34] on various transition-metal impurities show that the inhomogeneity probably has a strong static contribution from an effect linked to the spread in mass for Mo isotopes in natural abundance (nearly absent for the mentioned vanadium case), compatible with elongating spin coherence via spin-echo techniques. In addition, their work showed that the hyperfine coupling to the impurity nuclear spin can be resolved. There is thus clearly a prospect for storage times in quantum memory applications that are considerably longer than T_2^*.

3.7. Origin of anisotropic g-parameter

The anisotropic behavior of the g-factor that we observe for the Mo defects was also observed for vanadium and titanium in the EPR studies by Baur *et al.* [34] (they observed $g_\parallel \approx 1.7$ and $g_\perp = 0$ for the ground state). In these cases the transition metal has a single electron in its $3d$ orbital and occupies a Si-substitutional site with strong C_{3v} symmetry. We derive in Sec. 3.10.1 a physical picture that shows that this behavior can be traced back to a combination of a crystal field with C_{3v} symmetry and spin-orbit coupling for the specific case of an ion with one electron in its d-orbital.

The magneto-optical spectra experimentally observed for Mo defects arise from optical transitions between spin-1/2 ground and excited states. Since Mo has originally 6 electrons in its valence shell, it must be positively or negatively ionized to have eigenstates with half-integer spin. Considering that the Mo defect is only observed in p-doped samples, we conclude that the it is most likely related to a positively ionized impurity. Additionally, a single line associated with Mo defects is observed in both 4H-SiC and 6H-SiC, and no line is observed in 3C-SiC, indicating that the Mo impurity substitutes a Si atom in a *quasi*-hexagonal lattice site. In this case, the molybdenum bonds to the lattice in a tetrahedral geometry, sharing four electrons with its nearest neighbors. Since the impurity is additionally ionized, donating a single electron to the p-type SiC host material, it is left in a configuration Mo^{5+}, with one electron left in the $4d$ orbitals.

The $4d$ orbitals of the transition metal (that are originally degenerate in the presence of spherical symmetry), are split by the crystal field with C_{3v} symmetry into two orbital doublets and an orbital singlet. Whereas the singlet must have zero orbital angular momentum (the orbital angular momentum is quenched), the doublets may have orbital states with non-zero projection of the orbital angular momentum along the symmetry axis of the defect (see Sec. 3.10.1). When we consider also the spin of the single electron, spin-orbit coupling further splits the degeneracy of each orbital doublet, giving rise to two spin-orbit coupled Kramers doublets (KDs). These KDs act as effective-spin-1/2 doublets. That is, they interact with magnetic fields, but the particular strength of the interaction depends on both spin and orbital degrees of freedom.

The highly anisotropic Zeeman splitting observed for Mo defects in SiC, and in particular the term $g_\perp = 0$, arises from the fact that in the eigenstates that originate from orbital doublets, the orbital angular momentum projection is pinned along the crystal c-axis due to the symmetry of the defect. Due to SOC, spin and orbital angular momenta are strongly coupled, such that a magnetic field perpendicular to the crystal c-axis will only lead to observable Zeeman splittings if the electronic Zeeman energy is comparable to the spin-orbit coupling strength. This is only expected to happen at very large fields (above 15 T), much larger than those explored in this work.

3.8. Further discussion

An alternative scenario for our type of Mo impurities was proposed by Ivády *et al.* in earlier work. They proposed, based on theoretical work [36], the existence of the asymmetric split-vacancy (ASV) defect in SiC. An ASV defect in SiC occurs when an impurity occupies the interstitial site formed by adjacent silicon and carbon vacancies. The local symmetry of this defect is a distorted octahedron with a threefold symmetry axis in which the strong g-factor anisotropy ($g_\perp = 0$) may also be present for the $S = 1/2$ state [51]. Considering six shared electrons for this divacancy environment, the $\mathrm{Mo}^{5+}(4d^1)$ Mo configuration occurs for the singly charged $-|e|$ state. For our observations this is a highly improbable scenario as compared to one based on the $+|e|$ state, given the p-type SiC host material used in our work. We thus conclude that this scenario by Ivády *et al.* does not occur in our material. Interestingly, niobium defects have been shown to grow in this ASV configuration [52], indicating there indeed exist large varieties in the crystal symmetries involved with transition metal defects in SiC. This defect displays $S = 1/2$ spin with several optical transitions between $892 - 897$ nm in 4H-SiC and $907 - 911$ nm in 6H-SiC [52].

Another defect worth comparing to is the aforementioned chromium defect, studied by Koehl *et al.* [38] Like Mo in SiC, the Cr defect is located at a silicon substitutional site, thus yielding a $3d^2$ configuration for this defect in its neutral charge state. The observed $S = 1$ spin state has a zero-field splitting parameter of 6.7 GHz [38]. By employing optically detected magnetic resonance techniques they measured an inhomogeneous spin coherence time T_2^* of 37 ns [38], which is considerably shorter than observed for molybdenum in the present work. Regarding spin-qubit applications, the exceptionally low phonon-sideband emission of Cr seems favorable for optical interfacing. However, the optical lifetime for this Cr configuration (146 μs [38]) is much longer than that of the Mo defect we studied, hampering its application as a bright emitter. It is clear that there is a wide variety in optical and spin properties throughout transition-metal impurities in SiC, which makes up a useful library for engineering quantum technologies with spin-active color centers.

3.9. Summary and Outlook

We have studied ensembles of molybdenum defect centers in 6H and 4H silicon carbide with 1.1521 eV and 1.1057 eV transition energies, respectively. The ground-state and excited-state spin of both defects was determined to be $S = 1/2$ with large g-factor anisotropy. Since this is allowed in hexagonal symmetry, but forbidden in cubic, we find this to be consistent with theoretical descriptions that predict that Mo resides at a *quasi*-hexagonal lattice site in 4H-SiC and 6H-SiC [36, 39], and our p-type host environment strongly suggests that this occurs for Mo at a silicon substitutional site. We used the measured insight in the $S = 1/2$ spin Hamiltonians for tuning control schemes where two-laser driving addresses transitions of a Λ system, and observed CPT for such cases. This demonstrates that the Mo defect and similar transition-metal impurities are promising for quantum information technologies. In particular for the highly analogous vanadium color center, engineered to be in SiC material where it stays in its neutral $V^{4+}(3d^1)$ charge state, this holds promise for combining $S = 1/2$ spin coherence with operation directly at telecom wavelengths.

Acknowledgements

We thank A. Gali for discussions and M. de Roosz, J. G. Holstein, T. J. Schouten and H. Adema for technical support. Early discussions with Prof. Erik Janzén leading to initiation of this study are gratefully acknowledged. Financial support was provided by ERC Starting Grant 279931, the Zernike Institute BIS program, the Swedish Research Council grants VR 2016-04068 and VR 2016-05362, and the Carl-Trygger Stiftelse för Vetenskaplig Forskning grant CTS 15:339.

Author contributions

This chapter is based on a project initiated by CHvdW, OvZ, IGI and NTS. SiC materials were grown and prepared by AE and BM. Experiments were performed by TB, GJJL and OvZ, except for the PL measurements which were done by AG and IGI. Data analysis was performed by TB, GJJL, CMG, OvZ, FH, RWAH and CHvdW. CMG (aided by FH) developed the model explaining the g-parameter anisotropy and identifying the microscopic configuration of the defect. TB, GJJL and CHvdW had the lead on writing the experimental part of the paper, and CMG had the lead in writing the theoretical part. All authors read and commented on the manuscript.

3.10. Appendices

3.10.1. A toy model for understanding the anisotropic g-factor

Effective spin Hamiltonian and local configuration of the defect

An effective spin-Hamiltonian as the one used in Sec. 3.5 is a convenient tool which allows us to describe the behavior of the system in a wide range of configurations, as long as the effective parameters are experimentally determined and all relevant states are considered. It is often the meeting point between experimentalists, who measure the relevant parameters, and theoreticians, who attempt to correlate them to the Hamiltonian that describes the configuration of the system. A careful description of the latter, and how it modifies the parameters at hand, allows us to rationalize our choices when investigating defects with varying characteristics (such as a different charge state or element). This task is more approachable when we consider the group-theoretical properties of the system at hand. Here we combine group-theoretical considerations with ligand field theory in order to qualitatively describe the features observed in our experiment. In particular, we aim at explaining the large Zeeman splitting anisotropy observed in both ground and excited states, and correlating it to the charge and spatial configuration of the defect.

In our experiments, we observe a single zero-phonon line (ZPL) associated with optical transitions between two Kramers doublets (KD, doublets whose degeneracy is protected by time-reversal symmetry and is thus broken in the presence of a magnetic field) in defects which contain Mo. The presence of a single zero-phonon line in both 4H and 6H-SiC samples indicates that the defect occupies a lattice site with *quasi*-hexagonal symmetry. The lattice of 6H-SiC has two inequivalent sites with cubic symmetry. Thus, if the defect were to occupy sites of cubic symmetry, we would expect to observe two ZPLs closely spaced in this sample. The absence of the ZPL associated with this defect in samples of 3C-SiC [53] further corroborates this assumption. Additionally, we observe strong anisotropy in the Zeeman splitting of the ground and excited states. Specifically, when the magnetic field is perpendicular to the symmetry axis of the crystal, the Zeeman splitting of the ground state goes to zero, whereas that of the excited state is very small. This feature is observed in other transition-metal defects in SiC situated at Si substitutional sites of strong C_{3v} symmetry and with one electron in its $3d$ orbital [34], but we are not aware of a clear explanation of the phenomenon.

Ground and excited states are isolated KDs (that is, effective-spin-1/2 doublets), indicating that the defect contains an odd number of electrons. A Mo atom has 6 electrons in its valence shell. The atom can occupy a Si substitutional site ($\mathrm{Mo_{Si}}$), where it needs to bond to 4 neighboring atoms, or an asymmetric split vacancy (ASV) site ($\mathrm{Mo}_{V_{Si}-V_C}$), where it bonds to 6 neighboring atoms. If we assume that the localized states with mid-gap energies arise from electrons strongly localized around the TM impurity, these defects can, respectively, be described by a Mo ion in the configurations $4d^2$ and $4d^0$. Thus, the defect must be ionized in order to contain an odd number of electrons. Its charge state, which could be ±1, ±3, *etc.*, is determined by the Fermi level in the crystal of interest. We note that the ZPL could only be observed in p-doped samples, which indicates that the features investigated here are unlikely to arise from negatively charged defects. The defect $\mathrm{Mo}_{\mathrm{Si}}^{+1}$ (where +1 represents the charge state of the defect, not the Mo atom) can be approximately described by a Mo in a configuration $4d^1$, which facilitates the treatment of its configuration in terms of d orbitals. In contrast, the defect $\mathrm{Mo}_{\mathrm{V_{Si}-V_C}}^{+1}$ is described by an electronic configuration containing a hole in the bonding orbitals. These orbitals show strong hybridization between the d orbitals of the Mo and the orbitals of the ligands, and cannot be straight-forwardly analyzed using the formalism described below. Inspired by the similarities between our system and other transition-metal defects reported in SiC [34], we investigate the effect of the crystal field of $C_{3\mathrm{v}}$ symmetry on the one-electron eigenstates associated with the 5 $4d$ orbitals (10, if spin multiplicity is included) of a Mo atom. We qualitatively predict the spin-hamiltonian parameters expected for a Mo ion in a $4d^1$ configuration, and compare our analysis to the experimental results.

Ion in $4d^1$ configuration in the presence of crystal field of $C_{3\mathrm{v}}$ symmetry and spin-orbit coupling

The 5 degenerate sublevels of a $4d$-orbital are split by a crystal field of $C_{3\mathrm{v}}$ symmetry [51]. The energy splittings induced by this field are much smaller than the energy difference between the $4d$ shell and the next orbital excited state ($5s$). This allows us to, initially, consider the $4d$ orbitals as a complete set. Since Mo is a heavy atom, we cannot disregard the effect of spin-orbit interaction. However, we assume that the crystal field is larger than SOC, that is, $\Delta E_{free} \gg \Delta E_{crystal} \gg \Delta E_{spin-orbit} \gg \Delta E_{Zeeman}$, where ΔE denotes the energy splitting induced by each term (see Fig. 3.6).

The 5 orbital states of the d-orbital form a 5-dimensional irreducible representation (irrep) of the full rotation group SO(3). When the symmetry is lowered by the crystal field to $C_{3\mathrm{v}}$, the 5-dimensional representation is split into 2 doublets (E_1, E_2) and 1 singlet (A) that are irreps of $C_{3\mathrm{v}}$. Writing the 5 components of the $4d$ orbital in terms of the quadratic functions z^2, x^2-y^2, xy, xz, yz allows us to identify which orbitals are degenerate in the presence of a crystal field of trigonal symmetry. We find that the singlet A is composed of the orbital $4d_{z^2}$. Furthermore, the orbitals $4d_{xz}$ and $4d_{yz}$ are degenerate upon action of the crystal field and make up doublet E_1. Finally the orbitals $4d_{x^2-y^2}$ and $4d_{xy}$ correspond to doublet E_2. Group-theoretical considerations alone are not capable of elucidating which irrep corresponds to the ground state, that is, it does not provide information about the order of the energy levels.

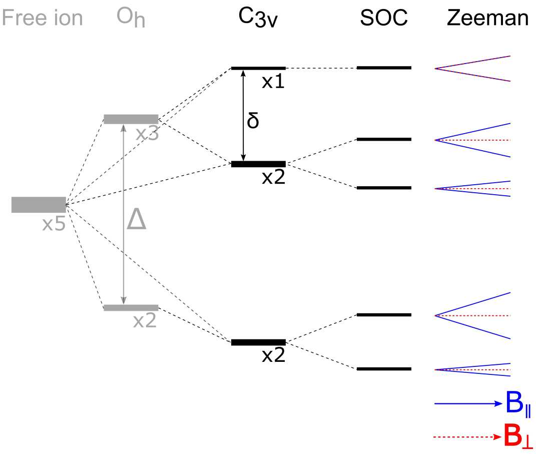

Figure 3.6: **Splitting of one-electron energy levels of a 4d orbital**, under the action of a crystal field and spin-orbit coupling. In the free atom, the 5 orbitals corresponding to the 4*d* shell (disregarding the spin) are degenerate. A crystal field of cubic symmetry breaks this degeneracy, generating an orbital triplet and a doublet, whereas a crystal field of C_{3v} symmetry, splits the 5 orbitals into one singlet and two doublets. In the text, we focus on a crystal field of C_{3v} symmetry, and disregard the cubic term. Although we recognize that this is an approximation, we argue that this approach clarifies the physics governing the strong magnetic anisotropy observed, and is thus justified. Spin-orbit coupling is responsible for splitting the doublets, generating in total 5 sets of Kramers doublets (here, the spin of the electron is taken into account). The energy splittings caused by a magnetic field within these KDs give rise to the effective-spin Hamiltonian parameters considered. We note that a group-theoretical approach alone is not capable of providing the order of the energy levels shown in the figure. We take this order to be the one observed in transition-metal defects in a tetrahedral crystal field with strong trigonal distortion [51].

Comparison between the cubic harmonic forming these 5 orbitals and the spherical harmonics which span a 5-dimensional space (that is, the spherical harmonics Y_l^m with $l = 2$) allows us to rewrite the relevant orbitals as linear combinations of the eigenstates of the operators L^2, L_z. This yields a new basis for each irrep considered above:

$$\mathrm{E}_1 : Y_2^{-2} = |d_{-2}\rangle\,; Y_2^2 = |d_2\rangle \qquad \text{1st orbital doublet} \tag{3.3}$$

$$\mathrm{E}_2 : Y_2^{-1} = |d_{-1}\rangle\,; Y_2^1 = |d_1\rangle \qquad \text{2nd orbital doublet} \tag{3.4}$$

$$\mathrm{A} : Y_2^0 = |d_0\rangle \qquad \text{orbital singlet} \tag{3.5}$$

When the spin multiplicity is considered, each orbital doublet yields 4 possible states, whereas the orbital singlet yields 2 possible states. Spin-orbit coupling (represented by the operator $H_{SO} = -\lambda \mathbf{L}\cdot\mathbf{S}$) is responsible for splitting these states into 5 different

Kramers doublets:

$$\text{KD1}: |d_{+2}, +\tfrac{1}{2}\rangle ; |d_{-2}, -\tfrac{1}{2}\rangle \tag{3.6}$$

$$\text{KD2}: |d_{+2}, -\tfrac{1}{2}\rangle ; |d_{-2}, +\tfrac{1}{2}\rangle \tag{3.7}$$

$$\text{KD3}: |d_{+1}, +\tfrac{1}{2}\rangle ; |d_{-1}, -\tfrac{1}{2}\rangle \tag{3.8}$$

$$\text{KD4}: |d_{+1}, -\tfrac{1}{2}\rangle ; |d_{-1}, +\tfrac{1}{2}\rangle \tag{3.9}$$

$$\text{KD5}: |d_{0}, +\tfrac{1}{2}\rangle ; |d_{0}, -\tfrac{1}{2}\rangle \tag{3.10}$$

where the basis vectors are given in terms of the quantum numbers m_l and m_s which denote the projection of the orbital and spin angular momentum along the quantization axis, respectively (Fig. 3.6). Here, the spin-orbit coupling is considered up to first order in the energy correction, whereas the wave function is not corrected.

A magnetic field lifts the degeneracy between the two components of each KD. This splitting is usually described phenomenologically by an effective Zeeman Hamiltonian in a system with effective-spin $\tilde{\mathbf{S}} = \frac{1}{2}$.

$$H_{eff} = -\mu_B \mathbf{B} \cdot \mathbf{g} \cdot \tilde{\mathbf{S}}_{1/2} \tag{3.11}$$

where μ_B is the Bohr magneton, $\mathbf{B}$ the magnetic field vector, $\tilde{\mathbf{S}}_{1/2}$ the pseudo spin $\frac{1}{2}$ operator and $\mathbf{g}$ the g-tensor. In the presence of axial symmetry, $\mathbf{g}$ can be diagonalized such that equation (3.11) can be rewritten in terms of the symmetry axis of the crystal

$$H_{eff} = -\mu_B \Big(g_{\parallel} B_z \tilde{S}_{1/2,z} + (g_{\perp} B_x \tilde{S}_{1/2,x} + g_{\perp} B_y \tilde{S}_{1/2,y}) \Big) \tag{3.12}$$

In terms of the eigenstates belonging to each KD, the splitting is described by the Zeeman Hamiltonian given by

$$H_{Zee} = -\mathbf{B} \cdot \mu = -\mu_B \mathbf{B} \cdot (g_0 \mathbf{S} + k\mathbf{L}) \tag{3.13}$$

where μ is the magnetic moment operator, g_0 the g-factor for a free electron, $\mathbf{S}$ the total spin operator, k the orbital reduction factor, and $\mathbf{L}$ the orbital angular momentum operator [51, 54]. The orbital reduction factor k, is a factor between 0 and 1 which corrects for partial covalent bonding between the orbitals of the TM and the ligands [51] (note that the value of k differs for each of the 5 KDs in equations (3.6-

3.10)). Comparison of equations (3.12) and (3.13) shows that

$$g_{\parallel} = 2\left\langle g_e S_z + kL_z \right\rangle = \frac{2\left\langle \mu_z \right\rangle}{\mu_B} \tag{3.14}$$

$$g_{\perp} = 2\left\langle g_e (S_x + S_y) + k(L_x + L_y) \right\rangle = \frac{2\left\langle \mu_x + \mu_y \right\rangle}{\mu_B} \tag{3.15}$$

As long as the magnitude of this Zeeman splitting is small compared to the spin-orbit interaction, we can consider the effect of the magnetic field in the sets formed by each KD independently. That is, we consider that the magnetic field does not mix states pertaining to two different KDs.

In order to calculate the values of $g_{\parallel}$ and $g_{\perp}$ for each KD defined by trigonal symmetry and spin-orbit coupling, we rewrite equation (3.13) as

$$H_{Zee} = -(B_z\mu_z + B_x\mu_x + B_y\mu_y) = -\left(B_z\mu_z + \tfrac{1}{2}(B_+\mu_- + B_-\mu_+)\right) \tag{3.16}$$

where the + and − subindices denote the raising and lowering magnetic moment operators and the linear combinations $B_x \pm iB_y$, respectively. When we consider the basis given in equations (3.6-3.9), the matrix elements of both μ_+ and μ_- are zero between two eigenvectors pertaining to one KD. This arises from the fact that the operators $\mu_\pm$ couples states with (m_l, m_s) to states with $(m_l \pm 1, m_s)$ or $(m_l, m_s \pm 1)$. Since, within a KD, there is a change in both m_l and m_s when going from one eigenvector to the other, the operators μ_+ and μ_- cannot couple these states to each other. Explicitly, for KD1 for example, we obtain

$$\left\langle d_{+2}, -\tfrac{1}{2} \middle| \mu_\pm \middle| d_{+2}, -\tfrac{1}{2} \right\rangle = 0 \tag{3.17}$$

$$\left\langle d_{+2}, -\tfrac{1}{2} \middle| \mu_\pm \middle| d_{-2}, +\tfrac{1}{2} \right\rangle = 0 \tag{3.18}$$

$$\left\langle d_{-2}, +\tfrac{1}{2} \middle| \mu_\pm \middle| d_{-2}, +\tfrac{1}{2} \right\rangle = 0 \tag{3.19}$$

and in a similar way for KDs 2 through 4. Thus, up to first order, a magnetic field applied perpendicular to the crystal c-axis is not capable of lifting the degeneracies of the 4 KDs given in equations (3.6)-(3.9). Comparing these results to equation (3.15) we conclude that, for the 8 sublevels of the KDs 1 through 4, $g_\perp = 0$. This arises from the effect of both the crystal field of C_{3v} symmetry and SOC in decoupling and isolating KDs with the properties mentioned above. This is not the case for KD5, given in equation (3.10). In this case,

$$\left\langle d_0, -\tfrac{1}{2} \middle| \mu_\pm \middle| d_0, +\tfrac{1}{2} \right\rangle \neq 0 \tag{3.20}$$

and the degeneracy of this KD is broken in the presence of a magnetic field perpendicular to the c-axis of the crystal.

We can consider in addition the effect of spin-orbit coupling in mixing the eigenstates presented in equations (3.6-3.10). Spin-orbit coupling is responsible for mixing between the eigenstates of KD2 and KD3 (equations (3.7) and (3.8)). Since both of these KDs show $g_\perp = 0$, this mixing does not modify the expected value of $g_\perp$ in neither KD. In contrast, the SOC induced mixing between KD4 and KD5 causes some deviation of $g_\perp$ from 0 in KD4, since $g_\perp \neq 0$ in KD5. The values of $g_\parallel$ and $g_\perp$ for one electron in each of the KDs described in this section are presented in table 3.2.

The tetrahedral part of the crystal field will further mix the KDs described in this section (this will be further discussed in Chapter 5). However, the physical mechanisms underlined here are still relevant in that case. The procedure to calculate the effective g-parameters from the electronic wavefunction remains the same, but the result must be summed over contributions with different orbital angular momentum components. Symmetry dictates that the tetrahedral field will lead to mixing between KDs 1, 4 and 5, giving rise to three different KDs that transform as the Γ_4 irrep of the double group $\bar{C}_{3v}$ (see Tab. A.1). In contrast, mixing between the KDs 2 and 3 gives rise to two KDs that transform as the $\Gamma_{5,6}$ irrep.

In addition, the optical transitions observed are mainly polarized along the crystal c-axis of the defect. Careful analysis of the selection rules associated with the double trigonal group (which includes, besides the spatial symmetry, the spin of the electron) has been reported by Kunzer *et al.* [55] and can be easily checked in Sec. 4.5.4. Comparing their results to the considerations presented in the previous paragraphs indicates that either ground and excited states are both of the Γ_4 type, or both are of the $\Gamma_{5,6}$ type. Finally, we note that we could not experimentally identify secondary ZPLs corresponding to transitions between other sets of KDs, even though they are allowed by symmetry. This could be explained by a series of factors. On the one hand, some of the KDs treated could have energies above the conduction band edge in the crystal, which would impede the observation of optical transitions from and into these levels. On the other hand, the presence of these lines could be masked by the intense phonon sideband at the red side of the ZPL, or the associated photon energies fall outside our detection window. Progressing insight shows that, for the V defect in SiC (see chapter 6), the lowest energy ground-state doublet is of the Γ_4 type. The ordering of the levels may differ, however, for Mo defects. We also show in the following chapters that magneto-spectra of hyperfine-coupled defects with non-zero nuclear spin provides unequivocal insight into the symmetry character of the electronic KD (chapter 5). However, since we could not detect in our work a subensemble with visible hyperfine-split eigenlevels, we cannot un-

Table 3.2: The g-factors of the Kramers doublets originated due to spin-orbit coupling within each subspace of the electronic eigenstates in a field of C_{3v} symmetry. Spin-orbit coupling is added as a perturbation, and included up to first order. The parameters λ and δ are as defined in the text and in Fig. 3.6. Note that the g-factor values in this table can take on negative values, while in our experimental analysis we can only extract $|g_\parallel|$ and $|g_\perp|$.

C_{3v}	Spin-Orbit	$g_\parallel$	$g_\perp$
Doublet, $m_l = \pm 2$	KD1, eq. 3.6	$2(2k+1)$	0
	KD2, eq. 3.7	$2(2k-1)$	0
Doublet, $m_l = \pm 1$	KD3, eq. 3.8	$2(k+1)$	0
	KD4, eq. 3.9	$2(k-1)$	$0 + \propto \frac{\lambda}{\delta}$
Singlet, $m_l = 0$	KD5, eq. 3.10	2	$2 - \propto \frac{\lambda}{\delta}$

equivocally determine the symmetry character of the ground-state doublet of the Mo defect in SiC.

Validity of our assumptions

The toy-model considered here is capable of qualitatively informing us about the behavior of orbitals with d character in the presence of trigonal crystal field and spin-orbit coupling. It is clear that the full description of the configuration of the defect is far more subtle than the simple model applied here. We intend to comment on this in the next paragraphs.

Symmetry of the crystal field. In our derivation, we assume that the trigonal crystal field is the prevailing term in the Hamiltonian describing the defect. This assumption is not rigorously correct, since the symmetry of defects in SiC is more accurately described by a ligand field of cubic symmetry – which determine most of its ground and excited state properties. This field is modified in the presence of axial symmetry, as is the case for defects in *quasi*-hexagonal lattice sites, which is generally included as a first-order perturbation term in the Hamiltonian. Nonetheless, it can be shown [51, 56] that the large anisotropy in the Zeeman response described above, with the cancelation of $g_\perp$, is also observed in the case of a cubic field with trigonal distortion and spin-orbit coupling of similar magnitudes. The analysis, in this case, is more laborious due to the fact that mixing of the orbitals is involved, and calculating the matrix elements of the operators $L_\pm$, $S_\pm$, L_z and S_z is less trivial. Furthermore, this analysis would not increase our level of understanding of the system at this point, since we were only capable of observing transitions between the sublevels of two KDs in this experiment. This approach would be more profitable if transitions between other sets of KDs were observed, allowing us to unravel several parameters associated with the system, such as the strength of the spin-orbit coupling and trigonal crystal field. This is the approach we take in chapter 5 for V defects in SiC.

Charge state of the defect. Similarly, it can be shown that the considerations presented here can be expanded to configurations where the $4d$ orbitals are filled by multiple electrons (for instance, a defect in a configuration $4d^3$). In this case, a doubly degenerate orbital configuration (in symmetry terms, a configuration of the kind $^m\mathrm{E}$, where m is the spin multiplicity) in the presence of a crystal field of $C_{3\mathrm{v}}$ symmetry gives rise to at least one KD with $g_\perp = 0$ when SOC is taken into account. Nonetheless, only a negatively charged Mo in a Si substitutional site would give rise to a defect in the configuration $4d^3$. The absence of the ZPL in n-doped samples indicates that this is unlikely.

In addition, a similar group theoretical analysis can show that one hole in a bonding orbital of symmetry E would also give rise to $g_\perp = 0$. Thus, the features observed here could also correspond to a positively charged $\mathrm{Mo}_{\mathrm{V_{Si}-V_C}}$ defect (where one of the six Mo electrons that participate in bonding is lost to the crystal lattice). Due to the strong hybridization between the Mo and the divacancy orbitals in this case, the description of this case is more subtle and will not be performed here.

Summary

We showed that an analysis of the effect of the defect symmetry on the Zeeman energy splittings of its ground and excited states, combined with the experimental observations, helps us unravel the configuration of the defect studied in this work. We show that, in $C_{3\mathrm{v}}$ symmetry, a combination of the crystal field and spin-orbit interaction is responsible for the strong magnetic anisotropy observed experimentally. Furthermore, the fact that the defect studied in this work is only observed optically in samples which are p-doped indicates that the charge of the defect is more likely positive than negative. In this way, we conclude that the most probable configuration of our defect is a Mo ion on a Si substitutional site of h symmetry, with a charge $+1$, which can be approximately described by a Mo atom in a $4d^1$ configuration. The absence of other lines associated with the defect prevents us from providing a more accurate description of the system. Nonetheless, we have developed a qualitative description based on symmetry, which explains the Zeeman splittings observed. The considerations presented here allow us to predict and rationalize the presence of strong anisotropy in other transition-metal defects in SiC. We expect neutrally charged vanadium defects in *quasi*-hexagonal lattice sites to show a magnetic behavior similar to the one observed in the Mo defects investigated in this work.

3.10.2. Methods

Materials The samples used in this study were ~1 mm thick epilayers grown with chemical vapor deposition, and they were intentionally doped with Mo during sample growth. The PL signals showed that a relatively low concentration of tungsten was present due to unintentional doping from metal parts of the growth setup (three PL peaks near 1.00 eV, outside the range presented in Fig. 3.1(a)). The concentration of various types of (di)vacancies was too low to be observed in the PL spectrum that was recorded. For more details see Ref. [43].

Cryostat During all measurements, the sample was mounted in a helium flow cryostat with optical access through four windows and equipped with a superconducting magnet system.

Photoluminescence (PL) The PL spectrum of the 6H-SiC sample was measured by exciting the material with an 892.7 nm laser, and using a double monochromator equipped with infrared-sensitive photomultiplier. For the 4H-SiC sample, we used a 514.5 nm excitation laser and an FTIR spectrometer.

Photoluminescence Excitation (PLE) The PLE spectrum was measured by exciting the defects using a CW diode laser tunable from 1050 nm to 1158 nm with linewidth below 50 kHz, stabilized within 1 MHz using feedback from a HighFinesse WS-7 wavelength meter. The polarization was linear along the sample c-axis. The laser spot diameter was $\sim$ 100 μm at the sample. The PL exiting the sample sideways was collected with a high-NA lens, and detected by a single-photon counter. The peaks in the PLE data were typically recorded at a rate of about 10 kcounts/s by the single-photon counter. We present PLE count rates in arb. u. since the photon collection efficiency was not well defined, and it varied with changing the angle ϕ. For part of the settings we placed neutral density filters before the single-photon counter to keep it from saturating. The excitation laser was filtered from the PLE signals using a set of three 1082 nm (for the 4H-SiC case) or 1130 nm (for the 6H-SiC case) longpass interference filters. PLE was measured using an ID230 single-photon counter. Additionally, to counter charge state switching of the defects, a 770 nm re-pump beam from a tunable pulsed Ti:sapphire laser was focused at the same region in the sample. Laser powers as mentioned in the main text.

Two-laser characterization The PLE setup described above was modified by focusing a detuned laser beam to the sample, in addition to the present beams. The detuned laser field was generated by splitting off part of the stabilized diode laser beam. This secondary beam was coupled into a single-mode fiber and passed through an electro-optic phase modulator in which an RF signal (up to ~5 GHz) modulated the phase. Several sidebands were created next to the fundamental laser frequency, the spacing of these sidebands was determined by the RF frequency. Next, a Fabry-Pérot interferometer was used to select one of the first-order sidebands (and it was locked to the selected mode). The resulting beam was focused on the same region in the sample as the original PLE beams (diode laser and re-pump) with similar spot size and polarization along the sample c-axis. Laser powers were as mentioned in the main text. Small rotations of the c-axis with respect to the magnetic field were performed using a piezo-actuated goniometer with 7.2 degrees travel.

Data processing For all graphs with PLE data a background count rate is subtracted from each line, determined by the minimum value of the PLE in that line (far away from resonance features). After this a fixed vertical offset is added for clarity. For each graph, the scaling is identical for all lines within that graph.

3.10.3. Single-laser spectroscopy

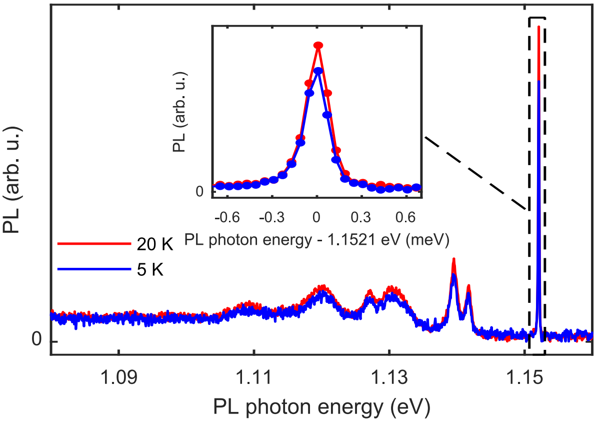

Figure 3.7: **Temperature dependence of Mo PL spectrum in 4H-SiC.** PL from excitation with a 514.5 nm laser, for 5 and 20 K sample temperatures and at zero magnetic field. The dashed box marks the ZPL at 1.1521 eV. The inset gives a magnified view of the ZPL. The broader peaks at lower photon energies are phonon replicas of the ZPL. There is almost no dependence on temperature in both ZPL and replicas. Data courtesy of A. Gällström.

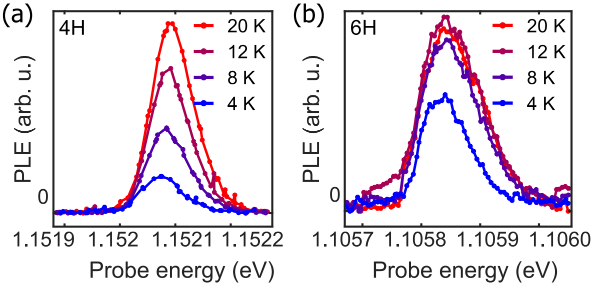

Figure 3.8: **Temperature dependence of the PLE signals from the Mo ZPL in 4H-SiC and 6H-SiC.** PLE signals from scanning a single CW narrow-linewidth laser across the ZPL photon-energy range. The temperature was varied between 4 and 20 K. A residual magnetic field of a few mT was present in the superconducting magnet, with unknown exact magnitude. The ZPL for Mo in (a) 4H-SiC is at 1.1521 eV, and for Mo in (b) 6H-SiC at 1.1057 eV. When the temperature is decreased, the height of the ZPL drops significantly, probably due to a combination between the reduced emission into the PSB at lower temperatures and optical spin-pumping.

3.10.4. Additional two-laser spectroscopy for Mo in 6H-SiC

Angle dependence. In addition to Fig. 3.2(b,c), we also measured the magnetic field dependence of the spin related emission signatures at intermediate angles ϕ. Figure 3.9 shows this dependence for $\phi = 37°$, $57°$ and $81°$. The spectroscopic position of emission lines L_n show a linear dependence on magnetic field, with slopes Θ_{Ln} (in Hertz per Tesla) that decrease as ϕ increases. The effective g-factors in Fig. 3.4 are acquired from the emission lines by relating their slopes to the Zeeman splittings in the ground and excited state. Using the four pumping schemes depicted in Fig. 3.3, we derive

$$\Theta_{L1} = \frac{\mu_B}{h} g_g \tag{3.21}$$

$$\Theta_{L2} = \frac{\mu_B}{h} |g_e - g_g| \tag{3.22}$$

$$\Theta_{L3} = \frac{\mu_B}{h} g_e \tag{3.23}$$

$$\Theta_{L4} = \frac{\mu_B}{h} \left(g_e + g_g\right) \tag{3.24}$$

where h is Planck's constant, μ_B the Bohr magneton and $g_{g(e)}$ the ground (excited) state g-factor.

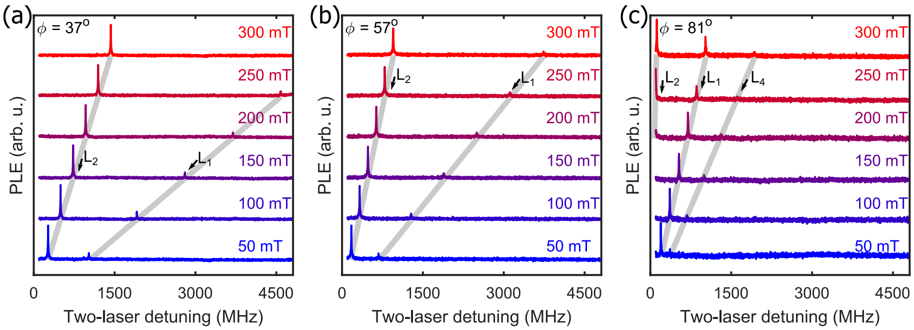

Figure 3.9: **Magneto-spectroscopy of two-laser spin signatures in PLE from Mo in 6H-SiC.** Magnetic field dependence of the PLE signal as a function of two-laser detuning, for angles ϕ between the magnetic field and c-axis set to $\phi = 37°$ (a), $\phi = 57°$ (b) and $\phi = 81°$ (c). Results for the temperature at 4 K. The labeling of the emission lines (L_1 - L_4) is consistent with Fig. 3.2. The data are offset vertically for clarity.

Temperature and photon-energy dependence. We also measured the dependence of the two-laser PLE signal on temperature, see Fig. 3.10(a). The PLE features disappear above 8 K in a much broader PLE background that starts to emit because of more rapid thermal spin mixing in the ground state. Other Mo systems in the ensemble for which the two-laser resonance condition is not met then also start emitting due to single-laser excitation (see also Fig. 3.8), since the optical pumping into an off-resonant state becomes shorter lived. Notably, the linewidths of the peaks in Fig. 3.10(a) do not change in the range 2 K to 8 K, indicating that the temperature does not affect the optical lifetime in this range. Above 8 K the temperature was a bit unstable during the measurements, which causes the drifting in the single-laser PLE contribution to this signal. Interestingly, the dip (L_3) is most pronounced at 6 K, since there are several competing processing responsible for this dip (see section 3.10.7).

Additionally, we measured how the two-laser PLE occurred throughout the inhomogenously broadened ensemble, by varying the photon energy of the control laser and sweeping the two-laser detuning for each case (Fig. 3.10(b)). For all photon energies the peaks are at the same position, indicating that all Mo atoms in the ensemble behave similarly. At 1.10561 eV the control laser is too far detuned from the ZPL to yield any two-laser PLE signal.

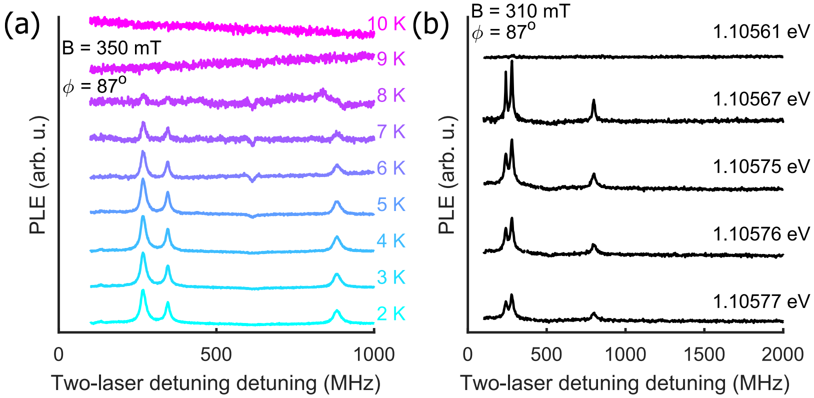

Figure 3.10: **Temperature and photon-energy dependence of two-laser emission features in 6H-SiC.** Temperature (a) and laser photon-energy (b) dependence of the PLE signal as a function of two-laser detuning. Results are offset vertically for clarity.

Two-laser spectroscopy for the $5-21$ GHz detuning range. In order to check for a possible presence of spin-related emission features at detunings larger than 5 GHz (checking for a possible zero-field splitting), we modified the setup such that we could control two-laser detunings up to 21 GHz. The electro-optical phase modulator (EOM) we used for generating the detuned laser field could generate first-order sidebands up to 7 GHz. In order to check for two-laser spectroscopy emission features at larger detunings, we removed the Fabry-Pérot (FP) filter, such that all sidebands (on the same optical axis) were focused onto the sample with

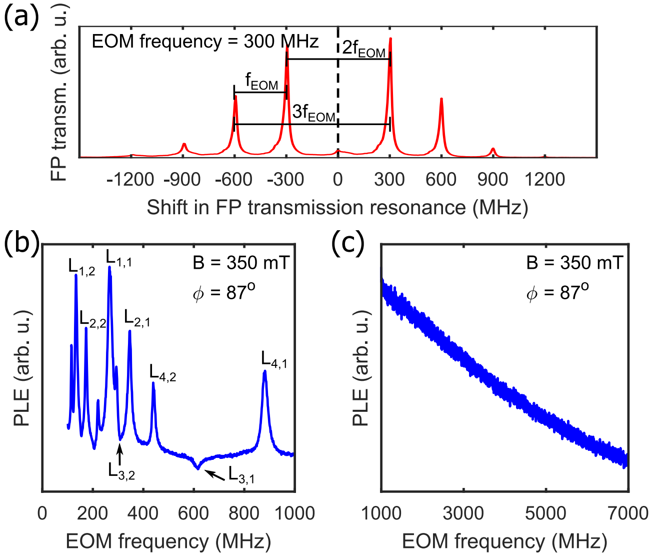

Figure 3.11: **Two-laser spin signatures of Mo in 6H-SiC at large detuning.** (a) Transmission scan of the Fabry-Pérot resonator, characterizing which optical frequencies are present in the beam after passing through the electro-optical modulator (EOM). The first-order sidebands at ±300 MHz have the highest intensity, whereas the fundamental laser frequency is suppressed (but not fully removed) by the EOM. Relevant sideband spacings are indicated. (b) Spin signatures at low two-laser detuning. Emission features similar to those in Fig. 3.2(c) of Fig. 3.2 are visible, and labeled $L_{n,m}$. (c) The PLE signal from two-laser spectroscopy at larger detuning. No peaked features from single, double or triple sideband spacings are visible.

2 mW total laser power. Apart from the re-pump beam, no additional laser was focused onto the sample in this experiment. In this way, the Mo defects could interact with several combinations of sidebands. Figure 3.11(a) shows the spectral content of this beam (here characterized by still using the FP resonator). The first and second order sidebands at negative and positive detuning take a significant portion of the total optical power. Hence, pairs of sidebands spaced by single, double or triple frequency intervals (EOM frequency f_{EOM}) now perform two-laser spectroscopy on the Mo defects. The relevant sideband spacings are indicated in Fig. 3.11(a).

Figure 3.11(b) presents results of these measurements, showing various peaks that we identified and label as $L_{n,m}$. Here n is identifying the peak as a line L_n as in Fig. 3.3, while the label m identifies it as a spectroscopic response for two-laser detuning at $m \cdot f_{\mathrm{EOM}}$ (that is, $m = 1$ is for first-order EOM sideband spacing, *etc*.). Note that second-order manifestations of the known peaks L_1-L_4 (from double sideband spacings, labeled as $L_{n,2}$) are now visible at $\frac{1}{2} f_{\mathrm{EOM}}$, and third-order response of the known L_1-L_4 occurs at $\frac{1}{3} f_{\mathrm{EOM}}$ (but for preserving clarity these have not been labeled in Fig. 3.11(b)).

Figure 3.11(c) depicts a continuation of this experiment with f_{EOM} up to 7 GHz with the same resolution as Fig. 3.11(b). No new peaks are observed. Considering that third-order peaks were clearly visible before, we conclude that no additional two-laser emission features exist up to 21 GHz.

3.10.5. Two-laser spectroscopy for Mo in 4H-SiC

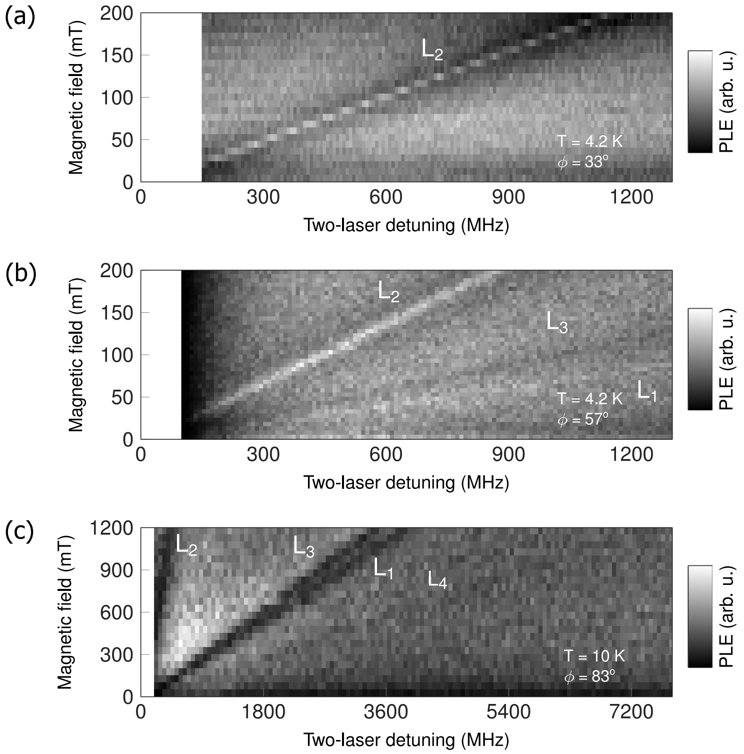

Figure 3.12: **Two-laser spin signatures of Mo in 4H-SiC.** PLE signal as a function of two-laser detuning and magnetic field strength, for various angles ϕ between the magnetic field and c-axis. (a) Measurement at 4.2 K, with $\phi = 33°$. A single emission line (peak) is visible, labeled L_2. (b) Measurement at 4.2 K, with $\phi = 57°$. Three emission lines are visible, labeled L_1, L_2 (peaks), and L_3 (dip). (c) Measurement at 10 K, with $\phi = 83°$. Four emission lines are visible, labeled L_1 through L_4 (all dips). Note that the measurement range of (c) is six time as large as (a) and (b), but the plot aspect ratio is the same. A gray-scale plot has been used for optimal contrast.

We also studied the spin-related fine structure of Mo defects in 4H-SiC. Our 4H-SiC sample suffered from large background absorption, which drastically lowered the signal-to-noise ratio. We relate this absorption to a larger impurity content (of unknown character, but giving broad-band absorption) in our 4H-SiC material as compared to our 6H-SiC material. Therefore, the lasers were incident on a corner of the sample, so as to minimize the decay of the emitted PL. We present the results in

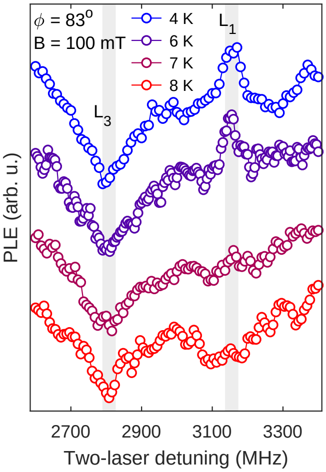

Figure 3.13: **Temperature dependence of PLE spin signatures from Mo in 4H-SiC.** PLE signal as a function of two-laser detuning and temperature with magnetic field at $\phi = 83°$ from the sample c-axis at 100 mT. As the temperature increases, the signal from L_1 changes from a peak to a broad dip, while L_3 remains a dip.

gray-scale plots in Fig. 3.12 for optimized contrast. The figure shows the magnetic field and two-laser detuning dependence of the PLE.

Analogous to Fig. 3.2 for 6H-SiC, the spectroscopic position features appear as straight lines that emerge from zero detuning, indicating the absence of a zero-field splitting. When the magnetic field is nearly perpendicular to the c-axis (Fig. 3.12(c)), four lines are visible. This is consistent with an $S = 1/2$ ground and excited state.

The data from Fig. 3.12(c) was measured at 10 K, whereas Fig. 3.12(a,b) was at 4.2 K. At 10 K, all emission lines become dips, while for 6H-SiC only the V system shows a dip. The temperature dependence of L_3 and L_1 is shown in Fig. 3.13 for the same configuration as in Fig. 3.12(c) ($\phi = 83°$). At low temperatures L_1 shows a peak and L_3 shows a dip. Upon increasing the temperature, both features become dips. This phenomenon was only observed for Mo in 4H-SiC, it could not be seen in 6H-SiC. We therefore conclude that this probably arises from effects where Mo absorption and emission is influenced by the large background absorption in the 4H-SiC material.

The labels in Fig. 3.12 are assigned based on the energy diagrams in Fig. 3.2. Like in Sec. 3.5, L_1 through L_4 indicate Λ, Π, V and X two-laser pumping schemes, respectively. The L_1 and L_3 labels are interchangeable in Fig. 3.12(c) when only considering the sum rules. However, the fact that the left feature in Fig. 3.13 shows a dip for all temperatures means that it should be related to a V scheme. Thus, the current assignment of the labels with corresponding pumping schemes is justified. Using equations 3.21 through 3.24, the effective g-factors can be determined. Fitting these to equation (3.2) gives the values for $g_{\parallel}$ and $g_{\perp}$ reported in Tab. 3.1.

3.10.6. Franck-Condon principle with respect to spin

The amplitude of the two-laser emission signatures is determined by the strength of the underlying optical transitions. For a transition $|g_i\rangle$-$|e_j\rangle$, this strength is determined by the spin overlap $\langle g_i|e_j\rangle$, according to the Franck-Condon principle with respect to spin [57]. The quantum states of the spin in the electronic ground and excited state can be described using effective spin Hamiltonian

$$H_{g(e)} = \mu_B \mathbf{B} \cdot \mathbf{g}_{g(e)} \cdot \tilde{\mathbf{S}} \tag{3.25}$$

with μ_B the Bohr magneton, $\mathbf{B}$ the applied magnetic field vector, $\tilde{\mathbf{S}}$ the effective spin vector, and where the ground (excited) state g-parameter is a tensor $\mathbf{g}_{g(e)}$. Using Cartesian coordinates this can be written as

$$\mathbf{g}_{g(e)} = \begin{pmatrix} g_\perp^{g(e)} & 0 & 0 \\ 0 & g_\perp^{g(e)} & 0 \\ 0 & 0 & g_\parallel^{g(e)} \end{pmatrix} \tag{3.26}$$

Here the z-axis is parallel to the SiC c-axis, and the x and y-axes lay in the plane perpendicular to the c-axis. Due to the symmetry of the defect, the magnetic field $\mathbf{B}$ can be written as

$$\mathbf{B} = \begin{pmatrix} 0 \\ B\sin\phi \\ B\cos\phi \end{pmatrix} \tag{3.27}$$

where B indicates the magnitude of the magnetic field. The resulting Hamiltonian $H_{g(e)}$ may be found by substituting $\mathbf{B}$ and $\mathbf{g}_{g(e)}$ into equation (3.25), and considering that $S = 1/2$. The basis of $H_{g(e)}$ can be found from the eigenvectors.

For the ground state $g_\perp^g$ is zero, thus the bases of H_g and S_z coincide, independent of ϕ. Therefore, there is no mixing of spins in the ground state. However, in the excited state $g_\perp^e$ is nonzero, causing its eigenbasis to rotate if a magnetic field is applied non-parallel to the c-axis. The new eigenbasis is a linear combination of eigenstates of S_x, S_y and S_z, such that there will be mixing for spins in the excited state for any nonzero angle ϕ.

We calculate the spin overlap for the $|g_i\rangle$-$|e_j\rangle$ transition from the inner product of two basis states $|g_i\rangle$ and $|e_j\rangle$. The strength of a two-laser pumping scheme is then the product of the strength of both transitions. For example, the strength of the Λ scheme from Fig. 3.3(a) equals the inner product $\langle g_1|e_2\rangle$ multiplied by $\langle g_2|e_2\rangle$. The resulting strengths for all four pumping schemes are depicted in Fig. 3.14.

We now compare these transition strengths to the data in Fig. 3.2(b,c) and Fig. 3.9 and 3.12. It is clear that the Π scheme is the strongest pumping scheme for all an-

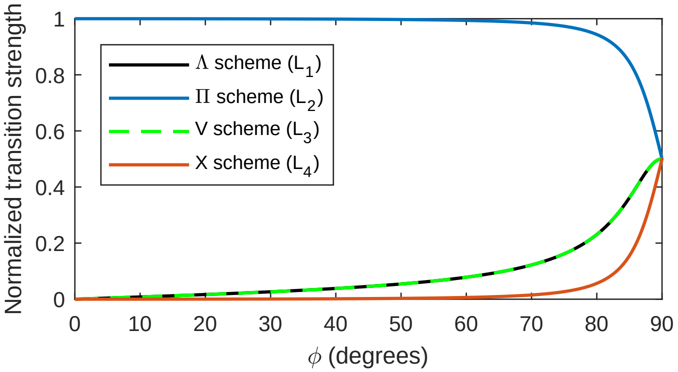

Figure 3.14: **Two-laser pumping scheme transition strengths.** For each scheme the product of the spin overlaps from both underlying transitions is shown. The strength of the Π scheme is near unity for large angles and never vanishes. The strengths of the Λ and V schemes are equal, they vanish at $\phi = 0°$. The X scheme strength vanishes more rapidly than any other scheme for angles ϕ close to 0°.

gles $\phi \neq 90°$. This explains the large relative amplitude of L_2 in our measurements. The Λ and V scheme transition strengths are equal, starting from zero for $\phi = 0°$ and increasing as ϕ approaches 90°. For the Λ scheme, this is consistent with the increasing relative amplitude of L_1. For ϕ close to 90° the amplitude of L_1 is even larger than for L_2. The reason for this is that a Λ scheme is emitting more effectively than a Π scheme. The V scheme is harder to observe in the background emission, such that L_3 is only visible for ϕ close to 90°. Finally, the transition strength of the X scheme is only significant for ϕ close to 90°, which is why we have not been able to observe L_4 below 81° in 6H-SiC.

3.10.7. V-scheme dip

Understanding the observation of a dip for the V pumping scheme in a four-level system (Fig. 3.2(c)) is less trivial than for the observation of peaks from the other three pumping schemes. The latter can be readily understood from the fact that for proper two-laser detuning values both ground states are addressed simultaneously, such that there is no optical pumping into dark states. In this section we will investigate how a dip feature can occur in the PLE signals. Our modeling will be based on solving a master equation in Lindblad form with a density matrix in rotating wave approximation for a four-level system with two near-resonant lasers [46].

Consider the four-level system depicted in Fig. 3.15(a). A control laser is near-resonant with the $|g_1\rangle$-$|e_1\rangle$ (vertical) transition and a probe laser near-resonant with $|g_1\rangle$-$|e_2\rangle$ (diagonal) transition. Here the two-laser detuning is defined as $\delta = \Delta_p - \Delta_c$, *i.e.* the difference between the detunings Δ of both lasers from their respective near-resonant transitions, such that the emission feature appears at zero two-laser

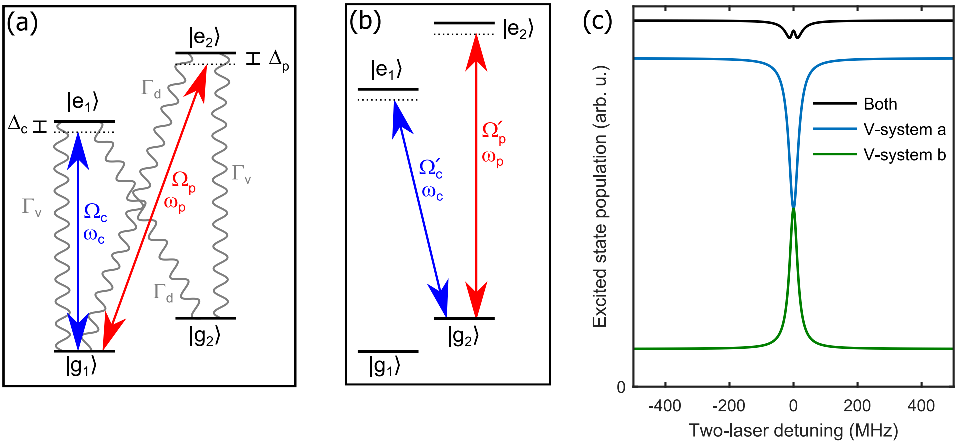

Figure 3.15: **Four-level V-scheme model.** (a) V pumping scheme in a four level system. Here Ω is the Rabi frequency for the control and probe lasers, and ω their (angular) frequency. Γ_v and Γ_d are the decay rates for vertical and diagonal decay, respectively. Δ represents the detuning from resonance of the control and probe beam. (a) V-scheme simultaneously resonant (with the scheme in panel (a)) for another part of the inhomogeneously broadened ensemble. Probe and control Rabi frequencies Ω' differ from (a), since both lasers drive other transitions with different dipole strengths. (c) Total population in the excited-state levels ($|e_1\rangle$ and $|e_2\rangle$) for both schemes separately (blue and green) as well as their sum (black).

detuning. The decay rates from the excited states are Γ_v and Γ_d for vertical and diagonal transitions, respectively. They are quadratically proportional to the spin-state overlap $\langle g_i|e_j\rangle$

$$\Gamma_v \propto |\langle g_1|e_1\rangle|^2\,, \tag{3.28}$$

$$\Gamma_d \propto |\langle g_1|e_2\rangle|^2\,. \tag{3.29}$$

These rates are unequal, since the spin-state overlap for diagonal transitions is generally smaller than for vertical transitions (see previous section). The decay rates Γ_e between excited-state levels and Γ_g ground-state levels are assumed very small compared to the decay rates from the excited-state levels. The decay rates from ground-state levels towards the excited-state levels are set to zero. Dephasing rates are taken relative to the $|g_1\rangle$ state ($\gamma_{g1} = 0$). The choices for parameters are listed in table 3.3. The Rabi frequencies Ω_c and Ω_p of the driven transitions are linearly proportional to the spin-state overlap

$$\Omega_c \propto |\langle g_1|e_1\rangle|\,, \tag{3.30}$$

$$\Omega_p \propto |\langle g_1|e_2\rangle|\,. \tag{3.31}$$

Table 3.3: **Parameter choices for V-scheme model**

parameter	value (Hz)	parameter	value (Hz)
Γ_v	$0.9 \cdot 10^7$	γ_{g1}	0
Γ_d	$0.1 \cdot 10^7$	γ_{g2}	$5 \cdot 10^6$
Γ_g	$1 \cdot 10^4$	γ_{g3}	$5 \cdot 10^6$
Γ_e	$1 \cdot 10^4$	γ_{g4}	$5 \cdot 10^6$
Δ_c	0	Ω_c	$\sqrt{.9} \cdot 10^7$
Δ_p	$\in [-500, 500] \cdot 10^6$	Ω_p	$\sqrt{.1} \cdot 10^7$

Additionally, we have to consider a secondary V-scheme (Fig. 3.15(b)) resonant with another part of the inhomogeneously broadened ensemble. The control and probe laser are swapped, as the former now addresses a diagonal transition, while the latter addresses a vertical one. The new Rabi frequency is taken to be $\Omega_c' = \sqrt{\frac{\Gamma_d}{\Gamma_v}}\Omega_c$ for the control beam, which is now driving a diagonal transition (with reduced strength). The probe beam is driving a vertical transition (with increased strength), and its Rabi frequency is $\Omega_p' = \sqrt{\frac{\Gamma_v}{\Gamma_d}}\Omega_p$.

Considering both V-schemes, we calculate the total population in both excited-state levels as it reflects the amount of photoluminescence resulting from decay back to the ground states. The two-laser detuning dependence of the excited-state population is shown in Fig. 3.15(c). The black curve considers both schemes simultaneously, which represents the situation in our measurements. Here the dip indeed appears, although both separate schemes (a and b) display a dip and peak (respectively). The competition between both schemes limits the depth of the observed dip, which explains our observation of shallow dips in contrast to sharp peaks in Fig. 3.2(c).

Interestingly, the black curve displays a peak within the dip, which might seem like a CPT feature. However, this feature is not visible in either curve from the two separate pumping schemes. This peak appears because the peak from the second V-scheme (green) is slightly sharper than the dip from the first one (blue). The peak might still be caused by CPT, as the blunting of the dip relative to the peak can be caused by a long dephasing time of the ground state.

Key to understanding the appearance of a dip in the total photoluminescence emission is the difference in decay rates, vertical decay being favored over diagonal decay. Consider the pumping scheme from Fig. 3.15(a). When the probe laser is off-resonant the control laser drives the $|g_1\rangle$-$|e_1\rangle$ transition. Decay will occur mostly towards the $|g_1\rangle$ state and occasionally to the dark $|g_2\rangle$ state. If the probe laser becomes resonant with the $|g_1\rangle$-$|e_2\rangle$ transition, the increased population in the $|e_2\rangle$ state will prefer to decay towards the dark $|g_2\rangle$ state. The overall decay towards the dark state is now increased. The secondary pumping scheme (Fig. 3.15(b)) works the other way around, where the diagonal transition is always driven by the control beam and a resonant probe beam will counteract some of the pumping into the dark state (now $|g_1\rangle$). However, the slightly increased emission from scheme b cannot fully counteract the decreased emission from scheme a (even when $\Omega_p = \Omega_c = \Omega'_p = \Omega'_c$).

3.10.8. Modeling of coherent population trapping

For fitting the CPT traces in Fig. 3.5, we use a standard CPT description [46], extended for strong inhomogeneous broadening of the optical transitions, and an approach similar to the one from the previous section. However (as compared to the previous section), the behavior of CPT has a more pronounced dependence on parameters, such that almost no assumptions have to be made. When taking the spin Hamiltonians as established input, the only assumption made is that the spin relaxation time in the ground state and excited state is much slower than all other decay process. This allows for setting up fitting of the CPT traces with only two free fit parameters, which correspond to the optical lifetime and the inhomogeneous dephasing time T_2^*.

Since two lasers couple both ground-state levels to a single common excited-state level, the other excited-state level will be empty. Therefore, we may describe this situation with a three-level system, where the PL is directly proportional to the excited-state population. The decay rates and Rabi frequencies are proportional to the Franck-Condon factors for spin-state overlaps $\langle g_i|e\rangle$ in the same way as before (equations (3.28)-(3.31)). At this angle ($\phi = 102°$) we calculate these factors to be

$$\langle g_1|e\rangle = 0.9793 \tag{3.32}$$

$$\langle g_2|e\rangle = 0.2022 \tag{3.33}$$

according to the reasoning in section 3.10.6. We take that the $|g_1\rangle$-$|e\rangle$ is a vertical transition and $|g_2\rangle$-$|e\rangle$ a diagonal one.

In order to account for inhomogeneous broadening throughout the ensemble, the solution of the master equation is computed for a set of control-laser detunings Δ_c (see Fig. 3.15(a)) around zero, its range extending far beyond the two-laser detuning values δ (since we experimentally observed an inhomogeneous broadening much in excess of the spin splittings). In this case the probe-laser detuning becomes $\Delta_p = \Delta_c + \delta$. The resulting excited-state populations are integrated along the inhomogeneous broadening Δ_c (up to the point where the signal contribution vanishes) to give the PL emission as a function of two-laser detuning δ. Analogous to the previous section, we have to consider a secondary Λ-scheme in order to fully account for the inhomogeneous broadening. The total PL emission is found by adding together the excited-state populations from both schemes.

We fit this model to the data presented in Fig. 3.5 after subtracting a static background. We extract the inhomogeneous dephasing time $T_2^* = 0.32 \pm 0.08$ μs and an optical lifetime of 56 ± 8 ns. The errors are estimated from the spread in extracted dephasing times and lifetimes throughout the data sets.

References

[1] T. Bosma et al., “Identification and tunable optical coherent control of transition-metal spins in silicon carbide”, npj Quantum Information **4**, 48 (2018).

[2] W. B. Gao, A. Imamoglu, H. Bernien, and R. Hanson, “Coherent manipulation, measurement and entanglement of individual solid-state spins using optical fields”, Nat. Photonics **9**, 363 (2015).

[3] E. Togan et al., “Quantum entanglement between an optical photon and a solid-state spin qubit”, Nature **466**, 730 (2010).

[4] F. Dolde et al., “High-fidelity spin entanglement using optimal control”, Nat. Commun. **5**, 3371 (2014).

[5] P. V. Klimov, A. L. Falk, D. J. Christle, V. V. Dobrovitski, and D. D. Awschalom, “Quantum entanglement at ambient conditions in a macroscopic solid-state spin ensemble”, Sci. Adv. **1**, e1501015 (2015).

[6] B. Hensen et al., “Loophole-free bell inequality violation using electron spins separated by 1.3 kilometres”, Nature **526**, 682 (2015).

[7] N. Kalb et al., “Entanglement distillation between solid-state quantum network nodes”, Science **356**, 928 (2017).

[8] D. Budker and M. Romalis, “Optical magnetometry”, Nat. Phys. **3**, 227 (2007).

[9] G. Balasubramanian et al., “Nanoscale imaging magnetometry with diamond spins under ambient conditions”, Nature **455**, 648 (2008).

[10] F. Dolde et al., “Electric-field sensing using single diamond spins”, Nat. Phys. **7**, 459 (2011).

[11] H. Kraus, V. A. Soltamov, F. Fuchs, D. Simin, A. Sperlich, P. G. Baranov, G. V. Astakhov, and V. Dyakonov, “Magnetic field and temperature sensing with atomic-scale spin defects in silicon carbide”, Sci. Rep. **4**, 5303 (2014).

[12] C. Bonato, M. S. Blok, H. T. Dinani, D. W. Berry, M. L. Markham, D. J. Twitchen, and R. Hanson, “Optimized quantum sensing with a single electron spin using real-time adaptive measurements”, Nat. Nanotechnol. **11**, 247 (2016).

[13] V. Dobrovitski, G. Fuchs, A. Falk, C. Santori, and D. Awschalom, “Quantum control over single spins in diamond”, Annu. Rev. Condens. Matter Phys. **4**, 23 (2013).

[14] L. Childress and R. Hanson, “Diamond NV centers for quantum computing and quantum networks”, MRS Bull **38**, 134 (2013).

[15] M. W. Doherty, N. B. Manson, P. Delaney, and L. C. L. Hollenberg, “The negatively charged nitrogen-vacancy centre in diamond: the electronic solution”, New J. of Phys. **13**, 025019 (2011).

[16] J. R. Maze, A. Gali, E. Togan, Y. Chu, A. Trifonov, E. Kaxiras, and M. D. Lukin, “Properties of nitrogen-vacancy centers in diamond: the group theoretic approach”, New J. of Phys. **13**, 025025 (2011).

[17] G. Thiering and A. Gali, “*Ab initio* calculation of spin-orbit coupling for an NV center in diamond exhibiting dynamic Jahn-Teller effect”, Phys. Rev. B **96**, 081115 (2017).

[18] A. G. Radnaev, Y. O. Dudin, R. Zhao, H. H. Jen, S. D. Jenkins, A. Kuzmich, and T. A. B. Kennedy, “A quantum memory with telecom-wavelength conversion”, Nat. Phys. **6**, 894 (2010).

[19] S. Zaske et al., “Visible-to-telecom quantum frequency conversion of light from a single quantum emitter”, Phys. Rev. Lett. **109**, 147404 (2012).

[20] A. Dréau, A. Tcheborateva, A. El Mahdaoui, C. Bonato, and R. Hanson, “Quantum frequency conversion of single photons from a nitrogen-vacancy center in diamond to telecommunication wavelengths”, Phys. Rev. Appl. **9**, 064031 (2018).

[21] J. R. Weber, W. Koehl, J. Varley, A. Janotti, B. Buckley, C. Van de Walle, and D. D. Awschalom, “Quantum computing with defects”, Proc. Natl. Acad. Sci. U.S.A. **107**, 8513 (2010).

[22] J. R. Weber, W. F. Koehl, J. B. Varley, A. Janotti, B. B. Buckley, C. G. Van de Walle, and D. D. Awschalom, “Defects in SiC for quantum computing”, J. Appl. Phys. **109**, 102417 (2011).

[23] H. J. Von Bardeleben, J. L. Cantin, A. Csóré, A. Gali, E. Rauls, and U. Gerstmann, “Nv centers in 3C, 4H, and 6H silicon carbide: a variable platform for solid-state qubits and nanosensors”, Phys. Rev. B **94**, 121202 (2016).

[24] S. A. Zargaleh et al., “Evidence for near-infrared photoluminescence of nitrogen vacancy centers in 4H-SiC”, Phys. Rev. B **94**, 060102 (2016).

[25] P. Friedrichs, T. Kimoto, L. Ley, and G. Pensl, *Silicon carbide*, Vol. 1 (Wiley, Weinheim, 2010).

[26] B.-S. Song, S. Yamada, T. Asano, and S. Noda, “Demonstration of two-dimensional photonic crystals based on silicon carbide”, Opt. Express **19**, 11084 (2011).

[27] W. F. Koehl, B. B. Buckley, F. J. Heremans, G. Calusine, and D. D. Awschalom, “Room temperature coherent control of defect spin qubits in silicon carbide”, Nature **479**, 84 (2011).

[28] D. J. Christle, A. L. Falk, P. Andrich, P. V. Klimov, J. U. Hassan, N. T. Son, E. Janzén, T. Ohshima, and D. D. Awschalom, “Isolated electron spins in silicon carbide with millisecond coherence times”, Nat. Mater. **14**, 160 (2015).

[29] O. V. Zwier, D. O’Shea, A. R. Onur, and C. H. van der Wal, “All–optical coherent population trapping with defect spin ensembles in silicon carbide”, Sci. Rep. **5**, 10931 (2015).

[30] D. Riedel et al., “Resonant addressing and manipulation of silicon vacancy qubits in silicon carbide”, Phys. Rev. Lett. **109**, 226402 (2012).

[31] H. Kraus, V. A. Soltamov, D. Riedel, S. Väth, F. Fuchs, A. Sperlich, P. G. Baranov, V. Dyakonov, and G. V. Astakhov, “Room-temperature quantum microwave emitters based on spin defects in silicon carbide”, Nat. Phys. **10**, 157 (2014).

[32] M. Widmann et al., “Coherent control of single spins in silicon carbide at room temperature”, Nat. Mater. **14**, 164 (2015).

[33] H. M. Hobgood, R. C. Glass, G. Augustine, R. H. Hopkins, J. Jenny, M. Skowronski, W. C. Mitchel, and M. Roth, “Semi-insulating 6H-SiC grown by physical vapor transport”, Appl. Phys. Lett. **66**, 1364 (1995).

[34] J. Baur, M. Kunzer, and J. Schneider, “Transition metals in SiC polytypes, as studied by magnetic resonance techniques”, Phys. Stat. Sol. A **162**, 153 (1997).

[35] B. Magnusson and E. Janzén, “Optical characterization of deep level defects in SiC”, Mater. Sci. For. **483**, 341 (2005).

[36] V. Ivády, A. Gällström, N. T. Son, E. Janzén, and A. Gali, “Asymmetric split-vacancy defects in SiC polytypes: a combined theoretical and electron spin resonance study”, Phys. Rev. Lett. **107**, 195501 (2011).

[37] N. T. Son, X. Thang Trinh, A. Gällström, S. Leone, O. Kordina, E. Janzén, K. Szász, V. Ivády, and A. Gali, “Electron paramagnetic resonance and theoretical studies of Nb in 4H-and 6H-SiC”, J. Appl. Phys. **112**, 083711 (2012).

[38] W. F. Koehl, B. Diler, S. J. Whiteley, A. Bourassa, N. T. Son, E. Janzén, and D. D. Awschalom, “Resonant optical spectroscopy and coherent control of Cr^{4+} spin ensembles in SiC and GaN”, Phys. Rev. B **95**, 035207 (2017).

[39] A. Csóré, A. Gällström, E. Janzén, and A. Gali, “Investigation of mo defects in 4H-SiC by means of density functional theory”, Mater. Sci. For. **858**, 261 (2016).

[40] K. F. Dombrowski, M. Kunzer, U. Kaufmann, J. Schneider, P. G. Baranov, and E. N. Mokhov, “Identification of molybdenum in 6H-SiC by magnetic resonance techniques”, Phys. Rev. B **54**, 7323 (1996).

[41] T. Kimoto, T. Nakajima, H. Matsunami, T. Nakata, and M. Inoue, “Formation of semi-insulating 6H-SiC layers by vanadium ion implantations”, Appl. Phys. Lett. **69**, 1113 (1996).

[42] A. Gällström, B. Magnusson, and E. Janzén, “Optical identification of Mo related deep level defect in 4H and 6H SiC”, Mater. Sci. For. **615**, 405 (2009).

[43] A. Gällström, *Optical characterization of deep level defects in SiC*, PhD dissertation No. 1674, ISSN 0345-7524 (Linköping University, 2015).

[44] N. B. Manson and C. Wei, “Transient hole burning in NV centre in diamond”, J. Lumin. **58**, 158 (1994).

[45] C. Santori et al., “Coherent population trapping in diamond NV centers at zero magnetic field”, Opt. Express **14**, 7986 (2006).

[46] M. Fleischhauer, A. Imamoglu, and J. P. Marangos, “Electromagnetically induced transparency: optics in coherent media”, Rev. Mod. Phys. 77, 633 (2005).

[47] H. J. Kimble, “The quantum internet”, Nature **453**, 1023 (2008).

[48] O. V. Zwier, *Two-laser spectroscopy and coherent manipulation of color-center spin ensembles in silicon carbide*, Zernike Institute PhD thesis series, ISSN 1570-1530 (University of Groningen, 2016).

[49] K. Beha, A. Batalov, N. B. Manson, R. Bratschitsch, and A. Leitenstorfer, “Optimum photoluminescence excitation and recharging cycle of single nitrogen-vacancy centers in ultrapure diamond”, Phys. Rev. Lett. **109**, 097404 (2012).

[50] G. Wolfowicz, C. P. Anderson, A. L. Yeats, S. J. Whiteley, J. Niklas, O. G. Poluektov, F. J. Heremans, and D. D. Awschalom, “Optical charge state control of spin defects in 4H-SiC”, Nat. Commun. **8**, 1876 (2017).

[51] A. Abragam and B. Bleaney, *Electron paramagnetic resonance of transition ions*, International series of monographs on physics (Clarendon Press, Oxford, 1970).

[52] A. Gällström et al., “Optical properties and Zeeman spectroscopy of niobium in silicon carbide”, Phys. Rev. B **92**, 075207 (2015).

[53] V. Ivády, B. Somogyi, V. Zólyomi, A. Gällström, N. T. Son, E. Janzén, and A. Gali, “Transition metal defects in cubic and hexagonal polytypes of SiC: site selection, magnetic and optical properties from *ab initio* calculations”, Mater. Sci. For. **717**, 205 (2012).

[54] L. F. Chibotaru, M. F. A. Hendrickx, S. Clima, J. Larionova, and A. Ceulemans, “Magnetic anisotropy of [Mo (CN) 7] 4-anions and fragments of cyano-bridged magnetic networks”, The Journal of Physical Chemistry A **109**, 7251 (2005).

[55] M. Kunzer, H. D. Müller, and U. Kaufmann, “Magnetic circular dichroism and site-selective optically detected magnetic resonance of the deep amphoteric vanadium impurity in 6H-SiC”, Phys. Rev. B **48**, 10846 (1993).

[56] R. E. Dietz, H. Kamimura, M. D. Sturge, and A. Yariv, “Electronic structure of copper impurities in zno”, Phys. Rev. **132**, 1559 (1963).

[57] M. Fox, *Optical properties of solids*, 2$^{\text{nd}}$ edition. (Oxford University Press, 2010).

chapter 4

Spin-relaxation times exceeding seconds for color centers with strong spin-orbit coupling in SiC

Spin-active color centers in solids show good performance for quantum technologies. Several transition-metal defects in SiC offer compatibility with telecom and semiconductor industries. However, whether their strong spin-orbit coupling degrades their spin lifetimes is not clear. We show that a combination of a crystal-field with axial symmetry and spin-orbit coupling leads to a suppression of spin-lattice and spin-spin interactions, resulting in remarkably slow spin relaxation. Our optical measurements on an ensemble of Mo impurities in SiC show a spin lifetime T_1 of 2.4 s at 2 K.

4.1. Introduction

Spin-active color centers in semiconductors have attracted significant interest for the implementation of quantum technologies, since several of these systems combine long-lived spin states with a bright optical interface [2–5]. Long-distance spin entanglement has been achieved for a variety of defects as stationary nodes [6–9]. However, finding suitable emitters that combine long-lived spins, short excited-state lifetimes and optical transitions compatible with telecommunication fiber-optic infrastructure in an industrially established material has remained elusive. Silicon carbide, a wide band-gap semiconductor with mature fabrication technology, hosts a range of defect centers with optical transitions near or at the telecom range [10, 11], including several defects containing transition metal (TM) impurities [12–18]. The electronic and spin properties of these defects derive largely from the character of the *d*-orbitals of the TM under the action of a crystal field determined by the lattice site [19–21]. Furthermore, the presence of a heavy atom in the defect implies that spin-orbit coupling (SOC) plays a significant role in the electronic structure of these color centers. Generally, as widely demonstrated by the solid

---

Parts of this chapter have been published in New Journal of Physics **22**, 103051 (2020) [1].

state spin-qubit community, combining favorable spin properties and strong SOC can be challenging [18, 22–24]. However, the extent to which the spin lifetimes of TM defects in SiC are limited by the strong influence of SOC is not clear.

We report here on slow spin relaxation with T_1 exceeding seconds below 4 K for a molybdenum defect ensemble in 6H-SiC, indicating that the defect spin is surprisingly robust with respect to spin relaxation despite the presence of strong SOC. In order to understand this, we measure the spin-relaxation time of the Mo defect in SiC between 2 and 7 K and identify the main processes leading to spin relaxation in this temperature range. We analyze the manifestation strength of these processes, while considering the electronic structure of the defect, and find that a combination of axial rotational symmetry and SOC suppresses several spin-relaxation mechanisms in this system, leading to unexpectedly long T_1. The analysis leading to these conclusions is general, relying on the character of the d-orbitals of the TM and the particular symmetry of the defect. Thus, a similar approach could be relevant in the interpretation of experiments on other point defects in crystals with analogous symmetries, such as vanadium defects in SiC (with optical transitions compatible with telecom infrastructure), group-IV defects in diamond and point-defects in transition metal dichalcogenides [15, 17, 19, 25–27].

4.2. Methods

We focus on the Mo defect associated with an optical transition line at 1121.3 nm in 6H-SiC, which consists of a Mo impurity in a Si substitutional site of *quasi*-hexagonal symmetry (Fig. 4.1(a), h site) [14, 16]. The defect is positively ionized, such that after binding to four neighboring carbons, the TM is left with one active unpaired electron in its 4d shell. In this lattice site – and only considering the rotational symmetry of the defect – both ground and excited states are two-fold orbitally degenerate, such that the orbital angular momentum is not quenched [21]. In the presence of SOC, the orbital degeneracy is broken, giving rise to two Kramers doublets (KD) in the ground and two KDs in the excited state (Fig. 4.1(b)) [14, 16], resembling what is observed for the group-IV defects in diamond [26].

Each KD is a doublet composed of a time-reversal pair: the doublet splits as an effective spin-1/2 system in the presence of a magnetic field, but its degeneracy is otherwise protected by time-reversal symmetry (see Sec. 4.5.4). The energy difference between the two spin-orbit split KDs in the ground state, Δ_{orb} in Fig. 4.1(b), is expected to be approximately 1 meV [16], in accordance with the appearance of a second zero-phonon line (ZPL) in resonant photoluminescence excitation (PLE) experiments at approximately 8 K (Fig. 4.1(c)). Finally, the presence of sharp phonon replicas of the ZPL in the photoluminescence spectrum indicates that the defect center couples strongly to localized vibrational modes (Fig. 4.1(b,d)).

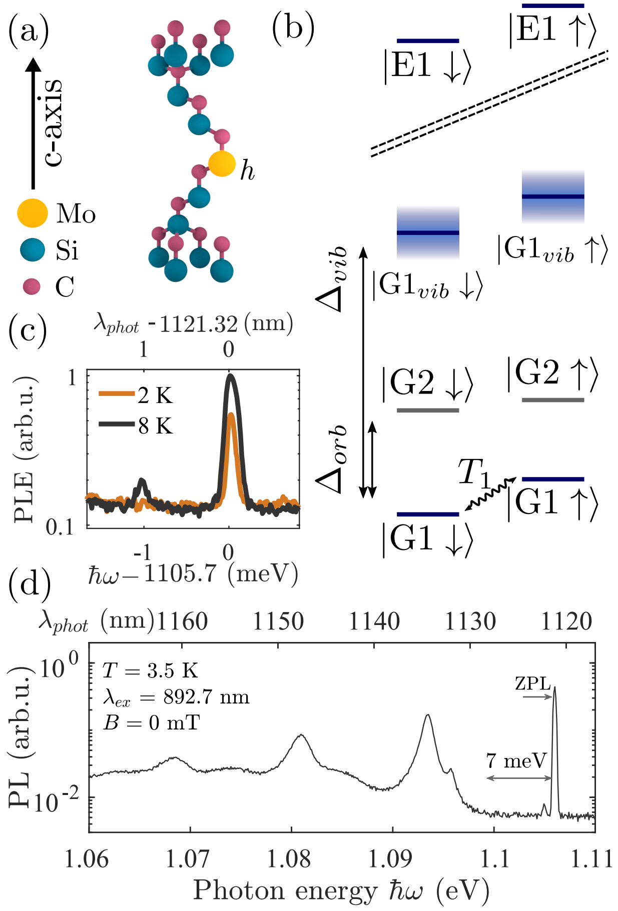

Figure 4.1: **Defect and electronic structure.** (a) The defect is composed of a Mo atom positively ionized substituting a Si at a *quasi*-hexagonal (h) lattice site. (b) Electronic structure of the Mo defect. Both ground ($|\mathrm{G1}\rangle$) and optically excited ($|\mathrm{E1}\rangle$) states are characterized by a spin doublet which is split by a magnetic field. Additionally, a second ground-state Kramers doublet ($|\mathrm{G2}\rangle$) is present approximately 1 meV above the ground state doublet, and the defect's electronic states can couple to local vibrational modes, giving rise to vibronic states $|\mathrm{G1}_{vib}\rangle$. (c) PLE spectrum showing the defect emission into the phonon-sideband versus energy of the excitation laser ($\hbar\omega$). A second zero-phonon line (ZPL) appears in the photoluminescence excitation (PLE) spectrum as the second doublet state is thermally occupied. (d) Photoluminescence of the Mo defect upon off-resonant excitation. The spectrum shows, besides the zero-phonon line and broad phonon-sideband emission, sharp phonon-replicas of the ZPL. These are evidence of the presence of localized vibrational modes.

We measure the spin-relaxation time of this defect by means of a pump-probe experiment as shown in Fig. 4.2. Experiments are performed on an ensemble of defects in a 6H-SiC sample previously investigated in Ref. [14]. The sample showed p-doped character, and the defect concentration was estimated to be between 10^{14} and 10^{16} cm^{-3}. We create pulses out of a CW laser beam by using a combination of an electro-optical phase modulator (EOM) and a Fabry-Pérot (FP) cavity. The EOM generates sidebands from our CW laser at frequency steps determined by an RF input signal; by tuning the FP cavity to transmit this sideband only, we create pulses that turn on/off as the RF generator turns on/off. These pulses resonantly drive optical transitions between ground and excited states, and we measure the photon emission into the phonon sideband with a single-photon counter after filtering out the laser line. We apply a magnetic field non-collinear with the c-axis of the sample such that spin-flipping transitions between ground and optically-excited states are allowed (Fig. 4.2(a-b)) [14]. In order to counteract slow ionization of the defects (see Sec. 4.5.3 for further details), we apply a repump laser in between measurements [14, 28–30].

4.3. Results

In the pump-probe experiment (Fig. 4.2(c)), the initial response of the sample to pulse P1, h_1, provides a measure of the population in the bright spin state $|G1\downarrow\rangle$ at thermal equilibrium (see the caption of Fig. 4.2 for an explanation of the terms dark and bright spin sublevels in this chapter). The sharp increase (decrease) of the PL signal as the pulse turns on (off) indicates that both the optical decay rate and the Rabi frequency are relatively fast (see Sec. 4.5.5 for further details). Optical excitation provided by P1 polarizes the spin ensemble in a dark spin sublevel ($|G1\uparrow\rangle$ in Fig. 4.2(b)) within the first few microseconds, as evidenced by the decrease and subsequent saturation of the PLE signal (the saturation level shows that the effective T_1 is lower when the laser is on, see Sec. 4.5.5). The leading-edge response of the ensemble to a second (probe) pulse P2, h_2, reflects the recovery of the population in the bright spin sublevel ($|G1\downarrow\rangle$ in Fig. 4.2(b)) during the time τ between the two optical pulses. Between 2 K and 7 K, we observe a monoexponential recovery of h_2 towards h_1 as a function of τ (Fig. 4.2(d)), which must correspond to the spin-relaxation time T_1 given the considerations presented below.

We repeat this experiment at zero magnetic field in order to confirm that the PL darkening observed within the first few microseconds of optical excitation corresponds to optical pumping of the ensemble into a dark spin sublevel. In this case, we observe no leading-edge peak in the PLE signal, indicating that no optical pumping occurs at this timescale if the spin sublevels are degenerate (see Sec. 4.5.2). The absence of PL darkening at zero magnetic field implies that we cannot trap Mo centers in state $|G2\rangle$ for observable times. This is the case if the optical decay rate between states $|E1\rangle$ and $|G2\rangle$ is smaller than the relaxation rate between the two ground state KDs $|G2\rangle$ and $|G1\rangle$ in the temperature range investigated. (We expect the optical decay rate between $|E1\rangle$ and $|G2\rangle$ to be small, since we observe no lines corresponding to this transition in PL and PLE scans.) Thus, we conclude that after optical pump-

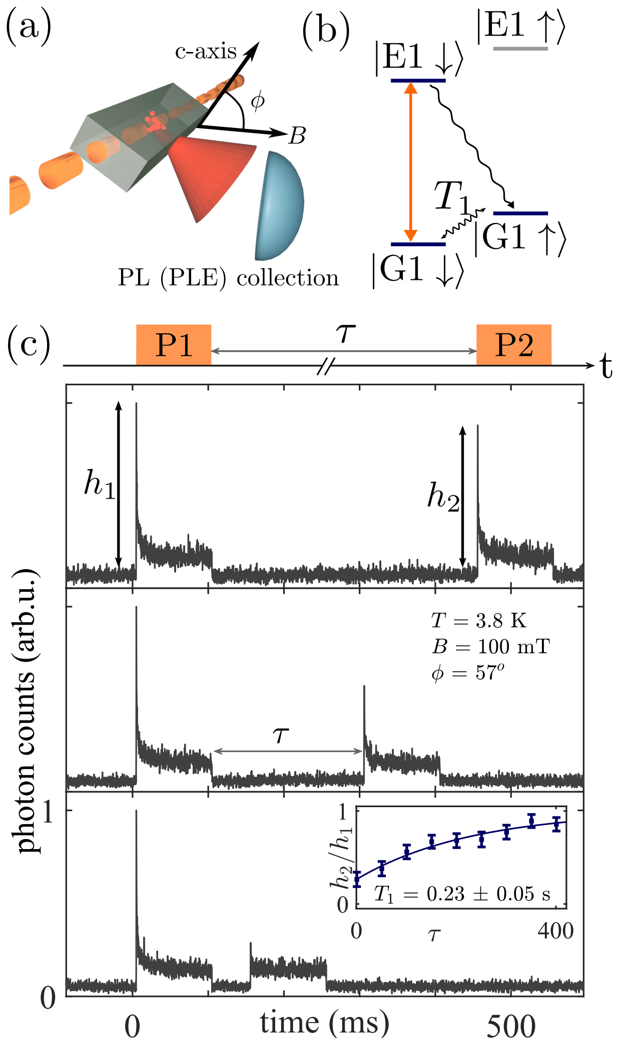

Figure 4.2: **Time-resolved hole burning experiment.** (a) In order to investigate T_1, we perform time-resolved pump-probe experiments where we resonantly excite the sample in the presence of a magnetic field and collect the phonon-sideband emission. (b) When the magnetic field is non-collinear with the symmetry axis of the defect, spin-flipping transitions between ground and optically-excited states are allowed. (c) The first pulse P1 probes the population at thermal equilibrium in the ground-state spin sublevel $|G1\downarrow\rangle$ (which we call bright state in this work, since it can be optically excited), and polarizes the spin population into a spin sublevel that cannot be optically excited, $|G1\uparrow\rangle$ (which we here call dark state). After a variable delay τ, a second pulse P2 probes the recovery of the population in the bright state. (inset) The ratio of the leading-edge peaks in the PLE signal (h_2/h_1) recovers monoexponentially as a function of the delay between the two pulses.

ing in the presence of a magnetic field, no significant population is trapped in state $|G2\rangle$, and relaxation dynamics via this level do not affect the signals used to derive

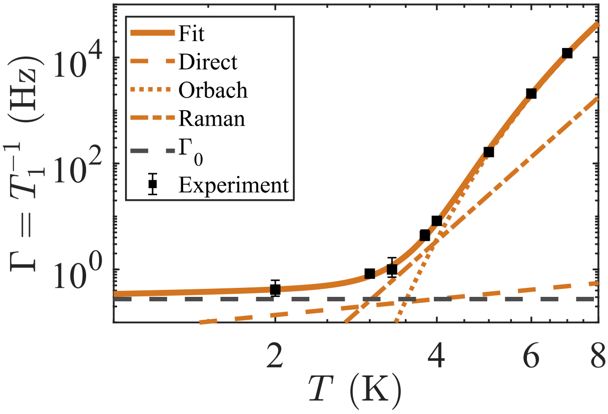

Figure 4.3: **Temperature dependence of spin relaxation.** The variation of $\Gamma = T_1^{-1}$ with temperature can be accurately described by a combination of direct (one-phonon), Raman and Orbach processes (two-phonon processes). The two-phonon processes happen due to coupling to an excited state approximately 6.5 meV above the ground state KD, compatible with coupling of the electronic state of the defect to localized vibrational modes. Error bars are extracted from the exponential fits of the data presented in the inset of Fig. 4.2(c) (for details, see Sec. 4.5.1), and are smaller than the data points when not visible.

T_1. Furthermore, we investigate the timescale associated with bleaching due to ionization [29, 30], which is found to be several orders of magnitude slower than the one associated with spin dynamics (see Sec. 4.5.3).

The temperature dependence of the spin-relaxation time spans several orders of magnitude, going from 2.4 s at 2 K to 83 μs at 7 K (Fig. 4.3). Concerning phonon mediated spin relaxation, the mechanisms leading to spin relaxation are well established [21, 31]. One (direct) and two-phonon (Raman, Orbach) processes are relevant when transitions between the levels involved are thermally accessible. Direct spin-flip processes are expected to lead to spin-relaxation rates ($\Gamma = T_1^{-1}$) that grow linearly with temperature ($\Gamma_{direct} \propto T$). In contrast, two-phonon processes mediated by an excited state give rise to spin-relaxation rates that grow superlinearly with temperature ($\Gamma_{Raman} \propto T^{5<n<11}$ and $\Gamma_{Orbach} \propto e^{-\Delta/k_B T}$, where Δ is the energy of the relevant excited state) [21, 31–33]. Additionally, interaction with paramagnetic moments in the material is expected to lead to temperature-independent spin relaxation. We fit the data presented in Fig. 4.3 to a combination of these processes and identify the temperature regimes where they are relevant (see Sec. 4.5.7 for additional details concerning the fitting procedure).

The defect has a rich electronic structure, with orbital and vibrational degrees of freedom at energies that are thermally accessible between 2 and 7 K (Fig. 4.1(b)). Thus, we expect two-phonon processes involving transitions into both orbital and vibrational excited states to contribute to the temperature dependence of Γ. Surprisingly, we find that not all available states contribute significantly to spin relaxation, leading to unexpectedly long spin lifetimes below 4 K.

Above 4 K, we identify an exponential growth of Γ as a function of temperature, indicating the prevalence of spin relaxation via Orbach processes in this temperature range. From the fit presented in Fig. 4.3, we extract $\Delta = 6.5 \pm 1$ meV for the energy of the excited state involved in these spin flips. This energy matches the difference observed in PL experiments between the ZPL and the onset of the phonon-sideband emission (Fig. 4.1(d)). The first phonon replica is observed 10 meV above the ZPL, but its broadened line indicates that the first available vibrational levels are lower in energy. Thus, we identify vibronic levels where the spin is coupled to localized vibrational modes as the relevant excited state for two-phonon mediated spin-relaxation processes that degrade T_1 above 4 K. As expected, these spin-relaxation mechanisms do not depend on the magnitude of the magnetic field (see Sec. 4.5.7).

We note that we cannot observe Orbach processes involving states $|\mathrm{G2}\rangle$. Between 2 and 7 K, the contribution of these processes to the spin relaxation is expected to be close to saturation, giving a flat temperature dependence in this range. Thus, the long spin-relaxation times observed at 2 K provide an upper bound to the spin-relaxation rates due to two-phonon processes mediated by $|\mathrm{G2}\rangle$, and are evidence that these processes are slow. This leads us to conclude that transitions between $|\mathrm{G1}\rangle$ and $|\mathrm{G2}\rangle$ are strongly spin-conserving. Based on this, we can estimate the timescale of phonon-induced transitions between the two doublets $|\mathrm{G1}\rangle$ and $|\mathrm{G2}\rangle$ to be on the order of miliseconds [34] (also, see Sec. 4.5.8). This process is orders of magnitude slower than the same process in SnV in diamond, a group-IV defect with similar mass to the Mo defect in SiC, [27, 35]. We note that, for this class of defects in diamond, the active electrons participate in bonding to the neighboring carbon atoms [26], which may change the character of the phonons responsible for spin-lattice interactions. In fact, the gap observed between the ZPL and the PSB for the Mo defect is absent in the PL spectrum of group-IV defects in diamond [36], indicating that the latter are more sensitive to low-energy phonons.

Spin-conserving phonon mediated transitions between the two orbital states are expected to contribute to decoherence [37], limiting the spin coherence time T_2 of the $|\mathrm{G1}\rangle$ spin to milisecond timescales at 4 K. This is significantly larger than the experimentally observed ensemble T_2^* [14], likely due to an inhomogeneus distribution of Zeeman splittings [19].

Below 4 K, the slow spin-relaxation rates observed must result from three mechanisms: *i*) processes whose temperature dependence is saturated in this range (as treated above); *ii*) direct one-phonon transitions between the two spin sublevels $|\mathrm{G1}\downarrow\rangle$ and $|\mathrm{G1}\uparrow\rangle$ and *iii*) temperature independent processes (such as spin-spin paramagnetic coupling). The long T_1 observed below 4 K is evidence that all three processes are relatively slow for this particular system. The first contribution has been discussed above. Below, we elaborate on how the electronic structure of this defect leads to a suppression of the latter two processes.

The two spin sublevels pertaining to a KD are strictly time-reversal symmetric with respect to each other, such that they must be degenerate eigenstates of any external field that preserves time-reversal symmetry. Thus, to first order, non-chiral phonons or electric fields cannot cause a direct spin-flip within pure KD pairs (but note that this does not concern transitions between levels belonging to different KDs, see Sec. 4.5.8). A magnetic field or the interaction with nearby nuclear spins leads to mixing between spin sublevels pertaining to different KDs, enabling direct spin-flips via interactions with single phonons. This mixing is inversely proportional to the energy separation between the various KDs, which is in turn largely determined by the spin-orbit splitting. Thus, large SOC protects the KD character of the ground-state spin doublet, suppressing direct spin-flipping processes within the spin doublet.

Additionally, SOC leads to a highly anisotropic Zeeman splitting of the ground-state spin sublevels [14], which hinders its interaction with a bath of paramagnetic impurities in the SiC crystal. Firstly, the spins are insensitive to magnetic fields perpendicular to their quantization axis, such that small fluctuations in the local magnetic field are not likely to induce a spin flip. Secondly, the spin doublet has a Zeeman splitting governed by a g factor that is at maximum 1.6 [14], suppressing resonant spin flip-flop interactions with neighboring paramagnetic impurities with $g \approx 2$.

The same arguments presented above to explain the long spin-relaxation times observed in this defect indicate that obtaining control of the defect spin via microwave fields is a challenge. Driving spin resonances between the two ground-state spin sublevels requires mixing of the various KDs by a perturbation that breaks time-reversal symmetry, such as a strong magnetic field (see Sec. 4.5.4). This is necessary to control the ground-state spin via microwaves, and is expected to contribute to spin-relaxation mechanisms.

4.4. Discussion and conclusion

As discussed above, in the particular case of a TM at a *quasi*-hexagonal site, such as the Mo center, a combination of rotational symmetry and strong SOC protects the effective spin from flipping: it gives rise to ground state effective spin which is an isolated KD, protected by time-reversal symmetry and magnetically isolated from other paramagnetic centers in the crystal due to its unique Zeeman structure. In this doublet, the crystal field locks the orbital angular momentum along the axis of rotational symmetry of the defect. Via the strong SOC, the electronic spin is stabilized, giving rise to robust effective-spin states with long spin-relaxation times.

Considering these processes alone, stronger SOC is thus expected to lead to slower spin-relaxation rates in TM color centers with an odd number of electrons and rotational symmetry. Nonetheless, our work shows that the presence of localized vibrational modes is pivotal in generating spin-flips, their energy determining the temperature where the onset of two-phonon relaxation mechanisms happens. Since the energy and density of states of the localized vibrational modes depend non-trivially on the mass of the defect, whether or not defects containing heavier TMs (where SOC is more prevalent) will exhibit longer spin-relaxation times remains a question. In fact, the class of group-IV defects in diamond show significantly faster spin relaxation, which depends non-trivially on the mass of the defect [27, 35]. Thus, it would be relevant to investigate these processes in defects containing 5d electrons in SiC. Tungsten defects, for example, have been observed with an optical transition at 1240 nm and an odd number of electrons, although their microscopic configuration is still unknown [38].

More generally, SOC should not be regarded as a detrimental feature when investigating solid-state defects for quantum communication applications. Transition metal defects in SiC offer interesting opportunities, such as charge-state switching [39, 40], emission in the near-infrared [15] and long spin lifetimes [18]. The maturity of the SiC-semiconductor industry means that a wide range of defects has been identified [19]. Nonetheless, their characterization with respect to optical and spin properties is still vastly unexplored.

Acknowledgements

We thank A. Gali, A. Csóré and P. Wolff for discussions. Technical support from H. de Vries, J. G. Holstein, T. J. Schouten, and H. Adema is highly appreciated. Financial support was provided by the Zernike Institute BIS program, the EU H2020 project QuanTELCO (862721), the Swedish Research Council grants VR 2016-04068 and VR 2016-05362, the Knut and Alice Wallenberg Foundation (KAW 2018.0071), and the Carl Tryggers Stiftelse för Vetenskaplig Forskning grant CTS 15:339.

Author contributions

The project was initiated by CHvdW and TB. SiC materials were grown and prepared by AE and BM Experiments were performed by TB, DvH and CMG, except for the PL measurements which were done by IGI Data analysis was performed by CMG, TB, DvH, FH and CHW. CMG, TB, and CHvdW had the lead on writing the paper, and CMG and TB are co-first author. All authors read and commented on the manuscript.

4.5. Appendices

4.5.1. Experimental methods

Setup The laser power is 200 μW for the resonant pulsed beam at 1121.32 nm. It is polarized linearly along the 6H-SiC c-axis. The repump beam accounting for charge state switching has 2 mW power at 770 nm, it is pulsed with 80 MHz repetition rate.

Reinitialization time After the pump-delay-probe sequence thermal equilibrium should be recovered before the next sequence can be started. To this end a reinitialization time needs to be considered. We chose sufficiently low repetition rates to account for this reinitialization time. For the measurements at 6 K and 7 K we kept the repetition rate fixed throughout the measurement (at 35.7 Hz and 243.9 Hz respectively). In this way the reinitialization time was always well beyond 20 times the observed T_1 time. This renders any errors due to incomplete reinitialization negligible. In order to save time and to keep a consistent reinitialization time at all delay times, we scaled the repetition rate along with the delay for the measurements at $2-5$ K. Here, the reinitialization time was always larger than 5 times the observed T_1 time. This limits the error in T_1 to 3%. Moreover, the error in this method is such that the measured T_1 value will always be lower than the true T_1 value, thus not affecting the integrity of our lower-bound measurement. Table 4.1 shows the reinitialization times for all temperatures for which T_1 was measured.

Fitting routine We extract the T_1 lifetimes from the time-resolved PLE experiments as in Fig. 4.2(c) by comparing the leading-edge response from the first pulse h_1 to that from the second pulse h_2. These are determined by taking the average of the first 20 bins (of varying size, dependent on the timescale at a certain temperature) of the responses to the pulses. The behavior of the fraction of h_2 and h_1 can be described as

$$\frac{h_2}{h_1} = \frac{h_0(1-e^{-t/T_1})+\delta}{h_0+\delta} \tag{4.1}$$

where δ is the baseline height, h_0 is the peak height at thermal equilibrium minus the baseline δ, and t is the delay between both pulses. This allows us to create a fit function

$$\frac{h_2}{h_1} = q(1-e^{-t/T_1})+1-q \tag{4.2}$$

with only two free parameters: T_1 and q, which represents the fraction $\frac{h_0}{h_0+\delta}$.

For the uncertainty in the T_1 (and q) fit parameters we take the 95% confidence interval from fitting. However, for the 2 K and 3.3 K measurements this method yields unrepresentative large error bars due to the small size of these data sets. For

Table 4.1: **Reinitialization times used**

Temperature	T_1	Reinitialization time
2.0 K	2.4 ± 0.8 s	30 s
3.0 K	1.2 ± 0.1 s	10 s
3.3 K	1.0 ± 0.4 s	10 s
3.8 K	0.23 ± 0.05 s	10 s
4.0 K	121 ± 8 ms	800 ms
5.0 K	6.1 ± 0.2 ms	70 ms
6.0 K	0.48 ± 0.03 ms	$26 - 23$ ms
7.0 K	83 ± 13 μs	$2.1 - 1.8$ ms

these measurements we estimate the error by first only deriving a value for the q parameter (with error bar), directly from the PLE traces in Fig. 4.12. The q parameter is determined by reading h_0 and δ from the PLE response traces of the initial pulses for those temperatures. Next, we use this range (set by error bar) of q values as input in an approach that only fits T_1, where we take for the uncertainty in T_1 again the 95% confidence interval. The way in which the error in determining h_0 and δ carries over into an error for T_1 is thus considered, but this is found to give a negligible contribution to the reported error.

Deadtime pile-up effect For the experiments in this work we used an avalanche photodiode single photon counter (SPC) for detection. After every detection event the detector has to reset its state, for which a predefined deadtime is used (10 μs in our case). This creates a pile-up effect in our experiments when integrating many pulse sequences. We investigated how this causes an error in determining T_1.

The probability of having a count at time t can be described by the combined probability that a photon is present and detected at the counter P_{photon} multiplied by the probability of not having measured a photon before for the duration of the deadtime Δt. We get the equation

$$P_{\text{count}}(t) = P_{\text{photon}}(t)\left(1 - \int_{t-\Delta t}^{t} P_{\text{count}}(\tau) d\tau\right) \tag{4.3}$$

The outcome is plotted in Fig. 4.4 for a square PLE response to a pulse where $P_{\text{photon}}(t) = 100$ kHz during the pulse, which saturates the SPC. Before the pulse, the detector is always ready to receive a photon, thus the initially measured count rate relates accurately to the number of photons present. For the duration of the deadtime (10 μs) the detector will be recovering and thus the count rate drops. This

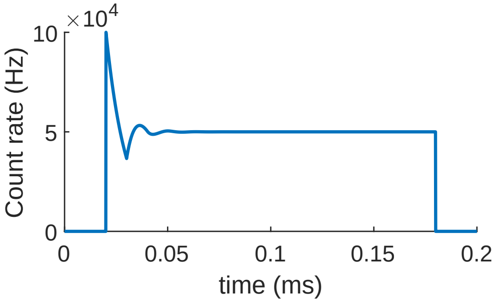

Figure 4.4: **Simulated count rate at the single-photon counter for signal above saturation values.** Probability of counting a photon at time t, for a square PLE signal above saturation ($1/(10\mu s)$).

is periodic, but it clearly damps out to a steady-state count rate due to a spread in the actual detection times. This behavior is consistent with what we observe experimentally when illuminating the SPC with constant, intense light. This effect becomes less relevant, however, when illumination conditions are far from the saturation of the avalanche photodiode, and we used these findings to minimize the effect of the saturation of the SPC while maximizing the signal to noise ratio obtained.

Generally, this pile-up effect will give a positive error ϵ_1 (ϵ_2) for the measured value of h_1 (h_2). At small t the magnitude of the error ϵ_2 is low and increases to ϵ_1 as $t \gg T_1$. If we rewrite Eq. 4.2 to represent the measured values it becomes

$$\frac{h_2}{h_1} = q'(1 - e^{-t/T_1}) + 1 - q' + \frac{\epsilon_1 - \epsilon_2}{h_0 + \delta - \epsilon_1} \tag{4.4}$$

where q' is represents the corrected fraction $\frac{h_0}{h_0+\delta-\epsilon_1}$. The final term in this equation makes the measured $\frac{h_2}{h_1}$ approach its asymptote faster than in reality. Thus, fitting $\frac{h_2}{h_1}$ to Eq. 4.2 will always yield shorter T_1 values compared to the true spin-flip times. Simulating the pile-up effect for our measurements yields errors in T_1 varying from 2% to 7%. We choose to not correct for this and report the lower-bound values for the T_1 spin-flip times. Background PLE and dark counts have been neglected in this analysis as we found them to be of little influence so long as they remain below 10% of the peak count rate.

Total error of h_2/h_1 data points The error in the estimation of the ratio h_2/h_1 in the insets of Fig. 4.2(c) and Fig. 4.12 is obtained from a combination of several contributions:

- Effects from saturation of SPC contribute errors of approximately $2-7\%$ when the intensity of the signal is large compared to the saturation threshold of the SPC. This is only relevant for the data set at 7 K;

- At low temperatures, when the full measurement sequence time is above seconds, a drift in the resonance frequency of the Fabry-Pérot cavity during the measurement causes the intensity of the second pulse to be different than the intensity of the first pulse. This difference can be estimated from the difference in the steady state emission (the height of the trailing edge of the PLE). For the data set presented in Fig. 4.2, that is, at 3.8 K, it contributes a maximum error of 7% to the value of h_2/h_1;
- When analyzing the data, we choose a time interval for which photon counts contribute to h_1, h_2. Varying this time interval changes the values of h_1, h_2 slightly, introducing errors to the ratio h_2/h_1. This error is also limited to 3%.

4.5.2. Zero-field measurement

To confirm that the T_1 lifetimes measured are actually from the spin from the $|\mathrm{G1}\rangle$ and not influenced by some other process, we performed zero-field experiments. Both ground-state spins are then degenerate and no spin pumping is expected. The results are shown in Fig. 4.5. The leading-edge peak in PLE as seen in Fig. 4.2(c) vanishes in Fig. 4.5(a). We note that thermal effects from laser driving at high intensities become more prominent at zero magnetic field, since darkening of the PLE no longer occurs. Additionally, we checked again the optical polarization dependence for these conditions at $B = 0$ mT, but this confirmed that the driving was still only sensitive to the component parallel to the c-axis.

In Fig. 4.6 we show the evolution of the PLE response with increasing magnetic field amplitude. Figure 4.6(e) summarizes this experiment, depicting the steady-state baseline of the PLE response together with the leading-edge peak heights (baseline subtracted) upon ramping the field. Up to 4 mT the baseline decreases, indicating that spin-pumping occurs to an increasing degree. Beyond 4 mT it stabilizes. At this field the spin-splitting (49 MHz at 4 mT) is well beyond the homogeneous linewidth (15 MHz [14]) of the spin-states, and a single laser can no longer drive transitions from both spin states.

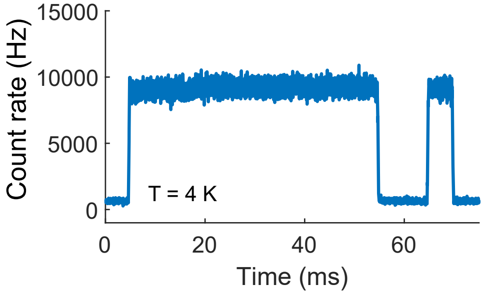

Figure 4.5: **Zero field measurement.** Time-resolved PLE measurement at $B = 0$ T, $T = 4$ K and 200 μW excitation power. For this particular experiment, the excitation pulses were right-circularly polarized, but we found no unexpected dependence on polarization: the PLE response was always proportional to the component of linear driving along the c-axis.

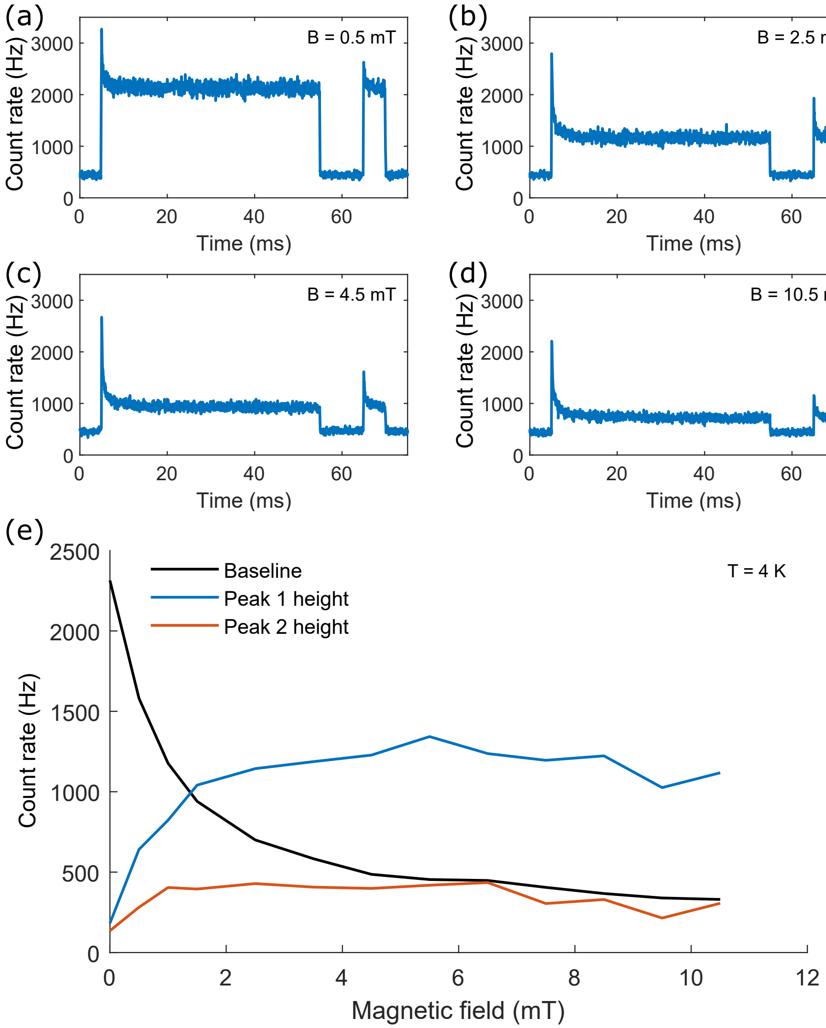

Figure 4.6: **Magnetic field dependence** (a-d) Time resolved measurements at various magnetic fields. (e) Baseline and leading-edge peak heights (baseline subtracted) versus magnetic field. A re-pump laser counteracting any bleaching was always present in these experiments. All measurements at $T = 4$ K.

4.5.3. Charge-state switching

When resonantly addressing optical transitions in the Mo defect in SiC, the PLE response drops over time. This is ascribed to charge-state switching of the defect. We investigate the timescales of this bleaching in order to rule out its influence on the measurements of the T_1 spin-flip times.

The experimental approach is depicted in Fig. 4.7(a). First, a repump beam (770 nm, pulsed) counteracts any prior bleaching [14], resetting the charge state for 60 seconds. Next, a probe beam resonant with the ZPL illuminates the sample, slowly bleaching the Mo defects. We can track the bleaching timescale by measuring the PLE response as function of time. After another 1000 seconds the repump beam is incident on the sample together with the probe beam, which allows us to track the recovery timescale. Finally, the repump is switched off for 60 seconds to check the initial decay of the PLE response. This sequence is repeated four times. We use a 2 mW repump beam and a 200 μW probe focused to approximately 100 μm diameter in the sample. The magnetic field strength is 100 mT at an angle of 57° with the c-axis.

The results are shown in Fig. 4.8. The bleaching between 60 and 1060 seconds occurs according to two timescales, both are fit with an exponential decay for the orange and blue curve. The yellow curve is an exponential fit to the recovery by the repump laser. All three timescales are plotted versus temperature in Fig. 4.7(b). For the T_1 experiments, where the repump beam was only on in between measurement runs, the two bleaching scales are most relevant. Both occur at rates that are at least one order of magnitude slower than the observed spin-relaxation times. Any bleaching occurring at faster timescales should have been visible in the zero-field measurements from section 4.5.2. Thus, the effect of bleaching on measuring T_1 can be deemed negligible.

Note the fast decay of PLE for 4 K (Fig. 4.8(a)) after the repump laser is blocked at 1300 seconds. We ascribe this to fast spin relaxation induced by the repump

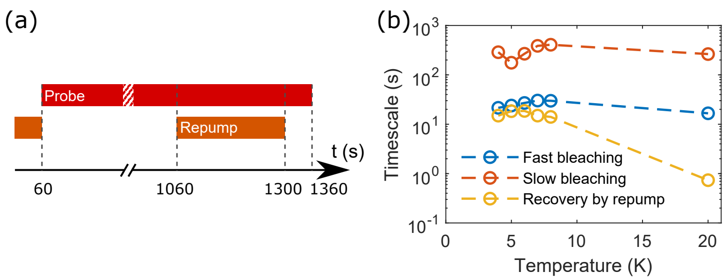

Figure 4.7: **Bleaching experiment** (a) Sequence of lasers used to measure the bleaching/repump timescales. (b) The acquired timescales versus temperature.

laser. When performing the experiments to measure T_1 with an omnipresent repump laser, we observe that T_1 is reduced by an order of magnitude (for similar laser powers). This fast decay is not visible in Fig. 4.8(b-f) since the spin-relaxation times are already quite short at higher temperatures.

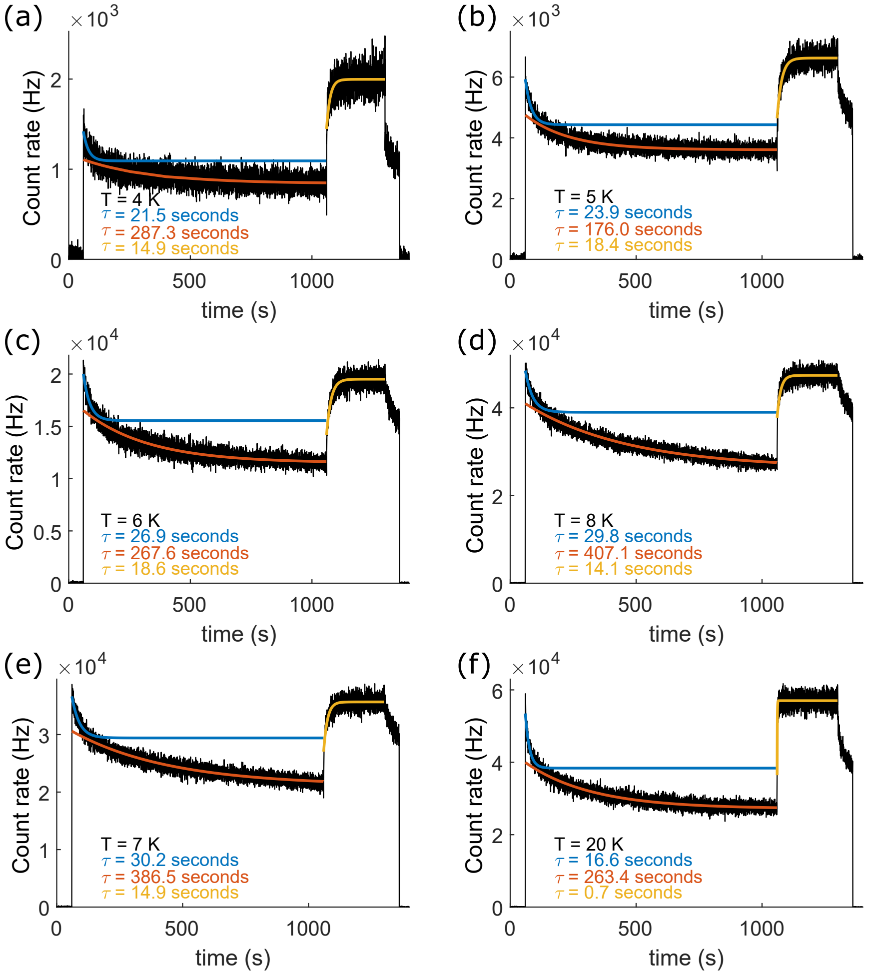

Figure 4.8: **Detailed bleaching results** (a-f) Dynamics of the resonant photoluminescence signal (PLE) over long time periods, at various temperatures. A static background is subtracted as well as a fluorescence background induced by the repump when it is on (measured during the first 60 seconds). When the repump is off, but the system is being renonantly driven, the PLE signal decays exponentially with two characteristics time constants (blue and red fits). As the repump is turned on, the PLE signal recovers quickly, with a single time constant (yellow fit).

4.5.4. Electronic structure: symmetry-related selection rules

As previously stated in chapter 3, the Mo defect is characterized by a single active spin in the 4d shell of a molybdenum impurity at a Si substitutional lattice site [14]. In this configuration, the Hamiltonian of the defect has a three-fold rotational symmetry and three vertical mirror planes, such that the eigenfunctions of the electronic orbital state transform according to the symmetry group C_{3v}. Despite the extensive literature available on the effect of crystal field and spin-orbit coupling on the electronic states of these defects [20, 39], we are unaware of a comprehensive report on the effect of symmetry on the coupling terms between the various specific spin sublevels and external fields based on the double group representations of the defect symmetry, and we present this analysis here. We apply a group-theoretical approach to obtain the symmetry of the eigenfunctions associated with a defect center in a crystal field of C_{3v} symmetry in the presence of spin-orbit coupling. Furthermore, we obtain and explain the selection rules governing the interaction of the electronic spin with magnetic and electric fields.

The group theoretical rules governing the selection rules presented here do not rely on a particular basis set for the description of the electronic wavefunction. By this, we mean that even if we consider hybridization of the wavefunction of the bare transition metal atom/ion with the nearest carbon atoms due to covalent bonding, the symmetry of the crystal-field Hamiltonian is preserved such that the new, modified wavefunctions will still obey the selection rules arising from a group-theoretical analysis. Nonetheless, it is instructive to start from an analysis of the effect of the Hamiltonian on the 10 spin-orbital states arising from a single electron sitting in one of the d-orbitals of the transition metal.

The transition metal at a silicon substitutional site shows tetrahedral coordination due to bonding to the 4 nearest carbons. In this configuration, the 5 different d orbitals split into an orbital doublet and an orbital triplet (which transform as the irreps E and T_2 of the symmetry group T_d), where the triplet lies highest in energy. Due to the hexagonal character of the lattice, the tetrahedral symmetry of these sites is lowered to C_{3v}, with the rotational axis aligned parallel to the growth axis of the crystal. Upon this symmetry reduction, the triplet further splits giving rise to an orbital doublet and a singlet, which transform respectively as E and A_2. The effect of this symmetry lowering operation is expected to be largest in the lattice sites of *quasi*-hexagonal symmetry (h), and to only modestly affect the lattice sites of *quasi*-cubic symmetry (k) (Fig. 4.9(a)).

A wavefunction transforming as a *non-degenerate* irrep of a given point-group cannot have an effective orbital angular momentum (in other words, the orbital angular momentum is quenched) [21]. However, this requirement is lifted in the presence of degeneracies, such that the eigenfunctions of the Hamiltonian transforming as E are allowed to have a non-zero orbital angular momentum. Thus, in order to fully describe our system, we must consider the effect of spin-orbit coupling. In a group-theoretical approach, this is done by extending the group of interest to include 2π rotations which bring a spin $\uparrow$ into $-\uparrow$ [41]. That is, this is done by considering the eigenfunctions as basis states of the irreps of the double group associated with the $C_{3\mathrm{v}}$ group, here denoted by $\bar{C}_{3\mathrm{v}}$.

In the double group including the effect of spin-orbit coupling, three irreps describing how half-integer spin wavefunctions transform are added to the group. These irreps are Γ_4, which is doubly degenerate, and $\Gamma_{5,6}$, two irreps that are connected by time-reversal symmetry and must thus be degenerate in the presence of time-reversal symmetry. The orbital singlet transforming as A_2 gives rise to a Kramers doublet (KD) transforming as Γ_4, whereas an orbital doublet transforming as E splits into two KDs, of which one transforms as irrep Γ_4, and the other transforms as irreps $\Gamma_{5,6}$. Thus, the symmetries mentioned above split the 10 states arising from an electronic configuration $^2\mathrm{D}$ into 5 Kramers doublets, of which 2 transform as $\Gamma_{5,6}$, and 3 transform as Γ_4 (Fig. 4.9(a)). The character table of the double group $\bar{C}_{3\mathrm{v}}$ is given in Tab. A.1. This table also explicitly shows the transformation properties of the vectors x, y, z and the axial vectors R_x, R_y, R_z, as well as how the cubic harmonics $z^2, x^2 - y^2, xy, xz, yz$ transform under the operations of the group.

We can investigate the role of small magnetic and electric fields in driving transitions between different KD (coupling between different KDs), and spin resonances (coupling between the two eigenstates pertaining to a single KD) in the framework of group-theory, given that these fields are small enough to preserve the symmetries of the Hamiltonian H_0. The selection rules between two wavefunctions can be obtained in a straight-forward way. If $|\psi_i\rangle$ and $|\phi_{i'}\rangle$ are two eigenstates of the Hamiltonian H_0 transforming respectively as irreps Γ_i, $\Gamma_{i'}$, the selection rules with respect to a perturbative Hamiltonian H' are given by the product $\langle\psi_i|\, H' \,|\phi_{i'}\rangle$. In order for this matrix element to be non-zero, it must transform as a scalar, that is, as the totally symmetric irrep A_1 [41]. Thus, the product of the representations $\Gamma_i^* \otimes \Gamma_j \otimes \Gamma_{i'}$, where the perturbation H' transforms as Γ_j and * denotes complex conjugation, must contain the totally symmetric irrep A_1.

Table A.2 gives the decomposition of the various products of Γ_4, $\Gamma_{5,6}$, in terms of irreps of the $C_{3\mathrm{v}}$ group. Based on this, we can obtain the selection rules for optical and microwave transitions between the different spin sublevels.

Optical transitions between various sets of KDs are allowed due to coupling to $\vec{E}_\parallel, \vec{E}_\perp$, which belong to irreps A_1 and E, respectively. We can extract polarization selection rules from Tab A.2. Electric-field driven transitions between two KDs transforming as $\Gamma_{5,6}$ will be polarized along the symmetry axis of the defect; transitions between two KDs transforming as Γ_4 can be polarized along any direction; transitions between a KD transforming as $\Gamma_{5,6}$ and a KD transforming as Γ_4 are only allowed for light polarized perpendicular to the symmetry axis. These properties are summarized in Fig. 4.9(b). The zero-phonon line studied in this work can be driven most strongly with an electric field parallel to the symmetry axis of the defect, indicating that ground and optically excited KDs are of the same symmetry type (either they are both of the Γ_4 type, or they are both of the $\Gamma_{5,6}$ type).

Transitions and energy splittings within each of the KDs can also be understood based on the symmetry of the defect. The anisotropic Zeeman structure observed for the ground-state spin doublet, which is insensitive to magnetic fields perpendicular to the crystal growth axis [14] can be understood based on the properties of the group. A magnetic field along the symmetry axis of the defect transforms as R_z, whereas a magnetic field perpendicular to this axis transforms as R_x, R_y. Within a doublet which transforms as $\Gamma_{5,6}$, no coupling is allowed with a magnetic field perpendicular to the symmetry axis since $\Gamma^*_{5,6} \otimes \mathrm{E} \otimes \Gamma_{5,6} = \mathrm{E} \not\supset \mathrm{A}_1$. This is not the case for a doublet transforming as Γ_4, such that the spin sublevels that transform as Γ_4 are allowed to couple to magnetic fields in the plane, and will not in general have $g_\perp = 0$. These states may, however, have accidental $g_\perp = 0$. As we show in following chapters, this is the case for the V defect in SiC, for example (chapters 5 and 6) Thus, we cannot conclude what is the symmetry character of the ground-state doublet. We do know, however, that it is not sensitive to magnetic fields in the plane perpendicular to the symmetry axis of the defect (Fig. 4.9(c)). As long as the quantization axis of the defect spin points parallel to the symmetry axis of the defect, we cannot rotate the spin via microwave spin resonances, since these spins are insensitive to magnetic or electric fields perpendicular to this axis.

If two spin sublevels are strictly connected by time-reversal symmetry (that is, they are a pure KD), they cannot be connected by operators that preserve time-reversal symmetry. This was proven by Kramers and became what is known as Kramers theorem [41]. Thus, within a pure KD, electric fields are not capable of driving transitions between the two spin sublevels.

Finally, we note that the effect of electric fields on the optical transition energy is more subtle. Strictly speaking, from Kramers theorem alone, we can say that the two spin sublevels pertaining to a KD must have the same energy when subject to an electric field, but the actual value of this energy can change depending on the electrostatic environment of the defect. Additionally, if the electronic wavefunctions were composed by the d-orbitals exclusively, we would observe no optical transition (due to the spatial parity of the d-orbitals and of the electric dipole moment operator). Thus, the fact that the defects are optically active means that the states show some hybridization of the d-orbitals with the lattice wavefunctions, and is thus sensitive to a spatially extended electrostatic environment. These two factors combined lead us to conclude that ground and excited state wavefunctions can show some spectral diffusion.

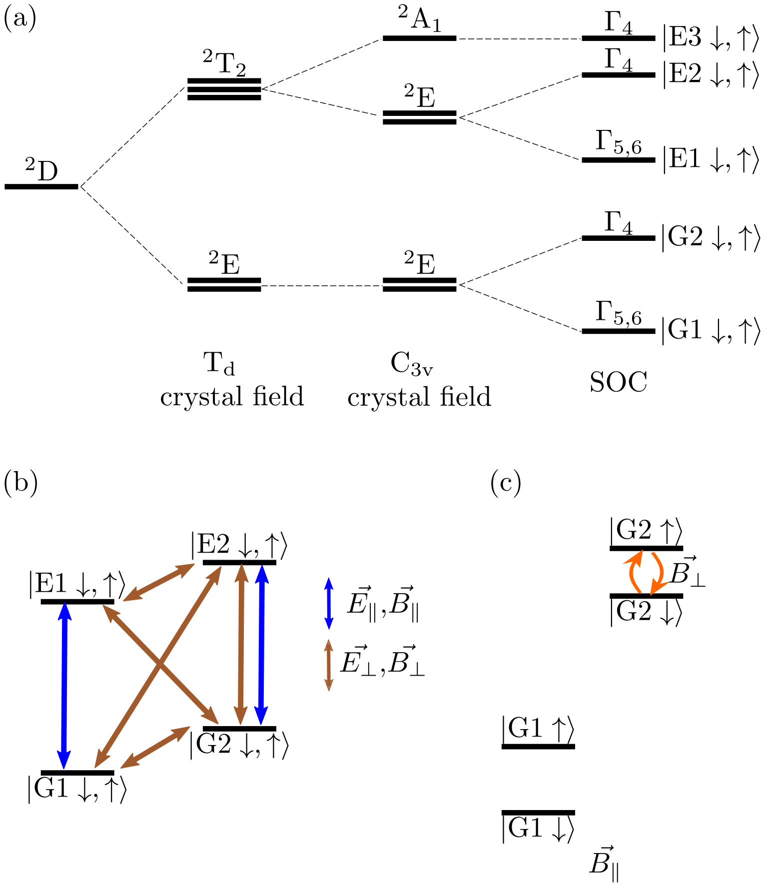

Figure 4.9: **Electronic Structure and selection rules based on group-theoretical analysis** (a) The 10 spin-orbital states corresponding to the ^{2}D configuration of the free ion are split into 5 Kramers doublets under the action of the crystal field and SOC, of which three transform as irrep Γ_4 and two transform as irrep $\Gamma_{5,6}$ of the double group C_{3v}. (b) Coupling between 2 KD transforming as $\Gamma_{5,6}$ is allowed under the action of an electric or magnetic field parallel to the symmetry axis; coupling between 2 KD transforming as Γ_4 is allowed under the action of an electric or magnetic field pointing in any direction; coupling between a KD transforming as $\Gamma_{5,6}$ and a KD transforming as Γ_4 is allowed under the action of an electric or magnetic field perpendicular to the symmetry axis. (c) A KD transforming as $\Gamma_{5,6}$ does not interact with a magnetic field perpendicular to the symmetry axis, whereas this is not necessarily the case for a KD transforming as Γ_4.

4.5.5. Simulation of raw data

Due to the large number of available states for the defect (vibrational levels, orbital state $|G2\rangle$ in Fig. 4.1, ionized states), it is not straight forward to obtain quantitative information from the shape of the raw data plots presented in Fig. 6.3. Nonetheless, we can apply a rate equation model to reproduce the data and, upon carefully taken assumptions, obtain a boundary for the values of the optical decay time and Rabi driving frequency in our experiments.

In order to minimize the set of free parameters and facilitate the analysis of the behavior of the system, we simulate this defect center as a three-level system (Fig. 4.11(a)), where the ground (state 1) and excited (state 3) states can be coupled by an optical field with Raby frequency Ω_R. From the optically-excited state, the system can decay either back into the ground state with a rate Γ_{31}, or into a shelving state 2 with a rate Γ_{32}. Additionally, population can be transferred between states 2 and 1 at a rate Γ_{21}, and between 1 and 2 at a rate $\Gamma_{12} = e^{-\Delta/kT}\Gamma_{21}$, where Δ is the energy difference between 2 and 1 and kT denotes the thermal energy of the system. We simulate the system with a simple set of rate equations for the populations of each state (P_1, P_2, P_3), without treating coherences explicitly. Finally, we consider that the photoluminescence observed is proportional to the population of the optically-excited state, P_3.

We try to reproduce the typical shape of the raw PL data obtained experimentally (Fig. 4.11(b)) in order to obtain a set of reasonable values for the Rabi driving frequency and optical decay rates in our system. We assume that states 1 and 2 correspond to the ground-state spin sublevels, $|G1\downarrow\rangle$ and $|G1\uparrow\rangle$ respectively. In this way, we can write Γ_{32} in terms of Γ_{31} by assuming that the branching ratios correspond to the overlap of the spin states in ground and optically-excited state [14]. This gives $\Gamma_{32} \sim 0.003\ \Gamma_{31}$. Previous experiments revealed an excited state lifetime of $\sim$ 56 ns, resulting in $\Gamma_{31} \sim 20$ MHz. Similar TM defects have been recently reported with optical excited state lifetime of $\sim$ 100 ns. Thus, we simulate the experiment for values of Γ_{31} of 2 and 20 MHz. For Γ_{21}, we use the values presented in Fig. 4.3 for the spin relaxation time.

We note that differences based on the exact value of Γ_{31} are barely noticeable. Thus, we cannot restrict our estimate for Γ_{31} further. Nonetheless, we can restrict the expected values of Ω_R by comparing the traces presented in Fig. 4.11(c,d) and the raw trace presented in Fig. 4.11(b). We note that if Ω_R is very small, of the order of a kHz, PL darkening is almost absent, unlike what is seen in experiment, where PL darkening is significant. In contrast, if Ω_R is of the order of a few MHz, the defect darkens completely within the time of the driving pulse. This is also in disagreement with the experimental data. Thus, we conclude that the Rabi frequency in our experiments is of a few tens to hundreds of kHz.

Furthermore, section 4.5.2 shows that we do not see any PL darkening when we perform the time-resolved measurements described in the main text at zero magnetic field. In this case, state 2 in our model corresponds to the orbital state $|G2\rangle$ from Fig. 4.1. We calculate the population in state 2 after optically driving the system for approximately 500 ms, with Rabi frequencies of the order of a few tens of kHz, and present these results in Fig. 4.10. We only transfer significant population into 2 (leading to PL darkening) when the optical decay rate into state 2 (Γ_{32}) is larger than the rate at which the system leaves state 2 (Γ_{21}). Since we do not observe any PL darkening, we conclude that $\Gamma_{32} \ll \Gamma_{21}$ such that, within the time of our measurements, no significant population is transferred into the orbital state $|G2\rangle$, and the presence of this state does not influence our measured value for the spin T_1.

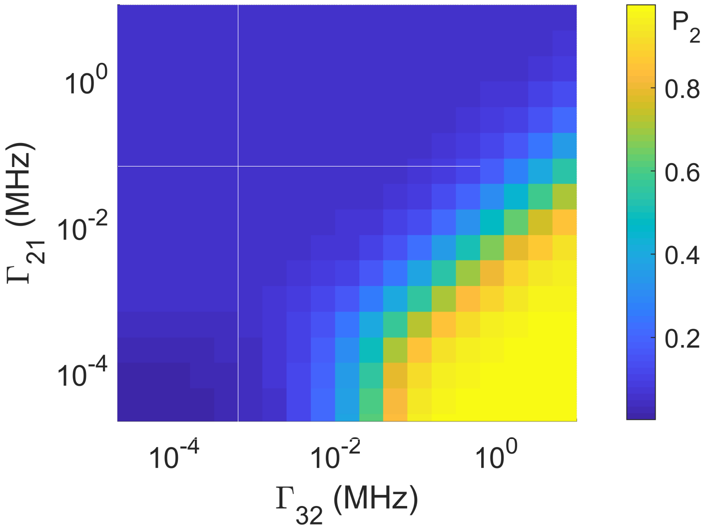

Figure 4.10: **Optical pumping into orbital state $|G2\rangle$** Significant population is only transferred into $|G2\rangle$ when $\Gamma_{32} \gg \Gamma_{21}$.

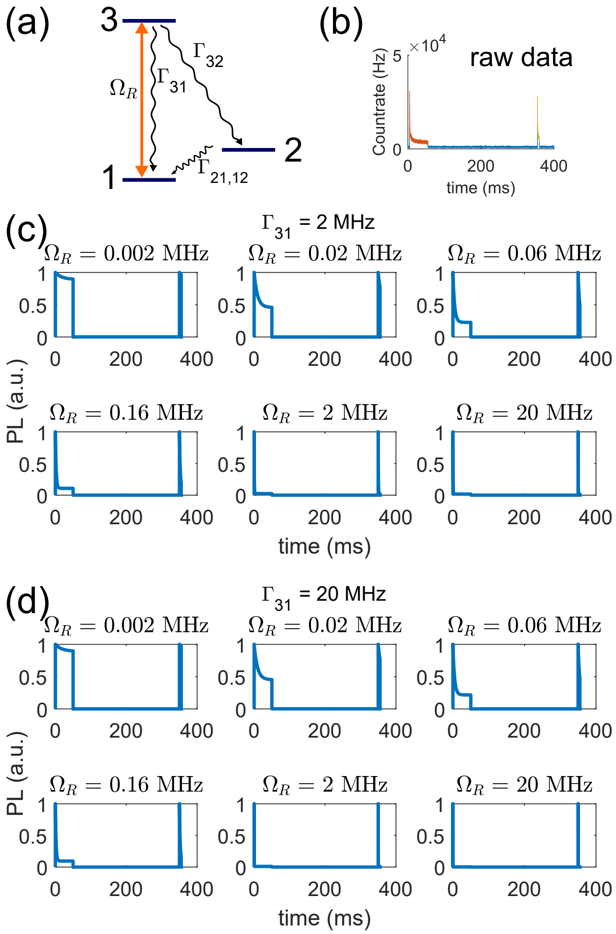

Figure 4.11: **Three-level model describing dynamics of defect in ms timescale** (a) The three level model inclued a ground and optically-excited states that are connected via optical driving with Rabi frequency Ω_R. The optically-excited state can decay into the ground state or into a shelving state, with rates Γ_{31} and Γ_{32}. Population can decay back from the shelving state into the ground state with a rate Γ_{21}. The photoluminescence excitation signal obtained is assumed to be proportional to the population in the optically-excited state. (b) Typical experimental data in the presence of a magnetic field consists of PLE signal with sharp on and offset as the laser turns on and off. After a leading-edge peak, the PLE signal decays back to a constant non-zero value, indicative of PL darkening due to optical pumping into shelving states within the first few microseconds of illumination. (c,d) Simulating the dynamics of the population in the excited state upon illumination and comparing these curves to the experimental data, we can determine that the Rabi frequencies observed in these experiments are of the order of a few tens of kHz.

4.5.6. T_1 vs Temperature

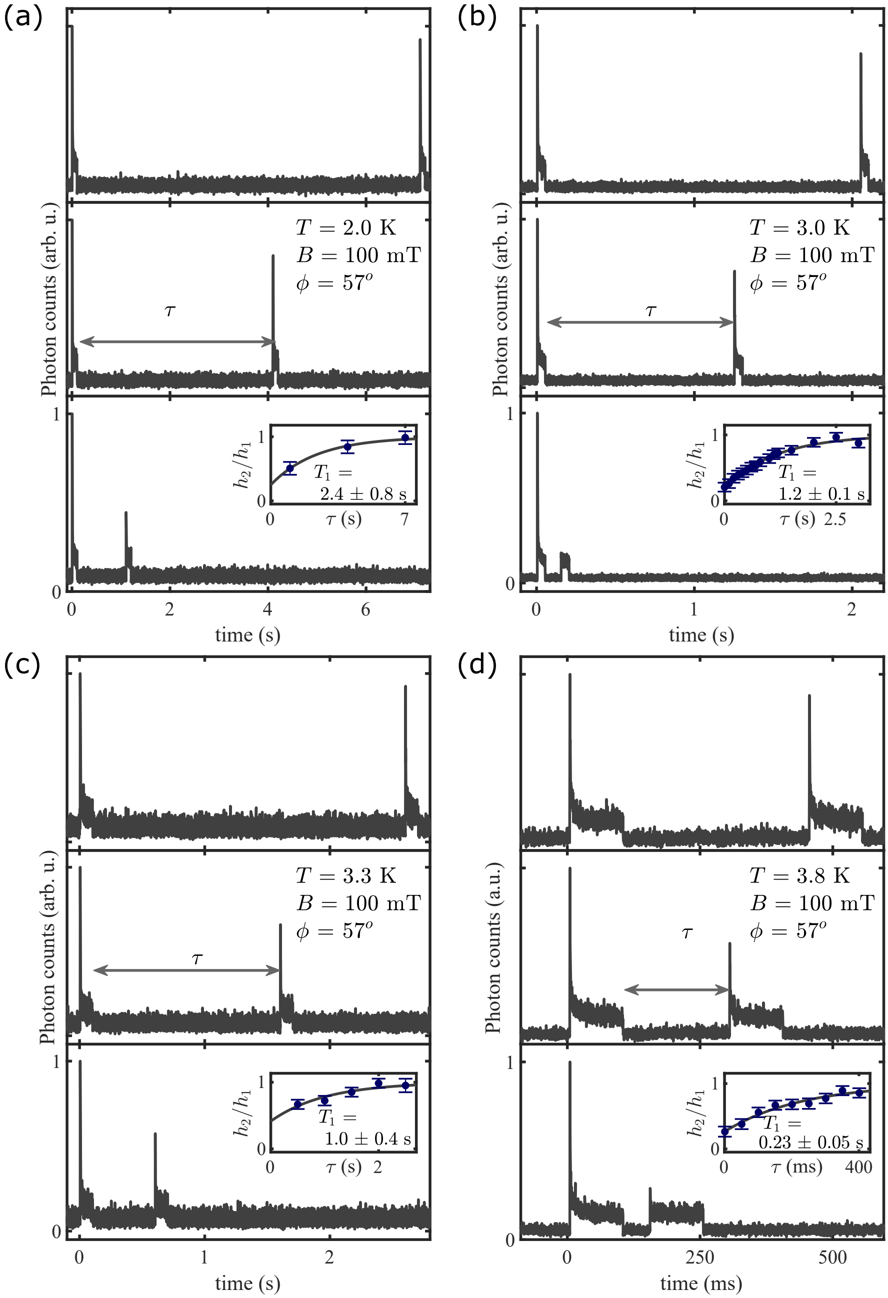

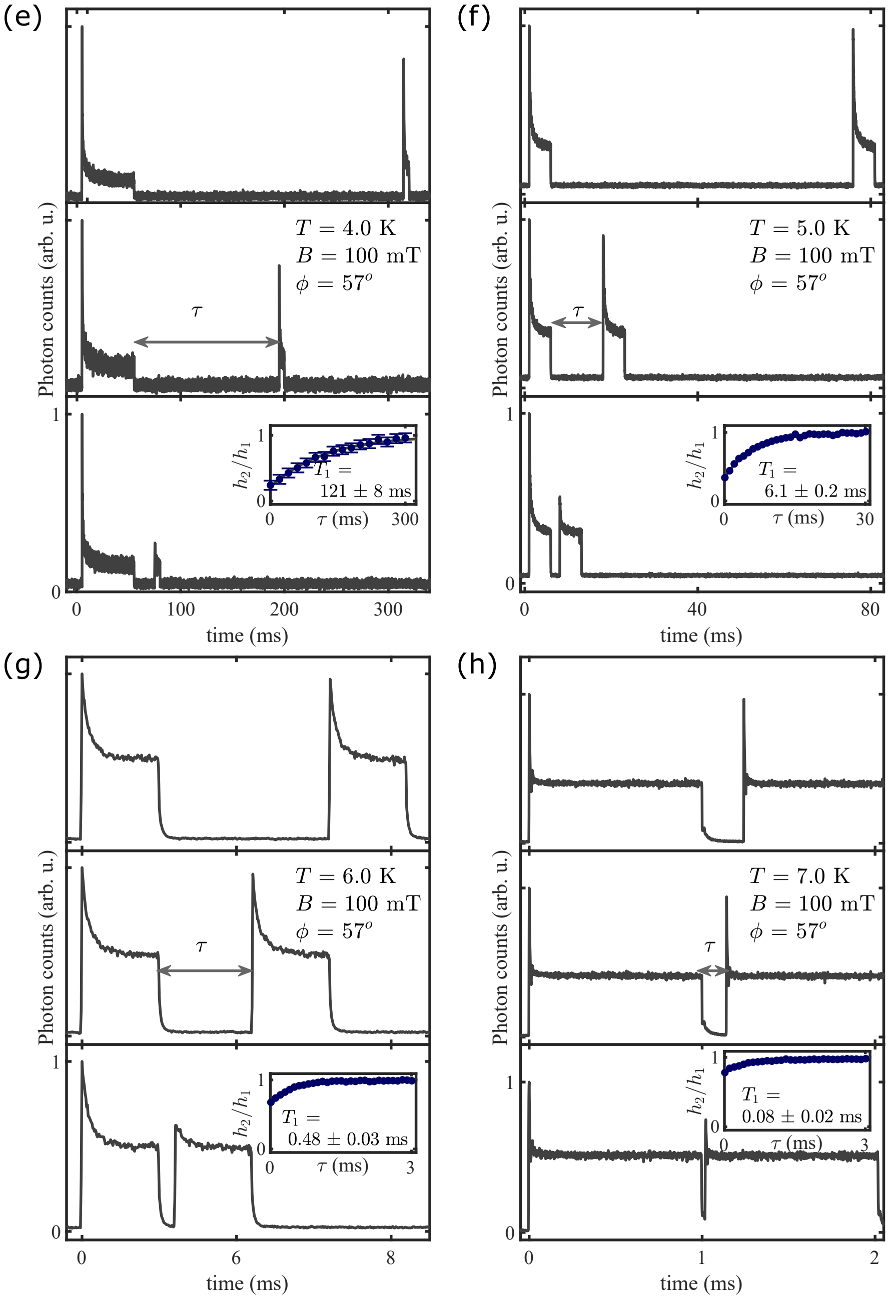

Figure 4.12: **Raw traces and exponential fits used to determine T_1 at various temperatures.** For the 5 – 7 K measurements the error bars on the h_2/h_1 datapoints in the inset are smaller than the marker size and thus not shown.

4.5.7. Fitting of T_1^{-1} vs temperature

The spin-lattice relaxation of single spins of substitutional defects in solid-state materials arises from a modulation of the crystal-field potential in time due to the presence of phonons, which perturbs the stationary crystal field ($V^{(0)}$) and couples various eigenstates of the time-independent Hamiltonian to each other [21]. Thus, the probability of a spin flip to occur depends largely on the matrix elements of the time-dependent crystal field $V^{(1)}$ between the various electronic levels accessible to the defect. We thus define the terms V_{orb} and V_{vib}, which indicate the order of magnitude of the matrix elements of $V^{(1)}$ connecting $\{|\mathrm{G1}\downarrow\rangle, |\mathrm{G1}\uparrow\rangle\}$ to $\{|\mathrm{G2}\downarrow\rangle, |\mathrm{G2}\uparrow\rangle\}$ and $\{|\mathrm{G1}_{vib}\downarrow\rangle, |\mathrm{G1}_{vib}\uparrow\rangle\}$ respectively (see Fig. 4.1 for definitions).

The direct process, a one-phonon interaction driving transitions between states $|\mathrm{G1}\downarrow\rangle$ and $|\mathrm{G1}\uparrow\rangle$ directly, is expected to show a temperature dependence of the kind $T_1^{-1} \propto (\hbar\omega)^2 |\langle G1\downarrow| V^{(1)} |\mathrm{G1}\uparrow\rangle|^2 T$ when $k_B T \gg \hbar\omega$ ($\hbar\omega$ is the Zeeman splitting between the spin sublevels $|\mathrm{G1}\downarrow\rangle$ and $|\mathrm{G1}\uparrow\rangle$). Since the states $|\mathrm{G1}\downarrow\rangle$ and $|\mathrm{G1}\uparrow\rangle$ are each other's time-reversal pair and $V^{(1)}$ preserves time-reversal symmetry, the matrix elements $|\langle G1\downarrow| V^{(1)} |\mathrm{G1}\uparrow\rangle|$ are identically zero (see section 4.5.4). Nonetheless, the presence of a magnetic field or hyperfine interaction perturbs states $|\mathrm{G1}\downarrow\rangle$ and $|\mathrm{G1}\uparrow\rangle$ by mixing in states higher in energy, in such a way that we expect the direct process to be present with a magnitude roughly proportional to $(\hbar\omega)^4 \frac{|V^{(1)}|^2}{\Delta^2} T$, where $V^{(1)}$ is now the matrix element of the time-dependent crystal field coupling states $|\mathrm{G1}\downarrow\rangle$, $|\mathrm{G1}\uparrow\rangle$ to a generic excited state $|E\rangle$ lying an energy Δ above $|\mathrm{G1}\downarrow\rangle$, $|\mathrm{G1}\uparrow\rangle$. All of the excited states shown in Fig. 4.1(b) are expected to contribute to this process, such that mixing with both the higher KD ($|\mathrm{G2}\downarrow\rangle$, $|\mathrm{G2}\uparrow\rangle$) and the vibronic states ($|\mathrm{G1}_{vib}\downarrow\rangle$, $|\mathrm{G1}_{vib}\uparrow\rangle$) should be considered. In this way, we expect a dependence of the kind $T_1^{-1} \propto (\hbar\omega)^4 (\frac{|V_{orb}|^2}{\Delta_{orb}^2} + \frac{|V_{vib}|^2}{\Delta_{vib}^2}) T$.

Additionally, a spin polarization in the defect ensemble can decay back to its equilibrium value via two-phonon processes comprising transitions into real (Orbach process) or virtual (Raman process) excited states. The former gives rise to an exponential temperature dependence of the type

$$T_1^{-1} \propto |\langle G1\downarrow| V^{(1)} |E\rangle \langle E| V^{(1)} |\mathrm{G1}\uparrow\rangle| \Delta^3 \exp(-\Delta/k_B T)$$

in the limit of $\Delta \gg k_B T$, where Δ is the energy difference between a generic excited state $|E\rangle$ and the KD $|\mathrm{G1}\downarrow\rangle$, $|\mathrm{G1}\uparrow\rangle$. Orbach processes relative to transitions into states $|\mathrm{G2}\downarrow\rangle$, $|\mathrm{G2}\uparrow\rangle$ are expected to give rise to a strong temperature dependence at temperatures below 1 K and saturate at higher temperatures, when $\Delta_{orb} \sim k_B T$, and its exponential behavior is thus not visible in our data. In contrast, Orbach processes relative to transitions into vibronic levels are expected to contribute significantly to the temperature dependence of T_1^{-1} at a few K, since $\Delta_{vib} \sim 10$ meV

$\gg k_B T$ between 2 and 8 K (Fig. 4.1(d)) .Thus, we expect the Orbach process to give rise to a temperature dependence of the kind $T_1^{-1} \propto |V_{vib}|^2 \Delta_{vib}^3 \exp(-\Delta_{vib}/k_B T)$.

Finally, second order Raman processes give rise to a temperature dependence of the kind $T_1^{-1} \propto |V^{(1)}|^4 T^5$ when $\Delta \ll k_B T$, or $T_1^{-1} \propto (\frac{|V^{(1)}|}{\Delta})^4 T^9$ when $\Delta \gg k_B T$, where Δ is the energy difference between levels $\{|\mathrm{G1} \downarrow\rangle, |\mathrm{G1} \uparrow\rangle\}$ and a generic level $|E\rangle$ which is coupled to $|\mathrm{G1} \downarrow\rangle$, $|\mathrm{G1} \uparrow\rangle$ via $V^{(1)}$. Thus, since $\Delta_{orb} \sim k_B T$, Raman processes involving states $|\mathrm{G2} \downarrow\rangle$, $|\mathrm{G2} \uparrow\rangle$ are expected to show a $|V_{orb}|^4 T^5$ dependence, whereas Raman processes involving virtual transitions into the vibronic levels $|\mathrm{G1}_{vib} \downarrow\rangle$, $|\mathrm{G1}_{vib} \uparrow\rangle$ are expected to contribute a term $(\frac{|V_{vib}|}{\Delta_{vib}})^4 T^9$ to T_1^{-1}.

We fit the data in Fig. 4.3 to a model of the type

$$T_1^{-1} = C_D T + C_R T^n + C_O \exp(-\Delta/k_B T) + \Gamma_0,$$

where $C_{D,R,O}$, Δ and Γ_0 are fitting parameters, and $n = 5, 9$. The parameter Γ_0 is included to account for temperature independent processes of spin relaxation. The fit quality does not improve significantly if we consider $n = 9$ instead of $n = 5$ for the Raman process involved. Thus, we are unable to determine which levels are involved in the Raman transitions responsible for spin relaxation between 3 and 4 K. In either case, however, the exponential increase of the spin relaxation rate above 4 K is accounted for by an Orbach process where two phonons drive transitions between the ground state $|\mathrm{G1}\rangle$ and the its vibrational excited state $|\mathrm{G1}_{vib}\rangle$ flipping its spin. From the fit, we extract $\Delta_{vib} \approx 6.5 \pm 1$ meV, consistent with the energies of the phonon-coupled states responsible for the onset of PSB emission in the photoluminescence spectrum.

Whereas the parameters C_O and Δ can be determined with large accuracy (errors of $\sim 0.1\%$) due to the undisputable exponential behavior of the relaxation rate at higher temperatures, this is not the case for parameters C_D, Γ_0 and C_R. At low temperatures, there is a large tradeoff between the coefficients C_D and Γ_0 – which in turn modify the magnitude of C_R – and various combinations of direct, temperature independent, and Raman processes can fit our data well. For example, a fit with C_D fixed to zero yields an increase of 6% in the root-mean-squared value of the residuals of the fit, and an increase of 62% in the value of Γ_0 and 15% in the value of C_R. On the other hand, a fit with Γ_0 fixed to zero yields an increase of 13% in the rms of the residuals of the fit, an increase of 250% in the value of C_D and a decrease of 30% in the value of C_R. Nonetheless, this uncertainty in the fit does not change the fact that, owing to the long spin-relaxation times in this range, all of the three processes must be relatively slow for these defects.

Finally, we note that the data can also be fit by a power law model of the type $T_1^{-1} = \alpha T + \beta T^{\gamma}$, with $\gamma \approx 13$. Spin-lattice relaxation of this type has been previously reported for heavy ions in solid-state environments [32]. In that work, a Raman process is observed with a power dependence with $\gamma \approx 11 > 9$. They justify the large power observed by noting that the spin sublevels in the KD are not exactly each other's time-reversal conjugate, in such a way that the 'Van Vleck' cancellation does not happen completely [21]. We exclude this as a relevant model in our case due to the fact that the power dependence necessary to explain our data is much higher, with $\gamma \approx 13$. Additionally, the consistency of Δ_{vib} observed by fitting the data with the energies observed in the PSB of the PL spectrum indicates that the rapid increase of the relaxation rate observed above 4 K is indeed related to exponential Orbach processes involving $|\mathrm{G1}_{vib}\downarrow\rangle$, $|\mathrm{G1}_{vib}\uparrow\rangle$.

4.5.8. Estimating T_2

Our goal here is to estimate the rate of decoherence induced by phonon-driven transitions between the two orbital states, $|\mathrm{G1}\rangle$ and $|\mathrm{G2}\rangle$. Our data shows that transitions between these levels are largely spin conserving. Nonetheless, these transitions introduce decoherence in the ground-state spin sublevels $|\mathrm{G1}\downarrow\rangle$, $|\mathrm{G1}\uparrow\rangle$ since the Zeeman splitting and, therefore, the Larmor precession rate of the electronic spin differs between states $|\mathrm{G1}\rangle$ and $|\mathrm{G2}\rangle$. Thus, the spin-coherence time of the defect will be limited by phonon-driven transitions between the two orbital states, which happen at a rate $\nu_{G1\rightarrow G2}$. In order to obtain an estimate for the contribution

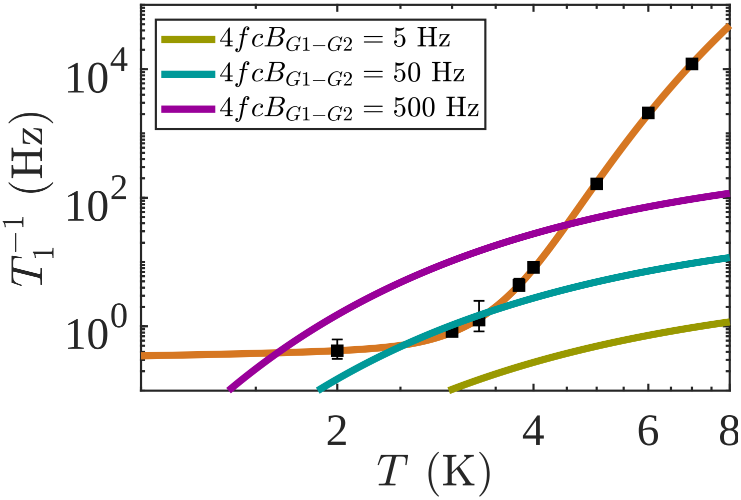

Figure 4.13: **Estimating a limit for T_2 from T_1.** Orbach processes between $|\mathrm{G1}\rangle$ and $|\mathrm{G2}\rangle$ happen with a prefactor $4fcB_{G1-G2}$ smaller than 50 Hz.

of this process to $T_{2,lim}$, we must obtain an estimate for the transition rate between the two orbital states, $\nu_{G1\rightarrow G2}$, given by

$$\nu_{G1\rightarrow G2} = \frac{B_{G1-G2}}{\exp(\Delta_{orb}/k_B T) - 1} \tag{4.5}$$

where Δ_{orb} is the energy difference between $|\mathrm{G1}\rangle$ and $|\mathrm{G2}\rangle$, and B_{G1-G2} is the Einstein coefficient for transitions beween the two orbital doublets.

We can obtain an estimate for the value of B_{G1-G2} from the T_1 data presented in Fig. 4.3. In order to do this, we start out by estimating a limit to the order of magnitude of the Orbach processes involving the orbital excited state $|\mathrm{G2}\rangle$. Subsequently, we compare these values with the expression obtained by Harris and Yngvesson in Ref. [34] to describe Orbach processes where the upwards and downards transition rates into the relevant excited state differ significantly. This is compatible with our model, if we assume that one of those transitions is spin conserving (fast rate), whereas the other one is spin flipping (slow rate).

Based on their model, we obtain an expression for the rate of Orbach transitions between the two spin eigenstates of $|\mathrm{G1}\rangle$ given by

$$\nu_{relaxation} = 2\left(\frac{B_{1\downarrow-2\downarrow}B_{1\uparrow-2\downarrow}}{B_{1\downarrow-2\downarrow}+B_{1\uparrow-2\downarrow}} + \frac{B_{1\downarrow-2\uparrow}B_{1\uparrow-2\uparrow}}{B_{1\downarrow-2\uparrow}+B_{1\uparrow-2\uparrow}}\right)\frac{1+0.5\exp(-\Delta_{orb}/k_B T)}{\exp(\Delta_{orb}/k_B T)+\exp(-\Delta_{orb}/k_B T)} \tag{4.6}$$

which reduces to the familiar $\exp(-\Delta_{orb}/k_B T)$ when $k_B T \ll \Delta_{orb}$. Here, $B_{1\downarrow-2\downarrow}$ and $B_{1\uparrow-2\uparrow}$ correspond to the Einstein coefficients for spin-conserving transitions, whereas $B_{1\uparrow-2\downarrow}$ and $B_{1\downarrow-2\uparrow}$ correspond to Einstein coefficients for spin-flipping transitions. We rewrite this in terms of the Einstein coefficient for the total transition probability between $|\mathrm{G1}\rangle$ and $|\mathrm{G2}\rangle$ B_{G1-G2}, and factors that represent the proportion of spin-flipping (f) and spin-conserving (c) transitions, such that $f + c = 1$

$$\nu_{relaxation} = 4fcB_{G1-G2}\frac{1+0.5\exp(-\Delta_{orb}/k_B T)}{\exp(\Delta_{orb}/k_B T)+\exp(-\Delta_{orb}/k_B T)} \tag{4.7}$$

Figure 4.13 shows the T_1 temperature dependence of the Mo defect, compared to the contribution of Orbach processes involving $|\mathrm{G2}\rangle$ with different values for the prefactor $4fcB_{G1-G2}$. In our experimental data, we see no signature of exponential increase of the spin-relaxation rate at the relevant temperatures (that is, between 2 and 4 K), leading us to conclude that Orbach processes involving $|\mathrm{G2}\rangle$ do not contribute significantly to T_1. These Orbach processes must happen with a prefactor that is at most $4fcB_{G1-G2} = 50$ Hz.

We conservatively assume that $4fcB_{G1-G2} = 50$ Hz. To obtain the product fc, we use the data and model presented in chapter 3, Sec. 3.10.6 to describe the ratio of the peaks in two-laser spectroscopy experiments. There, the product fc for spin-flipping and spin-conserving transitions between ground and optically-excited state corresponds to the intensity of the Λ line squared, $\sim 0.05^2$ for this configuration of magnetic field. We recognize that the excited state of interest here, $|\mathrm{G2}\rangle$, is different from the excited state of interest in that work, $|E\rangle$. Nonetheless, we expect from our model that taking this value leads to an underestimation of the product fc. Since B_{G1-G2} is inversely proportional to both fc and $T_{2,lim}$, this will lead to an underestimation of the limit of $T_{2,lim}$. Taking $fc = 0.05^2$, yields $B_{G1-G2} \approx 5$ kHz. Based on Eq. 4.5, this corresponds to a limit of $T_{2,lim}$ on the order of miliseconds at 4 K.

References

[1] C. M. Gilardoni, T. Bosma, D. van Hien, F. Hendriks, B. Magnusson, A. Ellison, I. G. Ivanov, N. T. Son, and C. H. van der Wal, “Spin-relaxation times exceeding seconds for color centers with strong spin–orbit coupling in SiC”, New J. of Phys. **22**, 103051 (2020).

[2] J. R. Weber, W. Koehl, J. Varley, A. Janotti, B. Buckley, C. Van de Walle, and D. D. Awschalom, “Quantum computing with defects”, Proc. Natl. Acad. Sci. U.S.A. **107**, 8513 (2010).

[3] D. D. Awschalom, L. C. Bassett, A. S. Dzurak, E. L. Hu, and J. R. Petta, “Quantum spintronics: engineering and manipulating atom-like spins in semiconductors”, Science **339**, 1174 (2013).

[4] I. Aharonovich, D. Englund, and M. Toth, “Solid-state single-photon emitters”, Nat. Photon. **10**, 631 (2016).

[5] M. Atatüre, D. Englund, N. Vamivakas, S.-Y. Lee, and J. Wrachtrup, “Material platforms for spin-based photonic quantum technologies”, Nat. Rev. Mat. **3**, 38 (2018).

[6] W. B. Gao, A. Imamoglu, H. Bernien, and R. Hanson, “Coherent manipulation, measurement and entanglement of individual solid-state spins using optical fields”, Nat. Photonics **9**, 363 (2015).

[7] B. Hensen et al., “Loophole-free bell inequality violation using electron spins separated by 1.3 kilometres”, Nature **526**, 682 (2015).

[8] A. Sipahigil, K. D. Jahnke, L. J. Rogers, T. Teraji, J. Isoya, A. S. Zibrov, F. Jelezko, and M. D. Lukin, “Indistinguishable photons from separated silicon-vacancy centers in diamond”, Phys. Rev. Lett. **113**, 113602 (2014).

[9] P. V. Klimov, A. L. Falk, D. J. Christle, V. V. Dobrovitski, and D. D. Awschalom, “Quantum entanglement at ambient conditions in a macroscopic solid-state spin ensemble”, Sci. Adv. **1**, e1501015 (2015).

[10] B. Magnusson and E. Janzén, “Optical characterization of deep level defects in SiC”, Mater. Sci. For. **483**, 341 (2005).

[11] S. A. Zargaleh et al., “Evidence for near-infrared photoluminescence of nitrogen vacancy centers in 4H-SiC”, Phys. Rev. B **94**, 060102 (2016).

[12] A. Gällström et al., “Optical properties and Zeeman spectroscopy of niobium in silicon carbide”, Phys. Rev. B **92**, 075207 (2015).

[13] W. F. Koehl, B. Diler, S. J. Whiteley, A. Bourassa, N. T. Son, E. Janzén, and D. D. Awschalom, “Resonant optical spectroscopy and coherent control of Cr^{4+} spin ensembles in SiC and GaN”, Phys. Rev. B **95**, 035207 (2017).

[14] T. Bosma et al., "Identification and tunable optical coherent control of transition-metal spins in silicon carbide", npj Quantum Information **4**, 48 (2018).

[15] L. Spindlberger et al., "Optical properties of vanadium in 4H silicon carbide for quantum technology", Phys. Rev. Appl. **12**, 014015 (2019).

[16] A. Csóré and A. Gali, "*Ab initio* determination of pseudospin for paramagnetic defects in SiC", Phys. Rev. B **102**, 241201(R) (2020).

[17] G. Wolfowicz, C. P. Anderson, B. Diler, O. G. Poluektov, F. J. Heremans, and D. D. Awschalom, "Vanadium spin qubits as telecom quantum emitters in silicon carbide", Sci. Adv. **6**, eaaz1192 (2020).

[18] B. Diler, S. J. Whiteley, C. P. Anderson, G. Wolfowicz, M. E. Wesson, E. S. Bielejec, F. J. Heremans, and D. D. Awschalom, "Coherent control and high-fidelity readout of chromium ions in commercial silicon carbide", npj Quantum Information **6**, 11 (2020).

[19] J. Baur, M. Kunzer, and J. Schneider, "Transition metals in SiC polytypes, as studied by magnetic resonance techniques", Phys. Stat. Sol. A **162**, 153 (1997).

[20] B. Kaufmann, A. Dörnen, and F. S. Ham, "Crystal-field model of vanadium in 6H silicon carbide", Phys. Rev. B **55**, 13009 (1997).

[21] A. Abragam and B. Bleaney, *Electron paramagnetic resonance of transition ions*, International series of monographs on physics (Clarendon Press, Oxford, 1970).

[22] Y. Tokura, W. G. van der Wiel, T. Obata, and S. Tarucha, "Coherent single electron spin control in a slanting zeeman field", Phys. Rev. Lett. **96**, 047202 (2006).

[23] F. Beaudoin, D. Lachance-Quirion, W. A. Coish, and M. Pioro-Ladriere, "Coupling a single electron spin to a microwave resonator: controlling transverse and longitudinal couplings", Nanotechnology **27**, 464003 (2016).

[24] T. Kobayashi et al., "Engineering long spin coherence times of spin-orbit qubits in silicon", Nat. Mater. **20**, 38 (2020).

[25] M. A. Khan, M. Erementchouk, J. Hendrickson, and M. N. Leuenberger, "Electronic and optical properties of vacancy defects in single-layer transition metal dichalcogenides", Phys. Rev. B **95**, 245435 (2017).

[26] C. Hepp et al., "Electronic structure of the silicon vacancy color center in diamond", Phys. Rev. Lett. **112**, 036405 (2014).

[27] C. Bradac, W. Gao, J. Forneris, M. E. Trusheim, and I. Aharonovich, "Quantum nanophotonics with group IV defects in diamond", Nat. Commun. **10**, 5625 (2019).

[28] K. Beha, A. Batalov, N. B. Manson, R. Bratschitsch, and A. Leitenstorfer, "Optimum photoluminescence excitation and recharging cycle of single nitrogen-vacancy centers in ultrapure diamond", Phys. Rev. Lett. **109**, 097404 (2012).

[29] G. Wolfowicz, C. P. Anderson, A. L. Yeats, S. J. Whiteley, J. Niklas, O. G. Poluektov, F. J. Heremans, and D. D. Awschalom, "Optical charge state control of spin defects in 4H-SiC", Nat. Commun. **8**, 1876 (2017).

[30] O. V. Zwier, D. O'Shea, A. R. Onur, and C. H. van der Wal, "All–optical coherent population trapping with defect spin ensembles in silicon carbide", Sci. Rep. **5**, 10931 (2015).

[31] K. W. H. Stevens, "The theory of paramagnetic relaxation", Rep. Prog. Phys. **30**, 189 (1967).

[32] A. Kiel and W. B. Mims, "Paramagnetic relaxation measurements on Ce, Nd, and Yb in $CaWO_4$ by an electron spin-echo method", Phys. Rev. **161**, 386 (1967).

[33] K. N. Shrivastava, "Theory of spin–lattice relaxation", Phys. Stat. Sol. B **117**, 437 (1983).

[34] E. A. Harris and K. S. Yngvesson, "Spin-lattice relaxation in some iridium salts i. relaxation of the isolated (IrCl6)2- complex", J. Phys. C **1**, 990 (1968).

[35] M. E. Trusheim et al., "Transform-limited photons from a coherent tin-vacancy spin in diamond", Phys. Rev. Lett. **124**, 023602 (2020).

[36] G. Thiering and A. Gali, "*Ab Initio* magneto-optical spectrum of group-IV vacancy color centers in diamond", Phys. Rev. X **8**, 021063 (2018).

[37] K. D. Jahnke, A. Sipahigil, J. M. Binder, M. W. Doherty, M. Metsch, L. J. Rogers, N. B. Manson, M. D. Lukin, and F. Jelezko, "Electron-phonon processes of the silicon vacancy centre in diamond", New J. of Phys. **17**, 043011 (2015).

[38] A. Gällström et al., "Optical identification and electronic configuration of tungsten in 4H and 6H-SiC", Physica B: Condensed Matter **407**, 1462 (2012).

[39] M. Kunzer, H. D. Müller, and U. Kaufmann, "Magnetic circular dichroism and site-selective optically detected magnetic resonance of the deep amphoteric vanadium impurity in 6H-SiC", Phys. Rev. B **48**, 10846 (1993).

[40] T. Dalibor, G. Pensi, H. Matsunami, T. Kimoto, W. J. Choyke, A. Schöner, and N. Nordell, "Deep defect centers in silicon carbide monitored with deep level transient spectroscopy", Phys. Stat. Sol. A **162**, 199 (1997).

[41] M. S. Dresselhaus, G. Dresselhaus, and A. Jorio, *Group theory, Application to the physics of condensed matter* (Springer-Verlag Berlin Heidelberg, 2008).

chapter 5

Hyperfine-mediated transitions between electronic spin-1/2 levels of transition metal defects in SiC

*Transition metal defects in SiC give rise to localized electronic states that can be optically addressed in the telecom range in an industrially mature semiconductor platform. This has led to intense scrutiny of the spin and optical properties of these defect centers. For spin-*1/2 *defects, a combination of the defect symmetry and the strong spin-orbit coupling may restrict the allowed spin transitions, giving rise to defect spins that are long lived, but hard to address via microwave spin manipulation. Here, we show via analytical and numerical results that the presence of a central nuclear spin can lead to a non-trivial mixing of electronic-spin states, while preserving the defect symmetry. The interplay between a small applied magnetic field and hyperfine coupling opens up magnetic microwave transitions that are forbidden in the absence of hyperfine coupling, enabling efficient manipulation of the electronic spin. We also find that an electric microwave field parallel to the c-axis can be used to manipulate the electronic spin via modulation of the relative strength of the dipolar hyperfine term.*

5.1. Introduction

Solid-state defects and molecular centers with optically addressable spin provide versatile platforms for the implementation of quantum technologies [2–9]. When placed in a crystal lattice, transition metal (TM) defects with active spins show strong analogy to molecular metal-organic centers [10–18]. Their spin properties arise from electrons strongly localized at the d-orbitals of the TM core, subject to the relevant point-group symmetries. The V and Mo defects in hexagonal SiC have been extensively investigated recently, motivated by the fact that their optical transitions are near or at telecom-standard wavelengths, and that SiC is an industrially mature semiconductor platform [14, 19–23]. When these defect centers are

---

Parts of this chapter have been published in New Journal of Physics **23**, 083010 (2021) [1].

in a charge state with one localized d-electron, they are largely analogous to each other, both having ground states with electronic spin-$1/2$ behavior.

Group theory predicts limited possibilities for driving spin transitions in these defect centers at moderate magnetic fields, compatible with the long spin-relaxation observed for Mo defects [19–21]. Nevertheless, experimental results [16, 17, 23, 24] demonstrate efficient electron-spin resonance on V defects with an oscillating magnetic field parallel to the symmetry axis. These results seem inconsistent, and have puzzled the community. Phenomenological interpretations of experiments [23] have considered a role for the central nuclear spin, but these are incompatible with the spatial symmetry of the defect.

Here, we develop a bottom-up analytical and numerical model of a single electron in the d-orbitals of the TM core, and include hyperfine interaction with the central nuclear spin. We focus on the energy levels and transitions between ground-state spin-$1/2$ levels of these defects, and find strong hyperfine-mediated matrix elements for transitions that are forbidden in a description without hyperfine coupling. This sheds light on the experimentally observed magnetic microwave driving. The anisotropic dipolar interaction between magnetic moments of the electron and nucleus leads to mixing between the electron-spin sublevels, which enables efficient electron paramagnetic resonance with oscillating magnetic fields parallel to the symmetry axis of the defect centers. In addition, we find that the mechanism of hyperfine-mediated spin resonance also allows for efficient driving with the electric-field component of microwave fields. An oscillating electric field along the growth axis of the crystal – a technologically relevant geometry with multiple fabrication possibilities [25–29] – also leads to hyperfine-mediated electron-spin transitions. While preserving the original uniaxial symmetry of the defects, these electric fields modulate the spatial distribution of electron density in the ground state, which in turn strongly influences the anisotropic dipolar interaction between nuclear and electronic spins. For specific relevance to V and Mo in SiC, we provide effective-spin Hamiltonians for the ground-state doublets in terms of parameters relating directly to the configuration of the defect centers. In this way, our approach provides an easy way to interpret these fitting parameters in terms of the microscopic configuration of the defect centers, and is complementary to purely group-theoretical methods [30] that yield symmetry-restricted effective-spin Hamiltonians that can be fit to experiments. Additionally, our approach is also complementary to results from *ab initio* calculations of the defects' geometric and electronic structure [20]: here, we include the different parts of the Hamiltonian one by one, and this allows us to determine what is the particular interplay of different interactions that leads to the experimentally observed behavior.

5.1.1. Review of literature and defect configuration

The Mo and V defects in hexagonal SiC that are optically active in the near infrared range are composed of a TM impurity substituting a Si atom in the lattice. Spectroscopic studies show that both ground and optically-excited state manifolds consist of two and three, respectively, sets of Kramers doublets (KD, effective spin-1/2 doublets), as in the right-panel schematic of Fig. 5.1(b) [14, 16, 22–24]. The two KDs in the ground-state manifold show strongly anisotropic interaction with magnetic fields. In particular, for the spin doublet with lowest energy, the spin-1/2 degeneracy is easily broken by a magnetic field parallel to the crystal c-axis (which coincides with the three-fold rotational axis of the defects), but a magnetic field perpendicular to this direction gives rise to a Zeeman splitting that is zero (or close to zero, depending on the particular lattice site occupied by the impurity). These spectral features can in good approximation be explained as a defect center in a Si-substitutional site that, after bonding to the lattice (and ionization in the case of Mo), is left with one unpaired electron spin in the d-orbitals of the TM core. In this case, the strongly anisotropic Zeeman spectrum is a consequence of a combination of the defect three-fold rotational symmetry and spin-orbit coupling [14, 19–21, 24], which gives rise to two ground-state KDs transforming as the Γ_4 and $\Gamma_{5,6}$ irreducible representations of the double group $\bar{C}_{3\mathrm{v}}$, and separated in energy due to spin-orbit coupling. These two doublets are spin-orbit split, such that they are respectively formed by states having orbital angular momentum antiparallel or parallel to the electron spin. As far as symmetry is concerned, a doublet transforming as Γ_4 transforms as states with spin projection along the symmetry axis $m_s = \pm 1/2$. Thus, these states may have contributions from orbitals with zero angular momentum (see also Sec. 5.5.1). In contrast, a doublet transforming as $\Gamma_{5,6}$ transforms as states with $m_s = \pm 3/2$. Thus, all orbitals that make up $\Gamma_{5,6}$ states have orbital angular momentum non-zero.

For KDs transforming as $\Gamma_{5,6}$, interaction with a magnetic field perpendicular to the rotational axis of the defect is strictly symmetry forbidden [19, 21]. Earlier work found it thus plausible that the KD of lowest energy should be the KD that transforms as $\Gamma_{5,6}$, due to the observed $g_\perp$ parameter being 0 [14, 16, 19, 24]. Progressing insight from this and parallel work [20, 30], however, shows that the KD with lowest energy is in fact the Γ_4 KD after all. Here, $g_\perp$ can also be near zero, but this only occurs for a certain parameter range for spin-orbit coupling and crystal-field strengths [21]. Spin doublets transforming as Γ_4 may thus also interact very weakly with magnetic fields perpendicular to the crystal c-axis, giving rise to near-zero Zeeman splittings, smaller than the accuracy of most experimental setups at magnetic fields below 1 T. Thus, the g-parameter alone cannot be used to distinguish between KDs of the two kinds in this magnetic field range. However, the two types of KDs are distinguishable via their hyperfine structure, since the effective-spin Hamiltonians associated with them differ significantly and give qualitatively a different spectrum, as recently observed [23] (see below for more details). This conclusion was obtained in parallel also using a purely group-theory approach [30]. Both V and Mo have naturally abundant isotopes with non-zero nuclear spin. Whereas 25% of stable molybdenum nuclei have spin-5/2 (the remaining isotopes have nuclear spin zero), over 99% of naturally occurring vanadium nuclei have spin-7/2. In this way, measurements on V ensembles at low magnetic fields [23] provide direct access to the defects' hyperfine structure, which allows us to determine that the lowest energy KD of V defects in SiC transforms as Γ_4.

5.2. Methods

We model the spin properties of the system by considering a single electron in the d-orbitals of the TM core. The d-orbitals of the TM core on itself are isolated in energy from other orbital states due to the Coulomb interaction with the nucleus, and are five-fold degenerate in the presence of spherical symmetry. Via a Hamiltonian of the type

$$H = H_{\text{crystal}} + H_{\text{SOC}} + H_{\text{HF}} + H_{\text{Zee}} \tag{5.1}$$

we consider the crystal-field potential arising from interaction with the lattice, spin-orbit coupling, hyperfine interaction with the central nuclear spin and Zeeman interaction with an external magnetic field, respectively, acting on these states.

We note that the full description of the electronic wavefunctions must be obtained from first-principles calculations that take hybridization with nearby atomic orbitals and the core orbitals of the TM core into account [20]. However, modeling the ground-state KDs as an electron localized in the d-orbitals of the TM provides a good approximation [14, 19, 20, 22, 24]. The approach of our work thereby encompasses and provides intuition into the relevant physical processes at play at low computational cost. Additionally, since we include the contributions to the Hamiltonian one by one, our approach also provides insight into how the combination of different interactions (crystal field, SOC, Zeeman and hyperfine) leads to non-trivial eigenstates. When considering the optically-excited states, the contribution from bonding with lattice states is more significant [20, 22], and the validity of our model for these KDs is limited. For this reason, we focus our analysis on the ground-state properties of these defect centers.

5.2.1. Crystal field potential

A TM impurity in a Si-substitutional site is surrounded by carbon atoms arranged in a tetrahedral configuration around it, such that the strongest contribution to the

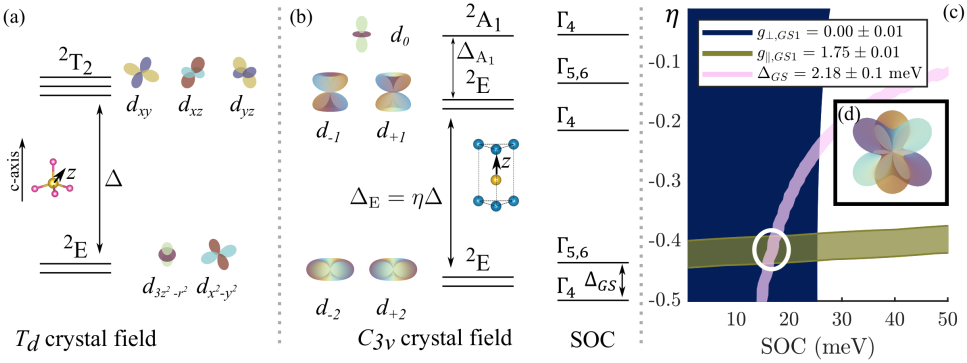

Figure 5.1: (a) Transition metal (TM) defects in hexagonal SiC in a substitutional site are composed of a central TM impurity (yellow in the inset) surrounded by nearest neighbors lattice atoms (pink in the inset) distributed in a tetrahedral configuration. This symmetry splits the five-fold degenerate d-orbitals of the transition metal core into a ground state orbital doublet and an excited state orbital triplet, separated by an energy Δ. These orbitals are most intuitively expressed in terms of cubic harmonic functions, where the z-axis points between two of the tetrahedral bonds. (b) The second-nearest neighbors and third-nearest neighbors are distributed in a trigonal prismatic configuration, which splits the excited state triplet into a doublet and a singlet, and rotates the natural basis associated with the crystal field. The trigonal-prismatic contribution to the crystal field is most intuitively expressed in the basis of spherical harmonics with a z-axis along the three-fold rotational axis. This three-fold rotational axis coincides with the crystal c-axis. Spin-orbit interaction further splits both doublets into two Kramers doublets, each transforming as the irreps Γ_4 and $\Gamma_{5,6}$ of the double group $\bar{C}_{3\text{v}}$. (c) We model the TM defect in SiC by considering the contributions of both a tetrahedral crystal field and a trigonal crystal field, with relative strengths provided by the parameter η. By varying both η and the strength of spin-orbit coupling, we can extract ranges where the model agrees with the experimentally measured energy splittings in the ground state (colored areas in the plot). (d) At the region where the model provides reliable spin-orbit and Zeeman energy splittings for the ground state KD (where all three shaded areas overlap, circled), the electronic wavefunctions of both ground state Kramers doublets have the electron density concentrated slightly above or below the transition metal ion. In the graphical representation of the wavefunctions, the color corresponds to a phase according to the scale bar in Fig. 5.2(b).

crystal field has tetrahedral symmetry (T_d). This crystal potential splits the five-fold degenerate d-orbitals into a ground state orbital doublet (^{2}E) and an excited state orbital triplet (^{2}T$_2$), separated by an energy splitting Δ, and with natural quantization along the high symmetry axis $\hat{z}$ pointing between two of the tetrahedral bonds (Fig. 5.1(a)). In hexagonal polytypes of SiC, the second and third nearest neighbors of the TM impurity are arranged in a trigonal configuration. On their own, these lattice atoms give rise to a crystal field with $C_{3\text{v}}$ symmetry that splits the d-orbitals into 2 orbital doublets (^{2}E) separated by an energy Δ_E and an orbital singlet (^{2}A$_1$) separated from the top doublet by an energy Δ_{A_1}. In this case, the eigenstates are given by linear combinations of the spherical harmonics with $l = 2$, with $\hat{z}$ pointing along the three-fold rotational axis (see Fig. 5.1(b)). Although the trigonal crystal field arises from the second and third nearest neighbors of the TM impurity, experimental results show that it is of significant importance for determining the spectral properties of the defect spin [20, 24]. For this reason, we do not include it as a perturbation, but rather diagonalize the full crystal field Hamiltonian with both trigonal and tetrahedral contributions. We parameterize the energy term Δ_E arising from the trigonal crystal field in terms of the energy term Δ arising from the tetrahedral crystal field, such that $\Delta_\mathrm{E} = \eta\Delta$ (Fig. 5.1), where η provides the relative strength between the trigonal and tetrahedral crystal field contributions. We can include the effect of electric fields or strain parallel to the three-fold rotational symmetry by considering deformations that preserve trigonal symmetry via small changes of η.

5.2.2. Spin-orbit coupling

We include the effect of spin-orbit coupling (in the same manner as Tissot *et al.*, [21]) via a Hamiltonian of the type

$$H_\mathrm{SOC} = \lambda k \mathbf{L} \cdot \mathbf{S} \tag{5.2}$$

where λ is the reduced matrix element indicating the strength of the spin-orbit interaction, $\mathbf{L}$ is the orbital angular momentum operator, which acts on the spatial part of the wavefunction, and $\mathbf{S}$ is the spin operator acting directly on the electron spin. The parameter k accounts for an empirical reduction of the orbital angular momentum of the electronic states due to bonding to nearby atoms or dynamic Jahn-Teller effects, for example.

In first-order, this spin-orbit coupling Hamiltonian gives rise to an additional splitting between the orbital doublets defined by the crystal field. Within the ground state space, two Kramers doublets arise, transforming as Γ_4 and $\Gamma_{5,6}$ respectively, and separated by an energy Δ_{GS} (see Fig. 5.1(b)) [14, 16, 19, 21]. Such a KD is an *effective* spin-1/2 system. Its overall spin properties depend on both the intrinsic spin of the electron and its orbital angular momentum [20].

5.2.3. Hyperfine interaction

We include the interaction with a central nuclear spin via a Hamiltonian of the type

$$H_\mathrm{HF} = A\left(k\mathbf{L}\cdot\mathbf{I} + 3\frac{(\mathbf{S}\cdot\vec{r})(\mathbf{I}\cdot\vec{r})}{r^2} - \mathbf{S}\cdot\mathbf{I}\right) \tag{5.3}$$

where $\vec{r}$ is the vector from nucleus to electron, and $\mathbf{I}$ is the nuclear spin operator. We define the term $A \equiv \frac{\mu_0}{4\pi}\frac{g_e\mu_B g_n\mu_N}{h^2}\frac{1}{r^3}$, where μ_0 is the vacuum permeability, g_e (g_n) is the electronic (nuclear) g-parameter, μ_B (μ_N) is the electron (nuclear) magnetic moment and h is Planck's constant. This Hamiltonian includes the classical dipolar interaction between the magnetic moments of the nucleus and electron, as well as the effective magnetic field at the nucleus due to the orbital angular momentum of the electron. We do not include the electric quadrupolar interaction since, to first order, it does not lead to mixing between two states belonging to a KD [31].

Here, we do not take into account the Fermi contact interaction between nuclear and electron spins. In an approach focused solely on the d-orbitals of the TM core, this term is zero due to the vanishing electron density at the nucleus associated with these orbital states. In a more general approach, this approximation is not valid since contributions from bonding with neighboring atoms, and exchange interaction with core s-orbitals of the TM will lead to a non-zero electron density at the nucleus. Exchange contributions from s orbitals are symmetry forbidden for a $\Gamma_{5,6}$ doublet, but may arise for a doublet transforming as Γ_4. This approximation does not, however, change the main conclusions of this work. When presenting our results, we will address the consequences of this approximation in more detail.

In our numerical calculations, we always consider a nuclear spin-5/2. We do this for simplicity and lean presentation in figures, since it reduces the number of electron-nucleus coupled states to consider, while it does not qualitatively change the results obtained. Note that the relevant isotopes for Mo and V defects have nuclear spins 5/2 and 7/2, respectively.

Finally, we note that the electronic spin can also interact with nuclear spins of neighboring lattice Si or C atoms. However, within an ensemble of TM impurities, only a fraction of the defects have a neighboring non-zero nuclear spin. Additionally, defects with different nuclear spin environments are spectrally resolvable [23], and SiC can be fabricated with high isotopic purity, such that one can in principle choose to experimentally address defects with only spin-zero neighboring nuclear spins.

5.2.4. Zeeman interaction

The Zeeman Hamiltonian acts on the spin-orbit coupled states via a Hamiltonian of the type

$$H_{\text{Zee}} = -\frac{\mu_B}{h}\mathbf{B}\cdot(k\mathbf{L} + g_e\mathbf{S}) - \frac{g_n\mu_N}{h}\mathbf{B}\cdot\mathbf{I} \tag{5.4}$$

where $\mathbf{B}$ is the applied magnetic field with components B_x, B_y and B_z, and magnitude B.

At small magnetic fields (such that $B\mu_B/h \ll \lambda k$) this Hamiltonian takes the shape of an effective-spin Hamiltonian for each Kramers doublet of the kind

$$H_{\text{Zee}} = -\frac{\mu_B}{h}\left(g_\parallel B_z\cdot\tilde{S}_z + g_\perp(B_x\cdot\tilde{S}_x + B_y\cdot\tilde{S}_y)\right) - \frac{g_n\mu_N}{h}\mathbf{B}\cdot\mathbf{I} \tag{5.5}$$

where $\tilde{\mathbf{S}}$ is the effective spin-1/2 operator.

5.2.5. Numerical and analytical methods

Below, we present both numerical and analytical results based on the model presented so far. On the one hand, we numerically obtain the matrix elements for various time-dependent perturbations arising from the interaction of the defects' electric and magnetic dipole moments with oscillating electric and magnetic fields. We achieve this by calculating these perturbations in terms of the basis states defined by the static Hamiltonian of Eq. (5.1). On the other hand, we obtain the analytical effective-spin Hamiltonians associated with each KD by investigating the effect of the hyperfine and Zeeman interactions on each KD independently. The basis states for each KD are obtained by diagonalizing the crystal-field Hamiltonian (see Sec. 5.5.1). We include SOC to zeroth-order, that is, we consider how it breaks the degeneracy between the two ground-state KDs, but disregard how it mixes ground and optically-excited manifolds.

5.3. Results

5.3.1. Parameters consistent with experiment

In the model presented so far, based on Eq. (5.1), there are several free-parameters (Δ, η, Δ_{A_1}, k and λ) which must be obtained either from first-principles calculations or from comparison with experimental results. We choose to take the latter approach to restrict the parameter space where our model effectively describes the ground states of Mo and V defects. We focus on V defects at the site associated with the α line in 4H-SiC [22, 32], since these are the defect centers most similar to Mo defects, which have promising features for quantum applications such as long spin-relaxation times in the ground-state [19]. Additionally, the experimental parameters for this particular defect are well established, with reproducible measurements from various groups being present in literature [17, 23]. A similar analysis for other V configurations can be found in Sec. 5.5.5.

The parameters Δ and Δ_{A_1} are only relevant to determine the energy difference between ground and optically-excited states, and the first-order correction to the electronic wavefunctions due to spin-orbit coupling. For this reason, we fix Δ at 1 eV, the order of magnitude of the optical energy splitting. We choose Δ_{A_1} to be on the order of 10 meV, but this choice has no consequence for the results obtained in the following. In contrast, the parameters η, k and λ have significant implications for the ground-state properties of these defect centers. In order to determine these parameters, we compare the energy eigenstates obtained from diagonalization of the Hamiltonian in Eq. (5.1) (without hyperfine coupling) with the experimental parameters reported in Ref. [23] for the splitting between the two ground-state KDs (Δ_{GS}) and the Zeeman splitting of the lowest KD (determined by $g_\parallel$ and $g_\perp$).

We consider a static magnetic field $B_0 = 100$ mT. We do this by finding regions where combinations k, η and λ give ground-state energy splittings that coincide with experiments within the experimental accuracy.

This agreement exists for k values between 0.18 and 0.37, and is shown graphically for $k = 0.3$ in Fig. 5.1(c). An *ab-initio* approach that takes into account hybridization with orbitals other than the d orbitals as well as dynamic Jahn-Teller effects gives an orbital reduction factor between 0.3 and 0.4 [20]. We find that using other values for k from this range does not alter our general conclusions, and only leads to small shifts in the relevant numerical estimates for the hyperfine coupling parameters (see Sec. 5.5.2). Lower k values require increasing $|\eta|$ to match experimental results, whereas the spin-orbit coupling parameter λ remains nearly constant (see Sec. 5.5.2 for analogous plots for other values of k). At $k = 0.3$, $\eta \approx -0.4$ and $\lambda \approx 15$ meV constitute the parameter range that reliably reproduces the experimental properties of the ground-state electronic spin of this defect. From here on in the text, we assume these parameters, and use these to generate the results presented in Fig. 5.2 and Fig. 5.3.

We note that the negative sign of η depends on the convention taken for the energy splitting Δ_E. A negative η implies that the trigonal crystal field causes the orbitals $d_{\pm 1}$ to have the lowest energy (see also Fig. 5.1(b)), possibly due to bonding or to the spatial distribution of electrons from the neighboring atoms [22, 33]. This configuration leads to a ground-state Kramers doublet that transforms as the Γ_4 irreducible representation of the double group $\bar{C}_{3\text{v}}$. The analytical effective-spin Hamiltonians obtained in parallel by us in Sec. 5.3.4 and by Tissot *et al.* in [30] for a doublet transforming as Γ_4 are in agreement with the experimental spectra of these V centers [23].

Fig. 5.1(d) presents for these values of k, λ and η the approximate electronic wavefunction of the ground state KD (and shows reasonable agreement with the wavefunction from reference [20]). In this graphical representation of the wavefunction in cartesian space, the azimuthal phase of the wavefunction at a certain point in space corresponds to its color according to the scale bar in Fig. 5.2(c). The wavefunction clearly has a winding azimuthal phase, corresponding to a non-zero orbital angular momentum parallel to the three-fold rotational axis. In this configuration, both ground state KDs have $g_\perp$ that would be measured as effectively 0 at low static magnetic fields (below 1 T). In contrast, a magnetic field parallel to the crystal c-axis breaks the degeneracy of the KDs, giving rise to eigenstates where the effective electronic spin points parallel or antiparallel to the magnetic field. From here on, we denote these eigenstates as $|\Gamma_i \uparrow\downarrow\rangle$, where Γ_i corresponds to the symmetry of the KD, and the arrows indicate the effective-spin direction.

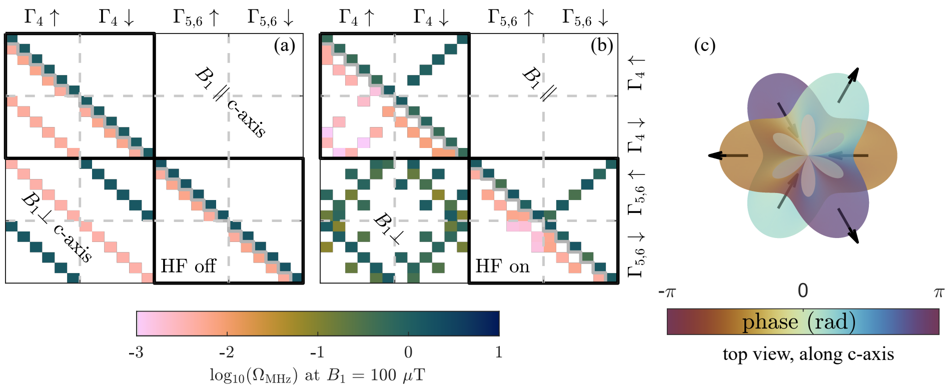

Figure 5.2: (a) Matrix elements due to an oscillating magnetic field parallel (diagonal and upper triangular elements) or perpendicular (lower triangular elements) to the c-axis, in the basis defined by the crystal field, spin-orbit coupling and a small magnetic field (20mT) along the c-axis, for the two ground state Kramers doublets ($|\Gamma_4, \uparrow\downarrow\rangle$ and $|\Gamma_{5,6}, \uparrow\downarrow\rangle$), without hyperfine coupling. White matrix elements correspond to zero. Within each KD (contoured block diagonal parts of the full matrix), a magnetic field parallel to the c-axis does not lead to magnetic microwave transitions, consistent with a picture where the electronic spin is fully quantized along the static magnetic field direction. A magnetic field perpendicular to the c-axis leads to very weak electron and nuclear spin transitions in the Γ_4 doublet, and only nuclear spin transitions in the $\Gamma_{5,6}$ doublet. (b) Same as (a), but with the hyperfine interaction between electron and the central nuclear spin added to the static Hamiltonian. In this case, the electronic spin can flip via magnetic microwave transitions driven by an oscillating field parallel to the c-axis. (c) Top view of the wavefunction presented in Fig. 5.1(d). The arrows indicate the direction of the dipolar field caused by the central nuclear spin at the points of high electron density. For this particular electron distribution, the dipolar part of the hyperfine interaction favors a perpendicular orientation of the spins, such that the eigenstates are superpositions of up and down effective-electronic spin.

5.3.2. Interaction with oscillating magnetic fields

In order to determine which spin transitions can be driven by oscillating magnetic fields, we numerically investigate the matrix elements of the Zeeman operator between the effective-spin eigenstates associated with a Hamiltonian including the crystal-field potential, spin-orbit coupling and the interaction with a static magnetic field ($B_0 = 20$ mT) parallel to the c-axis (Fig. 5.2(a,b)). We focus on the two ground-state KDs, such that the basis used in the matrix representation corresponds to the 24 lowest eigenstates associated with the two effective-spin-1/2 doublets, coupled to a nucleus with spin-5/2. We investigate the matrix elements arising from the interaction with an oscillating magnetic field parallel (diagonal elements, and upper-triangular elements) and perpendicular (lower-triangular elements) to the static magnetic field and the symmetry axis of the defect. Additionally, in Fig. 5.2(b) we include hyperfine interaction to the static Hamiltonian.

When hyperfine coupling between the electron and nuclear spin is not present, the $\Gamma_{5,6}$ doublet (bottom right block diagonal) is fully protected from effective-spin transitions due to oscillating magnetic fields (Fig. 5.2(a)). This is characterized by the absence of off-diagonal elements between states $|\Gamma_{5,6} \uparrow\rangle$ and $|\Gamma_{5,6} \downarrow\rangle$ when considering magnetic fields in either direction. Magnetic fields perpendicular to the defect symmetry axis may lead to nuclear-resonance transitions, as well as transitions between the $\Gamma_{5,6}$ and Γ_4 doublets. However, driving these latter transitions requires oscillating fiels in the sub-THz range. In contrast, within the Γ_4 doublet, a magnetic field perpendicular to the symmetry axis of the defect center gives rise to matrix elements between the $|\Gamma_4 \uparrow\rangle$ and $|\Gamma_4 \downarrow\rangle$ due to the small but non-vanishing $g_\perp$. These resonances, however, have very small Rabi frequencies due to the very weak interaction with magnetic fields in the plane. For an oscillating magnetic field with magnitude $B_1 = 100\ \mu$T, we expect a Rabi frequency on the order of 1 kHz.

When we include the hyperfine interaction with the central nucleus in the static Hamiltonian that determines the basis states for representation of the Zeeman perturbations, the matrix representation of the Zeeman operators shows significant changes (Fig. 5.2(b)). Most notably, off-diagonal matrix elements appear for interaction with oscillating magnetic fields parallel to the symmetry axis of the defect (and the static magnetic field), for both ground-state effective-spin doublets. This indicates that the hyperfine coupling leads to mixing between the two effective-electronic-spin eigenstates $|\Gamma_i \uparrow\rangle$ and $|\Gamma_i \downarrow\rangle$. An oscillating magnetic field parallel to the symmetry axis of the defect modulates the amount of mixing, and this leads to efficient effective-spin transitions. This hyperfine-induced mixing arises from the anisotropic hyperfine interaction.

In our model, the main contribution to this anisotropic interaction is the dipolar coupling between nuclear and electronic magnetic-dipole moments. Figs. 5.1(d) and 5.2(c) show the spatial configuration of the ground-state electronic wavefunction. We indicate with arrows the direction of the dipolar field at the points of high electron density due to a magnetic moment at the origin and parallel to the symmetry axis of the defect center. Due to the particular spatial distribution of the electronic wavefunction around the nucleus, this dipolar field tends to align the electronic and nuclear magnetic moments perpendicular to each other. A magnetic field along the symmetry axis of the defect, however, favors the alignment of both magnetic moments along its direction. These two effects compete, leading to a strong dependency of the eigenstate composition on the magnitude of the static mangetic field when the hyperfine and electronic-Zeeman energies are comparable (Fig. 5.3(a)). Thus, the influence of hyperfine is strongly dependent on the magnitude of the static magnetic field, and is most relevant for magnetic fields below 100 mT. Figure 5.3 presents this for the Γ_4 KD, which is lowest in energy. As a consequence, the Rabi frequencies for resonant driving with oscillating magnetic fields along the crystal c-axis decrease significantly as the magnitude of the static field in-

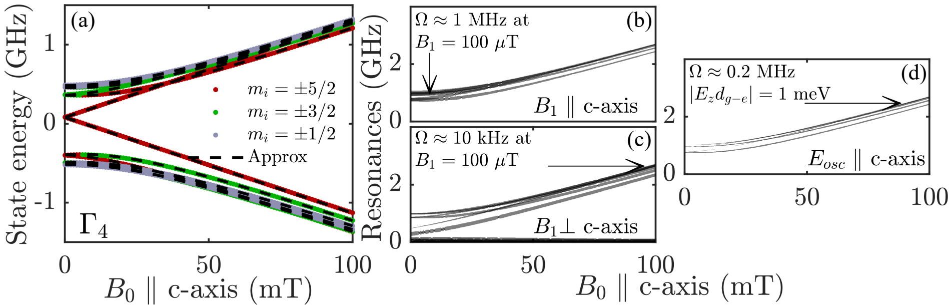

Figure 5.3: (a) Energies of the 12 eigenstates corresponding to the Γ_4 ground-state electronic-spin doublet, hyperfine-coupled to a central nucleus with a spin-5/2, as a function of the static magnetic field B_0 applied parallel to the c-axis. Results were obtained numerically (colored lines), and by diagonalizing the effective-spin Hamiltonian associated with a Γ_4 doublet (dashed line). (b-d) Microwave resonance lines obtained numerically for an oscillating magnetic field parallel (b) or perpendicular (c) to the c-axis, or an oscillating electric field parallel (d) to the c-axis. The thickness of the resonance lines correspond to their Rabi frequencies, with different scales in each figure. Scales are provided by the labels and arrows, indicating the Rabi frequency at a certain point. (b) If the static field is small (Zeeman splitting comparable to hyperfine coupling strength), a small oscillating magnetic field ($B_1 \approx 100\ \mu$T) parallel to the c-axis leads to very efficient electronic-spin transitions with Rabi frequencies on the order of 1 MHz. These resonances weaken significantly as the static magnetic field increases. (c) In a Γ_4 doublet, direct interaction with an oscillating field perpendicular to the c-axis leads to electronic microwave transitions with Rabi frequencies that are largely independent of the applied static field, but small due to the reduced $g_\perp$. (d) A large enough electric field parallel to the c-axis mixes ground and optically-excited states and deforms the electron density, modulating the influence of the anisotropic dipolar hyperfine coupling and leading to electronic-spin transitions.

creases. At low static magnetic fields (20 mT), Rabi frequencies as high as 1 MHz can be obtained for oscillating fields of $B_1 = 100\ \mu$T. At a static magnetic field of 100 mT, this value decreases by an order of magnitude (Fig. 5.3(b)). In contrast, when the oscillating field is perpendicular to the crystal c-axis and the static magnetic field, effective spin-transitions within the Γ_4 doublet arise from the non-zero $g_\perp$, and are very small but largely independent from the magnitude of the static magnetic field (Fig. 5.3(c)).

5.3.3. Interaction with oscillating electric fields

We now turn to considering whether the electric component of a resonant microwave field can also drive spin transitions within the ground-state KD. One way to consider the interaction of the ground-state KDs with oscillating electric fields is to investigate the matrix representation of the Hamiltonian

$$H_{\text{el}} = -e\vec{E} \cdot \vec{r} \tag{5.6}$$

where e is the electron charge and $\vec{E}$ is the electric-field vector, and H_{el} is obtained in the dipolar approximation. However, when we only consider the d-orbitals of the TM, this operator has all-zero matrix elements due to the spatial parity of these orbitals. Nonetheless, we know that the defect center does not have inversion symmetry, such that dipolar interactions with electric fields are in principle symmetry-allowed and will likely arise due to mixing with other orbital states (p-orbitals, for example). Additionally, the defect shows bright optical transitions between ground and optically-excited states, such that the matrix elements of the electric dipole moment between these states must be non-zero. To remedy this discrepancy we include the interaction with electric fields parallel to the symmetry axis of the crystal by considering an extra contribution to the crystal-field potential via a change of the parameter η.

Hence, we model an electric field in this direction as an additional contribution to the crystal field that alters the relative strengths between the original tetrahedral (Fig. 5.1(a)) and trigonal fields (figura 5.1(b)). Although an interaction of this type does not change the symmetry of the eigenstates, it does lead to mixing between ground and optically-excited states. In turn, this changes the spatial distribution of the electron density. Figures 5.1(d) and 5.2(c) show that the hyperfine interaction depends strongly on the spatial configuration of the electronic wavefunctions. Thus, an electric field along this direction modulates the relative strength of the isotropic and anisotropic components of the hyperfine interaction via modulating the spatial configuration of the electronic wavefunction. Overall, this causes that an electric field drives effective-spin transitions within the ground-state KDs (Fig. 5.3(c)). Notably, this effect only arises if hyperfine coupling is present. In its absence, effective-spin transitions are protected by Kramers theorem, even upon modulations of η.

Since these transitions arise from mixing between the ground and optically-excited states, the Rabi frequencies associated with this effect depend linearly on the ratio between the additional $C_{3\mathrm{v}}$ contribution to the crystal field and the original splitting between ground and optically-excited state (approximately Δ). Numerically, we estimate that a trigonal contribution of approximately 1 meV will give rise to Rabi frequencies of hundreds of kHz (Fig. 5.3(d) and Sec. 5.5.4). In order to estimate the magnitude of the electric fields necessary to drive the spin transitions at these rates, we need to have a reliable estimate for the relevant transition dipole moment $d_{g-e} = -e\,\langle\Gamma_i^g|z|\Gamma_i^e\rangle$, where $\Gamma_i^{g,e}$ correspond to the Γ_i eigenstates in ground and optically-excited states, respectively. This can be determined experimentally or via first-principles calculations. Given that the TM defects have radiative lifetimes on the order of 100 ns [22, 23], a conservative estimate for the transition dipole moment gives a magnitude of about $d_{g-e} \approx 1$ D $\approx 0.2\ e$Å. For this value, an oscillating electric field with magnitude $E_z = 50$ V/μm will drive effective-spin transitions at sub-MHz rates.

5.3.4. Effective-spin Hamiltonians

We can obtain analytical effective-spin Hamiltonians for the two ground state KDs based on the model presented so far. These expressions can be fit to experiments, directly connecting the theory developed here to experimental observations. In order to do this, we diagonalize the crystal-field Hamiltonian including both the tetrahedral and trigonal contributions, and focus on the two lowest Kramers doublets. (This is done explicitly in Sec. 5.5.6.) We include spin-orbit coupling in zeroth order – that is, we consider the energy splitting between the two KDs, but disregard the mixing between ground and optically-excited states caused by SOC. Finally, we investigate the effect of the hyperfine and Zeeman operators within each KD. We obtain effective-spin Hamiltonians of the type

$$H_{\Gamma_4} = H_{\mathrm{HF}}^{eff} + H_{\mathrm{Zee,el}}^{eff} + H_{\mathrm{Zee,nuc}}^{eff} \tag{5.7}$$

$$H_{\mathrm{HF}}^{eff} = a_{\parallel,\Gamma_4}\tilde{S}_z I_z + a_{\perp,\Gamma_4}(\tilde{S}_+ I_+ + \tilde{S}_- I_-) \tag{5.8}$$

$$H_{\mathrm{Zee,el}}^{eff} = -\mu_B\left(g_{\parallel,\Gamma_4} B_z \tilde{S}_z + g_{\perp,\Gamma_4}(B_x\tilde{S}_x + B_y\tilde{S}_y)\right) \tag{5.9}$$

$$H_{\mathrm{Zee,nuc}}^{eff} = -\mu_N g_n\left(B_z I_z + B_x I_x + B_y I_y\right) \tag{5.10}$$

$$H_{\Gamma_{5,6}} = H_{\mathrm{HF}}^{eff} + H_{\mathrm{Zee,el}}^{eff} + H_{\mathrm{Zee,nuc}}^{eff} \tag{5.11}$$

$$H_{\mathrm{HF}}^{eff} = (a_{\parallel,\Gamma_{5,6}}\tilde{S}_z + a_{\perp,\Gamma_{5,6}}\tilde{S}_y)I_z \tag{5.12}$$

$$H_{\mathrm{Zee,el}}^{eff} = -\mu_B g_{\parallel,\Gamma_{5,6}} B_z \tilde{S}_z \tag{5.13}$$

$$H_{\mathrm{Zee,nuc}}^{eff} = -\mu_N g_n\left(B_z I_z + B_x I_x + B_y I_y\right) \tag{5.14}$$

The approximate dependency of the parameters $a_{\parallel,\perp}$, $g_{\parallel,\perp}$ on the parameters describing the microscopic configuration of the system, k, η and Δ, is given in Sec. 5.5.6. The approximate energy levels obtained from these effective-spin Hamiltonians for the lowest-energy KD are plotted in Fig. 5.3(a), dashed lines, and overlap well with the numerical results.

These effective-spin Hamiltonians are different for KDs with different symmetries, and give rise to spectra that are clearly distinguishable (see Sec. 5.5.3 for the energies and magnetic resonance spectra of a KD transforming as $\Gamma_{5,6}$). Notably, microwave resonance spectra of Γ_4 doublets due to interaction with oscillating magnetic fields perpendicular to the crystal c-axis shows evidence of a pair of hyperfine sublevels whose energy depends linearly on the applied static magnetic field (Fig. 5.3(a,c)). This is absent for $\Gamma_{5,6}$ doublets (Sec. 5.5.3). Thus, hyperfine resolved magnetic resonance spectra of these defects' ground-state KDs can be used to determine their symmetry properties. As mentioned before, comparison with experiments shows that the lowest-energy KD of V defects in SiC transforms as Γ_4. For the configuration considered here, we find for this doublet $a_{\parallel} \approx -63$ MHz, and $a_{\perp} \approx 332$ MHz. When compared to the experimentally measured values, our model overestimates $|a_{\perp}|$ and underestimates $|a_{\parallel}|$ [30]. This could be explained by the fact that in our model we overlook the hyperfine Fermi-contact interaction and contributions from s-orbitals to the wavefunctions, which is in principle allowed for states transforming as Γ_4. The latter gives rise to an isotropic contribution with $a_{\parallel} \approx a_{\perp}$. This could be confirmed by first-principle calculations, for example.

5.4. Discussion and conclusion

The results of the previous section show that the apparent discrepancy between the symmetry protection of the TM spin-1/2 states (with respect to electronic-spin transitions) and the observed magnetic resonance results on V defects can be fully resolved by considering the interaction with a central nuclear spin. Our model, focused on an electron localized in the d-orbitals of the TM core, encompasses this behavior and shines light on the underlying physical mechanisms. For defects with a central nuclear spin, the hyperfine Hamiltonian is a combination of isotropic and anisotropic terms. Whereas the former favors parallel alignment of nuclear spin and electronic effective spins, the latter favors perpendicular alignment between them. A combination of both leads to mixing between the electronic-spin sublevels. Periodic modulation of the degree of this mixing by microwaves enables transitions, when the oscillating electric and magnetic fields are parallel to the symmetry axis of the defect. This anisotropic hyperfine interaction arises mostly from the classical dipolar coupling between the magnetic moments of the nucleus and electron, which is strongly dependent on the spatial configuration of the wavefunction. This dependency also means that the strength of the hyperfine coupling – and consequently also the electronic-spin eigenstates – is sensitive to local electric and magnetic inhomogeneities. This additional hyperfine-induced mixing of electronic spins may increase the rate of direct spin flips due to interactions with lattice phonons or with neighboring paramagnetic impurities, possibly limiting the spin relaxation at low magnetic fields.

This conclusion is still consistent with the seconds-long spin-relaxation times measured for an ensemble of Mo defects [19] at temperatures where direct spin-flips dominate the spin-relaxation processes. In this case, the most abundant Mo isotopes (~75%) have zero nuclear spin, such that hyperfine coupling does not play a role for the majority of the ensemble. Additionally, direct spin flips are not the limiting process leading to spin relaxation at low temperatures for these defects, such that these hyperfine-mediated spin flips are still likely to be slower than the seconds-long spin-relaxation times. For V ensembles, where all of the naturally occurring isotopes have a non-zero nuclear spin, hyperfine coupling to the central nucleus is always relevant. On the one hand, this coupling enables efficient microwave control of the electronic spin, which can subsequently be read out optically. On the other hand, these hyperfine-enabled electronic-spin transitions due to oscillating magnetic and electric fields may enhance the defect sensitivity to neighboring spins and lattice phonons, respectively. This may play a role on determining the spin-relaxation times of these defect centers at low magnetic fields [31], at temperatures where direct spin-flips dominate the spin relaxation processes. For this reason, a full characterization of the spin-relaxation time of V defects at low magnetic fields and temperatures remains relevant to determine whether there is indeed a trade-off between efficient spin control and slow spin relaxation. This will allow to identify optimal ranges or protocols for operation of these defect centers as optically active spin-qubits, where the defect centers are still addressable but robust against environment-mediated spin-relaxation.

For quantum operation, not only spin-relaxation times, but also spin-coherence times have significant implications. Our results indicate that the presence of hyperfine coupling may be responsible for extending the latter. The competing behavior of the hyperfine and the Zeeman interactions gives rise to energy eigenstates with anticrossing points. For the particular defect configuration and KD depicted in Fig. 5.3(a), these anticrossing points happen at zero magnetic field, and thus provide clock transitions at these points [12, 34, 35]. There, the energy levels are not dependent (to first order) on small variations of the magnetic field. This leads to a suppression of decoherence and dephasing processes related to spectral diffusion, which results in prolonged coherence times for the quantum states. For defects in SiC, these processes are already partly reduced at finite magnetic fields (when compared to silicon or diamond, for example) since the lattice contains two different types of nuclear spins, and flip-flop processes between lattice nuclei are rare [36, 37]. Nonetheless, the small dependence of the energy eigenlevels on the magnetic field magnitude means that, in this configuration, the defects are even less sensitive to the existing flip-flop events between lattice nuclei. In samples with high defect concentration, where individual defect centers feel each other, this decoherence protection is expected to be most relevant, leading to increased coherence close to these anticrossing configurations.

The coupling between the optically addressable electron spin and the potentially long-lived nuclear spin provides a key ingredient for advanced quantum communication and computation architectures [8, 38, 39]. In the ground-state eigenstates, electronic and nuclear spins are fully entangled [30]. At low magnetic fields and for the Γ_4 doublets, the eigenstates correspond to superpositions of nuclear spin states, which may impact the nuclear spin coherence lifetime. The detailed understanding of the coupling to external fields developed herein calls for experimental studies of the coherence properties, and the development of bespoke decoupling methods to protect the quantum states. Conversely, these characteristics offer a wealth of opportunities for the development of control methods which leverage the large Hilbert space within the electron-nuclear spin manifold: the possibility of driving spin transitions with oscillating electric fields along the symmetry axis of the defect centers is technologically relevant, and may enable very efficient device architectures [25–28]. Oscillating electric fields along this direction can be applied with high amplitudes and in a very homogeneous manner in devices with parallel plate capacitors, or in monolithic p-i-n junctions with defects embedded in the intrinsic layer. Additionally, these results also indicate that strain modulation can be used for electronic-spin control, enabling hybrid architectures where these defect centers are entangled with mechanical oscillation modes [40].

Acknowledgments

We thank J. Hendriks, T. Bosma, and A. Gali for discussions. We thank B. Tissot and G. Burkard for providing a preliminary version of their related manuscript. Financial support was provided by the Zernike Institute BIS program, and the EU H2020 project QuanTELCO (862721).

Author contributions

The project was initiated by CMG and CHvdW. II and FH contributed with theory and simulation work. MT contributed via discussions. CMG and CHvdW had the lead in writing the paper. All authors contributed via discussions, and read and commented on the manuscript.

5.5. Appendices

5.5.1. Matrix representation of crystal-field Hamiltonian

A TM defect with one active spin in the d-orbitals of the TM core corresponds to an electron with spin $s = 1/2$ and orbital angular momentum $l = 2$ (from the d-orbitals). Spatially, these states are affected by the combination of the cubic and trigonal crystal fields. If we disregard the effect of bonding and assume that these states are well-isolated from other core orbitals of the TM impurity due to the Coulomb interaction with the nucleus, the basis states for the d orbitals form a complete basis set to describe the electronic wavefunction.

In free space, the 5 spherical harmonics Y_2^m that span the d orbital states are degenerate. They form a 5-dimensional irreducible representation (irrep) of the full rotation group SO(3). The d orbital states can equally well be described by cubic harmonics, which can be written in terms of spherical harmonics as

$$|z^2\rangle = Y_2^0 \tag{5.15}$$

$$|xz\rangle = \left(Y_2^{-1} - Y_2^1\right)/\sqrt{2} \tag{5.16}$$

$$|yz\rangle = i\left(Y_2^{-1} + Y_2^1\right)/\sqrt{2} \tag{5.17}$$

$$|xy\rangle = i\left(Y_2^{-2} - Y_2^2\right)/\sqrt{2} \tag{5.18}$$

$$|x^2 - y^2\rangle = \left(Y_2^{-2} + Y_2^2\right)/\sqrt{2} \tag{5.19}$$

In hexagonal SiC, the predominant symmetry at the TM defect is tetrahedral at a silicon substitutional site [41]. The crystal field, which is the potential due to the surrounding crystal with which the d electron interacts, reflects this symmetry. The 5 spherical harmonics do not form an irrep of the cubic symmetry groups. Therefore they are split by the crystal field into irreps of these groups. How the states are split can be calculated using the theory of characters of representations. For tetrahedral symmetry, the 5 states of the d orbitals split into an orbital doublet and an orbital triplet. The doublet is composed of the cubic harmonics $|x'^2 - y'^2\rangle$ and $|z'^2\rangle$, and the triplet by $|x'y'\rangle$, $|x'z'\rangle$ and $|y'z'\rangle$. The primed cubic harmonics indicate the direction of the cartesian coordinates in these functions, and are such that the z'-axis coincides with a 4-fold rotational axis of the cubic field (between two of the tetrahedral bonds). In the basis cb' defined by the primed cubic harmonics, $cb' = \{|z'^2\rangle, |x'z'\rangle, |y'z'\rangle, |x'y'\rangle, |x'^2 - y'^2\rangle\}$, the Hamiltonian for the cubic field is diagonal, $H_{cub} = diag(E_{Od}, E_{Ot}, E_{Ot}, E_{Ot}, E_{Od})$, where E_{Od} and E_{Ot} denote the shift in energy of respectively the orbital doublet and triplet compared to the free d electron.

At some lattice sites the cubic field has a trigonal distortion, which means that the cubic symmetry is reduced to a C_{3v} symmetry with the C_3 axis along a body diagonal of the cubic field, or the direction of the distortion. An adequate basis set for this particular crystal field is the set $cb = \{|z^2\rangle, |xz\rangle, |yz\rangle, |xy\rangle, |x^2-y^2\rangle\}$, where the z-axis is parallel to the C_3 rotational axis. This particular symmetry splits the degeneracy of the states in cb into two orbital doublets and a singlet. The sets of cubic harmonics $\{|xz\rangle, |yx\rangle\}$ and $\{|xy\rangle, |x^2-y^2\rangle\}$, respectively, make up the orbital doublets, whereas the $\{|z^2\rangle\}$ corresponds to the orbital singlet. Thus, in the basis cb, the Hamiltonian for the trigonal field is $H_{trig} = diag(E_{C0}, E_{C1}, E_{C1}, E_{C2}, E_{C2})$, where E_{C0}, E_{C1} and E_{C2} denote the shift in energy of respectively the orbital singlet and doublets compared to the free d electron.

It is useful to take the basis states with the spin of the electron included. A convenient basis set is the direct product of spherical harmonics and spin states. Let $sb = \{|2\rangle, |1\rangle, |0\rangle, |-1\rangle, |-2\rangle\}$ be a basis in terms of spherical harmonics where $|m\rangle$ denotes the spherical harmonic Y_2^m. The basis we use is then $\{sb\,|\uparrow\rangle, sb\,|\downarrow\rangle\}$, where $|\uparrow\rangle$ and $|\downarrow\rangle$ denote the electron-spin projection along the z-axis. In order to transform H_{cub} and H_{trig} to this basis, the cubic harmonics need to be transformed to spherical harmonics, and H_{cub} also needs to be rotated from the primed to the unprimed basis. The transformation from cubic to spherical harmonics is given by equations (5.15) to (5.19). The rotation from the primed to unprimed basis can be described by the three Euler angles α, β and γ, around the z, x, and z axis respectively in this particular order. This rotation is described by $\beta = \arccos\left(1/\sqrt{3}\right)$ and $\gamma = \frac{3}{4}\pi$. The angle α has no effect on the direction of z-axis. However, choosing $\alpha = 0$ results in the simplest Hamiltonian. The rotation of spherical harmonics can be done by using the Wigner D matrix with these Euler angles. After H_{cub} and H_{trig} have been transformed to the basis sb, the total Hamiltonian can be written in block-diagonal form by reordering the basis states. The matrix blocks are

$$\mathcal{H}_1 = \mathcal{H}_2 = \begin{bmatrix} \frac{1}{3}(3E_{C2}+E_{Od}+2E_{Ot}) & -\frac{\sqrt{2}i}{3}(E_{Od}-E_{Ot}) & 0 \\ \frac{\sqrt{2}i}{3}(E_{Od}-E_{Ot}) & +\frac{1}{3}(3E_{C1}+2E_{Od}+E_{Ot}) & 0 \\ 0 & 0 & E_{C0}+E_{Ot} \end{bmatrix} \tag{5.20}$$

$$\mathcal{H}_3 = \begin{bmatrix} \frac{1}{3}(3E_{C1}+2E_{Od}+E_{Ot}) & \frac{\sqrt{2}i}{3}(E_{Od}-E_{Ot}) & 0 & 0 \\ -\frac{\sqrt{2}i}{3}(E_{Od}-E_{Ot}) & \frac{1}{3}(3E_{C2}+E_{Od}+2E_{Ot}) & 0 & 0 \\ 0 & 0 & \frac{1}{3}(3E_{C2}+E_{Od}+2E_{Ot}) & -\frac{\sqrt{2}i}{3}(E_{Od}-E_{Ot}) \\ 0 & 0 & \frac{\sqrt{2}i}{3}(E_{Od}-E_{Ot}) & \frac{1}{3}(3E_{C1}+2E_{Od}+E_{Ot}) \end{bmatrix} \tag{5.21}$$

with corresponding basis states

$$\mathcal{H}_1 : \Big(|2\rangle\,|\uparrow\rangle, \quad |-1\rangle\,|\uparrow\rangle, \quad |0\rangle\,|\downarrow\rangle \Big) \tag{5.22}$$

$$\mathcal{H}_2 : \Big(|-2\rangle\,|\downarrow\rangle, \quad |1\rangle\,|\downarrow\rangle, \quad |0\rangle\,|\uparrow\rangle \Big) \tag{5.23}$$

$$\mathcal{H}_3 : \Big(|1\rangle\,|\uparrow\rangle, \quad |-2\rangle\,|\uparrow\rangle, \quad |2\rangle\,|\downarrow\rangle, \quad |-1\rangle\,|\downarrow\rangle \Big) \tag{5.24}$$

The matrix blocks $\mathcal{H}_1$ and $\mathcal{H}_2$ are the same, and both have in general three distinct eigenvalues. This means that for each eigenstate of $\mathcal{H}_1$ there is an eigenstate of $\mathcal{H}_2$ with the same energy. Combined, the eigenstates of $\mathcal{H}_1$ and $\mathcal{H}_2$ describe three doublets. The matrix block $\mathcal{H}_3$ has only 2 distinct eigenvalues and therefore describes 2 doublets, meaning that all eigenstates of the total Hamiltonian are at least doubly degenerate. This is in accordance to Kramers theorem, which states that for systems with half integer spin and time-reversal symmetry every state is at least doubly degenerate. When the nuclear spin is not included, the two electronic-spin states in a doublet are each others time-conjugate. This is indeed the case for our system.

5.5.2. Effect of varying parameter k

In order to restrict the parameter range that we use to model the V defects in SiC associated with the α line, we look at regions where the model reproduces the experimental g-parameters and the spin-orbit splitting between ground state KDs. This agreement can be obtained for k values between 0.18 and 0.37. The k value has a strong influence on the relative trigonal crystal field strength η, but not on the SOC parameter λ (Fig. 5.4). Fig. 5.5(a-d) and 5.5(e-f) show the magneto-spectra obtained for the parameters corresponding to Fig. 5.4(a) and 5.4(b), respectively. The qualitative shape of the spectra does not change significantly when we consider different values of k, and neither does the order of magnitude of the Rabi frequencies obtained. We note, however, that lower k-values (which consequently require a larger trigonal crystal field) result in lower Rabi frequencies due to interactions with electric fields parallel to the crystal c-axis, and magnetic fields perpendicular to this direction.

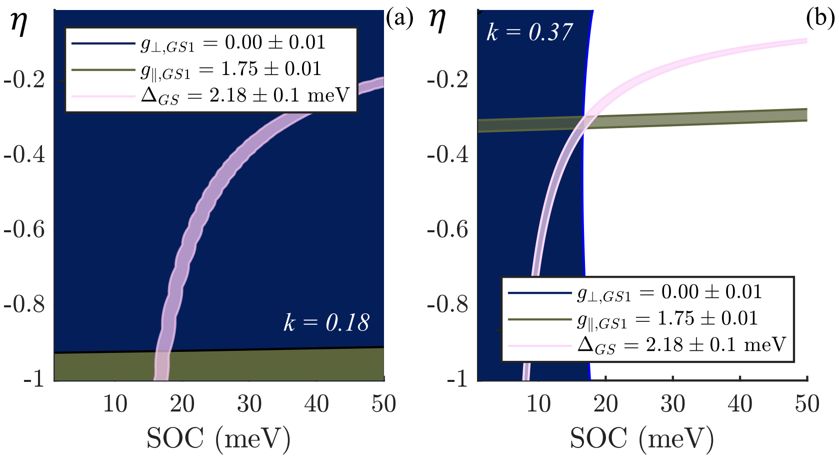

Figure 5.4: Effect of varying the parameter k on parameters η, λ that match experimental observations. Values of k between 0.18 (panel 5.4(a)) and 0.37 (panel 5.4(b)) provide parameter ranges that describe the experimental results well. Low k values require stronger trigonal crystal fields (larger η). In contrast, the value of the SOC parameter (λ) does not depend strongly on the value of k.

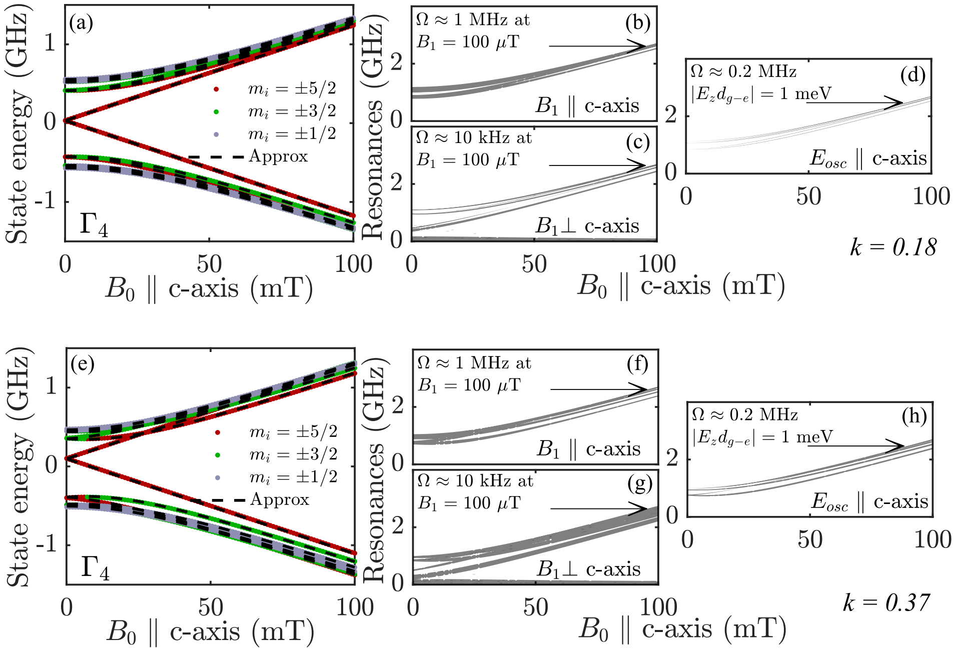

Figure 5.5: Effect of varying the parameter k on magneto-spectra of the Γ_4 doublets. Results are as presented in the main text for Fig. 5.3. We use the parameter range determined in Fig. 5.4(a) to obtain the plots in panels 5.5(a-d), and the parameters corresponding to Fig. 5.4(b) to obtain the plots in panels 5.5(e-f).

5.5.3. Eigenstates and allowed transitions for $\Gamma_{5,6}$ doublet

We can numerically obtain the results presented in Fig. 5.3 of the main text for the ground-state $\Gamma_{5,6}$ doublet. The shape of the magneto-spectrum differs from what Fig. 5.3 of the main text presents for the Γ_4 doublet. Fig. 5.6 shows that, for the $\Gamma_{5,6}$ doublet there are no levels whose energy increases purely linearly with the applied magnetic field. This is the most striking feature, and would be visible in magnetic resonance spectra. Additionally, the spacing between the hyperfine levels is larger and more clearly resolved than for the Γ_4 doublet. These features can be used to identify the experimentally observed lowest-energy doublet as being of the Γ_4 type.

Finally, we note that the $\Gamma_{5,6}$ doublet in the defect associated with the α line is 2.18 meV above the lowest energy KD, such that its equilibrium population is reduced at cryogenic temperatures according to the Boltzmann factor. Nonetheless, a weak signal of these states' spin properties may be visible at intermediary temperatures, where $k_B T \approx \Delta_{SOC}$. We note that, for the $\Gamma_{5,6}$ doublets, electronic magnetic resonance with oscillating fields perpendicular to the c-axis (Fig. 5.6(c)) is not possible due to the symmetry restricted $g_\perp = 0$. Only nuclear magnetic resonance lines are present in this case, at very low frequencies. Nonetheless, electronic magnetic resonance with an oscillating field along the symmetry axis of the defect remains possible (Fig. 5.6(d)).

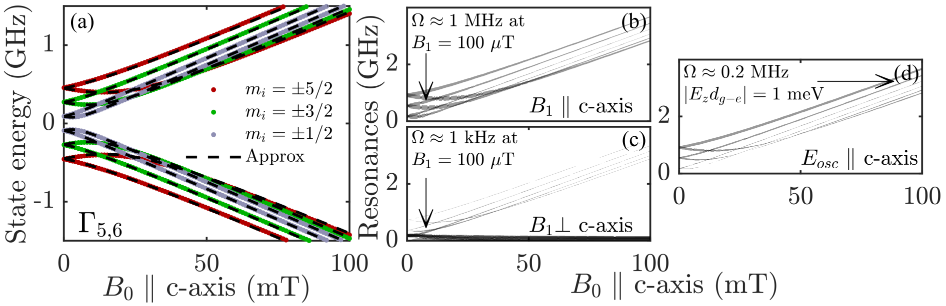

Figure 5.6: (a) Energies of the 12 eigenstates corresponding to the $\Gamma_{5,6}$ ground-state electronic-spin doublet, hyperfine-coupled to a central nucleus with a spin-5/2, as a function of the static magnetic field B_0 applied parallel to the c-axis. Results were obtained numerically (colored lines), and by diagonalizing the effective-spin Hamiltonian associated with a $\Gamma_{5,6}$ doublet (dashed line). (b-d) Microwave resonance lines obtained numerically for an oscillating magnetic field parallel (b) or perpendicular (c) to the c-axis, or an oscillating electric field parallel (d) to the c-axis. The thickness of the resonance lines corresponds to their Rabi frequencies, with different scales in each plot. Scales are provided by the labels and arrows, indicating the Rabi frequency at a certain point. (b) If the static field is small (Zeeman splitting comparable to hyperfine coupling strength), a small oscillating magnetic field ($B_1 \approx 100$ μT) parallel to the c-axis leads to very efficient electronic-spin transitions with Rabi frequencies on the order of 1 MHz. These resonances weaken significantly as the static magnetic field increases. (c) In a $\Gamma_{5,6}$ doublet, direct interaction with an oscillating field perpendicular to the c-axis is symmetry forbidden. Only nuclear spin transitions are observed in this case. (d) A large enough electric field parallel to the c-axis leads to electronic spin transitions as explained in the text.

5.5.4. Interaction with electric fields

We obtain the matrix representation of the effect of an oscillating electric field by investigating the matrix elements of a trigonal crystal field as in equations (5.20, 5.21), with $E_{Od} = E_{Ot} = 0$ and $E_{C2} - E_{C_1} = E_{C0} = 1$ meV. We use, as basis states, the $|\Gamma_i, \uparrow\downarrow\rangle$ as defined in the main text (see caption of Fig. 5.2 in the main text).

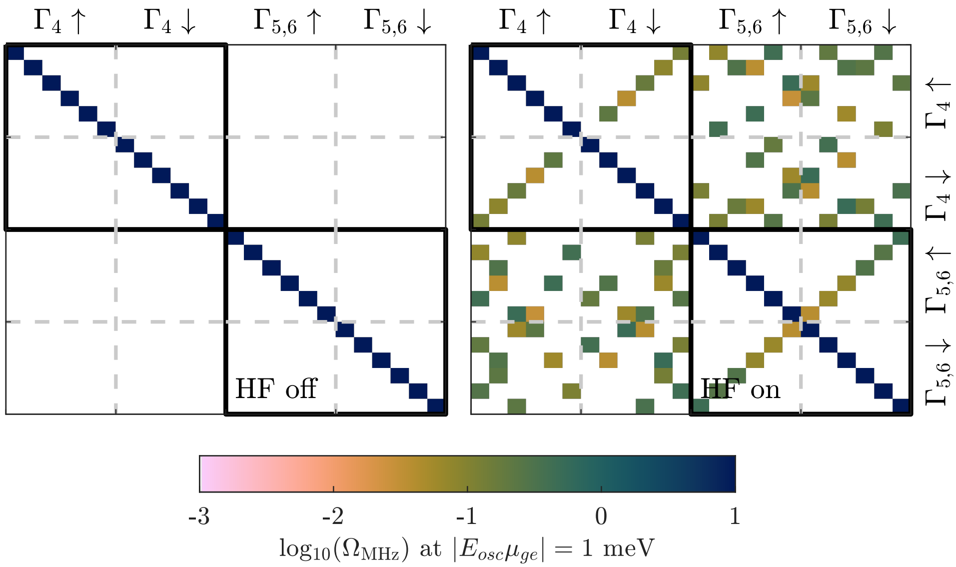

Figure 5.7: (a) Matrix elements due to an oscillating electric field parallel to the c-axis, in the basis defined by the crystal field, spin-orbit coupling and a small magnetic field (20 mT) along the c-axis, for the two ground state Kramers doublets ($|\Gamma_4, \uparrow\downarrow\rangle$ and $|\Gamma_{5,6}, \uparrow\downarrow\rangle$), without hyperfine coupling. White matrix elements correspond to zero. Within each KD (contoured block diagonal parts of the full matrix), an electric field parallel to the c-axis does not lead to electric microwave transitions, consistent with the restrictions from Kramers theorem [19, 21]. (b) Same as (a), but with the hyperfine interaction between electron and the central nuclear spin added to the static Hamiltonian. In this case, the electronic spin can flip via electric microwave transitions driven by an oscillating field parallel to the c-axis.

5.5.5. Results for β-line V defects

In 4H-SiC, V can occupy two different lattice sites, which gives rise to defects with distinct optical transitions and electronic configurations [17, 22–24]. The defect associated with the α line is subject to the strongest trigonal crystal field and shows the largest values for spin-orbit splitting between the two ground-state KDs. We base our analysis in the main text on this lattice site, since it is most similar to the recently explored Mo defects [14, 19]. Nonetheless, we can repeat the procedure of the main text for the defects associated with the β line as well, which we present here. Fig. 5.8 shows that in order to reproduce the experimentally observed energy splittings for the ground state of these defect centers, we need to take much weaker trigonal fields ($\eta = -0.2$ for the β line, versus $\eta = -0.4$ for the α line, with the same value of k). Also the spin-orbit parameter λ is reduced from 17 meV in the α-line defect to ~5 meV in the β-line defect.

Although the hyperfine spectra obtained with these parameters are qualitatively similar to those shown in the main text for the α defect, there are some differences that are worth noting. At large magnetic fields, the energies of the hyperfine sublevels of the Γ_4 doublet are more closely spaced (Fig. 5.9(a)), giving rise to magneto-resonance spectra where the hyperfine lines are less clearly distinguishable (Fig. 5.9(b-d)). This may have consequences for experimental schemes that rely on being able to resolve these spin transitions and address them independently. Additionally, we note that for the $\Gamma_{5,6}$ KD of the V defect in the β configuration, electronic-spin transitions due to oscillating magnetic fields perpendicular to the symmetry axis of the defect arise (Fig. 5.9(g)). This is in contrast to what Fig. 5.6(c) presents for the α line. In the β-line defect, since the SOC splitting between ground-state doublets is small, a magnetic field perpendicular to the symmetry axis can mix the Γ_4 and $\Gamma_{5,6}$ doublets. This causes that the symmetry protection with regards to spin transitions due to oscillating magnetic fields perpendicular to the c-axis observed for the α-line defect is not as effective at the β-line defect.

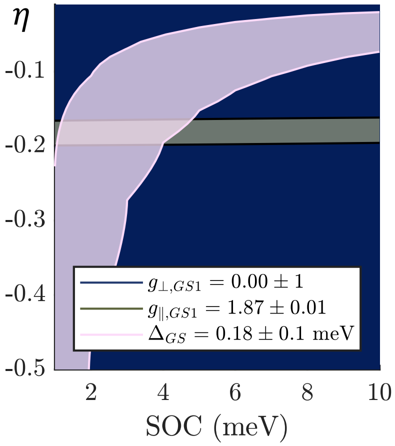

Figure 5.8: Parameters that reproduce the ground-state energy splittings of a V defect responsible for the β-line in 4H-SiC [23], for $k = 0.3$.

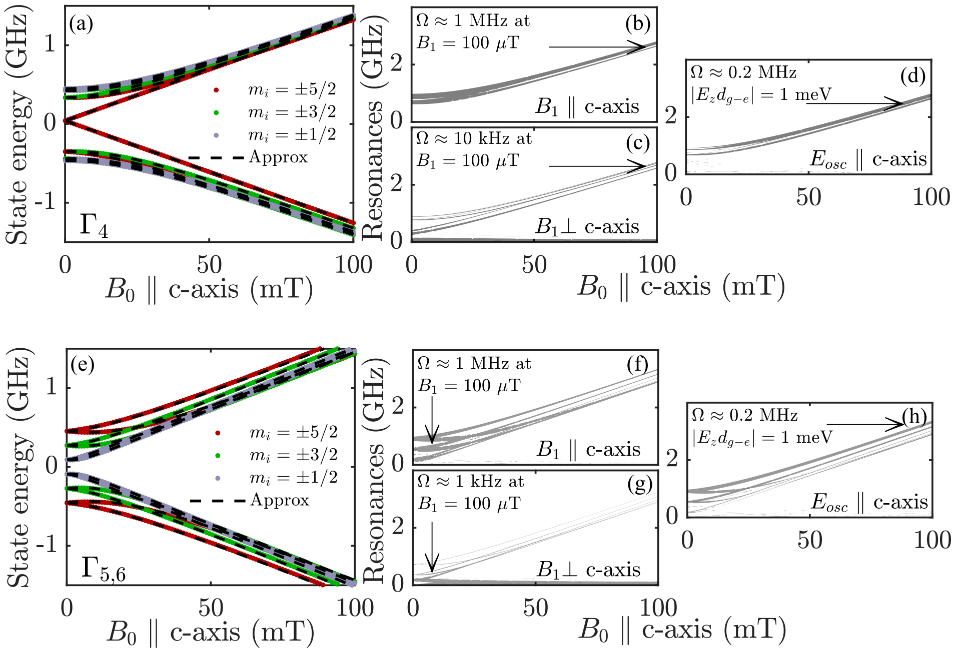

Figure 5.9: Hyperfine level structure and allowed microwave transitions of the Γ_4 (a-d) and $\Gamma_{5,6}$ (e-h) doublets in a β-line defect with parameters as obtained in Fig. 5.8.

5.5.6. Effective-spin Hamiltonian

In order to obtain analytical expressions for the effective-spin Hamiltonians, we diagonalize the Hamiltonians in equations (5.20, 5.21) algebraically. To do this, we parametrize the terms $E_{Od,Ot}$ and $E_{C0,C1,C2}$, such that

$$\Delta = E_{Ot} - E_{Od} \tag{5.25}$$

$$\Delta_E = E_{C1} - E_{C2} = \eta\Delta \tag{5.26}$$

$$\epsilon_{Td} = (E_{Ot} + E_{Od})/3 \tag{5.27}$$

$$\epsilon_{C3} = (E_{C1} + E_{C2}) \tag{5.28}$$

and pick $\epsilon_{Td}, \epsilon_{C3}$ such that the energies are centered at zero.

This results in a crystal-field Hamiltonian in terms of the parameters η, Δ and Δ_A (as defined in the main text)

$$\mathcal{H}_1 = \mathcal{H}_2 = \Delta \begin{bmatrix} -\frac{1}{2}(\eta-\frac{1}{3}) & \frac{\sqrt{2}i}{3} & 0 \\ -\frac{\sqrt{2}i}{3} & \frac{1}{2}(\eta-\frac{1}{3}) & 0 \\ 0 & 0 & E_{C0}+E_{Ot} \end{bmatrix} \tag{5.29}$$

$$\mathcal{H}_3 = \Delta \begin{bmatrix} \frac{1}{2}(\eta-\frac{1}{3}) & -\frac{\sqrt{2}i}{3} & 0 & 0 \\ \frac{\sqrt{2}i}{3} & -\frac{1}{2}(\eta-\frac{1}{3}) & 0 & 0 \\ 0 & 0 & \frac{1}{3}-\frac{1}{2}(\eta-\frac{1}{3}) & \frac{\sqrt{2}i}{3} \\ 0 & 0 & -\frac{\sqrt{2}i}{3} & \frac{1}{2}(\eta-\frac{1}{3}) \end{bmatrix} \tag{5.30}$$

Within the ground state manifold, composed by the lowest-energy Γ_4 and $\Gamma_{5,6}$ doublets, this Hamiltonian has eigenstates [20, 21]

$$|\Gamma_4^g, \uparrow\rangle = \sin(\phi)\,|2,\uparrow\rangle + i\cos(\phi)\,|-1,\uparrow\rangle \tag{5.31}$$

$$|\Gamma_4^g, \downarrow\rangle = \sin(\phi)\,|-2,\downarrow\rangle + i\cos(\phi)\,|1,\downarrow\rangle \tag{5.32}$$

$$|\Gamma_{5,6}^g, \uparrow\rangle = \sin(\phi)\,|-2,\uparrow\rangle + i\cos(\phi)\,|1,\uparrow\rangle \tag{5.33}$$

$$|\Gamma_{5,6}^g, \downarrow\rangle = \sin(\phi)\,|2,\downarrow\rangle + i\cos(\phi)\,|-1,\downarrow\rangle \tag{5.34}$$

in terms of the parameter

$$\phi = \operatorname{atan}\left(\frac{2\sqrt{2}}{1-3\eta+3\sqrt{1+\eta^2-\frac{2}{3}\eta}}\right) \tag{5.35}$$

The parameter ϕ thus indicates the relative strengths of the trigonal and tetrahedral crystal fields. For $\eta = 0$, where there is no trigonal component in the crystal field, $\phi = 35.26^o$. In contrast, if the trigonal contribution is much larger than the tetrahedral contribution, $\eta = \pm\infty$, such that $\phi = 90^o$ and $\phi = 0^o$, respectively. In these latter cases, the eigenstates fully coincide with the spherical harmonics with the z-axis along the C_3 symmetry axis.

In order to obtain the analytical expressions for the effective-spin Hamiltonians presented in the main text, we include spin-orbit coupling to first order. That is, we assume that the SOC energy splitting is big enough to isolate the KDs Γ_4^g and $\Gamma_{5,6}^g$ from each other, but disregard the effect of SOC in mixing ground and optically excited-state doublets. We then write the Hamiltonians corresponding to the Zeeman energy and the hyperfine interaction in the basis given by $\{|\Gamma_{4,(5,6)}, \uparrow\downarrow, m_i\rangle\}$), where m_i corresponds to the nuclear spin projection along the z-axis.

We obtain the effective-spin Hamiltonians presented in Eqs. 5.7-5.10, with parameters

$$\Gamma_4 \begin{cases} a_{\parallel} & = \frac{2}{7} A(7k-1)(3\sin^2(\phi)-1) \\ a_{\perp} & = \frac{6}{7} A\cos^2(\phi) \\ g_{\parallel} & = 2(k(3\sin^2(\phi)-1)+1) \\ g_{\perp} & = 0 \end{cases} \tag{5.36}$$

$$\Gamma_{5,6} \begin{cases} a_{\parallel} & = \frac{2}{7} A(7k+1)(3\sin^2(\phi)-1) \\ a_{\perp} & = \frac{6}{7} A\sin(2\phi) \\ g_{\parallel} & = 2(-k(3\sin^2(\phi)-1)+1) \\ g_{\perp} & = 0 \end{cases} \tag{5.37}$$

with parameteres A, k as defined in the main text. A first-order correction to the wavefunctions due to spin-orbit coupling modifies $g_{\perp}$ for the Γ_4 doublet, giving rise to a small non-zero $g_{\perp}$ on the order of $(k\lambda/\Delta)$. This does not happen for the $\Gamma_{5,6}$ doublet.

To obtain these values, we have relied on the fact that the hyperfine coupling and the Zeeman interaction with the magnetic fields are both much smaller than the spin-orbit related energy splitting between the KDs. This is valid in the case of the α-line defect. For the defects responsible for the β and γ lines, where the SOC splitting is smaller, mixing between the Γ_4 and $\Gamma_{5,6}$ KDs due to magnetic fields and interaction with the nuclear spin become relevant, and the validity of these effective-spin-1/2 Hamiltonians in describing the energy levels and allowed transitions is limited.

References

[1] C. M. Gilardoni, I. Ion, F. Hendriks, M. Trupke, and C. H. van der Wal, “Hyperfine-mediated transitions between electronic spin-1/2 levels of transition metal defects in SiC”, New J. of Phys. **23**, 083010 (2021).

[2] D. D. Awschalom, L. C. Bassett, A. S. Dzurak, E. L. Hu, and J. R. Petta, “Quantum spintronics: engineering and manipulating atom-like spins in semiconductors”, Science **339**, 1174 (2013).

[3] M. Atatüre, D. Englund, N. Vamivakas, S.-Y. Lee, and J. Wrachtrup, “Material platforms for spin-based photonic quantum technologies”, Nat. Rev. Mat. **3**, 38 (2018).

[4] A. Gaita-Arino, F. Luis, S. Hill, and E. Coronado, “Molecular spins for quantum computation”, Nat. Chemistry **11**, 301 (2019).

[5] E. Coronado, “Molecular magnetism: from chemical design to spin control in molecules, materials and devices”, Nat. Rev. Mater. **5**, 87 (2020).

[6] G. Wolfowicz, F. J. Heremans, C. P. Anderson, S. Kanai, H. Seo, A. Gali, G. Galli, and D. D. Awschalom, “Qubit guidelines for solid-state spin defects”, Nat. Rev. Mater. (2021).

[7] A. Chatterjee, P. Stevenson, S. De Franceschi, A. Morello, N. P. de Leon, and F. Kuemmeth, “Semiconductor qubits in practice”, Nat. Rev. Phys. **3**, 157 (2021).

[8] D. Awschalom et al., “Development of quantum interconnects (quics) for next-generation information technologies”, PRX Quantum **2**, 017002 (2021).

[9] S. Castelletto and A. Boretti, “Silicon carbide color centers for quantum applications”, Journal of Physics: Photonics **2**, 022001 (2020).

[10] M. Atzori, L. Tesi, E. Morra, M. Chiesa, L. Sorace, and R. Sessoli, “Room-temperature quantum coherence and Rabi oscillations in vanadyl phthalocyanine: toward multifunctional molecular spin qubits”, J. Am. Chem. Soc. **138**, 2154 (2016).

[11] M. K. Wojnar, D. W. Laorenza, R. D. Schaller, and D. E. Freedman, “Nickel(II) metal complexes as optically addressable qubit candidates”, J. Am. Chem. Soc. **142**, 14826 (2020).

[12] S. Giménez-Santamarina, S. Cardona-Serra, J. M. Clemente-Juan, A. Gaita-Ariño, and E. Coronado, “Exploiting clock transitions for the chemical design of resilient molecular spin qubits”, Chemical Science **11**, 10718 (2020).

[13] B. Diler, S. J. Whiteley, C. P. Anderson, G. Wolfowicz, M. E. Wesson, E. S. Bielejec, F. J. Heremans, and D. D. Awschalom, “Coherent control and high-fidelity readout of chromium ions in commercial silicon carbide”, npj Quantum Information **6**, 11 (2020).

[14] T. Bosma et al., “Identification and tunable optical coherent control of transition-metal spins in silicon carbide”, npj Quantum Information **4**, 48 (2018).

[15] A. Gällström et al., “Optical identification and electronic configuration of tungsten in 4H and 6H-SiC”, Physica B: Condensed Matter **407**, 1462 (2012).

[16] K. Maier, J. Schneider, W. Wilkening, S. Leibenzeder, and R. Stein, “Electron spin resonance studies of transition metal deep level impurities in SiC”, Mater. Sci. and Eng.: B **11**, 27 (1992).

[17] J. Baur, M. Kunzer, and J. Schneider, “Transition metals in SiC polytypes, as studied by magnetic resonance techniques”, Phys. Stat. Sol. A **162**, 153 (1997).

[18] T. Yamabayashi et al., “Scaling up electronic spin qubits into a three-dimensional metal-organic framework”, J. Am. Chem. Soc. **140**, 12090 (2018).

[19] C. M. Gilardoni, T. Bosma, D. van Hien, F. Hendriks, B. Magnusson, A. Ellison, I. G. Ivanov, N. T. Son, and C. H. van der Wal, “Spin-relaxation times exceeding seconds for color centers with strong spin–orbit coupling in SiC”, New J. of Phys. **22**, 103051 (2020).

[20] A. Csóré and A. Gali, “*Ab initio* determination of pseudospin for paramagnetic defects in SiC”, Phys. Rev. B **102**, 241201(R) (2020).

[21] B. Tissot and G. Burkard, “Spin structure and resonant driving of spin-1/2 defects in SiC”, Phys. Rev. B **103**, 064106 (2021).

[22] L. Spindlberger et al., “Optical properties of vanadium in 4H silicon carbide for quantum technology”, Phys. Rev. Appl. **12**, 014015 (2019).

[23] G. Wolfowicz, C. P. Anderson, B. Diler, O. G. Poluektov, F. J. Heremans, and D. D. Awschalom, “Vanadium spin qubits as telecom quantum emitters in silicon carbide”, Sci. Adv. **6**, eaaz1192 (2020).

[24] B. Kaufmann, A. Dörnen, and F. S. Ham, “Crystal-field model of vanadium in 6H silicon carbide”, Phys. Rev. B **55**, 13009 (1997).

[25] P. V. Klimov, A. L. Falk, B. B. Buckley, and D. D. Awschalom, “Electrically driven spin resonance in silicon carbide color centers”, Phys. Rev. Lett. **112**, 087601 (2014).

[26] A. L. Falk, P. V. Klimov, B. B. Buckley, V. Ivády, I. A. Abrikosov, G. Calusine, W. F. Koehl, A. Gali, and D. D. Awschalom, “Electrically and mechanically tunable electron spins in silicon carbide color centers”, Phys. Rev. Lett. **112**, 187601 (2014).

[27] C. P. Anderson et al., “Electrical and optical control of single spins integrated in scalable semiconductor devices”, Science **366**, 1225 (2019).

[28] M. Widmann et al., “Electrical charge state manipulation of single silicon vacancies in a silicon carbide quantum optoelectronic device”, Nano Lett. **19**, 7173 (2019).

[29] D. M. Lukin et al., “4H-silicon-carbide-on-insulator for integrated quantum and nonlinear photonics”, Nat. Photon. **14**, 330 (2019).

[30] B. Tissot and G. Burkard, “Hyperfine structure of transition metal defects in SiC”, Phys. Rev. B, accepted (2021).

[31] A. Abragam and B. Bleaney, *Electron paramagnetic resonance of transition ions*, International series of monographs on physics (Clarendon Press, Oxford, 1970).

[32] M. Kunzer, H. D. Müller, and U. Kaufmann, “Magnetic circular dichroism and site-selective optically detected magnetic resonance of the deep amphoteric vanadium impurity in 6H-SiC”, Phys. Rev. B **48**, 10846 (1993).

[33] A. Csóré, A. Gällström, E. Janzén, and A. Gali, “Investigation of mo defects in 4H-SiC by means of density functional theory”, Mater. Sci. For. **858**, 261 (2016).

[34] G. Wolfowicz et al., “Atomic clock transitions in silicon-based spin qubits”, Nat. Nanotechnol. **8**, 561 (2013).

[35] M. Shiddiq, D. Komijani, Y. Duan, A. Gaita-Arino, E. Coronado, and S. Hill, “Enhancing coherence in molecular spin qubits via atomic clock transitions”, Nature **531**, 348 (2016).

[36] H. Seo, A. L. Falk, P. V. Klimov, K. C. Miao, G. Galli, and D. D. Awschalom, “Quantum decoherence dynamics of divacancy spins in silicon carbide”, Nat. Commun. **7**, 12935 (2016).

[37] L.-P. Yang, C. Burk, M. Widmann, S.-Y. Lee, J. Wrachtrup, and N. Zhao, “Electron spin decoherence in silicon carbide nuclear spin bath”, Phys. Rev. B **90**, 241203(R) (2014).

[38] K. Nemoto et al., “Photonic architecture for scalable quantum information processing in diamond”, Phys. Rev. X **4**, 031022 (2014).

[39] C. T. Nguyen et al., “Quantum network nodes based on diamond qubits with an efficient nanophotonic interface”, Phys. Rev. Lett. **123**, 183602 (2019).

[40] S. J. Whiteley et al., “Spin–phonon interactions in silicon carbide addressed by gaussian acoustics”, Nat. Phys. **15**, 490 (2019).

[41] A. Gällström, B. Magnusson, and E. Janzén, “Optical identification of Mo related deep level defect in 4H and 6H SiC”, Mater. Sci. For. **615**, 405 (2009).

chapter 6

Spectroscopy and dynamics of vanadium defects in SiC

Transition metal defects in SiC give rise to localized electronic states that can be optically addressed in a material system widely used in the semiconductor industry. Vanadium defects in the neutral charge state in particular have optical transitions directly in the telecom O-band. Here, we characterize the optical spectrum of these defect centers based on emission and absorption techniques. We analyze these spectra in light of the electronic structure of the defect and experimentally determine the oscillator strength of the optical transitions. We characterize the spin structure of ground and excited states via two-laser spectroscopy. Based on time-resolved experiments, we show that these defects have ground-state spin relaxation times on the order of a ms at 2 K. The magnetic-field dependence of the spin-relaxation time provides evidence for hyperfine-induced pathways for spin relaxation.

6.1. Introduction

Defects in semiconductors that are optically active (color-centers) and have stable ground-state spins are an interesting platform for the implementation of quantum technologies [1–7]. Spins in these platforms can be entangled over long-distances via optical pulses [8–11] and integrated in semiconductor devices [12–15]. These are two important features for the development of quantum repeaters [6], which promise to extend the maximum entanglement distance in a quantum network via intermediary nodes capable of temporarily storing and extending the entangled state. Integrating the repeater network with existing telecommunications infrastructure is facilitated by spin-active color centers that have optical transitions in the telecom bands. Vanadium defects in SiC combine this last feature with an electronic spin-1/2 ground state and a naturally abundant spin-7/2 nucleus and have attracted significant interest in recent years [16–21]. The coupled electronic-nuclear spin system may lead to a hybrid qubit that benefits from the optical addressability of electronic spins and memory-compatible long coherence times of nuclear spins [22–25].

Recent work on these defect centers has unraveled a bright defect [16, 17] with a rich ground-state electronic structure due to the coupled nuclear and electronic spins. Combined, the large number of available hyperfine-coupled eigenlevels and the relatively short spin-relaxation times (μs) of these defects at 4 K [16] contribute to low contrast in optical experiments aimed at unraveling the defect level structure [26]. Additionally, V is an amphoteric (it is stable in several different charge states depending on the Fermi level of the crystal) impurity in the SiC lattice [27], such that disentangling charge and spin dynamics may be a challenge. Thus, the full characterization of the magneto-optical spectrum relies on both extending the spin-relaxation time, and designing and implementing spin-initialization protocols. The former requires identifying the physical mechanisms responsible for spin relaxation, whereas the latter requires characterization of the hyperfine-coupled spectrum with high contrast.

Here, we characterize an ensemble of V defects in 4H-SiC with respect to their optical transitions using all-optical techniques based on both emission and novel absorption approaches. The absorption spectra obtained allow us to experimentally determine the magnitude of the transition dipole moment for transitions between ground and optically-excited states in these defect centers, on the order of 0.1 to 1 D (1 D $\approx$ 0.2 eÅ). Furthermore, we show that absorption techniques provide increased contrast in two-laser spectroscopy experiments that allow us to access the spin-resolved optical transitions within the inhomogeneously broadened ensemble. These results allow us to improve on the previous determination of spin-Hamiltonian parameters [16, 20, 28]. Finally, we show that the spin-relaxation time of these defects is extremely temperature dependent in the few-kelvin range, improving by an order of magnitude when cooling from 3 to 2 K. The magnetic-field dependence of the spin-relaxation time shows that the spin-relaxation rate is maximum when the electronic Zeeman energy is comparable to the magnitude of the hyperfine interaction. This provides evidence that hyperfine-induced mixing of electronic states leads to additional relaxation pathways that dominate the spin-relaxation processes at these temperatures, as predicted in chapter 5.

6.1.1. The α-line V defect: review of earlier results

Vanadium defects in SiC that are optically active in the telecom bands are composed of a V impurity substituting a Si atom in the lattice (Fig. 6.1(a)). The substitutional impurity may occupy lattice sites with varying local symmetries, giving rise to defects that are optically active at different wavelengths. In 4H-SiC, two lines are present, denoted as α and β depending on their photon energy (the α-line happens at higher photon energy than the β-line). The α-line associated with V defects corresponds to optical transition at approximately 1278 nm or 0.968 eV (Fig. 6.1(c)).

These lines are associated with a defect center with the symmetries of the point group C_{3v}. Initial results assigned this line to a defect where V substitutes a Si atom in a *quasi*-hexagonal lattice site (Fig. 6.1(a)) in the SiC lattice [16, 29]. This was due to the fact that the *quasi*-hexagonal site has second-nearest neighbors distributed in a trigonal-prismatic geometry. Recent *ab initio* results [17, 19], however, have shown that the *quasi*-cubic site (Fig. 6.1(b)) may have stronger influence of a crystal field with C_{3v} symmetry due to the protruding p_z orbital of the third-nearest neighbor. To avoid confusion and be consistent with the existing literature we will refer to the defect as the α-line V defect.

As discussed previously in Sec. 5.1.1, the ground and optically-excited states of these defects are each composed of a set of two Kramers doublets (KDs) arising from spin-orbit-split orbital doublets [16, 19, 29, 30] (see Fig. 6.2(a,b)). The spin-orbit splitting is on the order of 2 meV in the ground state and 1 meV in the excited state. This electronic structure arises from an electron localized in the d orbitals of the transition metal (TM), in an environment with the symmetries of the point group C_{3v} and strong spin-orbit coupling. Each Kramers doublet behaves as an effective spin-$1/2$ system (where the effective-spin properties depend on both orbital and spin degrees of freedom), such that the degeneracy is broken in the presence of a static magnetic field.

We will denote each Kramers doublet according to their symmetry properties (that is, the irrep of point group C_{3v} that describes how these states transform) as Γ_4 or $\Gamma_{5,6}$ (see Tab. A.1 and Fig. 6.2(b)). These symmetry properties lead to well-defined selection rules for optical excitation and emission (Fig. 6.2(b), and see also Sec. 4.5.4). They also determine how the effective electronic spin couples to external magnetic fields. States transforming as $\Gamma_{5,6}$ only have contributions from orbital wavefunctions that have a non-zero orbital angular momentum projection along the symmetry axis of the defect. These states always have the electron spin and orbital angular momentum projections along the crystal c-axis, with spin projection pointing parallel or antiparallel to the orbital angular momentum projection [18, 19, 30, 31]. Due to symmetry, these states have identically-zero matrix elements for the Zeeman interaction with magnetic fields perpendicular to the symmetry axis of the defect center. These symmetry restrictions for interaction with magnetic fields perpendicular to the natural symmetry axis were also shown to suppress spin-relaxation mechanisms in the case of Mo defects in SiC (which are analogous to α-line V defects, see chapter 3 or Ref. [30]). In contrast, states transforming as Γ_4 may have contributions from orbital states with zero orbital angular momentum projection along the symmetry axis of the defect centers. These states may interact (albeit very weakly in some defect configurations) with magnetic fields perpendicular to the crystal c-axis.

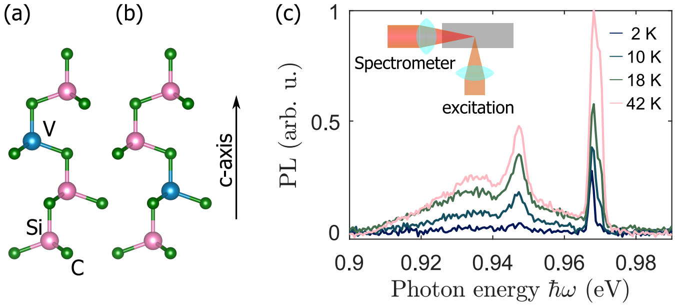

Figure 6.1: **Defect geometry and photoluminescence spectrum.** (a,b) Possible lattice sites occupied by a substitutional V defect in 4H-SiC. (c) Photoluminescence spectrum showing the α-line associated with V defects and its temperature dependence. The zero-phonon line has photon energy of ~ 0.97 eV and its first phonon-replica, ~0.95 eV. The phonon replica is surrounded by broad and temperature-dependent phonon-sideband emission. Photoluminescence is collected in a direction perpendicular to the excitation direction. The α-line is related to a defect with strong C_{3v} symmetry, with the rotational axis parallel to the crystal c-axis. It has been proposed that it is related to a defect where the V impurity substitutes a Si in a *quasi*-hexagonal (a) or *quasi*-cubic (b) lattice site.

The particular ordering of the doublets with respect to their symmetries has been a subject of confusion in recent literature. The magneto-optical spectra related to this defect showed no Zeeman splitting in the ground state when subject to an external magnetic field perpendicular to the crystal c-axis. This led to initial identification of the lowest-energy ground-state doublet as being of the $\Gamma_{5,6}$ type [16, 18, 29]. *Ab initio* results, however, suggested that the lowest-energy ground-state doublet should be of the Γ_4 type [19]. These findings were corroborated by a comparison of the hyperfine-resolved spectrum with the effective-spin Hamiltonians obtained theoretically for KDs of different symmetry types ([20, 21] and chapter 5).

For analysis of the hyperfine effects, it should be noted that over 99% of naturally occurring vanadium is of a single isotope type, with a nucleus with spin-7/2. The hyperfine interaction is much smaller than the spin-orbit energy splitting between different KDs [16], such that we can disregard hyperfine-induced mixing of different KDs. The form of the hyperfine coupling term in each KD depends on the KD symmetry as well, such that the effective-spin Hamiltonian of each doublet is irrep-dependent [20, 21], and can be found in Sec. 5.3.4. In chapter 5 we built on this to predict that the hyperfine interaction leads to additional spin-relaxation pathways for the electronic spin.

6.2. Ordering of states and optical-transition line properties

We characterize the electronic structure of the V defects associated with the α-line in 4H-SiC using various optical spectroscopy techniques. Initial characterization of the photoluminescence spectra related to these defects (see Sec. 6.6 for details on the measurement setup) shows a narrow zero-phonon line (ZPL) at approximately 0.97 eV ($\sim$ 1278 nm), followed by broad phonon-sideband (PSB) emission between 0.97 and 0.9 eV (1278 and 1377 nm). Spectroscopy with higher resolution (below) shows that the ZPL line consists in fact of multiple lines close in energy. The phonon-sideband emission is suppressed, but not absent, at low temperatures. Additionally, we can identify a sharp peak at $\sim$ 0.945 eV, corresponding to a phonon replica of the zero-phonon line. This phonon replica indicates that the defects' electronic states couple to quantized vibrational modes that are well-localized around the defect center. Besides this phonon replica, the phonon sideband also contains a very broad feature that starts (almost) at the ZPL energy. This broad feature indicates that the defect can also decay optically into vibrational states where the electronic ground state is coupled to very low-energy delocalized lattice vibrational modes. This is in contrast to what we observed for Mo defects (chapter 4), for which there is a gap between the ZPL and the onset of the phonon-sideband emission [31].

We investigate these defect centers using photoluminescence-excitation (PLE) and absorption spectroscopy at zero magnetic field (Fig. 6.2(d-g)) in order to resolve the different Kramers doublets pertaining to ground and optically-excited states. In these measurements, we excite the defect centers at resonance with a tunable continuous-wavelength (CW) laser while measuring the phonon-sideband emission or power of the transmitted laser beam (see Fig. 6.2(c)). Details of the measurement geometry and setup are provided in Sec. 6.6. We vary the polarization of the excitation laser such that the electric field is polarized parallel (Fig. 6.2(d,e)) or perpendicular (Fig. 6.2(f,g)) to the crystal c-axis. This axis coincides with the three-fold rotational axis of the defects. In the PLE spectra (Fig. 6.2(d,f)), we plot the normalized phonon-sideband emission as a function of laser energy. In contrast, in the absorption spectra (Fig. 6.2(e,g)) we plot the negative log of the transmitted power, normalized to the off-resonance transmitted power.

In these spectra, we can identify 4 optical transition lines, at energies 967.3, 968.1, 969.5 and 970.3 meV. The two lines at the highest energies are present at all temperatures in both PLE and absorption spectra. In contrast, the two lines of lowest energies are absent in both PLE and absorption spectra at low temperatures (2 K), and only appear as the sample is warmed up. This is evidence that these two latter optical transition lines arise from excitation of defects that are in the doublet $|G2\rangle$, where we use the notation of Fig. 6.2(a). This doublet is not thermally populated at 2 K. In this way, we can determine the spin-orbit energy splitting between the two Kramers doublets in the ground and optically-excited states to be respectively 2.2 and 0.8 meV, in agreement with previous experimental results [16, 29].

The selection rules for the optical transitions allow us to unequivocally deter-

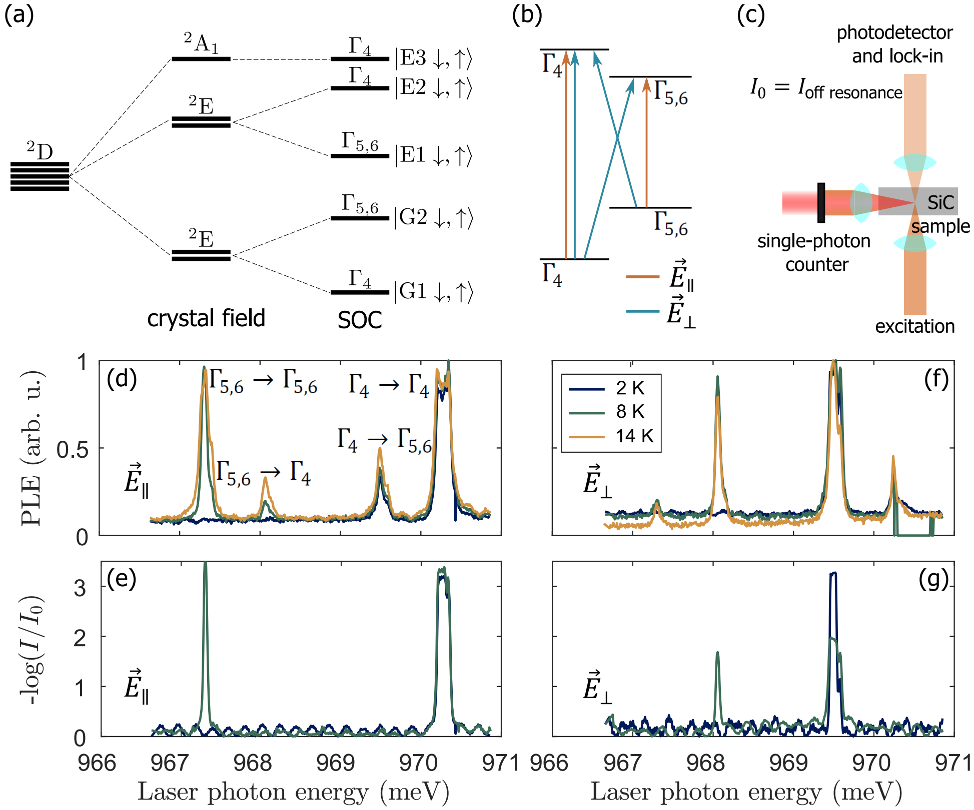

Figure 6.2: **Photoluminescence-excitation and absorption spectroscopy.** (a) Electronic structure of the defects, arising from a single electron in the d-orbitals of the transition metal impurity in an environment with strong C_{3v} symmetry and spin-orbit coupling. (b) Ground and optically-excited states are each composed of two KDs, with specific symmetry-related selection rules for optical transitions due to electric fields parallel or perpendicular to the crystal c-axis. (c) Experimental geometry for PLE (spectra in d,f) and absorption (spectra in e,g) detection. (d,f) Sample phonon-sideband emission as a function of the excitation laser photon energy for optical electric fields polarized parallel (d) and perpendicular (f) to the crystal c-axis. (e,g) Power of a transmitted beam through the sample as a function of the excitation laser photon energy, for optical electric fields polarized parallel (e) and perpendicular (g) to the crystal c-axis. The temperature and polarization dependence of the spectra (see main text) allow us to determine that the ordering of ground and excited state doublets with regards to symmetry properties is as shown in (b). The excited state $|\mathrm{ES}_3\rangle$ is far above $|\mathrm{ES}_2\rangle$ in energy [16, 17] and cannot be seen in these spectra.

mine what the symmetry character of each doublet is. Group theory determines that transitions between two doublets transforming as $\Gamma_{5,6}$ are only allowed with light polarized parallel to the symmetry axis of the defect. Transitions between a doublet transforming as Γ_4 and a doublet transforming as $\Gamma_{5,6}$ (and vice-versa) are only allowed with light polarized perpendicular to this symmetry axis, and transitions between two doublets transforming as Γ_4 are allowed with light polarized both parallel and perpendicular to the symmetry axis (see Fig. 6.2(b), Sec. 4.5.4). We check this via PLE and absorption spectroscopy. It should be noted that in absorption, since we measure the power of the transmitted laser beam, the polarization of the excitation beam is homogeneous throughout the addressed ensemble. This provides maximum dependency of the line strength on the polarization of the excitation beam. In contrast, PLE signals may have contributions from defects that are optically driven by scattered light. Thus, these measurements show weaker dependence on the polarization of the excitation beam. Inspection of the PLE and absorption spectra in Fig. 6.2(d-e) shows that the outer optical transition lines (at 967.3 and 970.3 meV) appear when we excite the sample with light polarized parallel to the symmetry axis of the defects. In contrast, the inner lines (at 968.1 and 969.5 meV) appear when the excitation laser is polarized perpendicular to the crystal c-axis. Thus, we conclude that the lowest Kramers doublet in the ground-state manifold has Γ_4 symmetry character, in agreement with predictions based on *ab initio* calculations and analysis of the hyperfine structure of the doublet ([19–21] and chapter 5). In the optically-excited state manifold, the ordering of the doublets is inverted, such that the $\Gamma_{5,6}$ doublet is lowest in energy (see Fig. 6.2(b,d)).

The homogeneous linewidth associated with these defects is expected to be orders of magnitude narrower than the ensemble-broadened inhomogeneous lines [16, 17]. Thus, the PLE and absorption linewidths are dominated by inhomogeneous broadening of the optical transitions. In both PLE and absorption spectra, each of the four different optical transition lines is broadened by different amounts, indicating that the KDs differ in how sensitive they are to lattice inhomogeneities. The $\Gamma_4 \rightarrow \Gamma_4$ transition is the broadest in both PLE and absorption spectra, whereas the $\Gamma_{5,6} \rightarrow \Gamma_{5,6}$ transition is the narrowest. In the absorption spectrum in Fig. 6.2(e), these optical transitions have full widths at half maximum of 0.17 meV and 0.05 meV, respectively (corresponding to 41 and 14 GHz). This indicates that the energies of states transforming as Γ_4 are more susceptible to inhomogeneous broadening due to varying local environments. According to symmetry, the energy of states transforming as $\Gamma_{5,6}$ should be, in first order, insensitive to electric fields perpendicular to the symmetry axis of the defect (see Sec. 4.5.4 and Tab. A.2). This is not true for states transforming as Γ_4.

Finally, we can estimate the transition dipole moments for the optical transitions based on the absorption spectra in Fig. 6.2(e,g) (see Sec. 6.7.1). This estimation depends inversely on the square root of concentration of defect centers responsible for the optical transitions. As we mentioned before, V defects can occupy different lattice sites, and can exist in different charge states. The ratio of defects in different sites depends on the formation energy for each defect configuration and crystal growth temperature [32–34]. We do observe in our samples photoluminescence from both α and β defect configurations with similar efficiency, which indicates significant population of both types of defects. The distribution of charge states depends mainly on the Fermi level of the SiC crystal, but also on the strain configuration of the lattice. In our experiments, we could see no slow ionization of the defects [30, 35–37], indicating that the optically addressed charge state is relatively stable. Our samples are specified to be semi-insulating, with total V concentration on the order of 10^{17} cm^{-3}. This value provides an estimate for the transition dipole associated with the $\Gamma_4 \rightarrow \Gamma_{5,6}$ transition at 969.5 eV on the order of 0.1 D. Since only part of the vanadium impurities occupies the correct lattice site and charge state, this value provides a lower bound for the actual transition dipole moment associated with these defect centers. Thus, this value is in reasonable agreement with an estimate obtained based on the radiative lifetime of the optically-excited state [17, 21] ($\approx$ 1 D).

6.3. Hyperfine structure

In order to characterize the hyperfine-coupled energy levels associated with these defect centers we use a two-laser spectroscopy technique [39–41]. Here, we apply a magnetic field at an angle ϕ with respect to the crystal c-axis, as shown in the inset of Fig. 6.3(a). We use two excitation beams to excite the sample, and we scan the detuning between the photon energies in each beam with sub-MHz resolution (see Sec. 6.6 for details). We focus on the optical transition at 969.5 eV, since this line shows moderate inhomogeneous broadening and is related to the lowest-energy ground-state doublet. This means that we focus on characterizing the spin properties of the Γ_4 ground-state doublet and the $\Gamma_{5,6}$ excited-state doublet. Both excitation beams are polarized perpendicular to the crystal c-axis. We use a lock-in setup and temporal modulation of the excitation beams (Fig. 6.3(a), and Sec. 6.6 for details) to greatly reduce the influence of single-laser absorption processes in our signal, focusing instead on the component of the transmitted signal due to simultaneous excitation with the two optical fields.

Using this technique, we can resolve energy splittings smaller than the inhomogeneous broadening of the optical transition lines. This is due to the fact that the splitting between hyperfine-coupled sublevels is much less sensitive to crystal inhomogeneities than the splitting between ground and optically-excited states. Due to the inhomogeneous broadening of the optical transition line, a single laser drives transitions from different ground-state hyperfine-coupled spin sublevels in different defects in the ensemble. If the optical field is sufficiently strong, the single laser depletes the population of this hyperfine-coupled spin sublevel in each defect after a few optical excitation and decay cycles [16, 30]. If the rate at which the defect's

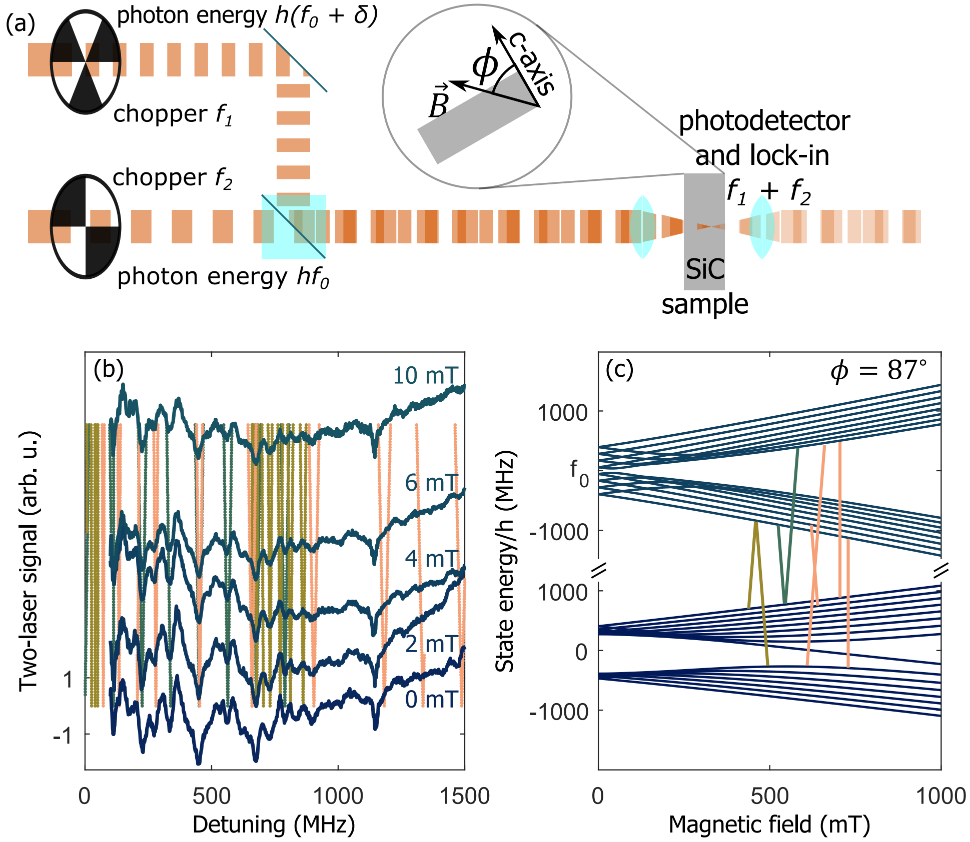

Figure 6.3: **Two-laser spectroscopy.** (a) Details on the measurement geometry. We use two laser beams to excite the sample simultaneously. Independent temporal modulation of each beam allows us to detect only the two-laser transmission through the sample via lock-in filtering techniques. We apply a magnetic field (as labeled) at an angle ϕ with respect to the crystal c-axis (inset) and vary the difference in photon-energy between the two optical fields (detuning δ). (b) Two-laser spectra of the defect centers at a sample temperature of 2 K and various magnetic field amplitudes. We can identify several features relate them to two-laser driving schemes based on the energy eigenlevels of ground and optically-excited states (c). We obtain these energy eigenlevels based on symmetry-specific effective-spin Hamiltonians (see main text) and parameters present in literature [16, 38]. See main text also for color coding.

ground-state electronic spin is changed through optical excitation and decay cycles exceeds the rate at which the original ground-state spin sublevel is repopulated (the spin-relaxation rate), excitation with a single laser leads to a suppression of the photoluminescence and absorption signals. When a second detuned laser is brought onto the ensemble, if the difference between the photon energies in the two optical fields (the detuning) matches one of the many available hyperfine-resolved energy splittings within the ground or optically-excited states, this second laser modifies the rate at which the original ground-state hyperfine-coupled sublevel is repopulated. Thus, an absorption spectrum as a function of the detuning between the two optical fields shows increased or decreased absorption features as the detuning between the levels matches the energy splittings between the hyperfine-coupled spin sublevels.

This results in two-laser spectra as shown in Fig. 6.3(b). Here, we plot the two-laser transmission at various magnetic field amplitudes. The magnetic field direction is almost perpendicular to the crystal c-axis, with $\phi = 87°$, and the sample is kept at 2 K. We chose this geometry in order to maximize the probability of spin-flipping optical transitions (see Sec. 3.10.6). The spectra at each magnetic field amplitude are normalized by the maximum transmission of the combined data set, and are offset for clarity. We can identify several peaks and dips in this data (the sharp dip at ~1100 MHz is related to an artifact from the measurement setup). These features become shallower and broader as the magnetic field increases. This trend continues at larger magnetic fields (see Fig. 6.5), and eventually all features disappear at approximately 60 mT. Additionally, we cannot see any two-laser features at higher temperatures (above 2.5 K). At these temperatures, the spin-relaxation time is significantly shortened, leading to reduced two-laser contrast.

The various possible two-laser driving schemes are depicted as vertical lines in Fig. 6.3(c). In a Λ-scheme (brown vertical lines), the two excitation beams drive transitions from two different ground-state sublevels to a common excited-state sublevel. A V-scheme (green vertical lines) corresponds to the case where the two excitation beams couple a single ground-state sublevel to two different excited-state sublevels. Finally, X and Π-schemes (pink vertical lines) correspond to detunings where the two optical fields couple two different ground-state sublevels to two different excited-state sublevels. These driving schemes are overlayed on theory-predicted ground (lowest manifold) and excited state (highest manifold) eigenlevels. In order to obtain the energy eigenstates as a function of external magnetic fields, we diagonalize the effective-spin Hamiltonians

$$H = \mathbf{S} \cdot \mathbf{A} \cdot \mathbf{I} - \mu_B \mathbf{B} \cdot \mathbf{g} \cdot \mathbf{S} - \mu_N g_N \mathbf{B} \cdot \mathbf{I} \tag{6.1}$$

$$\mathbf{A}_{\Gamma_4} = \begin{bmatrix} a_\perp & 0 & 0 \\ 0 & -a_\perp & 0 \\ 0 & 0 & a_\parallel \end{bmatrix}, \quad \mathbf{g}_{\Gamma_4} = \begin{bmatrix} g_\perp & 0 & 0 \\ 0 & g_\perp & 0 \\ 0 & 0 & g_\parallel \end{bmatrix}, \tag{6.2}$$

$$\mathbf{A}_{\Gamma_{5,6}} = \begin{bmatrix} 0 & 0 & a_\perp \\ 0 & 0 & a_\perp \\ 0 & 0 & a_\parallel \end{bmatrix}, \quad \mathbf{g}_{\Gamma_{5,6}} = \begin{bmatrix} 0 & 0 & 0 \\ 0 & 0 & 0 \\ 0 & 0 & g_\parallel \end{bmatrix}. \tag{6.3}$$

for the ground (Γ_4) and excited state ($\Gamma_{5,6}$) manifolds, respectively [20, 21]. Here, **S** and **I** are the effective-spin-1/2 and nuclear spin-7/2 operators, respectively, **B** is the magnetic field, **A** and **g** are the hyperfine and g-parameter coupling tensors, g_N

is the nuclear g-parameter for V and μ_B and μ_N are the Bohr and nuclear magnetons. We use for the effective-spin Hamiltonian parameters ($a_{\perp,\parallel}$ and $g_{\perp,\parallel}$) values present in the literature [16, 20] or obtained through private communications [26, 38], adjusted slightly to better fit our data (see Tab. 6.1). Based on these energy levels, we can calculate the detuning at which the different two-laser schemes are driven as a function of the magnetic field (see Sec. 6.7.2). We overlay, on the two-laser spectra in Fig. 6.3(b), the position of the allowed two-laser driving schemes. This shows that most of the features in our experimental spectra can be well-explained by the effective-spin Hamiltonians present in literature. The discrepancies could be mitigated with better estimates for the parameters $a_{\perp,\parallel}$ and $g_{\perp,\parallel}$. This is hard to obtain from our data due to our measurement geometry: a magnetic field close to perpendicular to the crystal c-axis provides a very small energy splitting between the levels due to the small $g_\perp$. Additionally, a field in this direction slightly breaks the symmetry of the defect, leading to many possible optical transitions as the field increases. At magnetic fields of ~60 mT we can no longer resolve the many possible optical two-laser driving schemes, preventing us from identifying individual features (see Fig. 6.5). Reproducing this experiment in a geometry where the magnetic field is along the natural symmetry axis of the defect centers, however, should provide a high-contrast picture of the evolution of the hyperfine-coupled eigenlevels as a function of the magnetic field (in progress at time of this writing). This would lead to a more accurate estimate for the effective-spin Hamiltonian parameters.

6.4. Evidence for hyperfine-mediated spin relaxation

Finally, we characterize the spin-relaxation time of these defects at various temperatures and magnetic fields with time-resolved techniques based on both emission (Fig. 6.4(a,c)) and absorption (Fig. 6.4(a,b)). Data obtained via time-resolved PLE experiments (see Fig. 6.6(b)) provides direct access to the timescales related to optical excitation, excited-state lifetime, optically-driven spin flips and spin-relaxation processes. In contrast, the absorption-based measurements aided by a lock-in amplifier presented here only inform us about the spin-relaxation dynamics, but can be performed in a fraction of the time and allow us to characterize a much bigger parameter space. For this reason, we choose to combine both techniques.

At an intermediate magnetic field orientation ($\phi = 54°$), we measure the phonon-sideband emission in a time-resolved manner as we excite the sample resonantly at the ZPL with pump and probe pulses. Details on the creation of the pulses and detection geometry are provided in Sec. 6.6. The ensemble response to the pump pulse shows a sharp initial photoluminescence peak proportional to the equilibrium population of the different optically driven ground-state sublevels across the inhomogeneous ensemble. This initial peak is followed by a plateau of lower photoluminescence, indicating that a single laser drives dissipative optical spin-flips within the first 50 μs of optical excitation. As the pump pulse is turned off, the ensemble evolves towards its equilibrium configuration. We denote the characteristic timescale in which this happens as T_1. If the delay between pump and probe pulses τ is smaller or comparable to T_1, this leading-edge peak in the photoluminescence response will be reduced when the probe pulse excites the sample. We characterize the population recovery at each delay τ by the ratio of the integrated number of photons emitted by the sample within the first 15 μs of the probe (I_{probe}) and pump (I_{pump}) pulses, I_{probe}/I_{pump}. We obtain the spin-relaxation time by fitting this ratio as a function of delay τ to a monoexponential recovery function (see Fig. 6.7 and caption).

At a geometry where $\phi = 87°$, we use time-resolved absorption measurements to investigate the spin-relaxation times (Fig. 6.4(a,c)). In these measurements, we directly detect the integrated absorption during a 30 μs probe pulse. Each probe pulse is applied after a pump pulse of 1 ms, with a delay of duration τ between them. Details on this measurement can be found in Sec. 6.6. In this case, the transmission signal decreases as τ increases. At short delays, defects that have not relaxed back to their equilibrium configuration cannot absorb photons, increasing the transmitted power. Thus, we fit this data set (normalized) to a monoexponential decay function (see Fig. 6.6 and caption).

Both absorption and emission measurements show a significant decrease of the spin-relaxation time as the sample temperature is increased from 2 to 3 K. Figure 6.4(a) shows the spin-relaxation rate ($\Gamma = T_1^{-1}$) as a function of the sample temperature in various configurations. All measurements show a one-order of magnitude increase of the spin-relaxation rate as the temperature increases by only one kelvin. This sharp superlinear dependence (see also inset of Fig. 6.4(a), where the green data is presented in a linear scale) indicates that, at these temperatures, two-phonon processes assisted by a low-lying excited state are the dominating mechanisms for spin-relaxation [31, 42] (see also Sec. 4.5.7). Our measurements at 1.8 K indicate that this trend continues towards lower temperatures (that is, the spin-relaxation time is further extended at lower temperatures). In the millikelvin range, these two-phonon processes should be suppressed, allowing for significantly longer spin-relaxation times. The low-lying excited states that mediate rapid spin relaxation could be both vibrational or orbital states (see chapter 4). Our measurements do not cover a wide-enough temperature range to identify which particular states are involved in these processes.

In Mo defects in SiC, a highly analogous system to α-line V defects but with 74.5% naturally abundant nuclear-spins zero, we found that spin relaxation was suppressed in the ground-state KD, leading to seconds-long spin relaxation times at

2 K. This was due to the fact that, within a KD, time-reversal symmetry prevents direct spin-flips due to interactions that preserve time-reversal symmetry. Additionally, the defect does not interact with magnetic fields perpendicular to the crystal c-axis, such that it is also insensitive to magnetic field perturbations in this direction [31] (see also chapter 4). In chapter 5 we showed that the hyperfine interaction enables otherwise forbidden direct spin flips between states pertaining to an electronic KD [20, 21]. Thus, these observations in the case of Mo defects are expected to be only partially observed for α-line V defects.

We investigate the dependence of the spin-relaxation times on the applied magnetic field at 2 K (Figs. 6.4(b,c)). At zero magnetic field, the 16 hyperfine-coupled states are split by the hyperfine coupling (see Fig. 6.3(c)). Thus, we expect to observe a time-resolved signal indicating optical depletion of spin sublevels and the subsequent recovery of the equilibrium distribution of the population also at zero magnetic field. This is in fact observed (see Fig. 6.4(a), green data), and gives a relaxation time of approximately 700 μs at 2 K. In this configuration, we cannot distinguish between nuclear and electronic spin-relaxation times, since the ground-state eigenstates associated with the Hamiltonian in Eq. 6.1-6.2 at zero field are composed of strongly entangled nuclear and electronic spins [20]. Increasing the magnetic field modifies the mixing between the different hyperfine-coupled states, as evidenced by the anticrossing points in the energy levels presented in Fig. 6.3(c) and Fig. 6.4(b). Experimentally, we observe a peak in the spin-relaxation rate as a function of the applied magnetic field at the field value where the electronic Zeeman energy is comparable to the hyperfine coupling energy (Fig. 6.4(c,d)). Since the Zeeman interaction is strongly anisotropic, this peak happens at different magnetic-field amplitudes depending on the angle ϕ (Fig. 6.4(b-d)). At high magnetic fields almost perpendicular to the crystal c-axis (Fig. 6.4(c)), the spin-relaxation rate saturates at a value larger than the zero-field rate. This does not happen when the field is at a smaller angle with respect to the c-axis (Fig. 6.4(d)). The magnetic field component perpendicular to the c-axis leads to mixing with the second KD in the orbital ground state manifold ($|\mathrm{GS}_2\rangle$ in Fig. 6.2(a)) [18, 31], and this could lead to faster spin relaxation.

6.5. Discussion and conclusion

The results of the previous section constitute important but non-exhaustive milestones for the implementation of telecom-compatible quantum communication protocols based on V defects in SiC. Storing single-photons in solid-state defect ensembles based on the DLCZ protocol [43, 44] requires optically thick samples with highly homogeneous ensembles, where the interaction between the ensemble and the optical signals can be detected in transmission with high quality. Here, we

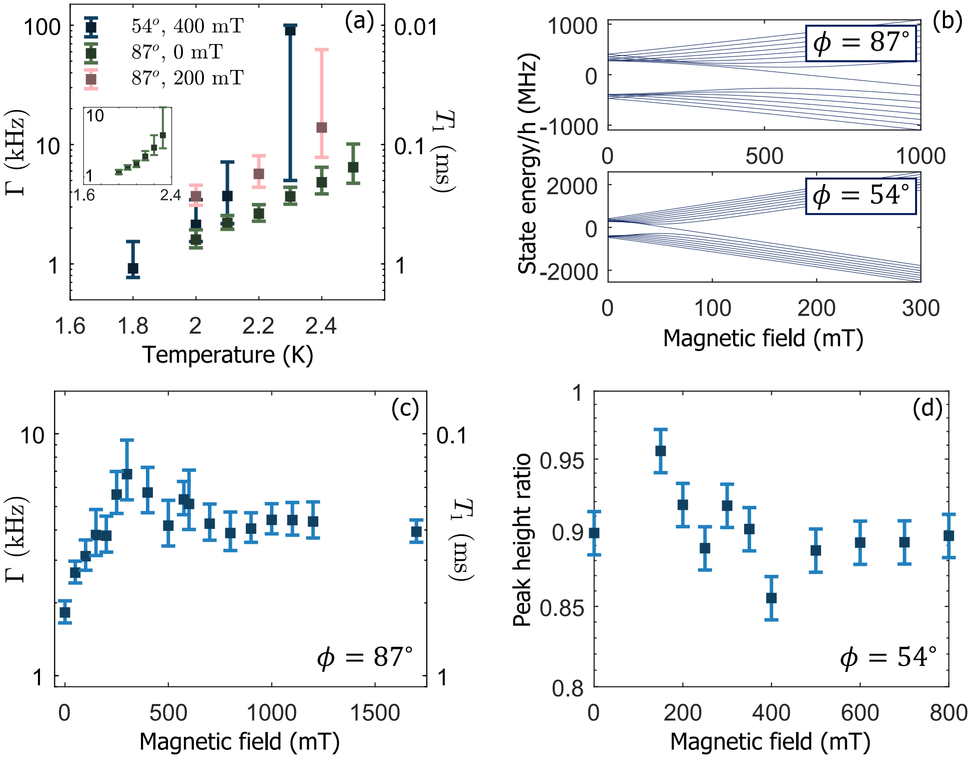

Figure 6.4: **Temperature and magnetic field dependence of spin-relaxation rates.** (a) The spin-relaxation rate increases by an order of magnitude as the temperature increases from 2 to 3 K in various measurement geometries (see main text). The inset presents the green data between 1 and 10 kHz in a linear scale, showing the superlinear temperature dependence of the relaxation rate. The trend continues to lower temperatures (see point at 1.8 K), indicating that the spin-relaxation times should be significantly longer at millikelvin temperatures. (b) Energy eigenlevels of the ground-state doublet hyperfine-coupled levels as a function of the magnetic field amplitude, for fields in two different directions. The anisotropic interaction with magnetic fields leads to the situation where the mixing of hyperfine levels due to an applied magnetic field – evidenced by the anticrossing points in the energy eigenlevels – depends strongly on the orientation of the field. (c) Spin relaxation rate measured in absorption as a function of the field amplitude, for a field oriented at $\phi = 87°$. (d) Peak height ratio between the leading edge peaks observed in the PLE response of the sample to pump and probe optical pulses with a fixed 300μs delay between the pulses, at various magnetic field amplitudes. The magnetic field is oriented at an angle $\phi = 54°$ with respect to the c-axis. As a function of the applied magnetic field, the spin-relaxation rate shows a non-trivial behavior at 2 K. We see a peak in the spin-relaxation rate at magnetic fields where the electronic Zeeman energy is comparable to the hyperfine coupling constants. Since the electronic Zeeman energy is highly anisotropic, the position of the peak in the spin-relaxation rate as a function of the magnetic field depends on the magnetic field direction identified by ϕ.

demonstrate several of these requirements. Based on absorption techniques, we have shown that V defects in fact interact strongly with optical fields. We estimate for these defect centers an electric dipole moment between ground and optically-excited states on the order of 0.1 to 1 D, comparable to well-established quantum emitters like NV centers or SiV in diamond [45]. Additionally, our results show that the inhomogeneous broadening of the optical transition is a factor 3 smaller when addressing the $\Gamma_{5,6}$ optically-excited state instead of the Γ_4 optically-excited state, due to the fact that $\Gamma_{5,6}$ doublets are symmetry-protected with respect to interactions with external electric fields perpendicular to the crystal c-axis. A defect with a ground-state doublet transforming as $\Gamma_{5,6}$ could provide a defect platform with even narrower inhomogeneous linewidths. Therefore, from a theoretical perspective, it is worthwhile to explore similar substitutional transition metal defects with a single active d-shell electron or hole with regards to their stability and ground-state electronic wavefunction symmetry properties.

Although the nuclear spin-7/2 of the V defects offers interesting possibilities for quantum information storage [23, 24, 46, 47], controlling the high nuclear spin also proves challenging. Optical pumping of the spin population into a single ground-state sublevel is hindered by the relatively short spin-relaxation times (between 10 μs and 1 ms at the temperatures and magnetic fields investigated here) when compared to the radiative lifetime of the optically-excited state [17]. We show that two-phonon processes assisted by low-lying orbital or vibrational excited states are responsible for the rapid increase of the spin-relaxation rates at the few-kelvin range. Thus, enhanced optical initialization of the ensemble should be achievable at millikelvin temperatures, where these two-phonon processes are not thermally achievable. Additionally, more accurate determination of the ground and optically-excited-state Hamiltonians will enable theoretical investigation of single or multi-laser protocols for efficient ground-state spin initialization and advanced multi-pulse sequences aimed at decoupling the defect centers from their environments [23, 25, 48–52].

Finally, the data presented here provides evidence that hyperfine-mediated spin relaxation plays an important role in the relaxation processes of the ground-state electronic spin of V defects in SiC, as predicted in chapter 5. The hybrid electronic-nuclear spin system can relax via processes that are symmetry forbidden in the case of the isolated electronic spin. This is evidenced by the magnetic-field dependence of the spin-relaxation rate that we present in this work. Although this coupling between electronic and nuclear spins is detrimental to the spin-relaxation times observed for these defects at certain magnetic field configurations, it is also a necessary component for resonantly addressing and controlling the ground-state spin via microwaves [21]. Additionally, it offers a path to using highly coherent nuclear spin states for quantum state storage [22, 53], if the electronic and nuclear spins can be (partially) decoupled at high magnetic fields or due to ionization of the defect center to remove the spin-active electron. In magnetic field configurations where electronic and nuclear spins are strongly coupled, a counter-intuitive situation may arise where the spin-relaxation time is shortened by the presence of the central nuclear spin, but the coherence times associated with the hybrid electronic-nuclear spin system are lengthened due to the presence of clock-transitions [54–56]. At some anticrossing points, the ground-state energy levels may have limited sensitivity to time and spatially varying local electric and magnetic fields, leading to increased coherence. These considerations call for a full characterization of the coherence properties of these defect centers.

Finally, we note that other defects in SiC may have similar properties to V defects in SiC, but with a much simpler electronic structure. Tungsten defects, for example, are stable in 4H and 6H-SiC and have optical transitions just below the O-band (1240 nm) [57, 58]. These defects have an odd number of d-shell valence electrons and symmetries analogous to those of V and Mo defects. Additionally, W has a single stable nuclear isotope with nuclear spin-1/2. Thus, ensembles of these defects would benefit from the intrinsic nuclear spin for long-term storage of quantum states, but with much cleaner optical transition spectra that may enable more reliable mechanisms for ground-state spin initialization.

6.6. Materials and experimental methods

Samples We study two 4H-SiC samples doped with V. The first sample, used to obtain the results in Fig. 6.1(b) was provided by academic collaborators (group of N. T. Son at Linköping University). This sample has a concentration of V on the order of 10^{17} cm^{-3}, but strong EPR signal from the negatively charged V defect. All other results were obtained on a commercial sample from II-VI Semiconductors. This sample also has nominal V concentration on the order of 10^{17} cm^{-3}. The samples were cooled in a liquid-helium flow cryostat with optical access and equipped with a superconducting magnet system.

Optical characterization

Photoluminescence We excite the defects with 900 nm (1.37 eV) photons, and collect the light emitted by the sample in a direction orthogonal to the propagating direction of the excitation beam (see Fig. 6.1(b), inset). The 5 mW excitation beam is focused to a 100 μm spot size. The photoluminscence from the sample is detected by a table-top near-infrared spectrometer with 0.4 nm resolution.

Photoluminescence excitation We excite the defects resonantly with a CW diode laser tunable from 1260 to 1330 nm. The specified laser linewidth is below 50 kHz, and the energy of the laser emission is stabilized within 1 MHz via active feedback. The beam diameter at the sample is approximately 100 μm. We vary the polarization of the laser at the sample. The sample emission in a direction perpendicular to the propagation of the excitation beam is collected using a high-NA lens, and detected using a single-photon counting avalanche photodetector. Scattered excitation light and emission into the zero-phonon line is filtered out from the detected light using a series of three 1300 nm long-pass filters (Fig. 6.2(c)), such that only phonon-sideband emission from V defects is really detected.

Absorption We excite the defects in the same setup as in PLE experiments, and detect the transmitted laser beam using a near-infrared variable gain photodetector. Additionally, we temporally modulate the excitation beam with an optical chopper. The chopper frequency is fed as a reference to a lock-in amplifier. The lock-in amplifier extracts from the photodetector output signal the component that oscillates at the reference frequency. This is done to remove from the signal backgrounds related to scattered light in the optical table, and electrical drift and noise. We normalize the transmitted power at resonance by the off-resonance transmitted power.

Two-laser excitation We excite the sample with two laser fields. The first beam (control beam) is obtained from the laser directly, and has the same wavelength stability as discussed above. The second beam (probe beam) is obtained from the same laser. This second beam is modified by an electro-optical phase modulator controlled by an RF signal to create sidebands at a certain detunings (determined by the RF frequency) from the laser output frequency. The most intense sideband is transmitted through a Fabry-Perot cavity that filters out the remaining sidebands. We modulate control and probe beams in time with different frequencies (f_1 and f_2, respectively, typically between 100 and 200 Hz) by physically chopping the beams (see Fig. 6.3(a)). The beams have similar powers (on the order of 20 μW). They are merged in a beam-splitter and focused into a 100 μm spot in the sample. The transmitted beam is detected with a near-infrared photodetector. With the help of a lock-in amplifier, we detect the component of the transmitted signal that oscillates at the sum frequency $f_1 + f_2$. This provides the transmitted signal in the presence of the two beams only, and filters out background effects due to single-laser absorption or scattered light.

Time-resolved PLE We create pulses from the CW laser output with the help of a digital-delay generator (DDG), the EOM and the Fabry-Perot cavity. The EOM creates sidebands detuned from the central laser frequency, where the detuning is determined by the RF frequency. The FP cavity is tuned such that it only transmits one of the detuned sidebands. The DDG controls the RF source. As the RF source turns on (off), the detuned sidebands appear (or disappear), such that the optical signal is also modulated on/off. The pulse sequence rise/fall time is estimated to be on the order of 20 ns. The sample emission into the phonon sideband is collected as in the PLE experiment, and detected in a time-resolved manner with a single-photon counting avalanche photodetector. An additional trigger pulse is used to identify the zero-time of each cycle. Each cycle is composed of a trigger pulse (to identify the zero-time), a pump pulse and a probe pulse separated by a delay τ and a recovery time following the probe pulse. The recovery time used is approximately 10 times the estimated spin-relaxation time.

Time-resolved absorption We create pulses from a CW laser output in the same manner as above, in the time-resolved PLE experiment. We detect the full time dependence of the power of the transmitted beam through the sample in a near-infrared variable gain photodetector, with estimated 5 MHz bandwidth. We modify the pulse sequence such that each cycle contains two long pump pulses (1 ms long) separated by a fixed recovery time (15 ms, much longer than any observable spin dynamics). Between the first and the second pump pulses, we add a short 30 μs long probe pulse. In this way, the pump pulse occurs at a frequency $2f_{ref}$, whereas the probe pulse occurs at a frequency f_{ref} (see Fig. 6.4(b)). With the help of a lock-in amplifier, we detect the component of the absorption signal oscillating at a frequency f_{ref}. This removes from the signal the background due to absorption of the pump pulses.

Acknowledgments

We thank B. Tissot, G. Burkard, M. Trupke, T. Astner and P. Koller for discussions. Financial support was provided by the Zernike Institute BIS program, and the EU H2020 project QuanTELCO (862721). We thank the technical support from H. de Vries and J. G. Holstein.

Author contributions

CMG, JH and CHvdW initiated the project. CMG and JH performed the experiments. CMG took the lead in the writing process. All authors contributed via discussion, and read and gave input into the manuscript.

6.7. Appendices

6.7.1. Estimating the transition dipole moment

According to Beer's Law [59, 60], a beam traveling a distance L in a sample with density of absorbers N has its intensity attenuated such that

$$I = I_0 e^{-\sigma N L}. \tag{6.4}$$

Here, I_0 is the intensity of an off-resonance beam traveling the same path (that is, it takes into account attenuation mechanisms other than resonant excitation, like reflection from interfaces), I is the transmitted intensity of the on-resonance beam and σ is the scattering cross-section for a single defect. In this way, $-\log(I/I_0) = \sigma N L$.

The scattering cross section σ depends on fundamental constants, the wavelength of the interacting light and the transition dipole moment between the two states taking part in the transition. The frequency-integrated absorption cross section, $\hat{\sigma} = \int_{\infty}^{\infty} \sigma d(\nu)$, is given by [60]

$$\hat{\sigma}_{1-2} = \frac{2}{3h}\frac{\pi^2}{\epsilon_0 c}\nu_{1-2}|-\langle\psi_2|e\mathbf{r}|\psi_1\rangle|^2 \tag{6.5}$$

where h is Planck's constant, ϵ_0 is the vacuum permittivity, c is the speed of light, ν_{1-2} is the frequency of the photons associated with the optical transition. We denote the matrix element of the transition dipole moment between states $|\psi_1\rangle$ and $|\psi_2\rangle$ by $-\langle\psi_2|e\mathbf{r}|\psi_1\rangle$. In this way, we can integrate the absorption line to obtain the transition dipole moment between the two states involved in the transition. In our estimates, we use the sample length of 0.5 cm and a vanadium defect concentration of 10^{17} cm^{-3}. The defect concentration is likely an over estimate of the concentration of V defects in an α-line configuration as stated in the main text.

6.7.2. Two-laser driving schemes and high-field data

In order to estimate the energy of the two-laser driving schemes, we restrict ourselves to considering combinations of allowed optical transitions. Since the ground-state is an electronic doublet of the Γ_4 type and the optically-excited state is of the $\Gamma_{5,6}$ type, optical transitions between ground and optically-excited states are allowed with light polarized in the plane perpendicular to the symmetry axis of the defect centers. For light circularly polarized, stricter selection rules arise [18, 20]. In our experiment, however, we use light linearly polarized in this plane, such that both spin-conserving and spin-flipping optical transitions are allowed. That is, for the electronic part of the wavefunction, all optical transitions between $|\Gamma_4, \uparrow\downarrow\rangle$ and $|\Gamma_{5,6}, \uparrow\downarrow\rangle$ are possible. For the nuclear spin part of the wavefunctions, we assume that

Figure 6.5: **Two-laser transmission signal at higher fields** Two-laser transmitted power as a function of detuning between the photon energies in the two optical beams (see Fig. 6.3 and main text for details and color coding), at various magnetic field amplitudes for a field at 87° from the crystal c-axis. The transmission signal is normalized and offset for clarity. On the data, we overlay the position of the expected two-laser features. At higher fields, the magnetic field near-perpendicular to the symmetry axis of the defect gives rise to many possible two-laser driving schemes. These many driving schemes are no longer resolvable at fields above ~60 mT and thus the features in the two-laser signal disappear.

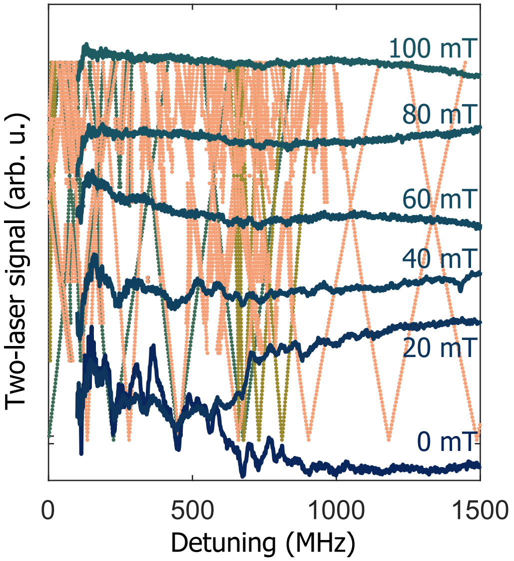

optical transitions preserve the nuclear spin, such that an optical transition between two hyperfine-coupled spin sublevels in ground and excited states is only allowed if both states involved have a component with identical nuclear spin projection m_i.

Table 6.1: **Effective-spin Hamiltonian parameters**. Parameters used to obtain the energy eigenstates in Fig. 6.3(c) and 6.4(b), based on the effective-spin Hamiltonians in Eqs. 6.1.

	$g_\parallel$	$g_\perp$	$a_\parallel$ (MHz)	$a_\perp$ (MHz)
ground	1.75	0	−228	165
excited	2.25	0	−220	50

6.7.3. Time-resolved measurement details

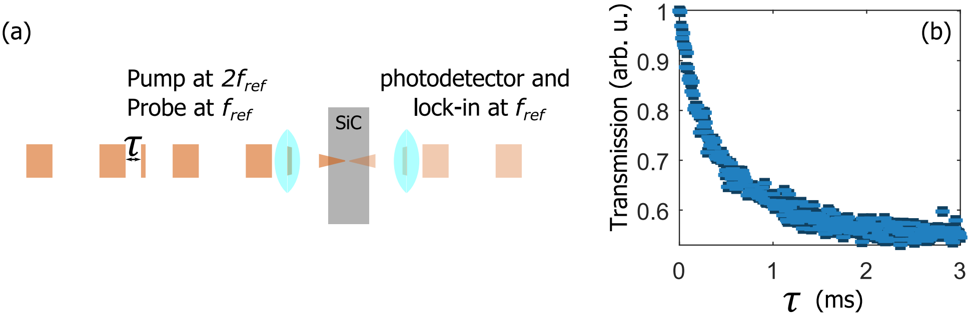

Figure 6.6: **Details of the time-resolved absorption experiments** (a) Measurement geometry for time-resolved absorption experiments. We measure the integrated transmitted laser beam signal in a photodetector with the help of a lock-in setup. We create pulse sequences of the type pump-probe-pump, such that in time the pump beam is modulated at twice the frequency of the probe pulse. In the lock-in we detect the component of the photodetector voltage modulated at the probe-pulse frequency. The probe pulse is 30 μs long, and two subsequent pump pulses are separated by a fixed recovery time of 15 ms (see also Sec. 6.6). (b) Lock-in signal as a function of the delay τ between pump and probe pulses. The lock-in signal decays as a function of the delay between pump and probe pulses. We fit this decay to a function of the type $I_{out} = Ae^{(-\tau/T_1)} + C$ to allow for a saturation of the transmission signal above zero at large delays.

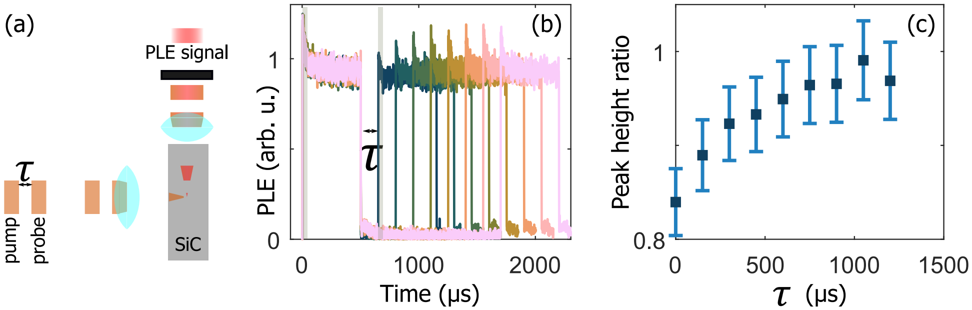

Figure 6.7: **Details of the time-resolved PLE experiments** (a) Measurement geometry for time-resolved PLE experiments. We measure the photons emitted by the sample into the phonon-sideband in a time-resolved manner with a single-photon counter. We create from a CW laser pump and probe pulses separated by a delay τ (see Sec. 6.6). Between the probe and the next pump pulse the sample is allowed to recover for a time that is at least 10 times larger than the measured relaxation time. (b) Photon emission by the sample versus measurement time. The photons are collected in a time-resolved manner, providing information on the dynamics of excitation, emission and spin relaxation of the defects. From each data set we subtract the background counts (such that we count 0 photons when the sample is not illuminated) and we normalize it by the 95th percentile of the data set. We determine the peak height ratio for each measurement run by calculating the ratio of the photon emission by the sample during the first 15 μs of illumination by probe and pump pulses respectively (gray shaded regions). The error in the peak height-ratio obtained is related to the Poisson statistics of the number of photons in each time bin, and close to 3%. (c) The peak height ratio as a function of the delay between the pump and probe pulses recovers in a monoexponential fashion. We fit this recover to a function of the type $I_{probe}/I_{pump} = 1 - Ae^{(-\tau/T_1)} + C$. The parameter A indicates that only partial darkening of the sample emission happens upon illumination (see also Sec. 4.5.1).

References

[1] J. R. Weber, W. Koehl, J. Varley, A. Janotti, B. Buckley, C. Van de Walle, and D. D. Awschalom, “Quantum computing with defects”, Proc. Natl. Acad. Sci. U.S.A. **107**, 8513 (2010).

[2] D. D. Awschalom, L. C. Bassett, A. S. Dzurak, E. L. Hu, and J. R. Petta, “Quantum spintronics: engineering and manipulating atom-like spins in semiconductors”, Science **339**, 1174 (2013).

[3] I. Aharonovich, D. Englund, and M. Toth, “Solid-state single-photon emitters”, Nat. Photon. **10**, 631 (2016).

[4] G. Wolfowicz, F. J. Heremans, C. P. Anderson, S. Kanai, H. Seo, A. Gali, G. Galli, and D. D. Awschalom, “Qubit guidelines for solid-state spin defects”, Nat. Rev. Mater. (2021).

[5] A. Chatterjee, P. Stevenson, S. De Franceschi, A. Morello, N. P. de Leon, and F. Kuemmeth, “Semiconductor qubits in practice”, Nat. Rev. Phys. **3**, 157 (2021).

[6] D. Awschalom et al., “Development of quantum interconnects (quics) for next-generation information technologies”, PRX Quantum **2**, 017002 (2021).

[7] S. Castelletto and A. Boretti, “Silicon carbide color centers for quantum applications”, Journal of Physics: Photonics **2**, 022001 (2020).

[8] W. B. Gao, A. Imamoglu, H. Bernien, and R. Hanson, “Coherent manipulation, measurement and entanglement of individual solid-state spins using optical fields”, Nat. Photonics **9**, 363 (2015).

[9] B. Hensen et al., “Loophole-free bell inequality violation using electron spins separated by 1.3 kilometres”, Nature **526**, 682 (2015).

[10] A. Sipahigil, K. D. Jahnke, L. J. Rogers, T. Teraji, J. Isoya, A. S. Zibrov, F. Jelezko, and M. D. Lukin, “Indistinguishable photons from separated silicon-vacancy centers in diamond”, Phys. Rev. Lett. **113**, 113602 (2014).

[11] P. V. Klimov, A. L. Falk, D. J. Christle, V. V. Dobrovitski, and D. D. Awschalom, “Quantum entanglement at ambient conditions in a macroscopic solid-state spin ensemble”, Sci. Adv. **1**, e1501015 (2015).

[12] M. E. Bathen and L. Vines, “Manipulating single-photon emission from point defects in diamond and silicon carbide”, Adv. Quantum Technol., 2100003 (2021).

[13] C. P. Anderson et al., “Electrical and optical control of single spins integrated in scalable semiconductor devices”, Science **366**, 1225 (2019).

[14] A. L. Crook et al., “Purcell enhancement of a single silicon carbide color center with coherent spin control”, Nano Lett. **20**, 3427 (2020).

[15] P. V. Klimov, A. L. Falk, B. B. Buckley, and D. D. Awschalom, “Electrically driven spin resonance in silicon carbide color centers”, Phys. Rev. Lett. **112**, 087601 (2014).

[16] G. Wolfowicz, C. P. Anderson, B. Diler, O. G. Poluektov, F. J. Heremans, and D. D. Awschalom, “Vanadium spin qubits as telecom quantum emitters in silicon carbide”, Sci. Adv. **6**, eaaz1192 (2020).

[17] L. Spindlberger et al., “Optical properties of vanadium in 4H silicon carbide for quantum technology”, Phys. Rev. Appl. **12**, 014015 (2019).

[18] B. Tissot and G. Burkard, “Spin structure and resonant driving of spin-1/2 defects in SiC”, Phys. Rev. B **103**, 064106 (2021).

[19] A. Csóré and A. Gali, “*Ab initio* determination of pseudospin for paramagnetic defects in SiC”, Phys. Rev. B **102**, 241201(R) (2020).

[20] B. Tissot and G. Burkard, "Hyperfine structure of transition metal defects in SiC", Phys. Rev. B, accepted (2021).

[21] C. M. Gilardoni, I. Ion, F. Hendriks, M. Trupke, and C. H. van der Wal, "Hyperfine-mediated transitions between electronic spin-1/2 levels of transition metal defects in SiC", New J. of Phys. **23**, 083010 (2021).

[22] P. V. Klimov, A. L. Falk, D. J. Christle, V. V. Dobrovitski, and D. D. Awschalom, "Quantum entanglement at ambient conditions in a macroscopic solid-state spin ensemble", Sci. Adv. **1**, e1501015 (2015).

[23] M. H. Abobeih, J. Randall, C. E. Bradley, H. P. Bartling, M. A. Bakker, M. J. Degen, M. Markham, D. J. Twitchen, and T. H. Taminiau, "Atomic-scale imaging of a 27-nuclear-spin cluster using a quantum sensor", Nature **576**, 411 (2019).

[24] M. Gulka et al., "Room-temperature control and electrical readout of individual nitrogen-vacancy nuclear spins", Nat. Commun. **12**, 4421 (2021).

[25] A. L. Falk, P. V. Klimov, V. Ivády, K. Szász, D. J. Christle, W. F. Koehl, Á. Gali, and D. D. Awschalom, "Optical polarization of nuclear spins in silicon carbide", Phys. Rev. Lett. **114**, 247603 (2015).

[26] M. Trupke, *Private communication*, 2021.

[27] M. Kunzer, H. D. Müller, and U. Kaufmann, "Magnetic circular dichroism and site-selective optically detected magnetic resonance of the deep amphoteric vanadium impurity in 6H-SiC", Phys. Rev. B **48**, 10846 (1993).

[28] J. Baur, M. Kunzer, and J. Schneider, "Transition metals in SiC polytypes, as studied by magnetic resonance techniques", Phys. Stat. Sol. A **162**, 153 (1997).

[29] B. Kaufmann, A. Dörnen, and F. S. Ham, "Crystal-field model of vanadium in 6H silicon carbide", Phys. Rev. B **55**, 13009 (1997).

[30] T. Bosma et al., "Identification and tunable optical coherent control of transition-metal spins in silicon carbide", npj Quantum Information **4**, 48 (2018).

[31] C. M. Gilardoni, T. Bosma, D. van Hien, F. Hendriks, B. Magnusson, A. Ellison, I. G. Ivanov, N. T. Son, and C. H. van der Wal, "Spin-relaxation times exceeding seconds for color centers with strong spin–orbit coupling in SiC", New J. of Phys. **22**, 103051 (2020).

[32] A. Csóré, A. Gällström, E. Janzén, and A. Gali, "Investigation of mo defects in 4H-SiC by means of density functional theory", Mater. Sci. For. **858**, 261 (2016).

[33] G. Zhang, Y. Cheng, J.-P. Chou, and A. Gali, "Material platforms for defect qubits and single-photon emitters", Appl. Phys. Rev. **7**, 031308 (2020).

[34] V. Ivády, A. Gällström, N. T. Son, E. Janzén, and A. Gali, "Asymmetric split-vacancy defects in SiC polytypes: a combined theoretical and electron spin resonance study", Phys. Rev. Lett. **107**, 195501 (2011).

[35] K. Beha, A. Batalov, N. B. Manson, R. Bratschitsch, and A. Leitenstorfer, "Optimum photoluminescence excitation and recharging cycle of single nitrogen-vacancy centers in ultrapure diamond", Phys. Rev. Lett. **109**, 097404 (2012).

[36] G. Wolfowicz, C. P. Anderson, A. L. Yeats, S. J. Whiteley, J. Niklas, O. G. Poluektov, F. J. Heremans, and D. D. Awschalom, "Optical charge state control of spin defects in 4H-SiC", Nat. Commun. **8**, 1876 (2017).

[37] O. V. Zwier, D. O'Shea, A. R. Onur, and C. H. van der Wal, "All–optical coherent population trapping with defect spin ensembles in silicon carbide", Sci. Rep. **5**, 10931 (2015).

[38] B. Tissot, *Private communication*, 2021.

[39] O. V. Zwier, *Two-laser spectroscopy and coherent manipulation of color-center spin ensembles in silicon carbide*, Zernike Institute PhD thesis series, ISSN 1570-1530 (University of Groningen, 2016).

[40] N. B. Manson and C. Wei, “Transient hole burning in NV centre in diamond”, J. Lumin. **58**, 158 (1994).

[41] C. Santori et al., “Coherent population trapping in diamond NV centers at zero magnetic field”, Opt. Express **14**, 7986 (2006).

[42] A. Abragam and B. Bleaney, *Electron paramagnetic resonance of transition ions*, International series of monographs on physics (Clarendon Press, Oxford, 1970).

[43] L.-M. Duan, M. D. Lukin, J. I. Cirac, and P. Zoller, “Long-distance quantum communication with atomic ensembles and linear optics”, Nature **414**, 413 (2001).

[44] M. D. Lukin, “Colloquium: trapping and manipulating photon states in atomic ensembles”, Rev. Mod. Phys. **75**, 457 (2003).

[45] F. Jelezko and J. Wrachtrup, “Single defect centres in diamond: a review”, Phys. Stat. Sol. (a) **203**, 3207 (2006).

[46] M. N. Makhonin, K. V. Kavokin, P. Senellart, A. Lemaitre, A. J. Ramsay, M. S. Skolnick, and A. I. Tartakovskii, “Fast control of nuclear spin polarization in an optically pumped single quantum dot”, Nat. Mater. **10**, 844 (2011).

[47] L. Childress, M. V. Gurudev Dutt, J. M. Taylor, A. S. Zibrov, F. Jelezko, J. Wrachtrup, P. R. Hemmer, and M. D. Lukin, “Coherent dynamics of coupled electron and nuclear spin qubits in diamond”, Science **314**, 281 (2006).

[48] C. Lei, S. Peng, C. Ju, M. H. Yung, and J. Du, “Decoherence control of nitrogen-vacancy centers”, Sci. Rep. **7**, 11937 (2017).

[49] Z.-H. Wang, G. de Lange, D. Ristè, R. Hanson, and V. V. Dobrovitski, “Comparison of dynamical decoupling protocols for a nitrogen-vacancy center in diamond”, Phys. Rev. B **85**, 155204 (2012).

[50] C. G. Yale, B. B. Buckley, D. J. Christle, G. Burkard, F. J. Heremans, L. C. Bassett, and D. D. Awschalom, “All-optical control of a solid-state spin using coherent dark states”, Proc. Natl. Acad. Sci. U.S.A. **110**, 7595 (2013).

[51] V. Ivády, P. V. Klimov, K. C. Miao, A. L. Falk, D. J. Christle, K. Szász, I. A. Abrikosov, D. D. Awschalom, and A. Gali, “High-fidelity bidirectional nuclear qubit initialization in SiC”, Phys. Rev. Lett. **117** (2016).

[52] V. Ivády, K. Szász, A. L. Falk, P. V. Klimov, D. J. Christle, E. Janzén, I. A. Abrikosov, D. D. Awschalom, and A. Gali, “Theoretical model of dynamic spin polarization of nuclei coupled to paramagnetic point defects in diamond and silicon carbide”, Phys. Rev. B **92** (2015).

[53] S. Yang et al., “High-fidelity transfer and storage of photon states in a single nuclear spin”, Nat. Photonics **10**, 507 (2016).

[54] G. Wolfowicz et al., “Atomic clock transitions in silicon-based spin qubits”, Nat. Nanotechnol. **8**, 561 (2013).

[55] S. Giménez-Santamarina, S. Cardona-Serra, J. M. Clemente-Juan, A. Gaita-Ariño, and E. Coronado, “Exploiting clock transitions for the chemical design of resilient molecular spin qubits”, Chemical Science **11**, 10718 (2020).

[56] M. Shiddiq, D. Komijani, Y. Duan, A. Gaita-Arino, E. Coronado, and S. Hill, “Enhancing coherence in molecular spin qubits via atomic clock transitions”, Nature **531**, 348 (2016).

[57] A. Gällström et al., “Optical identification and electronic configuration of tungsten in 4H and 6H-SiC”, Physica B: Condensed Matter **407**, 1462 (2012).

[58] B. Magnusson, A. Ellison, and E. Janzén, “Properties of the UD-1 deep-level center in 4H-SiC”, Mater. Sci. For. **389-393**, 505 (2002).

[59] M. Fox, *Optical properties of solids*, 2nd edition. (Oxford University Press, 2010).

[60] O. Axner, J. Gustafsson, N. Omenetto, and J. D. Winefordner, “Line strengths, A-factors and absorption cross-sections for fine structure lines in multiplets and hyperfine structure components in lines in atomic spectrometry — a user’s guide”, Spectrochimica Acta Part B: Atomic Spectroscopy **59**, 1 (2004).

chapter 7

Symmetry evolution of spin scattering processes in TMDs

Transition metal dichalcogenides (TMDs) combine interesting optical and spintronic properties in an atomically-thin material, where the light polarization can be used to control the spin and valley degrees-of-freedom for the development of novel opto-spintronic devices. These promising properties emerge due to their large spin-orbit coupling in combination with their crystal symmetries. Here, we provide simple symmetry arguments in a group-theory approach to unveil the symmetry-allowed spin scattering mechanisms, and indicate how one can use these concepts towards external control of the spin lifetime. We perform this analysis for both monolayer (inversion asymmetric) and bilayer (inversion symmetric) crystals, indicating the different mechanisms that play a role in these systems. We show that, in monolayer TMDs, electrons and holes transform fundamentally differently – leading to distinct spin-scattering processes. We find that one of the electronic states in the conduction band is partially protected by time-reversal symmetry, indicating a longer spin lifetime for that state. In bilayer and bulk TMDs, a hidden spin-polarization can exist within each layer despite the presence of global inversion symmetry. We show that this feature enables control of the interlayer spin-flipping scattering processes via an out-of-plane electric field, providing a mechanism for electrical control of the spin lifetime.

7.1. Introduction

Thin layers of transition metal dichalcogenides (TMD) offer the possibility of electrically and optically addressing spin, valley and layer degrees of freedom of charge carriers [2–6]. This has led to increased interest in these materials for applications in novel electronic and spintronic devices [7–12]. These properties arise from the symmetries of these intrinsically two-dimensional crystals, combined with the large spin-orbit coupling imprinted on electrons by the heavy transition metal atoms in the lattice [2, 5, 13]. Several experimental and theoretical works explore

---

Parts of this chapter have been published in Physical Review B **103**, 115410 (2021) [1].

the spin and valley lifetimes in monolayer, bilayer, and bulk TMDs, with often contrasting results. In the particular case of spin lifetime in TMDs, experimental values span over 5 orders of magnitude [14–19]. Group-theory-based analysis of the symmetries in this class of materials has been useful in unraveling their optical [14, 20, 21] and spintronic [22–24] properties, including how electrons, holes and excitons couple to phonons and external magnetic fields, for example. This approach can be very powerful to connect and compare seemingly contrasting results, as well as giving powerful symmetry-based predictions for the design of future experiments. However, literature still lacks a pedagogical derivation of the mechanisms leading to spin scattering in monolayer and, particularly, bilayer TMDs based solely on the symmetry of these materials. Moreover, a careful analysis and understanding of the impact of crystal symmetries on the spintronic properties of these materials can lead to better device engineering which exploit symmetry breaking for active control over the spin information.

Here, we apply group-theoretical considerations to obtain the symmetry of the electronic wavefunctions at the edges of the bands in these semiconductors, for both monolayer and bilayer systems. In order to do this, we use double groups to unravel the transformation properties of the Bloch wavefunctions including spin at the high symmetry points in the Brillouin zone (BZ), in the absence of external fields. Based on these results, we derive the first-order selection rules for spin-scattering processes in a single-particle picture. This allows us to determine how electron and hole spins couple to phonons and external fields, and which mechanisms dominate spin-flipping processes at low temperatures. Based on these results, we find that electrons and holes in these materials transform differently. In particular, a combination of rotational symmetry and strong spin-orbit coupling (SOC) strongly suppresses low-temperature spin scattering mechanisms for conduction-band electrons in monolayer TMDs. For bilayer (and few-layer) systems where individual layers are partially decoupled, we find that an electric field enhances interlayer spin-scattering processes, enabling electrical control of an optically created spin polarization. Despite being based on several approximations, the group-theoretical framework developed here allows us to intuitively understand various spin properties of this class of materials in a straight-forward manner, and in line with recent experimental results.

This paper is organized as follows: in part I, we focus on monolayer TMDs and their symmetries. We obtain the transformation properties of the Bloch wavefunctions including spin at the high-symmetry points of the BZ. Based on the symmetries of these wavefunctions, we derive which perturbations (electromagnetic fields and lattice phonon modes) can couple eigenstates with opposite spin, which allows us to determine the processes most likely to lead to spin flips at low temperatures. In part

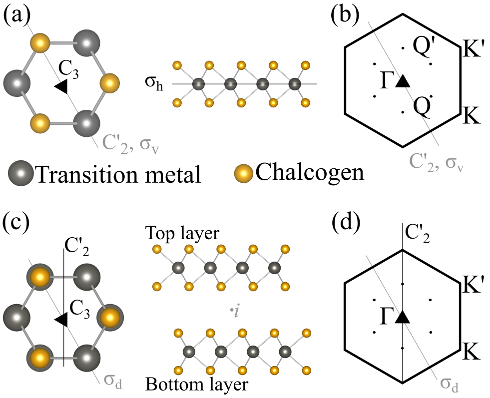

Figure 7.1: **Symmetry of the group of the wave vector at the K and K' points.** Lattice structure in real and reciprocal space for monolayer (a-b) and bilayer (c-d) TMDs. The symmetry of the full crystal (that is, the symmetry at the Γ point in the BZ) is D_{3h} for the monolayer, and D_{3d} for the bilayer, for which the symmetry operations are shown explicitly. Operations that, although present in the Γ point of the BZ, are absent in the K and K' points (b,d) are shown in light gray. The absence of these symmetry operations at the K and K' points reduces the symmetry at these points to the point groups C_{3h} for monolayers and D_3 for bilayers.

II, we repeat this analysis for bilayer TMDs. Finally we summarize the main conclusions and elaborate on the impact of our findings on past and future experiments in the field.

7.2. Monolayer TMD

7.2.1. Symmetries of the spatial eigenstates

In order to derive the spin-scattering selection rules at the edges of the bands, one must first obtain the symmetry properties of the eigenstates at the K and K' points of the BZ. These properties are determined by the point group describing the crystallographic symmetry at these points, the orbital character of the wavefunctions and the spin of the charge carriers in these states [13]. In this way, we can classify the electronic eigenstates at the band edges in these materials by their transformation properties, which are summarized by the irreducible representation (irrep) of the suitable point group.

A TMD monolayer (ML) is composed of transition metal and chalcogen atoms, arranged in a hexagonal lattice. Although the coordination between these atoms can vary, the most widely studied TMD polytypes (2H types) have a transition metal atom bound to 6 chalcogen atoms in a trigonal prismatic geometry (Fig. 7.1(a)), giving rise to the crystallographic point group D_{3h}. However, the edges of the valence and conduction bands in ML TMDs are located at the K and K' points of the BZ, where not all symmetries of the lattice are preserved. Here, only the three-fold rotational symmetry axis (C_3), the horizontal mirror plane (σ_h), and their combinations are valid symmetry operations, such that the wavefunctions at the K and K' points of the BZ transform according to the point group C_{3h} [13, 20, 22]. Figure 7.1(a) shows the symmetry operations at the K and K' points in black, and the additional symmetry operations in the Γ point in gray.

Ab-initio calculations and tight-binding models of these materials show that the orbital character of the electronic wavefunctions at the K and K' points are largely composed of the d-orbitals of the transition metal atoms [25–27]. The valence band wavefunctions are composed predominantly of linear combinations of $d_{x^2-y^2}$ and d_{xy} orbitals, while the conduction band wavefunctions are composed predominantly of the d_{z^2} orbital localized at the transition metal atoms. Based on this, we can visualize the transformation properties of the wavefunctions at the edges of the valence and conduction bands (Fig. 7.2(a)). To obtain the symmetry adapted eigenstates delocalized through the lattice, one takes the wavefunction centered at a single transition metal atomic-site and performs on it all symmetry-group operations. Due to the nonzero momentum at the K and K' point, a symmetry operation that changes the atomic-site of the orbital incurs an additional phase factor ($e^{\pm i2\pi/3}$). The total (symmetry-adapted) eigenstate is found by summing the results of all symmetry operations, including these phase factors (Fig. 7.2(b)). Additionally, a phase factor must also be considered when the atomic orbital itself is rotated, which depends on its azimuthal phase (represented by the color in Fig. 7.2(a,b)). The conduction band states at the K (K') points are formed mainly by d_{z^2} orbitals, which do not have any azimuthal phase. For these eigenstates, the only phase contribution when combining orbitals in different lattice sites arises from the winding of the k-vectors, leading to an out-of-site phase winding. Thus, the conduction band wavefunctions at the K (K') points transform according to the E'$_+$ (E'$_-$) irrep of the point group $C_{3\text{h}}$. In contrast, valence band states are formed predominantly by linear combinations of the $d_{x^2-y^2}$ and d_{xy} orbitals. These states are combined either as $(d_{x^2-y^2} + id_{xy})$ or as $(d_{x^2-y^2} - id_{xy})$, such that they have an orbital angular momentum-like phase winding within the atomic orbital (small arrows in 7.2(b), lower panel). This is in contrast with the out-of-site phase winding of the conduction band states, which gives implications to the spin-orbit coupling as explained in the following paragraphs. These linear combinations gain a phase factor of $e^{i2\pi/3}$ or $e^{-i2\pi/3}$, respectively, when subject to a three-fold rotation. Combined with the phase acquired due to the winding of the k-vector, this gives rise to a wavefunction composed of a fully in-phase linear combination of orbitals in adjacent lattice sites. In symmetry terms, these valence band wavefunctions transform as the A' irrep of the $C_{3\text{h}}$ point group. We note that, to describe the full microscopic character of the VB and CB wavefunctions, we should also consider contributions from the chalcogen orbitals. We chose not to do this in our approximation since it will not impact the symmetry character of the wavefunctions, although being relevant for quantitatively estimating matrix elements and energy splittings.

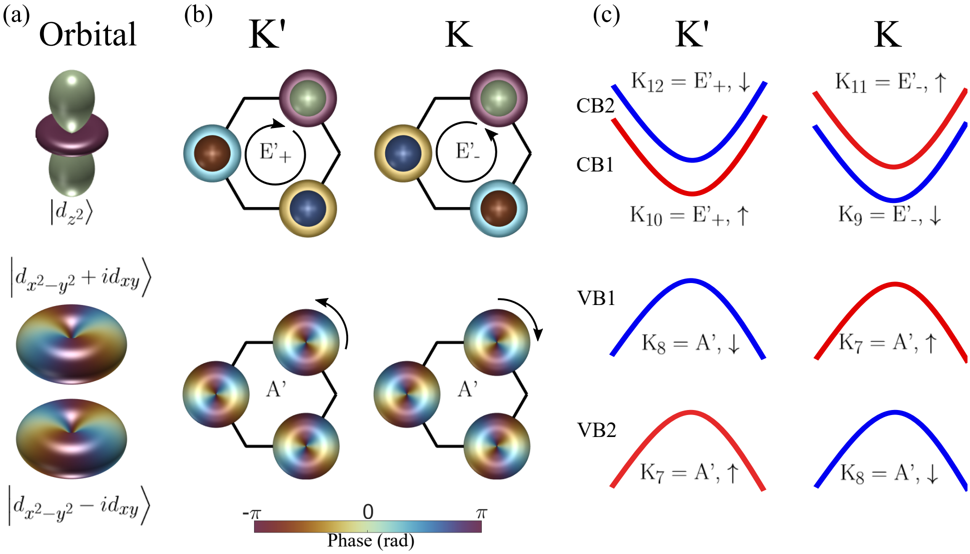

Figure 7.2: **Electronic wavefunctions at the K and K' points.** We can obtain the symmetry of the wavefunctions at the K and K' points by applying the symmetry operations of the system to the atomic d-orbitals localized around the TM atoms (a). In a monolayer, the electronic wavefunction at the edge of the conduction band is mainly composed of TM $|d_{z^2}\rangle$ atomic orbitals, which has constant azimuthal phase. (In (a) and (b), the magnitude of the wavefunction in real space is indicated by the surface, whereas the color corresponds to the azimuthal phase according to the scale in the color bar). When considering also the phase acquired due to translation, the electronic wavefunction at the K (K') point transforms as the E'$_+$ (E'$_-$) (b, top). In the valence band, the electronic wavefunction at the K and K' points is mostly composed of TM $|d_{x^2-y^2}\rangle$ and $|d_{xy}\rangle$ atomic orbitals, which can be combined into the spherical harmonics with $L = 2, m_l = \pm 2$. The phases acquired due to rotation of the spherical harmonics and translation cancel out, to give a final state that transforms as A' in both K and K' points (b, bottom). When considering also the properties of the spin under rotation, we obtain the symmetry of the spin-orbit split wavefunctions in valence and conduction bands by multiplying the irreps of (b) with the irreducible representations associated with spin up and down (K_7 and K_8, respectively) (c). Hybridization with other orbitals will not change the particular symmetry of the wavefunctions.

7.2.2. Symmetries of the spin-orbit coupled eigenstates

Finally, we must also take into account the electron and hole spin when obtaining the symmetry of the wavefuntions. This can be done by the use of a double group approach [28]. The symmetry of the spin-orbit coupled wavefunction can be obtained by taking the product $\Gamma_{spatial} \times \Gamma_{spin}$, where $\Gamma_{spatial}$ is the irrep describing the transformation properties of the spatial wavefunction, and Γ_{spin} describes the transformation properties of a spin $1/2$. A free spin up transforms as the irrep ${}^2\bar{E}_3$ of the double group $\bar{C}_{3\text{h}}$, whereas a free spin down (its time-reversal conjugate) transforms as irrep ${}^1\bar{E}_3$. Note here that a rotation by 2π adds a phase of -1 on the spin $1/2$ state. Based on this, we can obtain the symmetry properties of the spin-resolved wavefunctions at the edges of the valence and conduction bands at K and K' points, shown in Fig. 7.2(c).

All irreps of the double group $\bar{C}_{3h}$ are non-degenerate. This means that, as has been widely established [2, 5, 16, 22, 29], spin and valley degrees of freedom are coupled in both valence and conduction bands, giving rise to non-degenerate spin-polarized states. In this way, spin-up and spin-down states in both valence and conduction bands are split by a spin-orbit energy splitting. The sign and magnitude of this spin-orbit energy splitting depends on the material properties and cannot be obtained from this purely group-theoretical approach. Despite the differences between the various TMDs, however, this spin-orbit splitting is in general an order of magnitude larger in the valence band (usually hundreds of meVs) than in the conduction band (usually tens of meVs) [26]. We can understand this order-of-magnitude difference based on the considerations above. For wavefunctions in the valence band, the orbital angular momentum arises from the atomic orbitals themselves, which show an azimuthal phase winding around the transition metal nuclei (as indicated by the color and small arrows in the lower panel of Fig. 7.2(b)). This is clear if we rewrite the linear combinations of $d_{x^2-y^2}$ and d_{xy} in terms of spherical harmonics. This large and well defined orbital angular momentum, localized around the nuclei, gives rise to a large spin-orbit coupling energy. In contrast, in the conduction band states, there is an intercellular angular momentum arising from phase-winding between different lattice sites [30, 31]. In addition to that, we note that hybridization with p-orbitals also plays a role on the SOC magnitude in the valence band, which is not explicitly considered here.

We note that the ordering of states as depicted in Fig. 7.2(c) is valid for tungsten based TMDs; for molybdenum based TMDs, the order in energy of CB1 and CB2 is reversed [26]. Nonetheless, the group-theoretical considerations presented here do not depend on the energy ordering of states, and remains valid for both cases. In what follows, we will focus on the symmetry-restricted scattering processes for charge carriers in the top sub-band of the valence band (VB1, transforming as $\mathrm{K}_{7,8}$), and in the two sub-bands of the conduction band (CB1,2 transforming as K_{9-12}). We disregard the impact of states belonging to the lower sub-band of the valence band (VB2) due to the large SOC energy splitting of hundreds of meV. Nonetheless, since these states also transform as $\mathrm{K}_{7,8}$, this does not incur in any loss of generality since all scattering mechanisms obtained involving VB1 would be the same as the ones involving VB2.

7.2.3. Selection rules

Given the symmetries of the various wavefunctions at the band-edges, we can obtain the selection rules governing the spin-flipping scattering processes in these materials at low temperatures. According to Fermi's golden rule, a charge carrier in a state $|\psi_i\rangle$ can only scatter into a state $|\psi_f\rangle$ due to a perturbation H' if the matrix

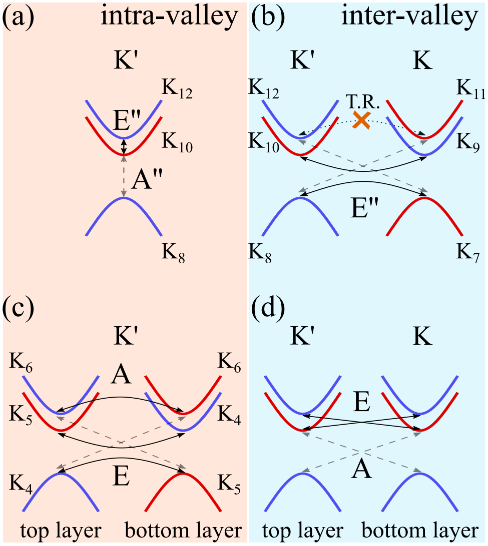

Figure 7.3: **Symmetries of spin-flipping scattering mechanisms in ML and BL TMDs.** In monolayer TMDs, only operators transforming as the E" and A" irrep of the C_{3h} group can lead to either intra-valley (a) or inter-valley (b) spin-flipping scattering processes. In these materials, states transforming as $K_{11,12}$ distinguish themselves since energy conserving scattering between these states is forbidden by time-reversal symmetry (see text). In contrast, in bilayer TMDs, additional inter-layer spin-flipping scattering processes arise (c,d), that can couple to external fields transforming as either the A or E irrep of the C_3 point group. Here, optical transitions are denoted by a dashed line.

element $\langle\psi_i|H'|\psi_f\rangle$ is nonzero. In symmetry terms, this means that the scattering is only possible when the product of irreps $\Gamma_i^* \otimes \Gamma_{H'} \otimes \Gamma_f$ contains the fully symmetric representation, *i.e.* A'. Here, $\Gamma_{i(f)}$ indicates the irrep of the initial (final) states, whereas $\Gamma_{H'}$ indicates the irrep of the operator responsible for the perturbation. Additionally, we note that phonons interact with electrons via the electric fields created by atomic displacements. In this way, we can also consider selection rules for phonon-driven transitions by looking at the symmetries of these electric fields. Using this, we can determine which spin-flipping scattering processes a perturbation can cause, just by looking at the symmetry of the perturbation. In the following we focus on the spin flipping mechanisms at the K and K' points of the BZ. In Sec. 7.5.1 we provide the product tables and the analysis also for spin-conserving transitions and scattering into other points of the BZ.

These selection rules (for spin-flipping transitions only) are presented comprehensively for a monolayer TMD in Fig. 7.3(a,b). Only operators transforming as A" and E" can generate spin-flipping transitions in ML TMDs. In Fig. 7.3, dashed arrows indicate optical transitions. These transitions can be actively driven by electromagnetic fields in the optical spectrum, or arise from radiative electron-hole recombination. Comparison with Tab. 7.1 shows that spin-flipping direct optical transitions are associated with absorption or emission of electric fields polarized perpendicular to the plane of the TMD layer. The creation of these so-called 'dark' excitons via this process has been demonstrated by illuminating the TMD monolayer with a parallel beam polarized out-of-plane [32]. Additionally, it has been shown that an external in-plane magnetic field can also 'brighten' these transitions, which can be

Table 7.1: Symmetries of operators and phonon modes according to the group of the wavevector at the K and K’ points for monolayer TMDs. LA (LO), TA (TO) and ZA (ZO) correspond to longitudinal, transverse and out-of-plane acoustic (optical) phonon modes, respectively, [13, 34]

C_{3h} irrep	EM fields	Acoustic phonons		Optical phonons	
		$\Gamma, \mathbf{q} = 0$	$K, \mathbf{q} \neq 0$	$\Gamma, \mathbf{q} = 0$	$K, \mathbf{q} \neq 0$
A’	$\mathbf{B}_\perp$		LA/TA	ZO	LO/TO
A”	$\mathbf{E}_\perp$	ZA		ZO	LO/TO
E’	$\mathbf{E}_\parallel$	LA/TA	LA/TA	LO/TO	LO/TO
E”	$\mathbf{B}_\parallel$		ZA	LO/TO	LO/TO/ZO

understood as a mixing between the two states belonging to CB1 and CB2 [20, 33].

Besides this spin-flipping optical transition, only operators transforming as E” of the C_{3h} point group can give rise to spin-scattering transitions between electronic states at the various band edges in ML TMDs. These operators correspond to magnetic fields in the plane of the ML, out-of-plane phonons at the K-point of the acoustic phonon band and optical phonons at both Γ- and K-points, for example (see Tab. 7.2). These phonon modes have energies on the order of hundreds of meVs [13, 34]. Thus, they will be very weakly populated at cryogenic temperatures, leading to a suppression of phonon-related upwards scattering processes. We note that this is valid also for Mo-based TMDs, despite their small SOC splitting between CB1 and CB2. In this case, even though the bands are close in energy, hot phonons are required to drive the transition. In contrast, downwards scattering processes ($K_{12} \rightarrow K_{10}$) can happen via the emission of a phonon even at low temperatures. This process should be distinct for molybdenum and tungsten based TMDs, since the order of the two bands are interchanged, while the optical transition used to generate a spin-valley population ($K_8 \rightarrow K_{12}$) is the same. Our analysis then indicates that, at low temperatures, the spin lifetime for electrons in molybdenum-based TMDs should be in principle longer than when compared to tungsten-based ones. This can be used to understand the long spin-lifetimes recently reported for $MoSe_2$, which persist up to room temperature [18]. We do note that in-plane magnetic fields will be more effective in driving intra-valley spin-flips of spins in the CB of Mo-based TMDs, when compared to W-based TMDs. This is because the energy splitting between CB1 and CB2 is much smaller in the former, and thus easier to overcome by Zeeman-like energy terms.

When considering inter-valley scattering processes, we must note that additional selection rules arise due to time-reversal symmetry and Kramers theorem. Kramers theorem states that, if time-reversal symmetry is preserved, wavefunctions connected by conjugation have the same energy, that is, a spin-up in a K valley and the corresponding spin-down in the K’ valley have the same energy. This implies that energy-conserving spin-flipping scattering processes between the K and

K' valleys (inter-valley) can only arise due to perturbations that break time-reversal symmetry. Transitions between time-conjugate pairs transforming as $K_7 \leftrightarrow K_8$ and $K_9 \leftrightarrow K_{10}$ can arise due to perturbations transforming as E". Since in-plane magnetic fields and K-phonons transforming as E" break time-reversal symmetry, these scattering processes are thus fully allowed, also by time-reversal (TR) symmetry [35]. This is in line with the experimental observations that identify out-of-plane K-phonons as the main sources of hole spin-valley depolarization in both W and Mo-based TMDs [3, 4, 16]. In contrast, transitions between states transforming as $K_{11} \leftrightarrow K_{12}$ are allowed – considering only spatial symmetry – when these states interact with external fields transforming as A". Out-of-plane electric fields and Γ-point phonons (see Tab. 7.1) preserve time-reversal symmetry, such that they cannot drive these transitions. In contrast, chiral K-phonons in the optical phonon bands [35] do break time-reversal symmetry and could drive these transitions. Nonetheless, these are high-energy phonon modes which are not populated at low temperatures.

The results of the last paragraph point to a fundamental asymmetry in the behavior of electron and hole spin scattering processes in these materials, and are in line with existing literature. For example, the selection rules obtained above provide an intuitive interpretation of theoretical and experimental results showing that, in Mo-based TMDs, phonon-related spin decay affects holes in VB1 much more efficiently than electrons in CB1 at low temperatures [18] (note that in Mo-based TMDs, states in CB1 transform as $K_{11,12}$). Additionally, despite the seemingly simplistic single-particle picture presented here, these results also provide an explanation for the recently observed asymmetry between bright and dark excitons concerning direct to indirect exciton scattering in W-based TMDs [36], where indirect excitons are composed of an electron and a hole in opposite valleys.

Finally, the selection rules derived in this section imply that, in monolayer TMDs, spin scattering is relatively robust with respect to the presence of noisy electric fields, such as randomly-distributed Coulomb scatterers and local strain. Only out-of-plane electric fields can cause spin-flipping scattering transitions; however, these transitions are either in the optical range – such that they must be actively driven or arise from electron-hole radiative recombination – or forbidden by the requirements of Kramers theorem. Thus, in the low energy scattering regime, local (due to the electrostatic environment, strain of the material, substrate effects, *etc.*) or global electric fields will have limited influence on the prevalence of various spin-scattering processes. This also means that spin scattering rates in ML TMDs should not be greatly influenced by the symmetry breaking created by a particular substrate. In contrast, in-plane magnetic fields, either extrinsic or intrinsic to the sample due to spin-active defects or nuclear spins, can cause both intra- and inter-valley spin flips. On the one hand, these results indicate that the spin-lifetimes in ML devices can be enhanced by ensuring a low concentration of deep-level spin-active lattice defects. On the other hand, they also indicate that control over the spin-polarization in these materials relies on externally applying magnetic fields, which is a slow and practically challenging process.

7.3. Bilayer TMDs

7.3.1. Symmetries and eigenstates

Figures 7.1(c,d) show the symmetries of bilayer 2H-TMDs in both real and reciprocal space (symmetry operations valid at the Γ point but absent at K and K' points are shown in gray). When compared to monolayer crystals, bilayer stacks of 2H-TMDs have some notable symmetry changes (see Fig. 7.1) [13]. In particular, bilayers lack a horizontal mirror plane, but do have an inversion point which brings the top layer into the bottom one. The presence of inversion symmetry means that, if we consider the entire stack, spin-valley coupling is not allowed to exist – electronic eigenstates at the K and K' points are spin degenerate. However, a local spin polarization of the bands may arise when inversion symmetry is present at a global scale, but is locally broken [37]. Since interlayer coupling is small compared to the other intrinsic energy scales in 2H-TMDs [29, 38], this local spin polarization arises within each ML making up the multilayer stacks, giving rise to a spin-valley-layer coupling [37, 38] which has been experimentally observed [39–42]. These results are evidence that the layers are partially decoupled, such that the system can be approximately described by a stack of two distinguishable monolayers whose crystallographic symmetry corresponds to point-group C_{3v}. The horizontal mirror plane and two-fold axes in Fig. 7.1(a,b) are not valid symmetry operations anymore, since the top and bottom environments of each layer differ. At the K and K' points, this symmetry is reduced to C_3, such that the electronic eigenstates at the edges of the bands in each layer transform as irreps of the double group $\bar{C}_3$. Since the bottom layer is inverted with respect to the top layer, the direction of phase winding of the eigenstates at the K and K' points of the BZ happens in opposite directions for each of the layers. This means that, at a given energy and at a given point of the BZ, eigenstates in different layers will have opposite orbital and spin angular momentum. This results in a alternating spin-valley ordering according to the layer number, *i.e.* the top of the valence band of the valley K of one layer has the same spin (and symmetry) as the top of the valence band of the opposite valley (K') of the adjacent layer. The resulting band structure, with the respective symmetries of each of the eigenstates, can be found in Sec. 7.5.2.

C_3 irrep	EM fields	Acoustic phonons		Optical phonons	
		$\Gamma, \mathbf{q} = 0$	$K, \mathbf{q} \neq 0$	$\Gamma, \mathbf{q} = 0$	$K, \mathbf{q} \neq 0$
A	$\mathbf{E}_\perp, \mathbf{B}_\perp$	ZA	LA/TA	ZO	LO/TO
E	$\mathbf{E}_\parallel, \mathbf{B}_\parallel$	LA/TA	LA/TA/ZA	LO/TO	LO/TO/ZO

Table 7.2: Symmetries of operators and phonon modes according to the group of the wavevector at the K and K’ points for bilayer TMDs.

7.3.2. Selection Rules

Treating the layers as distinguishable does not mean that they are fully independent. This means that the additional layer degree-of-freedom of TMD bilayers allows for additional inter-layer scattering processes. The intra-layer scattering processes are the same as the ones treated in detail in Sec. 7.2 and will not be repeated here. The selection rules for the inter-layer processes can be obtained in the same manner as before, now considering eigenstates and operators transforming as irreps of the double group $\bar{C}_3$. These additional spin-flipping scattering pathways are shown in Fig. 7.3(c,d).

Notably, the situation is drastically different for spins that are protected from energy-conserving spin-flipping scattering processes in a ML due to TR symmetry. These states transform as $\text{K}_{11,12}$ in a ML, and as K_6 in the bilayer. These charge carriers can now flip their spin by going from one layer into the other after interacting with an operator transforming as the A irrep of the point group C_3. This is because, for states in the K valley for example, a spin-up in the top layer and a spin-down in the bottom layer are not TR conjugates of each other, such that this scattering is not protected by TR symmetry. These scattering processes can arise from electromagnetic fields perpendicular to the layer plane, or due to out-of-plane acoustic phonons, which enhance the interlayer coupling (see Tab. 7.2). The availability of acoustic phonons at the Γ point at low temperatures and the presence of environmental charge noise implies that spins in CB2 (CB1) states in W based (Mo based) TMDs will suffer from significantly faster relaxation than their counterparts in ML TMDs.

Additional inter-layer energy conserving spin-flipping scattering processes also arise for states transforming as $\text{K}_{4,5}$. These processes must be driven by operators transforming as the E irrep of the point group C_3, corresponding to electromagnetic fields in the layer plane, and longitudinal and transverse acoustic phonon modes in the Γ point (Tab. 7.2). Again, these processes are expected to be prevalent even at low temperatures, leading to fast spin relaxation.

Finally, additional inter-layer spin-flipping processes that modify the linear momentum of charge carriers, *i.e.* inter-layer inter-valley processes (Fig. 7.3(d)), also arise. Due to requirements of momentum conservation, these processes must be accompanied by the emission or absorption of a K-phonon. Since they involve a change in the energy of the charge carriers of at least a few tens of meVs, upward scattering processes (CB1 → CB2) are likely suppressed at low temperatures. Relaxation of hot carriers accompanied by a spin flip and change in linear momentum (CB2 → CB1) however may arise via the emission of K-phonons transforming as E. Additionally, in-plane momentum transfer from the the CB at the K point of one layer into the VB at the K' point of the other layer (transitions denoted by dashed lines in Fig. 7.3(d)), are only allowed by second-order processes involving a photon and a phonon, transforming as the irrep A of group C_3. Therefore, these transitions should be suppressed at low temperatures.

The considerations in the past paragraphs imply that inter-layer scattering processes in bilayers (or few-layer stacks) lead to additional spin relaxation channels, hindering their application in the field of spintronics. However, they also imply that, in these materials, we have additional control over spin-flipping processes. Kerr rotation experiments in W based bulk TMDs show that the spin polarization in these materials decays within tens of ps [39]. Although much shorter than their counterparts in ML samples [19, 43, 44], these spin lifetimes still enable optical detection with high resolution. The group-theoretical results of this section indicate that externally applied electric fields, for example, could be used to manipulate the spin scattering rates in these materials, allowing us to turn these optically induced spin signals on/off electrically [38, 43]. Furthermore, in-plane and out-of-plane electric fields studies could unravel the charge character of the spin polarization. This results from the fact that in-plane electric fields will impact the spin-scattering processes of optically created holes, whereas out-of-plane electric fields will impact the scattering processes of optically created electrons.

Several approaches could be used to enhance the spin lifetimes in bilayer TMDs. On the one hand, we expect that encapsulating bilayer and bulk devices with van der Waals insulators like hBN will be important in reducing the electrostatic influence of substrate or adsorbed charges. The electrostatic environment of the BL could be further controlled by gating, possibly leading to longer spin lifetimes. On the other hand, heterostructures of TMDs will have different interlayer coupling and interfacial electric dipoles, depending on the particular combination of materials. Engineering these parameters, for example, could significantly suppress interlayer scattering mechanisms, leading to spin lifetimes more similar to those found in ML TMDs [45]. Additionally, the phonon spectra can also be modified by strain or the coupling to other van der Waals materials in heterostructures. In these devices, one could think of deliberately enhancing interlayer scattering processes via applied electric fields, combining the long spin lifetimes observed in ML TMDs with the enhanced electrical control of spin polarization provided by multilayer stacks.

Finally, we note that optical fields, such as circularly polarized light, will couple to a certain spin species according to the selection rules established above. When one applies an additional static electric or magnetic field that induces state mixing between different layers, this picture still does not change, *i.e.* circularly polarized light will still couple to the same spin species. However, when the optical field is turned off, the spin polarization will evolve according to the coupled Hamiltonian given by the perturbing static electric or magnetic field. This leads to an oscillation between the two states in time, reminiscent of what is observed in experiments studying the coherent evolution of optically created spins in III-V and II-VI semiconductors, for example [46, 47]. These (Rabi) oscillations will decay according to the characteristic spin relaxation and dephasing times [38].

7.4. Conclusion

Group theory is a powerful tool in the analysis of both equilibrium and out-of-equilibrium physical processes in a variety of materials, including TMDs. It allows one to gain insight into complex physical phenomena from a mathematically simple and comprehensive tool, without needing the specifics of the material of interest. Additionally, it allows one to broadly generalize insights obtained for one material or set of electronic eigenstates without additional computational cost. This approach is simplistic, and relies on a series of approximations. Nonetheless, we have shown here that it helps to unveil the fundamental processes at play in various experiments on TMDs. Even the behavior of excitons – for which the presence of exchange interaction is not encompassed by the single-particle approach undertaken here – can often be explained qualitatively by this group-theoretical model, by treating the electron and hole separately [20].

Based on this group-theoretical approach, we could identify fundamental symmetry properties of spins in TMDs and the subsequent selection rules for spin-scattering processes. In ML TMDs, charge carriers in each of the sub-bands of the CB behave in a fundamentally different manner: for one of the CB sub-bands, energy conserving spin-flipping processes are forbidden by TR symmetry, suppressing most of the phonon-related spin-flips at low temperatures. This is not true for the other sub-band of the CB, and for the VB, such that charge carriers in these states can have their spin flipped via scattering from a K-phonon. Thus, in Mo-based TMDs – where the states that are symmetry protected with regards to spin-flips sit at the bottom of the CB and the SOC splitting in the CB is smaller – magnetic impurities should be the main source of spin-flipping scattering at low temperatures. In these materials, the quality of the sample can drastically enhance the spin lifetime of electrons in the edge of the CB, possibly explaining the broad variation of spin lifetimes reported in literature. Additionally, we find that spin-scattering in ML TMDs is very robust with respect to electric fields, with only fields in the optical range actually giving rise to spin-flips, and for a restricted set of states. In contrast, in BL TMDs, all electronic states can undergo spin-flips after interacting with electric fields that cause interlayer momentum-conserving transitions. Thus, noisy electric fields, an inhomogeneous electrostatic environment, and acoustic phonons are expected to greatly suppress a spin polarization induced in these materials, and decrease their lifetime. Nonetheless, this feature can also be harnessed to gain control over optically created and detected spin polarization in these materials via electrostatic gating, for example. There, one can use an out-of-plane electric field to efficiently control the spin relaxation in these materials, making it a viable option for spin-based information processing.

Acknowledgments

This work was supported by the Zernike Institute for Advanced Materials and the Dutch Research Council (NWO, STU.019.014).

Author contributions

CMG and MG initiated the project. CMG and FH developed the theory. CMG and MG took the lead in the writing process. All authors contributed via discussion, and read and gave input into the manuscript.

7.5. Appendices

7.5.1. Eigenstates and selection rules for monolayer TMDs

Here, we present the derivation of the symmetry of the electronic eigenstates at the high symmetry points of the Brillouin Zone (BZ), and the subsequent symmetry restricted selection rules for spin scattering processes for the monolayer. The symmetries of the group of the wave vector at various points of the BZ were previously derived and can be found also in literature [13]. These symmetries are presented in more detail and can be visualized in Fig. 7.1 of the main text. At the Γ point of the BZ, wavefunctions have the symmetries of the point group $D_{3\mathrm{h}}$. At the K and K' points, this symmetry is reduced to $C_{3\mathrm{h}}$. At the Q and Q' points, it is further reduced to $C_{\mathrm{s}xy}$ (also denoted by $C_{1\mathrm{h}}$).

In order to account for the transformation properties of spin-half states, we make use of the double groups with the symmetries mentioned above [28]. The character tables referring to these double groups are shown explicitly in App. A. We obtain the symmetries of the electronic eigenstates at the high symmetry points of the BZ based on the symmetry of the crystal (Γ_{equiv}) and of the atomic orbitals most prevalent in each of the eigenstates (Γ_{orb}). Finally, we use the symmetries of these eigenstates to obtain the selection rules regarding spin-scattering processes.

Character tables

In Appendix A, we provide the character tables for the double groups of interest here. We denote the irreducible representations (irrep) by the point of the BZ associated with each particular group (Γ, K and Q). In parenthesis, we also provide the Mulliken symbol associated with each irrep. The irreps indicating the transformation properties of spin-1/2 states (or spin $N/2$, with odd N) are indicated by an overbar. The symbol ω corresponds to $e^{2\pi i/3}$, whereas ω^* corresponds to $e^{-2\pi i/3}$.

The character tables for the point groups $D_{3\mathrm{h}}$, $C_{3\mathrm{h}}$ and $C_{1\mathrm{h}}$ are presented, respectively, in Tabs. A.3, A.4, A.5.

Band structure and symmetry

As stated in the main text, the atomic orbital character of the electronic eigenstates in the high symmetry points of the BZ has been obtained in literature based on both tight-binding and density functional theory models [22, 26, 27]. Table 7.3 presents, for the three high symmetry points of the BZ, the point-group associated with the group of the wave vector (GWV) in column PG (for point-group), the atomic orbital character and its symmetry (Γ_{orb}) and the symmetry of the equivalent representation (Γ_{equiv}). Combined, this information allows us to obtain the symmetry of the delocalized Bloch wavefunction at each high-symmetry point of the BZ, given by $\Gamma_{\mathrm{spatial}}$. For the states in the K and K' points, this derivation is performed visually and explained thoroughly in the main text. For the valence band states in the K and K' points, the 2-fold degenerate atomic orbitals, combined with the 2-fold degenerate equivalent representation gives rise to a total of 4 spatial wavefunctions. Nonetheless, only those transforming as A' are of importance here, since the other ones (identified in parenthesis in the last column of Tab. 7.3) are much lower in energy, deep into the VB.

Table 7.3: Spatial character of the wavefunctions at edges of CB and VB at various points of the BZ of monolayer TMDs and their symmetries.

BZ point	PG	Atomic Orbital	Γ_{orb}	Γ_{equiv}	$\Gamma_{\text{spatial}} = \Gamma_{\text{equiv}} \otimes \Gamma_{\text{orb}}$
Γ, VB	$D_{3\text{h}}$	d_{z^2}	A_1'	$2\text{A}_1'$	$2\text{A}_1'$
K (K'), VB	$C_{3\text{h}}$	d_{xy,x^2-y^2}	$\text{E}_+' + \text{E}_-'$	$\text{E}_+' + \text{E}_-'$	$2\text{A}' + (\text{E}_+' + \text{E}_-')$
K (K'), CB	$C_{3\text{h}}$	d_{z^2}	A'	$\text{E}_+' + \text{E}_-'$	$\text{E}_+' + \text{E}_-'$
Q (Q'), CB	C_s^{xy}	d_{xy,x^2-y^2}	$2\text{A}'$	A'	$2\text{A}'$

The double groups $\bar{C}_{3\text{h}}$ and $\bar{C}_{1\text{h}}$ do not have any irrep of dimension 2 or greater. This means that all eigenstates in the K (K') or Q (Q') of the BZ are non-degenerate, even when spin is included. Degeneracy here is restricted to cases where two states have the same energy at the same point of the BZ (thus, states with the same energy but at K and K' points are not considered degenerate). In contrast, at the Γ point, spin up and down states must be degenerate in the presence of time-reversal symmetry, since all spin-1/2 irreps of the group $D_{3\text{h}}$ are two-fold degenerate.

In tables 7.4 and 7.5 we present, respectively for valence and conduction band states, the symmetries of the electronic eigenstates including spin. This is given in column $\Gamma_{\text{spatial}} \otimes \Gamma_{\text{spin}}$. This information is also compiled visually in Fig. 7.4. In order to obtain the selection rules between states at different points in the BZ (which have different symmetries), we must take into account the compatibility relations between different point groups [28]. These compatibility relations state how an irrep of a certain point group splits into a sum of irreps of a different group upon lowering the symmetry. In tables 7.4 and 7.5, we also provide the compatibility relations for the irreps corresponding to the electronic eigenstates at each high symmetry point of the BZ, for all three point groups of interest.

Table 7.4: For valence band wavefunctions, we can obtain the symmetry of the electronic eigenstates including spin by considering the irreps of the double groups. We present also the compatibility relations for irreps of the double groups D_{3h}, C_{3h} and C_{1h}.

BZ point	VB wf	$\Gamma_{\text{spatial}} \otimes \Gamma_{\text{spin}}$	D_{3h}	C_{3h}	C_{1h}
Γ	$A_1' \otimes E_{1/2}$	Γ_7		$K_7 + K_8$	$Q_3 + Q_4$
K (K')	$A' \otimes E_{1/2\uparrow}$	K_7	Γ_7		Q_3
	$A' \otimes E_{1/2\downarrow}$	K_8			Q_4

Table 7.5: For conduction band wavefunctions, we can obtain the symmetry of the electronic eigenstates including spin by considering the irreps of the double groups. We present also the compatibility relations for irreps of the double groups D_{3h}, C_{3h} and C_{1h}.

BZ point	CB wf	$\Gamma_{\text{orb}} \otimes \Gamma_{\text{spin}}$	D_{3h}	C_{3h}	C_{1h}
T (T')	$2A' \otimes E_{1/2\uparrow}$	$2Q_3$			
	$2A' \otimes E_{1/2\downarrow}$	$2Q_4$			
K(K')	$E_+' \otimes E_{1/2\uparrow}$	K_{10}	Γ_8		Q_3
	$E_-' \otimes E_{1/2\downarrow}$	K_9			Q_4
	$E_+' \otimes E_{1/2\downarrow}$	K_{12}	Γ_9		Q_4
	$E_-' \otimes E_{1/2\uparrow}$	K_{11}			Q_3

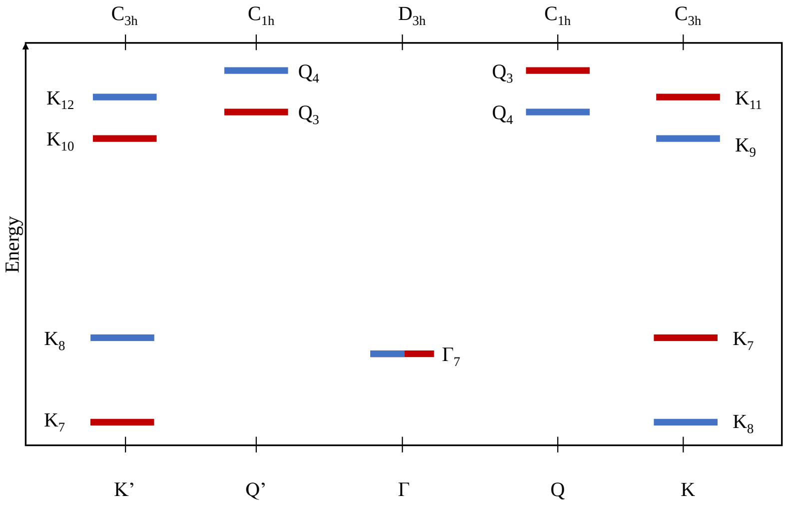

Figure 7.4: **Energy diagram ML** Blue lines represent spin down states, whereas red lines represent spin up states. Lines of both colors represent degeneracies protected by symmetry. The irreps associated with each state are those of the group of the wave vector at each point of the BZ, indicated at the top.

Possible scattering processes

According to Fermi's golden rule, the probability of going from an initial state $|\Psi_i\rangle$ to a final state Ψ_f when interacting with a perturbation H' is proportional to the matrix element $\langle\Psi_f|H'|\Psi_i\rangle$. This matrix element must be a scalar, that is, it must transform as the fully symmetric representation A (or A_{1g}). Thus, the matrix element can only be nonzero if the product of the representations $\Gamma_f^* \otimes \Gamma_{H'} \otimes \Gamma_i$, respectively indicating the symmetry properties of $|\Psi_f\rangle$, H' and $|\Psi_i\rangle$, contains the fully symmetric representation. When states $|\Psi_i\rangle$ and $|\Psi_f\rangle$ occur at different points in the BZ, we must consider their symmetry properties according to the point group of lowest symmetry by use of the previously mentioned compatibility relations. In this way, we can calculate all matrix elements which may be nonzero. We do so, and compile the results in table 7.6. Here, we classify the transitions with respect to whether they preserve spin or valley information. Furthermore, we identify the external electromagnetic field component which transforms according to each of the irreps and is, thus, capable of driving a certain transition. Optical transitions are highlighted in red. We highlight these transitions since they involve a large change in the energy of the electronic eigenstate and can be addressed by light. Thus, at low temperatures, these transitions will only happen upwards if actively driven (the downwards transition can happen via spontaneous emission of a photon). Furthermore, we did not present the selection rules for optical transitions that do not conserve linear momentum. These transitions happen in two steps, via the emission of a photon and a phonon, such that these processes are already considered here.

Finally, we highlight transitions between states that are each other's time-reversal conjugate in blue. Transitions between these states are further protected by time reversal symmetry, according to Kramers Theorem. If two states $|\Psi_i\rangle$ and $|\Psi_f\rangle$ are each other's time reversal conjugate (and they are both spin-$1/2$ states), the matrix element $\langle\Psi_f|H'|\Psi_i\rangle$ is nonzero only if the perturbation H' breaks time reversal symmetry. Examples of such perturbations are external magnetic fields, magnetic scatterers and circularly polarized light.

Table 7.6: Scattering mechanisms for electrons in K and K$'$ points in monolayer TMDs. The abbreviations Magn. and El. stand for magnetic and electrical fields, respectively, whereas i.p. and o.o.p stand for in plane and out of plane with respect to the TMD layer. We identify optical transitions in red, and transitions between states connected by time-reversal conjugacy in blue.

Sym. C_{3h}	Physical Mechanism	Intra-valley Spin cons.	Intra-valley Spin flip.	Inter-valley Spin cons.	Inter-valley Spin flip.
A'	Magn. o.o.p			$\mathrm{K_{VB}} \rightarrow \Gamma_{\mathrm{VB}}$ $\mathrm{K'_{VB}} \rightarrow \Gamma_{\mathrm{VB}}$ $\mathrm{K(K')_{CB}} \rightarrow \mathrm{Q(Q')_{CB}}$	
A''	El. o.o.p.		$\mathrm{K_{VB}} \rightarrow \mathrm{K_{CB1}}$ $\mathrm{K'_{VB}} \rightarrow \mathrm{K'_{CB1}}$		$\mathrm{K_{CB2}} \rightarrow \mathrm{K'_{CB2}}$ $\mathrm{(K, K)'_{CB}} \rightarrow \mathrm{Q(Q')_{CB}}$
E'_{+}	El. i.p. σ_{+}	$\mathrm{K_{VB}} \rightarrow \mathrm{K_{CB2}}$		$\mathrm{K_{CB1}} \rightarrow \mathrm{K'_{CB2}}$ $\mathrm{K_{CB2}} \rightarrow \mathrm{K'_{CB1}}$ $\mathrm{K(K')_{CB}} \rightarrow \mathrm{Q(Q')_{CB}}$	
E''_{+}	Magn. i.p.		$\mathrm{K_{CB1}} \rightarrow \mathrm{K_{CB2}}$ $\mathrm{K'_{CB2}} \rightarrow \mathrm{K'_{CB1}}$		$\mathrm{K'_{VB}} \rightarrow \mathrm{K_{VB}}$ $\mathrm{K'_{CB1}} \rightarrow \mathrm{K_{CB1}}$ $\mathrm{K'_{VB}} \rightarrow \Gamma_{\mathrm{VB}}$ $\mathrm{K(K')_{CB}} \rightarrow \mathrm{Q(Q')_{CB}}$
E'_{-}	El. i.p. σ_{-}	$\mathrm{K'_{VB}} \rightarrow \mathrm{K'_{CB2}}$		$\mathrm{K'_{CB1}} \rightarrow \mathrm{K_{CB2}}$ $\mathrm{K'_{CB2}} \rightarrow \mathrm{K_{CB1}}$ $\mathrm{K(K')_{CB}} \rightarrow \mathrm{Q(Q')_{CB}}$	
E''_{-}	Magn. i.p.		$\mathrm{K'_{CB1}} \rightarrow \mathrm{K'_{CB2}}$ $\mathrm{K_{CB2}} \rightarrow \mathrm{K_{CB1}}$		$\mathrm{K_{VB}} \rightarrow \mathrm{K'_{VB}}$ $\mathrm{K_{CB1}} \rightarrow \mathrm{K'_{CB1}}$ $\mathrm{K_{VB}} \rightarrow \Gamma_{\mathrm{VB}}$ $\mathrm{K(K')_{CB}} \rightarrow \mathrm{Q(Q')_{CB}}$

7.5.2. Eigenstates and selection rules for bilayer TMDs

Here, we repeat the steps described previously for the monolayer, now applied to the electronic states in bilayer TMDs.

Character tables

When we consider the full symmetry of the bilayer stack, the double groups of interest are $\bar{D}_{3\mathrm{d}}$ at the Γ point of the BZ, and $\bar{D}_3$ at the K and K' points. At the Q and Q' points, the double group of interest is $\bar{C}_2$. In the main text, we explain that it is interesting to look at the bilayer as a stack of two monolayers. In this case, the symmetry of the Γ point becomes $\bar{D}_3$, whereas the symmetry of the K and K' points becomes $\bar{C}_3$. The character tables for these point groups are presented in the Appendix A. These are, respectively, Tabs. A.6, A.7, A.8, A.9

Band structure and symmetries

As we did previously for the monolayer, in Tab. 7.7 we present the symmetry group associated with the different points of the BZ (PG column), the atomic orbital character of wavefunctions at these points, and their symmetries (Atomic Orbital and Γ_{orb} columns respectively), the irrep associated with the equivalent representation for wavefunctions at these points (Γ_{equiv}) and, lastly, the full symmtery of the spatial part of the Bloch wavefunctions at these points of the BZ ($\Gamma_{\mathrm{spatial}}$).

In tables 7.8 and 7.9 we present the symmetry of the Bloch wavefunctions at the high-symmetry points of the BZ including spin, as well as the compatibility relations necessary to obtain the selection rules for scattering between points of the BZ with different symmetries.

Table 7.7: Spatial character of the wavefunctions at edges of CB and VB at various points of the BZ of bilayer TMDs and their symmetries.

BZ point	PG	Atomic Orbital	Γ_{orb}	Γ_{equiv}	$\Gamma_{\mathrm{spatial}} = \Gamma_{\mathrm{equiv}} \otimes \Gamma_{\mathrm{orb}}$
Γ, VB	D_{3d}	d_{z^2}	A_{1g}	A_{1g}	A_{1g}
K (K'), VB	D_3	d_{xy,x^2-y^2}	E	E	$\mathrm{A}_1 + \mathrm{A}_2 + E$
K (K'), CB	D_3	d_{z^2}	A_1	E	E
Q (Q'), CB	C_2	d_{xy,x^2-y^2}	2A	A	2A

Table 7.8: For valence band wavefunctions, we can obtain the symmetry of the electronic eigenstates including spin by considering the irreps of the double groups. We present also the compatibility relations for irreps of the double groups $D_{3\mathrm{d}}$, D_3 and C_2 and C_3.

BZ point	VB wf	$\Gamma_{\mathrm{orb}} \otimes \Gamma_{\mathrm{spin}}$	D_{3d}	D_3	C_2	C_3
Γ	$\mathrm{A}_{1g} \otimes \mathrm{E}_{1/2}$	Γ_7		K_4	$\mathrm{Q}_3 + \mathrm{Q}_4$	$2\,(\mathrm{E}_{-1/2} + \mathrm{E}_{1/2})$
K	$\mathrm{A}_1 \otimes \mathrm{E}_{1/2}$	K_4	Γ_7		$(\mathrm{Q}_3 + \mathrm{Q}_4)$	$2\,(\mathrm{E}_{-1/2} + \mathrm{E}_{1/2})$

Table 7.9: For conduction band wavefunctions, we can obtain the symmetry of the electronic eigenstates including spin by considering the irreps of the double groups. We present also the compatibility relations for irreps of the double groups $D_{3\mathrm{d}}$, C_2 and C_3.

BZ point	CB wf	$\Gamma_{\mathrm{orb}} \otimes \Gamma_{\mathrm{spin}}$	D_{3d}	C_2	C_3
Q	$2A \otimes (\mathrm{Q}_3 + \mathrm{Q}_4)$	$2(\mathrm{Q}_3 + \mathrm{Q}_4)$		$2(\mathrm{Q}_3 + \mathrm{Q}_4)$	$2\,(\mathrm{E}_{-1/2} + \mathrm{E}_{1/2})$
K	$\mathrm{E} \otimes \mathrm{E}_{1/2}$	$\mathrm{K}_4 + \mathrm{K}_5 + \mathrm{K}_6$	$\Gamma_7 + \Gamma_8$	$2(\mathrm{Q}_3 + \mathrm{Q}_4)$	$2(\mathrm{E}_{-1/2} + \mathrm{E}_{1/2}) + 2\mathrm{E}_{3/2}$

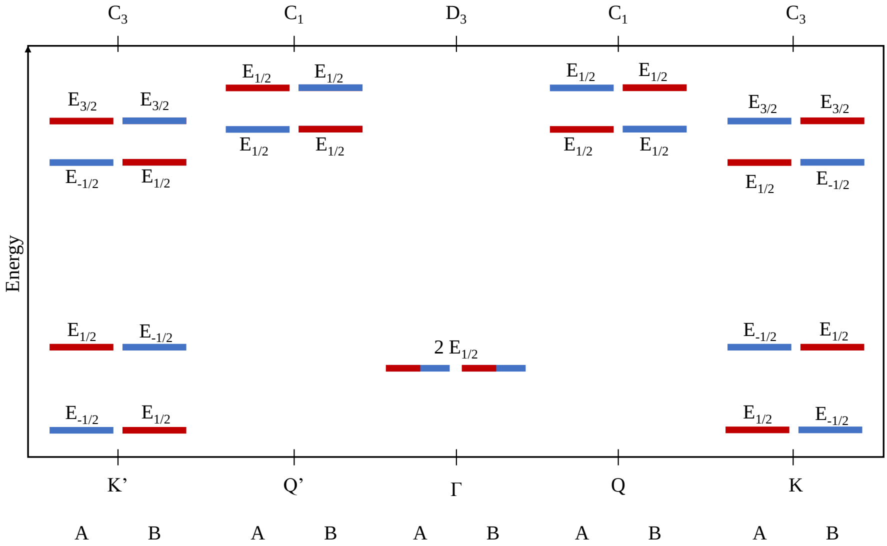

Figure 7.5: **Energy diagram BL** Blue lines represent spin down states, whereas red lines represent spin up states. Lines of both colors represent degeneracies protected by symmetry. The irreps associated with each state are those of the group of the wave vector at each high symmetry point, indicated at the top. State's localization at each monolayer is indicated by the A and B label at the bottom.

Possible scattering processes

Here, we derive the allowed scattering processes for electrons and holes at the high-symmetry points of the BZ. We focus specifically on processes leading to inter-layer scattering processes, since the intra-layer processes are analogous to those seen in monolayer TMDs (Sec. 7.5.1). Again, we highlight optical transitions in red. Since electronic states localized in different layers cannot be each other's time-reversal conjugates, here we observe no transitions that are protected by time-reversal symmetry.

Table 7.10: Inter-layer scattering mechanisms for electrons in K and K' points in bilayer TMD. The abbreviations Magn. and El. stand for magnetic and electrical fields, respectively, whereas i.p. and o.o.p stand for in plane and out of plane with respect to the TMD layers. We identify optical transitions in red.

Sym. C_3	Physical Mechanism	Intra-valley Spin cons.	Intra-valley Spin flip.	Inter-valley Spin cons.	Inter-valley Spin flip.
A	Magn. o.o.p El. o.o.p.		$K_{CB2} \rightarrow K_{CB2}$	$K_{VB} \rightarrow K'_{VB}$ $K_{CB1} \rightarrow K'_{CB1}$ $K_{CB2} \rightarrow K'_{CB2}$ $K_{VB} \rightarrow \Gamma_{VB}$ $K(K')_{CB} \rightarrow Q(Q')_{CB}$	$K(K')_{CB} \rightarrow Q(Q')_{CB}$
E_+	Magn. i.p. El. i.p.	$K_{VB} \rightarrow K_{CB1}$ $K_{CB1} \rightarrow K_{CB2}$	$K_{VB} \rightarrow K_{CB2}$ $K_{VB} \rightarrow K_{VB}$ $K_{CB1} \rightarrow K_{CB1}$		$K_{CB1} \rightarrow K'_{CB2}$ $K_{VB} \rightarrow \Gamma_{VB}$
E_-	Magn. i.p. El. i.p.	$K'_{VB} \rightarrow K'_{CB1}$ $K'_{CB1} \rightarrow K'_{CB2}$	$K'_{VB} \rightarrow K'_{CB2}$ $K'_{VB} \rightarrow K'_{VB}$ $K'_{CB1} \rightarrow K'_{CB1}$		$K'_{CB1} \rightarrow K_{CB2}$ $K'_{VB} \rightarrow \Gamma_{VB}$

References

[1] C. M. Gilardoni, F. Hendriks, C. H. van der Wal, and M. H. D. Guimarães, "Symmetry and control of spin-scattering processes in two-dimensional transition metal dichalcogenides", Phys. Rev. B **103**, 115410 (2021).

[2] D. Xiao, G. B. Liu, W. Feng, X. Xu, and W. Yao, "Coupled spin and valley physics in monolayers of MoS_2 and other group-VI dichalcogenides", Phys. Rev. Lett. **108**, 196802 (2012).

[3] K. F. Mak, K. He, J. Shan, and T. F. Heinz, "Control of valley polarization in monolayer MoS_2 by optical helicity", Nat. Nanotechnol. 7, 494 (2012).

[4] H. Zeng, J. Dai, W. Yao, D. Xiao, and X. Cui, "Valley polarization in MoS_2 monolayers by optical pumping", Nat. Nanotechnol. 7, 490 (2012).

[5] X. Xu, W. Yao, D. Xiao, and T. F. Heinz, “Spin and pseudospins in layered transition metal dichalcogenides”, Nat. Phys. **10**, 343 (2014).

[6] G. Wang, A. Chernikov, M. M. Glazov, T. F. Heinz, X. Marie, T. Amand, and B. Urbaszek, “Colloquium: excitons in atomically thin transition metal dichalcogenides”, Rev. of Mod. Phys. **90** (2018).

[7] K. F. Mak and J. Shan, “Photonics and optoelectronics of 2D semiconductor transition metal dichalcogenides”, Nature Photonics **10**, 216 (2016).

[8] Y. Liu, N. O. Weiss, X. Duan, H.-C. Cheng, Y. Huang, and X. Duan, “Van der Waals heterostructures and devices”, Nature Reviews Materials **1**, 16042 (2016).

[9] J. R. Schaibley, H. Yu, G. Clark, P. Rivera, J. S. Ross, K. L. Seyler, W. Yao, and X. Xu, “Valleytronics in 2D materials”, Nat. Rev. Mater. **1**, 16055 (2016).

[10] D. Zhong et al., “Van der Waals engineering of ferromagnetic semiconductor heterostructures for spin and valleytronics”, Sci. Adv. **3**, e1603113 (2017).

[11] Y. K. Luo, J. Xu, T. Zhu, G. Wu, E. J. McCormick, W. Zhan, M. R. Neupane, and R. K. Kawakami, “Opto-valleytronic spin injection in monolayer $\mathrm{MoS_2}$/few-layer graphene hybrid spin valves”, Nano Lett. **17**, 3877 (2017).

[12] A. Avsar, D. Unuchek, J. Liu, O. L. Sanchez, K. Watanabe, T. Taniguchi, B. Ozyilmaz, and A. Kis, “Optospintronics in graphene via proximity coupling”, ACS Nano **11**, 11678 (2017).

[13] J. Ribeiro-Soares, R. M. Almeida, E. B. Barros, P. T. Araujo, M. S. Dresselhaus, L. G. Cancado, and A. Jorio, “Group theory analysis of phonons in two-dimensional transition metal dichalcogenides”, Phys. Rev. B **90**, 115438 (2014).

[14] D. Lagarde, L. Bouet, X. Marie, C. R. Zhu, B. L. Liu, T. Amand, P. H. Tan, and B. Urbaszek, “Carrier and polarization dynamics in monolayer $\mathrm{MoS_2}$”, Phys. Rev. Lett. **112**, 047401 (2014).

[15] C. Mai, Y. G. Semenov, A. Barrette, Y. Yu, Z. Jin, L. Cao, K. W. Kim, and K. Gundogdu, “Exciton valley relaxation in a single layer of $\mathrm{WS_2}$ measured by ultrafast spectroscopy”, Phys. Rev. B **90**, 041414(R) (2014).

[16] W. T. Hsu, Y. L. Chen, C. H. Chen, P. S. Liu, T. H. Hou, L. J. Li, and W. H. Chang, “Optically initialized robust valley-polarized holes in monolayer $\mathrm{WSe_2}$”, Nat. Commun. **6**, 8963 (2015).

[17] L. Y. Yang, N. A. Sinitsyn, W. B. Chen, J. T. Yuan, J. Zhang, J. Lou, and S. A. Crooker, “Long-lived nanosecond spin relaxation and spin coherence of electrons in monolayer $\mathrm{MoS_2}$ and $\mathrm{WS_2}$”, Nat. Phys. **11**, 830 (2015).

[18] M. Ersfeld, F. Volmer, P. de Melo, R. de Winter, M. Heithoff, Z. Zanolli, C. Stampfer, M. J. Verstraete, and B. Beschoten, “Spin states protected from intrinsic electron-phonon coupling reaching 100 ns lifetime at room temperature in $\mathrm{MoSe_2}$”, Nano Lett. **19**, 4083 (2019).

[19] X. Song, S. Xie, K. Kang, J. Park, and V. Sih, “Long-lived hole spin/valley polarization probed by kerr rotation in monolayer wse2”, Nano Lett. **16**, 5010 (2016).

[20] C. Robert et al., “Fine structure and lifetime of dark excitons in transition metal dichalcogenide monolayers”, Phys. Rev. B **96**, 155423 (2017).

[21] C. Robert et al., “Measurement of the spin-forbidden dark excitons in $\mathrm{MoS_2}$ and $\mathrm{MoSe_2}$ monolayers”, Nat. Commun. **11**, 4037 (2020).

[22] Y. Song and H. Dery, “Transport theory of monolayer transition-metal dichalcogenides through symmetry”, Phys. Rev. Lett. **111**, 026601 (2013).

[23] A. Kormányos, V. Zóyomi, V. I. Fal’ko, and G. Burkard, “Tunable Berry curvature and valley and spin Hall effect in bilayer $\mathrm{MoS_2}$”, Phys. Rev. B **98**, 035408 (2018).

[24] J. Forste et al., “Exciton g-factors in monolayer and bilayer WSe_2 from experiment and theory”, Nat. Commun. **11**, 4539 (2020).

[25] J. Silva-Guillén, P. San-Jose, and R. Roldán, “Electronic band structure of transition metal dichalcogenides from ab initio and slaterâ€“koster tight-binding model”, Applied Sciences **6**, 284 (2016).

[26] A. Kormányos, G. Burkard, M. Gmitra, J. Fabian, V. Zóyomi, N. D. Drummond, and V. Fal’ko, “**K p** theory for two-dimensional transition metal dichalcogenide semiconductors”, 2D Materials **2**, 022001 (2015).

[27] G.-B. Liu, W.-Y. Shan, Y. Yao, W. Yao, and D. Xiao, “Three-band tight-binding model for monolayers of group-VIB transition metal dichalcogenides”, Phys. Rev. B **88**, 085433 (2013).

[28] M. Dresselhaus, G. Dresselhaus, and A. Jorio, *Group theory, Application to the physics of condensed matter* (Springer-Verlag Berlin Heidelberg, 2008).

[29] C. Jiang, F. Liu, J. Cuadra, Z. Huang, K. Li, A. Rasmita, A. Srivastava, Z. Liu, and W. B. Gao, “Zeeman splitting via spin-valley-layer coupling in bilayer $MoTe_2$”, Nat. Commun. **8**, 802 (2017).

[30] G. Aivazian et al., “Magnetic control of valley pseudospin in monolayer WSe_2”, Nat. Phys. **11**, 148 (2015).

[31] A. Srivastava, M. Sidler, A. V. Allain, D. S. Lembke, A. Kis, and A. Imamo□lu, “Valley zeeman effect in elementary optical excitations of monolayer WSe_2”, Nat. Phys. **11**, 141 (2015).

[32] G. Wang et al., “In-plane propagation of light in transition metal dichalcogenide monolayers: optical selection rules”, Phys. Rev. Lett. **119**, 047401 (2017).

[33] X. X. Zhang et al., “Magnetic brightening and control of dark excitons in monolayer WSe_2”, Nat. Nanotechnol. **12**, 883 (2017).

[34] X. Zhang, X. F. Qiao, W. Shi, J. B. Wu, D. S. Jiang, and P. H. Tan, “Phonon and raman scattering of two-dimensional transition metal dichalcogenides from monolayer, multilayer to bulk material”, Chem. Soc. Rev. **44**, 2757 (2015).

[35] L. Zhang and Q. Niu, “Chiral phonons at high-symmetry points in monolayer hexagonal lattices”, Phys. Rev. Lett. **115**, 115502 (2015).

[36] Y. C. Wu, S. Samudrala, A. McClung, T. Taniguchi, K. Watanabe, A. Arbabi, and J. Yan, “Up- and down-conversion between intra- and intervalley excitons in waveguide coupled monolayer WSe_2”, ACS Nano **14**, 10503 (2020).

[37] X. W. Zhang, Q. H. Liu, J. W. Luo, A. J. Freeman, and A. Zunger, “Hidden spin polarization in inversion-symmetric bulk crystals”, Nat. Phys. **10**, 387 (2014).

[38] Z. Gong, G. B. Liu, H. Yu, D. Xiao, X. Cui, X. Xu, and W. Yao, “Magnetoelectric effects and valley-controlled spin quantum gates in transition metal dichalcogenide bilayers”, Nat. Commun. **4**, 2053 (2013).

[39] M. H. D. Guimaraes and B. Koopmans, “Spin accumulation and dynamics in inversion-symmetric van der Waals crystals”, Phys. Rev. Lett. **120**, 266801 (2018).

[40] J. M. Riley et al., “Direct observation of spin-polarized bulk bands in an inversion-symmetric semiconductor”, Nature Physics **10**, 835 (2014).

[41] J. Ye, Y. Li, T. Yan, G. Zhai, and X. Zhang, “Ultrafast dynamics of spin generation and relaxation in layered WSe_2”, J Phys Chem Lett. **10**, 2963 (2019).

[42] Y. Li, X. Wei, J. Ye, G. Zhai, K. Wang, and X. Zhang, “Gate-controlled spin relaxation in bulk WSe_2 flakes”, AIP Advances **10**, 045315 (2020).

[43] A. M. Jones, H. Y. Yu, J. S. Ross, P. Klement, N. J. Ghimire, J. Q. Yan, D. G. Mandrus, W. Yao, and X. D. Xu, “Spin-layer locking effects in optical orientation of exciton spin in bilayer WSe_2”, Nat. Phys. **10**, 130 (2014).

[44] F. Volmer, S. Pissinger, M. Ersfeld, S. Kuhlen, C. Stampfer, and B. Beschoten, “Intervalley dark trion states with spin lifetimes of 150 ns in WSe_2”, Phys. Rev. B **95**, 235408 (2017).

[45] P. Rivera, H. Yu, K. L. Seyler, N. P. Wilson, W. Yao, and X. Xu, “Interlayer valley excitons in heterobilayers of transition metal dichalcogenides”, Nat. Nanotechnol. **13**, 1004 (2018).

[46] J. M. Kikkawa, I. P. Smorchkova, N. Samarth, and D. D. Awschalom, “Room-temperature spin memory in two-dimensional electron gases”, Science **277**, 1284 (1997).

[47] A. V. Kimel, F. Bentivegna, V. N. Gridnev, V. V. Pavlov, R. V. Pisarev, and T. Rasing, “Room-temperature ultrafast carrier and spin dynamics in GaAs probed by the photoinduced magneto-optical Kerr effect”, Phys. Rev. B **63**, 235201 (2001).

chapter 8

Conclusion and afterword

Our goal in this work was not to deliver an industry-ready material platform for quantum communication. Instead, we aimed at shining light on the relationship between the microscopic structure of defect centers and various important figures of merit for quantum-based applications. These results provide insight useful for recently suggested novel approaches towards the engineering of defects based on application-specific requirements [1, 2]. The possibility of various valence states associated with transition metal (TM) impurities and the strong localization of the active spins around the impurity leads to a situation where the probable optical and electronic properties of a multitude of possible defect centers can be rationalized based on simple and computationally inexpensive group-theoretical considerations. Similar approaches should be considered as an initial filter in the design of novel defect centers with desirable properties, in order to generate a pool of potential candidates to be further explored with *ab initio* or experimental means. Below, we present a summary of some lessons learned based on this work for electronic states localized at transition metal ions. These lessons are general and could be of relevance for related systems and materials, such as organometallic centers and TM impurities in semiconductors with hexagonal symmetry. Additionally, we present the immediate challenges concerning the direct application of TM defects in SiC for quantum communication applications, and how these might be mitigated in other defect centers and material platforms.

Lessons for TM-localized electronic states

- An odd number of electrons occupying doubly degenerate transition-metal *d*-orbitals in geometries with axial rotational symmetry give rise to Kramers doublet states due to the strong spin-orbit coupling arising from the TM. When isolated – in our case, when the nuclear spin can be neglected – these electronic states are protected from direct transitions between effective-spin-up and down, leading to robust electronic spins with long spin-relaxation times and zero dipole moments for interactions with magnetic or electric fields.

- Thermal population of localized vibrational modes (analogous to molecular vibrational modes) leads to significant spin relaxation of TM defects in SiC at high temperatures. Any attempt to extend the operational temperature of

TM defects in solids must rely on defect engineering to increase the energy of the localized vibrational modes. Alternatively, one could also consider suppressing the phonon population at the relevant energies via phononic device engineering.

- Interaction between the electronic spin and a central nuclear spin may be an important resource for controlling the electronic-spin state via magnetic and electric microwave excitation. There is an important trade-off, however, between the possibility of spin control and spin relaxation due to interactions with the environment, and this additional control pathway is concurrent with significantly shorter spin-relaxation times. This is exemplified by the shorter spin-relaxation times observed for V defects (for which 99% of the naturally abundant isotopes have non-zero nuclear spin) when compared to Mo defects (for which $\sim$ 75% of naturally abundant isotopes have zero nuclear spin).
- The interaction between electronic states and environmental perturbations depends on the particular symmetry properties of the electronic states themselves. Thus, defects with various accessible optically excited states may show optical transition lines that vary in how susceptible they are to varying local electric fields. This may offer a path towards the engineering of defects with narrow and highly stable optical linewidths in crystals that lack inversion symmetry.

Challenges and opportunities for implementation of TM defects in SiC for quantum-based applications

Based on the work presented in this thesis, it becomes clear that direct application of TM defects as a material platform for telecom-compatible quantum repeaters requires further characterization steps. For V defects in particular, characterization of spin-relaxation and coherence properties at millikelvin temperatures, as well as the development of protocols for high-fidelity optical or microwave initialization of the nuclear spin are the most urgent developments to be tackled. In the few-kelvin range, for which we provide experimental data in this thesis, the near-millisecond spin-relaxation times (significantly shorter than observed for Mo defects with nuclear spin zero), and the large Hilbert space associated with the hyperfine-coupled ground-state Kramers doublet lead to incomplete optical spin initialization, severely limiting the fidelities of light-matter entanglement protocols. Thus, any future application of these defect centers will necessarily be based on accessible and affordable dilution-fridge technology or advanced optical pumping schemes.

Another pressing question that has been only briefly mentioned so far is whether the stability of spin-coherence parameters of V defects depends on the doping level of the SiC host material. It is well known that V is a very effective amphoteric impurity in SiC, meaning it can exist within the host material in various charge configurations. On the one hand, this property may be useful for long-term storage of quantum states in nuclear spins via ionization of the defects into an electron-spin-free configuration enabled by device integration with electrostatic control. On the other hand, it calls for a better understanding of how the charge dynamics of these defect centers impacts their spin-coherence properties, and how to control this via Fermi-level engineering.

Despite these challenges, V defects in SiC still present themselves as competitive platforms due to their favorable optical properties. Single implanted V defects have been observed with relatively narrow optical transition lines that are stable over the course of hours, demonstrating that these defects are likely to preserve their optical properties when integrated into photonic or electronic devices [3].

Related systems and materials

Other TM defects in SiC A systematic investigation of the series of defects with increasing mass composed of V, Mo, and W (and also Nb and Ta) defects in SiC would consolidate our findings. These elements all belong to groups 5 and 6 in the periodic table, such that they are contenders for forming defects with the same charge state and analogous electronic structures to each other. Tungsten in particular is known to form stable and optically active defects in SiC. When compared to Mo and V, W is heavier, which may lead to defect centers with larger spin-orbit-related energy splittings. Additionally, the larger mass of W with respect to Mo could lead to more energetic vibrational modes, possibly extending the temperature range for operation of these defect centers. Tungsten defects in SiC are still poorly characterized with respect to optical and spin properties. Nonetheless, we know that these defects have optical transitions between the Mo and V-related lines and a ground state composed of an odd number of active electronic spins [4]. The small distance between the optical transition lines of these defects and the O-band ($\sim$ 10 meV for 4H-SiC) could potentially be overcome by embedding these impurities in other SiC polytypes. Like Mo, W atoms appear in a variety of naturally abundant isotopes, from which most have zero nuclear spin. The remaining W isotopes have a nuclear spin-1/2. Thus, Mo and W defects in SiC obtained during growth or via ion implantation with isotopically purified precursors may allow for defect centers with deterministic zero or non-zero nuclear spins, depending on the desired properties of the defect centers. For example, the uniaxial magnetic field sensitivity of Mo and V defects could be interesting for applications in magnetic field sensing, and these would most likely benefit from a nuclear-spin-free environment that warrants a linear dependence between the Zeeman energy levels and the external magnetic field. In contrast, defects with a non-zero nuclear spin could lead to robust optically addressable hybrid registers with long spin-coherence times, if the challenges involved with initializing the nuclear spin can be overcome. Multi-photon protocols to initialize the nuclear spin will likely be more easily implemented in systems with nuclear spin-1/2, in contrast to vanadium's nuclear spin-7/2.

Alternative material platforms Transition metal impurities in other semiconductor materials with hexagonal symmetry could behave similarly to the defect centers studied in this thesis. In particular, we point out that TM impurities are also stable in II-VI semiconductors (ZnSe, CdSe, ZnTe, and CdTe), with some being optically active in the infrared and near-infrared ranges of the spectrum [5]. Initial characterization of these defect centers with respect to charge stability, optical transition energies, and ground-state spin parameters was performed in the end of the last century. We could, however, find no further thorough investigation focused on observing and characterizing optical control of spin coherences in these platforms. These semiconductors can be grown from isotopically purified precursors, providing host materials with a nuclear spin-free environment that are crucial for extending the spin-coherence times of embedded defect centers. Although these materials are not as widely used in the semiconductor industry as Si and SiC, the larger mass of the lattice atoms could lead to defects with larger vibrational energies, potentially enabling quantum operation at higher temperatures.

Another class of relevant hexagonal semiconductors and insulators, namely two-dimensional materials like TMDs and hBN, could also host defects with analogous behavior to those studied in this thesis. These material platforms offer less flexibility in terms of large-scale materials-processing technologies but could be of importance for the integration into two-dimensional-materials-based heterostructures and circuits.

References

[1] L. C. Bassett, A. Alkauskas, A. L. Exarhos, and K.-M. C. Fu, “Quantum defects by design”, Nanophotonics **8**, 1867 (2019).

[2] G. Wolfowicz, F. J. Heremans, C. P. Anderson, S. Kanai, H. Seo, A. Gali, G. Galli, and D. D. Awschalom, “Qubit guidelines for solid-state spin defects”, Nat. Rev. Mater. (2021).

[3] G. Wolfowicz, C. P. Anderson, B. Diler, O. G. Poluektov, F. J. Heremans, and D. D. Awschalom, “Vanadium spin qubits as telecom quantum emitters in silicon carbide”, Sci. Adv. **6**, eaaz1192 (2020).

[4] A. Gällström et al., “Optical identification and electronic configuration of tungsten in 4H and 6H-SiC”, Physica B: Condensed Matter **407**, 1462 (2012).

[5] H.-J. S. J. Kreissl, “Transition-metal impurities in II-VI semiconductors: characterization and switching of charge states”, Joumal of Crystal Growth **161**, 239 (1996).

chapter A

Relevant character tables

A.1. $C_{3\text{v}}$ symmetry

Table A.1: **Character table of the double group** $\bar{C}_{3\text{v}}$. The upper bar represents an operation followed by a 2π rotation that brings a spin ↑ into $-$ ↑.

$\bar{C}_{3\text{v}}$	E	$\bar{E}$	$2C_3$	$2\bar{C}_3$	$3\sigma_v$	$3\bar{\sigma}_v$		
A_1	1	1	1	1	1	1	z	z^2, x^2+y^2
A_2	1	1	1	1	-1	-1	R_z	
E	2	2	-1	-1	0	0	$(x,y), (R_x, R_y)$	$(x^2-y^2, 2xy), (xz, yz)$
Γ_4	2	-2	1	-1	0	0		
$\Gamma_{5,6}$	1	-1	-1	1	i	$-i$		
	1	-1	-1	1	$-i$	i		

Table A.2: **Product table of the double group** $\bar{C}_{3\text{v}}$.

	A_1	A_2	E	Γ_4	Γ_5	Γ_6
A_1	A_1	A_2	E	Γ_4	Γ_5	Γ_6
A_2	A_2	A_1	E	Γ_4	Γ_6	Γ_5
E	E	E	$\text{A}_1 \oplus \text{A}_2 \oplus \text{E}$	$\Gamma_4 \oplus \Gamma_5 \oplus \Gamma_6$	Γ_6	Γ_5
Γ_4^*	Γ_4	Γ_4	$\Gamma_4 \oplus \Gamma_5 \oplus \Gamma_6$	$\text{A}_1 + \text{A}_2 + \text{E}$	E	E
$\Gamma_5^* = \Gamma_6$	Γ_6	Γ_5	Γ_4	E	A_1	A_2
$\Gamma_6^* = \Gamma_5$	Γ_5	Γ_6	Γ_4	E	A_2	A_1

A.2. $D_{3\mathrm{h}}$ symmetry

Table A.3: **Character table of the double group** $\bar{D}_{3\mathrm{h}}$.

$\bar{D}_{3\mathrm{h}}$	E	$\bar{E}$	$C_3^+ C_3^-$	$\bar{C}_3^+ \bar{C}_3^-$	$\sigma_h \bar{\sigma}_h$	$S_3^+ S_3^-$	$\bar{S}_3^+ \bar{S}_3^-$	$C'_{2i} \bar{C}'_{2i}$	$\sigma_{vi} \bar{\sigma}_{vi}$
Γ_1 (A'_1)	1	1	1	1	1	1	1	1	1
Γ_2 (A'_2)	1	1	1	1	1	1	1	−1	−1
Γ_3 (A''_1)	1	1	1	1	−1	−1	−1	1	−1
Γ_4 (A''_2)	1	1	1	1	−1	−1	−1	−1	1
Γ_5 (E'')	2	2	−1	−1	−2	1	1	0	0
Γ_6 (E')	2	2	−1	−1	2	−1	−1	0	0
Γ_7 ($\bar{\mathrm{E}}_1$)	2	−2	1	−1	0	$\sqrt{3}$	$-\sqrt{3}$	0	0
Γ_8 ($\bar{\mathrm{E}}_2$)	2	−2	1	−1	0	$-\sqrt{3}$	$\sqrt{3}$	0	0
Γ_9 ($\bar{\mathrm{E}}_3$)	2	−2	−2	2	0	0	0	0	0

A.3. $C_{3\mathrm{h}}$ symmetry

Table A.4: **Character table of the double group** $\bar{C}_{3\mathrm{h}}$. $\omega = e^{-2\pi i/3}$

$\bar{C}_{3\mathrm{h}}$	E	C_3^+	C_3^-	σ_h	S_3^+	S_3^-	$\bar{E}$	$\bar{C}_3^+$	$\bar{C}_3^-$	$\bar{\sigma}_h$	$\bar{S}_3^+$	$\bar{S}_3^-$
K_1 (A')	1	1	1	1	1	1	1	1	1	1	1	1
K_2 ($^2\mathrm{E}'$)	1	ω	ω^*	1	ω	ω^*	1	ω	ω^*	1	ω	ω^*
K_3 ($^1\mathrm{E}'$)	1	ω^*	ω	1	ω^*	ω	1	ω^*	ω	1	ω^*	ω
K_4 (A'')	1	1	1	−1	−1	−1	1	1	1	−1	−1	−1
K_5 ($^2\mathrm{E}''$)	1	ω	ω^*	−1	$-\omega$	$-\omega^*$	1	ω	ω^*	−1	$-\omega$	$-\omega^*$
K_6 ($^1\mathrm{E}''$)	1	ω^*	ω	−1	$-\omega^*$	$-\omega$	1	ω^*	ω	−1	$-\omega^*$	$-\omega$
K_7 ($^2\bar{\mathrm{E}}_3$)	1	$-\omega$	$-\omega^*$	i	$-i\omega$	$i\omega^*$	−1	ω	ω^*	$-i$	$i\omega$	$-i\omega^*$
K_8 ($^1\bar{\mathrm{E}}_3$)	1	$-\omega^*$	$-\omega$	$-i$	$i\omega^*$	$-i\omega$	−1	ω^*	ω	i	$-i\omega^*$	$i\omega$
K_9 ($^2\bar{\mathrm{E}}_2$)	1	$-\omega$	$-\omega^*$	$-i$	$i\omega$	$-i\omega^*$	−1	ω	ω^*	i	$-i\omega$	$i\omega^*$
K_{10} ($^1\bar{\mathrm{E}}_2$)	1	$-\omega^*$	$-\omega$	i	$-i\omega^*$	$i\omega$	−1	ω^*	ω	$-i$	$i\omega^*$	$-i\omega$
K_{11} ($^2\bar{\mathrm{E}}_1$)	1	−1	−1	i	$-i$	i	−1	1	1	$-i$	i	$-i$
K_{12} ($^1\bar{\mathrm{E}}_1$)	1	−1	−1	$-i$	i	$-i$	−1	1	1	i	$-i$	i

A.4. $C_{1\mathrm{h}}$ symmetry

Table A.5: **Character table of the double group $\bar{C}_{1\mathrm{h}}$.**

$\bar{C}_{1\mathrm{h}}$	E	σ_h	$\bar{E}$	$\bar{\sigma}_h$
Q_1 (A')	1	1	1	1
Q_2 (A'')	1	−1	1	−1
Q_3 ($^1\bar{\mathrm{E}}$)	1	i	−1	$-i$
Q_4 ($^2\bar{\mathrm{E}}$)	1	$-i$	−1	i

A.5. $D_{3\mathrm{d}}$ symmetry

Table A.6: **Character table of the double group $\bar{D}_{3\mathrm{d}}$.**

$\bar{D}_{3\mathrm{d}}$	E	$\bar{E}$	$2C_3$	$2\bar{C}_3$	$3C_2$	i	$2S_6$	$2\bar{S}_6$	$3\sigma_d$
Γ_1 (A_{1g})	1	1	1	1	1	1	1	1	1
Γ_2 (A_{2g})	1	1	1	1	−1	1	1	1	−1
Γ_3 (E_g)	2	2	−1	−1	0	2	−1	−1	0
Γ_4 (A_{1u})	1	1	1	1	1	−1	−1	−1	−1
Γ_5 (A_{2u})	1	1	1	1	−1	−1	−1	−1	1
Γ_6 (E_u)	2	2	−1	−1	0	−2	1	1	0
Γ_7 ($\bar{\mathrm{E}}_{1/2}$)	2	−2	1	−1	0	0	$\sqrt{3}$	$-\sqrt{3}$	0
Γ_8 ($\bar{\mathrm{E}}_{3/2}$)	2	−2	−2	2	0	0	0	0	0
Γ_9 ($\bar{\mathrm{E}}_{5/2}$)	2	−2	1	−1	0	0	$-\sqrt{3}$	$\sqrt{3}$	0

A.6. D_3 symmetry

Table A.7: **Character table of the double group $\bar{D}_3$.**

$\bar{D}_3$	E	$\bar{E}$	$2C_3$	$2\bar{C}_3$	$3C_2$	$3\bar{C}_2$
K_1 (A_1)	1	1	1	1	1	1
K_2 (A_2)	1	1	1	1	−1	−1
K_3 (E)	2	2	−1	−1	0	0
K_4 ($\bar{\mathrm{E}}_{1/2}$)	2	−2	1	−1	0	0
K_5 ($\bar{\mathrm{E}}_{-3/2}$)	1	−1	−1	1	i	$-i$
K_6 ($\bar{\mathrm{E}}_{+3/2}$)	1	−1	−1	1	$-i$	i

A.7. C_2 symmetry

Table A.8: **Character table of the double group** $\bar{C}_2$.

$\bar{C}_2$	E	C_2	$\bar{E}$	$\bar{C}_2$
Q_1 (A)	1	1	1	1
Q_2 (B)	1	-1	1	-1
Q_3 ($\bar{E}_{-3/2}$)	1	i	-1	$-i$
Q_4 ($\bar{E}_{+3/2}$)	1	$-i$	-1	i

A.8. C_3 symmetry

Table A.9: **Character table of the double group** $\bar{C}_3$. $\omega = e^{-2\pi i/3}$

$\bar{C}_3$	E	$\bar{E}$	C_3^+	C_3^-	$\bar{C}_3^+$	$\bar{C}_3^-$
K_1 (A)	1	1	1	1	1	1
K_2 (E_+)	1	1	ω	ω^*	ω	ω^*
K_3 (E_-)	1	1	ω^*	ω	ω^*	ω
K_4 ($\bar{E}_{-1/2}$)	1	-1	$-\omega$	$-\omega^*$	ω	ω^*
K_5 ($\bar{E}_{1/2}$)	1	-1	$-\omega^*$	$-\omega$	ω^*	ω
K_6 ($\bar{E}_{3/2}$)	1	-1	-1	-1	1	1

Acknowledgements

It was always natural for me, growing up in my house, to want to do a PhD. Little did I know, as a kid, how much effort it takes! The last four years were incredibly challenging, but also rewarding. Finishing this journey was only possible because I was able to rely on so many people along the way.

I am lucky to have been raised – personally and scientifically – among **female scientists**, and I can only start by acknowledging and thanking them for paving the way. To the closest and dearest of them, I owe a special thanks. To **my mother**, for showing me it is ok to be unapologetically good. To **my sister**, for being proof that unexpected paths are sometimes the most rewarding ones. And to **my abuela**, for staying hopeful and curious after 90 years on the road. Besides them, I have enjoyed the guidance and support of various strong female mentors who have shown me that being a female scientist is a plural experience. For this, I am thankful.

The PhD path is sometimes one of self-doubt. I could not have asked for a better supporter through it than **Caspar**. Your trust in my work was and still is so reassuring, and I truly feel like you are invested in my success. You have always challenged me and provided a much-needed outside perspective to my approaches. Most importantly, you've taught me that if the story is not easily understandable, there is probably a missing link. I am also thankful for the independence and agency you provided me during my PhD track; It was sometimes challenging, but I am sure I am a better professional because of it.

Remco, I can with all honesty say that the work in this thesis derives for a great part from my experience teaching with you. I learned so much during those two semesters teaching quantum concepts to chemistry students. It was such a fun experience. I truly admire how dedicated you are to your students. Here, I would like to also thank Professors **Shirin Faraji**, **Floris Zwanenburg** and **Mete Atatüre** for being in my reading committee, and **Jagoda Slawinska** and **Patrick van der Wel** for being in my defense committee.

During the last two years, I have had the pleasure of working within the context of the European consortium QuanTELCO. It has been incredibly rewarding to work alongside collaborators with so many different perspectives. I would like to thank all of the contributors, but especially **Michael Trupke**, **Adam Gali**, **Guido Burkard**, **Benedikt Tissot**, **András Csóré**, **Thomas Astner**, **Philipp Koller** for all the long, sometimes puzzling and often clarifying scientific discussions. Also, thank you to the Linköping team – and in particular **Son**, **Ivan** and **Jawad** – for providing us the SiC samples.

The work in this thesis would not be possible without the technical support from **Johan**, **Hans**, **Tom S.**, **Herman**, **Frits**, **Arjun**, **Marleen** and **Anna**. Thank you all for being promptly helpful and thinking along to solve all issues that arise when we're doing experiments, or trying to get around bureaucratic sinkholes. Also thank you to the cryogenics department team, for keeping the liquid helium flowing.

One of the reasons I decided to work in the Quantum Devices group was the work environment and the small group, where we were able to harness the best of our abilities and interests for a common goal. With **Tom**, **Gerjan** and **Joop** this has worked out superbly! Thank you for your patience in teaching me all sorts of experimental tricks. Tom, I hope life in Denmark is treating you well! Joop, thank you so much for translating my summary to dutch. I was also able to work with (and most importantly learn from) amazing students in the last few years. **Freddie**, thank you for bearing with me through my first year as a PhD candidate, when I was still trying to figure things out! I am glad we were able to collaborate time and time again after that. **Irina**, Covid hit halfway into your Master project. Despite the chaos, you were able to deliver work that led to a publication I am very proud of. I hope you are too! **Wastu** and **Pieter**, I still consult your Bachelor theses every once in a while. Thank you for the effort you've put into it.

The Zernike Institute as a whole is full of people who have been gracious enough to offer me mentorship – both professional and personal. **Marcos**, I have had the pleasure of collaborating with you in a publication together, and the even bigger pleasure of calling you a friend. It is funny to see that we are very similar in a lot of ways, but also so different in so many others. I hope I can count on your support for years to come. **Bart**, I have always enjoyed our discussions – whether it's in a group meeting or over a few beers. **Petra** and **Tamalika**, you two have been such important examples and mentors to me, since my Master's studies.

I joined the Physics of Nanodevices group in 2014. Since then, so many people have come and gone that I could not possibly list them all here without unfairly forgetting someone. Thus, I will just leave a note of my heartfelt appreciation to all of you. Our weekly science discussions were truly inspiring, and I learned so much! By name, I will mention our lunch crowd: **Christian** (thank you so much for the friendship, and for hosting me in Munich. I hope we can meet more often in a post-Covid era), **Julian**, **Jorge** (I miss you so much in the office, dear friend! I still owe you a visit in Salamanca to pick up my sunglasses), **Dennis**, **Talieh**, **Pep**, **Alexey**, **Frank**, **Sytze**. Our lunches were always a much-needed break.

I have also enjoyed learning about the ins and outs of University management in the Board of the Graduate School and the PhD Council of the FSE. Thank you **Marco Koopman** and **Ika Neven** for all the support in that realm. I hope to see the new development forms for PhD candidates that we worked on together implemented soon. Thank you also to all members, past and current, of the PhD council, **Monique**, **Renate**, **Vincent**, **Alka**, **Yvonne**, **Laurent**, **Taichi**, for all the borrels, courses and workshops planned together.

To my Topmaster companions, **Saurabh**, **Tian**, **Arjan**, **Henry**, **Herman**, **Arash**, **Michael**, **Jeroen**, **Chen**, **Ivar**, I am happy to see where you all are four years down the road. Saurabh, you are such a great friend, I hope we will keep each other posted no matter where we end up! Tian and Arjan, thank you also for being such awesome office mates!

My Brazilian crowd, **Amandinha** (miss you so very deeply!), **Tabitha**, **Renato**, **Marina**, **Leo**, **Marcel**, **Héctor** and **Heika** (not Brazilians yet, but very welcome *agregados*). You have been family away from family, and kept me connected when the homesickness hit. We have enjoyed all sorts of happy, angry, sad moments together. I am glad we partied so much during 2019, little did we know what was coming next! I know our bond will outlast our time in Groningen, and this brings me excitement. **Cloudy**, thank you for helping us keep some order. **Obed**, my partner of house, lockdown and, now, of daily joys and struggles. Thank you for so graciously enduring all my strong opinions. I am my happiest with you.

At last, my paranymphs. **Xu**, you went from being my supervisor to being one of the most loyal and enriching presences in my life since then! I am eager to see what you come up with in life, and I will keep bugging you for a long time, beware! I hope your new job in Munich brings you a world of happiness. **Rapha**, my first *husband*. You made Groningen feel like home to me, and you are probably the person who knows me best (the good and the bad) nowadays. We were always so in sync, and I am happy that, despite some bumps in the road every once in a while, we keep being each others' biggest supporters!

Finally, those who matter most. **My parents**, who have always nurtured our curiosity and provided the best possible example that questioning things is a fundamental part of life. I am only here today because of you. My siblings, **Rafa** and **Paula**. I feel like I grew closer to you two after moving away (be it age or something else), and I feel so lucky for this. Paula, you have grown into one of the kindest, most thoughtful persons I know. I am so proud of you. Rafa, our first beer together as a pair of grown-ups during my visit to New York is one of the highlights of my adult life. The hardest part about this path I've chosen is to be far away from the four of you.

Carmem M. Gilardoni
Groningen, October 2021

List of Publications

1. C. M. Gilardoni *et al.*, *Spectroscopy and time-resolved dynamics of vanadium defects in SiC*, in preparation [chapter 6].
2. C. M. Gilardoni, I. Ion, F. Hendriks, M. Trupke and C. H. van der Wal, *Hyperfine-mediated transitions between electronic spin-1/2 levels of transition metal defects in SiC*, New Journal of Physics **23**, 083010 (2021) [chapter 5].
3. C. M. Gilardoni, F. Hendriks, C. H. van der Wal, and M. H. D. Guimarães, *Symmetry and control of spin-scattering processes in two-dimensional transition metal dichalcogenides*, Physical Review B **103**, 115410 (2021) [chapter 7].
4. C. M. Gilardoni[1], T. Bosma[1], D. van Hien, F. Hendriks, B. Magnusson, A. Ellison, A. Gällström, I. G. Ivanov, N. T. Son, C. H. van der Wal, *Spin-relaxation times exceeding seconds for color centers with strong spin-orbit coupling in SiC*, New Journal of Physics **22**, 103051 (2020) [chapter 4].
5. T. Bosma[1], G. J. J. Lof[1], C. M. Gilardoni, F. Hendriks, O. V. Zwier, B. Magnusson, A. Ellison, A. Gällström, I. G. Ivanov, N. T. Son, R. W. A. Havenith, C. H. van der Wal, *Identification and tunable optical coherent control of transition-metal spins in silicon carbide*, npj Quantum Information **4**, 48 (2018) [chapter 3].

---

[1] These authors contributed equally to this work

Curriculum Vitæ

Carmem Maia Gilardoni

18-02-1993 Born in Brasilia, Brazil.

Education

2017–2021 Ph.D. research in the Zernike Institute for Advanced Materials
University of Groningen, the Netherlands
Thesis: Optically addressable spins in silicon carbide and related 2D materials
Promotor: Prof. dr. ir. C. H. van der Wal

2015–2017 Top Master of Nanoscience
University of Groningen, the Netherlands
Thesis: Transport properties of graphene field-effect transistors functionalized with photosystem I
Promotor: Prof. dr. ir. C. H. van der Wal

2011-2014 Bachelor degree in Physics
Universidade de Brasília, Brazil

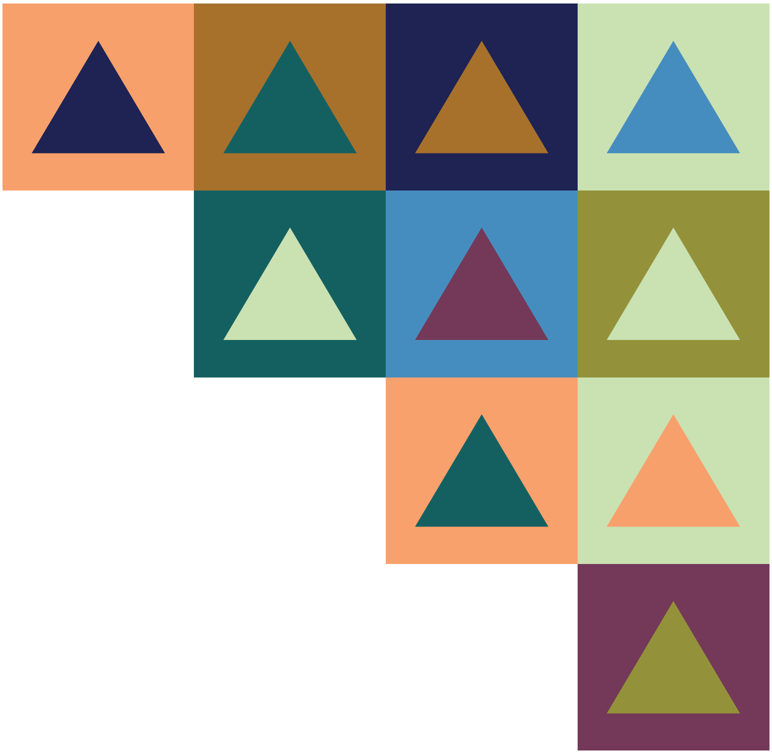

university of
groningen

faculty of science
and engineering

zernike institute for
advanced materials

Zernike PhD thesis series 2021/32
ISSN: 1570-1530